UNIVERSITÉ DU QUÉBEC À CHICOUTIMI

THESIS PRESENTED TO THE

UNIVERSITY OF QUEBEC AT CHICOUTIMI

IN PARTIAL FULFILLMENT OF

THE REQUIREMENT FOR THE DEGREE OF

DOCTOR OF PHILOSOPHY IN ENGINEERING

BY

JACOBO HERNANDEZ SANDOVAL

IMPROVING THE PERFORMANCE OF 354 TYPE ALLOY

AUGUST 2010

UNIVERSITÉ DU QUÉBEC À CHICOUTIMI

THÉSE PRÉSENTÉE À

L'UNIVERSITÉ DU QUÉBEC À CHICOUTIMI

COMME EXIGENCE PARTIELLE

DU DOCTORAT EN INGÉNIERIE

PAR

JACOBO HERNANDEZ SANDOVAL

AMÉLIORATION DE LA PERFORMANCE DES ALLIAGES DE TYPE 354

AOÛT 2010

RÉSUMÉ

En plus de réduire le poids des véhicules et de diminuer la consommation de carburant et les émissions polluantes, les efforts de recherche en cours dans l'industrie automobile ont été axées sur l'amélioration des performances à haute température des composants clés du moteur en particulier en ce qui concerne la préservation des propriétés mécaniques des alliages d'aluminium moulés utilisés dans ces composants à des températures de 200°C à 300°C. L'utilisation de nickel et de zirconium comme éléments d'ajouts pour accroître la résistance à haute température dans ces alliages est basée sur la formation des précipités de Al_3Ni et Al_3Zr reconnus pour leur stabilité à des températures élevées, ces particules sont en mesure de mieux supporter le survieillissement à des températures plus élevées que les précipités de Al_2Cu et Mg_2Si normalement présents dans les alliages d'aluminium moulés.

L'objectif principal du présent travail de recherche était de déterminer les effets des ajouts mineurs de nickel et de zirconium, ainsi que des dispersoïdes Al_2O_3 et SiC, sur la résistance à haute température des alliages de fonderie 354. Des expérimentations basées sur l'analyse thermique ont été menées pour acquérir une compréhension des principaux constituants de la microstructure des alliages, tels que les phases intermétalliques et les précipités, ainsi que leur évolution au cours du vieillissement à différentes températures et temps, à savoir 155°C, 170°C, 190°C, 240°C , 300°C et 350°C pendant des périodes allant de 2 à 100 heures. Les propriétés de traction des échantillons tels que coulés et traités thermiquement ont été déterminées à température ambiante et à haute température (190°C, 250°C, 350°C) pour les alliages sélectionnés/conditions basées sur les résultats obtenus des tests à température ambiante. Les échantillons ont été produits dans une moule permanent métallique ASTM-B108. Les résultats des essais de traction ont été examinés en terme des caractéristiques microstructurales des alliages correspondants, afin d'analyser et de comprendre les principaux paramètres impliqués dans le renforcement de l'alliage 354 à des températures élevées.

Les résultats montrent que, comme pour l'alliage 319 qui présente des réactions associées à de phases contenant du Cu, l'alliage 354 présente des réactions bien définies à des températures inférieures à 500°C liés aux phases contenant du Cu. Le zirconium réagit seulement avec Ti, Si et Al. Les phases intermétalliques riches en Zr observées dans cette étude se présentent sous deux formes différentes: la phase $(Al, Si)_2(Zr, Ti)$ contenant une forte teneur en silicium et ayant la forme d'un bloc, et la phase $(Al, Si)_3(Zr, Ti)$ contenant une forte teneur en d'aluminium et ayant la forme d'une aiguille. Il n'y a pas d'empoisonnement observable dans l'affinage de la taille des grains après l'addition de Zr dans les alliages étudiés comme cela a été observé dans les microstructures des échantillons d'analyse thermique obtenues à haute vitesse de refroidissement, pour les alliages contenant du Zr et Ti. Les expériences d'analyse thermique réalisées à la haute vitesse de refroidissement, à savoir 4°C sec^{-1}, ont révélé la présence d'une réaction dans la gamme de

température de 667-671°C, qui semble être liée à la précipitation de la phase riche en Zr, qui n'était pas possible d'observer à faible vitesse de refroidissement de 0,35°C sec^{-1}.

L'utilisation des graphiques d'indice de qualité est une méthode jugée satisfaisante pour la présentation des résultats des essais de traction, et pour évaluer les effets des ajouts de Ni, Zr et des micro-particules (Al_2O_3, SiC) à l'alliage de base, ainsi qu'une évaluation des conditions de traitements thermiques appliqués aux sept alliages de type 354 étudié en relation avec lesdites propriétés. À partir des graphiques d'indice de qualité construits pour ces alliages, l'indice de qualité atteint les valeurs minimales et maximales, 259 MPa et 459 MPa, pour les conditions tel que coulé et mise en solution, ainsi que les limites d'élasticité maximales et minimales observées sont de 345 MPa et de 80 MPa, respectivement, dans toute la série de vieillissement. L'ajout de faible pourcentage de micro-oxydes/carbures (0.5%) à l'alliage 354 n'a pas amélioré les propriétés de traction, mais favorise l'apparition de défauts tels que la ségrégation des micro-particules et la porosité, qui diminue les propriétés de traction. Une diminution des propriétés de traction de 10% par l'ajout de 0,4% de nickel est attribuée à la relation entre le nickel et le cuivre qui interfère avec la formation de précipités Al_2Cu. La phase aiguille $(Al,Si)_3(Zr,Ti)$ est l'élément principal dans les microstructures des échantillons de traction des alliages avec des additions de Zr. La réduction des propriétés mécaniques causée par l'addition de différents éléments est attribuée principalement à l'augmentation du pourcentage des intermétalliques formés lors de la solidification; ces particules agiraient comme des concentrateurs de contraintes diminuant la ductilité des alliages. Les résultats des essais de traction à température ambiante montrent une légère augmentation (10%) dans les alliages avec Zr et Zr/Ni, en particulier à des températures de vieillissement supérieures à 240°C. Le principal effet de l'addition de Zr est une réduction drastique de la taille des grains, de ~40%, à comparer à l'alliage de base, plutôt que d'accroître les propriétés mécaniques à température ambiante. L'ajout de Zr et Zr/Ni augmente les propriétés de traction à température élevée, en particulier pour les alliages avec 0,2% Zr et 0,2% Ni, lesquels augmentent de plus de 30% les propriétés en traction à 300°C par rapport à l'alliage de base. En résumé, les meilleures propriétés de traction à haute température apparaissent pour l'alliage contenant 0,2% Zr +% 0.2% Ni à la condition telle que coulée.

ABSTRACT

In addition to reducing vehicle weight and lowering fuel consumption and emissions, current research efforts in the automotive industry have been focused on improving the high temperature performance of key engine components, specifically in relation to preserving the mechanical properties of the cast aluminum alloys used in such components at temperatures of 200°C to 300°C. The use of nickel and zirconium as additions to increase high temperature strength in these alloys is based on the production of Al_3Ni and Al_3Zr precipitates. Known for their stability at elevated temperatures, such particles are better able to support overaging at higher temperatures than the Al_2Cu and Mg_2Si precipitates normally present in cast aluminum alloys. Dispersoids in the form of the micro-particulates Al_2O_3 and SiC in aluminum are also useful in applications requiring high temperature strength.

The principal aim of the present research work was to investigate the effects of minor additions of nickel and zirconium, as well as of the micro-ceramic dispersoids Al_2O_3 and SiC, on the strength of cast aluminum alloy 354 at high temperatures. Thermal analysis experiments were conducted to acquire an understanding of the principal microstructural constituents of the alloys, such as phases, intermetallics, and precipitates, and their evolution during aging at different temperatures and times, namely 155°, 170°, 190°, 240°, 300°, and 350°C for times ranging from 2 to 100 hours. Tensile properties of the as-cast and heat-treated alloys were determined at room temperature and at high temperatures (190°, 250°, 350°C) for selected alloys/conditions based on the room temperature tensile data. The tests were carried out on ASTM B-108 permanent mold test bars. The tensile test results were examined in light of the microstructural features of the corresponding alloy samples, in order to analyze and understand the major parameters involved in the strengthening of alloy 354 at high temperatures.

The results show that, similar to the case of 319 alloys, reactions corresponding to precipitation of Cu-containing phases are also observed in the 354 alloy at temperatures below 500°C. Zirconium reacts only with Ti, Si, and Al. The Zr-rich intermetallic phases observed in this study appears in two different forms: the phase $(Al,Si)_2(Zr,Ti)$ containing high levels of silicon which is block-like in form, and the phase $(Al,Si)_3(Zr,Ti)$ containing high levels of aluminum, which appears in needle-like form. There is no observable poisoning effect on the refinement of grain size after the addition of Zr to the alloys investigated in this study, as was observed from the macrostructures of the thermal analysis samples obtained at high cooling rates, for the alloys containing Zr and Ti. In the thermal analysis experiments carried out at a higher cooling, namely 4°C sec^{-1}, there is an observable reaction within the temperature range of 667°-671°C which appears to be related to the precipitation of Zr-rich phases; it was not possible to observe this reaction at the lower general cooling rate of 0.35°C sec^{-1}.

The use of quality index charts was judged as a satisfactory means of presenting the tensile test results, and for assessing the effects of the Ni, Zr and micro-particulate (Al_2O_3, SiC) additions to the base alloy, as well as evaluating the heat treatment conditions applied to the seven 354 type alloys studied in relation to said properties. From the quality index

charts constructed for these alloys, Quality index attains minimum and maximum values, 259 MPa and 459 MPa, in the as-cast and solution-treated conditions; as well as maximum and minimum yield strengths are observed at 345 MPa and 80 MPa, respectively, within the whole series of aging treatments applied. The addition of low percentage of micro-oxides/carbides (0.5wt%) to alloy 354 did not improve the tensile properties, but rather promoted the occurrence of defects such as segregation of micro-particles and porosity, which decreased the tensile properties. A decrease in tensile properties of ~10% with the addition of 0.4 wt% nickel is attributed to a nickel-copper reaction which interferes with the formation of Al_2Cu precipitates. The needle-like phase $(Al,Si)_3(Zr,Ti)$ is the main feature in the microstructures of the tensile samples of alloys with Zr additions. The reduction in mechanical properties due to addition of different elements is attributed principally to the increase in the percentage of intermetallic phases formed during solidification; such particles would act as stress concentrators, decreasing the alloy ductility. Tensile test results at ambient temperatures show a slight increase (10%) in alloys with Zr and Zr/Ni additions, particularly at aging temperatures above 240°C.The principal effect of Zr addition lies in a drastic reduction of grain size, of ~40%, compared with the grain size of the base alloy, rather than in increasing mechanical properties at ambient temperature. Additions of Zr and Zr+Ni increase the high temperature tensile properties, in particular for the alloy containing 0.2 wt% Zr + 0.2 wt% Ni, which exhibits an increase of more than 30% in the tensile properties at 300°C compared with the base 354 alloy. In summary, the best high temperature tensile properties are displayed by the alloy containing 0.2 wt% Zr + 0.2wt% Ni in the as-cast condition.

AKNOWLEDGEMENTS

I thank God for my beautiful life.

I would like to express my gratitude to my supervisors, Professors F. H. Samuel and A. M. Samuel for their support and hard work during the different stages of my studies at UQAC. I appreciate the participation and cooperation of Dr. Lyne St-Georges and Dr. Herbert Dotty during the research. I would like to extend my sincere gratitude to the TAMLA group members: Alain Bérubé, Mathieu Paradis and Mme Sinclair. My best regards to all of them for their invaluable assistance.

I wish to express my grateful thanks to the Natural Sciences and Engineering Research Council of Canada (NSERC), General Motors Powertrain Group (U.S.A.), Corporativo Nemak (Mexico), and the Fondation de l'Université du Québec à Chicoutimi (FUQAC) for offering me their financial support in the form of a scholarship. Special thanks to Dr. Salvador Valtierra who gave me the opportunity to come to Chicoutimi.

Finally, I would like to acknowledge the members of my family, my parents, Francisco Hernández Polina and Bertha Sandoval Dimas, my aunt Oralia Hernández Polina, my brother Abraham and my sister Patricia, all of them, for loving and encouraging me to be a better man.

TABLE OF CONTENTS

RÉSUMÉ ..... **i**

ABSTRACT ..... **iii**

AKNOWLEDGEMENTS ..... **v**

TABLE OF CONTENTS ..... **vi**

LIST OF TABLES ..... **x**

LIST OF FIGURES ..... **xii**

CHAPTER 1 INTRODUCTION **1**

1.1 Introduction 2

1.2 Objectives 4

CHAPTER 2 REVIEW OF THE LITERATURE **6**

2.1 Introduction 7

2.2 Recycling and Cast Aluminum Alloys 7

2.3 Al-Si Casting Alloys 9

2.4 Al-Si-Cu and Al-Si-Cu-Mg Alloys 11

2.5 Alloy 354 13

2.6 Melt Treatment of Eutectic Al-Si Alloys 13

2.6.1 Chemical Modification in Eutectic Al-Si Alloys 14

2.6.2 Chemical Grain Refinement in Eutectic Al-Si Alloys 16

2.6.3 Titanium-Boron Refinement 18

2.7 Heat Treatment of Cast Aluminum Alloys 19

2.7.1 Age Hardening of Cast Aluminum Alloys 19

2.7.2 Solution Heat Treatment 20

2.7.3 Quenching 25

2.7.4 Artificial Aging 25

2.8 Effects of Temperature on Cast Aluminum Alloys 29

2.9 Effects of Micro-Ceramic Particulates (Al_2O_3 and SiC) on Mechanical Properties in Cast Aluminum Alloys 34

2.10 Effects of Zirconium on Cast Aluminum Alloys 37

2.11 Effects of Nickel on Cast Aluminum Alloys 40

2.12 Quality Index Charts 42

CHAPTER 3 EXPERIMENTAL PROCEDURES 49

3.1 Introduction 50

3.2 Schedule for Experimental Procedures 52

3.3 Materials and Procedures 54

3.3.1 Materials 54

3.3.2 Castings 59

3.3.3 Heat Treatment 61

3.4 Mechanical Tests 62

3.4.1 Tensile Tests at Room Temperature 62

3.4.2 High Temperature Tensile Tests 64

3.5 Characterization of the Microstructure 66

3.5.1 Thermal Analysis 66

3.5.2 Optical Microstructure 68

3.5.3 Electron Probe Microanalysis. 69

CHAPTER 4 MICROSTRUCTURE OF THERMAL ANALYSIS SAMPLES 71

4.1 Introduction 72

4.2 Chemical Analysis and Volume Fraction 74

4.3 Thermal Analysis: Alloys A, D, E, F, and G 76

4.3.1 Alloy A 76

4.3.2 Alloy D 80

4.3.3 Alloy E 85

4.3.4 Alloy F 87

4.3.5 Alloy G 89

4.4 Thermal Analysis for Detection of Zr-rich Phases 95

CHAPTER 5 AMBIENT AND HIGH TEMPERATURE TENSILE PROPERTIES 110

5.1 Introduction 111

5.2 Microstructure of Tensile Test Samples 112

5.2.1 Difference between Thermal Analysis and Tensile Test Samples 112

5.2.2 Alloy A 113

5.2.3 Microstructural Features of Tensile Test Samples. 117

5.2.4 Micro-particulates Al_2O_3 and SiC in the microstructure of tensile test samples of alloys B and C 120

5.2.5 Alloy D 124

5.2.6 Alloys with Zr (Alloys E, F, and G) 124

5.3 Tensile Results for Alloy A 129

5.4 Mechanical Properties of Alloys A, B, and C (Effects of micro-particulates) 150

5.5 Alloy D (Effects of 0.4 wt. pct. Ni) 162

5.6 Alloy E (Effects of 0.4 wt. pct. Zirconium) 167

5.7 Alloy F (Effects of 0.4 wt. pct. Zr + 0.4 wt. pct. Ni) 172

5.8 Alloy G (Effects of 0.2 wt. pct. Zr + 0.2 wt. pct. Ni) 177

5.9 The Obtainable Quality Parameter ($Q_{Obtainable}$) 181

5.10 High Temperature Tensile Tests 184

CHAPTER 6 CONCLUSIONS AND RECOMMENDATIONS 190

6.1 Conclusions 191

6.2 Recommendations for future work 194

REFERENCES 195

APPENDIX I 209

LIST OF TABLES

Table 2.1 Composition of common aluminum-silicon casting alloys (a) [16] 10

Table 2.2 Characteristics of aluminum-silicon casting alloys[16] 12

Table 2.3 Minimum mechanical properties[15] for casting alloy 354[a] (T6[b]) at room temperature. 13

Table 2.4 Summary of Elevated-Temperature Fracture Behavior[48] 32

Table 3.1 Artificial aging conditions used for room temperature tensile tests 53

Table 3.2 Chemical composition of the as-received 354 alloy 54

Table 4.1 Chemical composition of the alloys used in this work (wt%) 75

Table 4.2 Volume fraction of undissolved phases observed in the matrix of alloys A through G used for this research. 75

Table 4.3 Grain Size and SDAS values observed in the alloys studied 76

Table 4.4 Proposed main reactions occurring during solidification of alloys A, D, E, F, and G [29,102,108,109] 77

Table 4.5 WDS analysis of phases observed in Alloy A 80

Table 4.6 WDS analysis of phases observed in Alloy D 83

Table 4.7 WDS analysis of phases observed in Alloy E 86

Table 4.8 WDS analysis of phases observed in Alloy F 87

Table 4.9 WDS analysis of phases observed in Alloy G. 91

Table 4.10 Chemical composition of the alloys used for thermal analysis at $4°Cs^{-1}$ 98

Table 4.11 Suggested precipitated phases for thermal analysis peaks observed during solidification of experimental alloys J1 to J4 100

Table 4.12 WDS Analysis of the Phases Observed in Alloy J2 103

Table 4.13 WDS Analysis of the Phases Observed in Alloy J3 104

Table 4.14 WDS Analysis of the Phases Observed in Alloy J4 105

Table 5.1 SDAS, Porosity %, Grain Size, Level of Modification, and Volume Fraction of Intermetallics for Alloys A through G 118

Table 5.2 Silicon Particle Characteristics for Alloys A through G. 120

Table 5.3 Characterization of Micro-Oxides in Tensile Test Samples 121

Table 5.4 Mechanical Values, UTS, YS and %Elongation for Alloy A 129

Table 5.5 Tensile test results for Alloy A, solution heat-treated condition 136

Table 5.6 Mean values of UTS, YS, Total and Plastic Strain obtained for Alloy A subjected to different heat treatment conditions; Q values obtained with Eq. 2.10 140

Table 5.7 K and n values obtained for Alloy A from single sample σ-ε plots; Q values obtained from Equation 2.9 141

Table 5.8 Mean values of UTS, YS, and Plastic Strain; Q values obtained using Equation 2.10 applying a single K=500 MPa for Alloy A at 190°C. 148

Table 5.9 K and n values obtained for Alloy A from the single sample σ-ε plots; Q values obtained from Equation 2.9 148

Table 5.10 Standard deviation calculation from the UTS values obtained for Alloy A at 170°C aging temperature and different aging times 158

Table 5.11 Obtainable Q parameters observed for the alloys used in this study 182

Table 5.12 Tensile properties of Alloy 354-T6 (from Reference 88) 185

Table 5.13 Tensile properties values at different test temperatures 185

LIST OF FIGURES

Figure 1.1 Plot from a presentation showing a particular requirement in the automotive market related to high temperature performance, as expressed by the *customer voice.*[1] 2

Figure 2.1 Portion of the equilibrium binary Al-Si phase diagram. 11

Figure 2.2 Schematic diagram of impurity induced twinning. A punctual defect (modifier atom in black) is presented during the solidification process causing twinning on the solidification front which crystallizes after the absorption of the modifier atom.[19] 15

Figure 2.3 Alloy 319 (a) unmodified, and (b) modified with 0.012 wt% Sr. 16

Figure 2.4 Portion of the Al-Ti phase diagram and a schematic representation of the nucleation of α (Al) through the peritectic reaction in the Al-Ti system.[22] 17

Figure 2.5 Macrographs of Alloy 319 (SDAS = 40μm); (a) not refined, and (b) refined with 0.01% of TiB_2. 19

Figure 2.6 Hypothetical phase diagram. 20

Figure 2.7 Diagram showing the three steps for precipitation hardening. 21

Figure 2.8 Cooling curve and its first derivative curve of the 319 alloy (0% wt Sr). 23

Figure 2.9 Schematic characterization of the three stages of spheroidization and coarsening of the eutectic silicon phase. 24

Figure 2.10 Optical micrographs of the microstructures of (a) as-cast, and (b) solution heat treated (SHT) samples of an Al-Si-Mg alloy. 24

Figure 2.11 Schematic diagram showing: a) particle coherent with the matrix, and b) non-coherent particle within the matrix. 26

Figure 2.12 Schematic diagrams showing the Orowan dislocation process of interaction between dislocations and precipitates. 26

Figure 2.13 Schematic diagram showing the evolution of precipitates from a coherency zone to a non-coherency zone during the process of aging affecting the hardness of an aluminum alloy. 27

Figure 2.14 Schematic diagram showing the stress-strain flow curves in a hypothetical alloy where there exist different behaviors related to the coherency (or non-coherency) between matrix and precipitates. 28

Figure 2.15 Typical stress-strain curves for permanent-mold A356-T6 castings at various temperatures (exposure time = 1hr).[17] 30

Figure 2.16 Schematic showing classification of the type of fracture at different test temperatures for the study of an A356 alloy (SCU = sand cast, unmodified; SCM = sand cast, modified; PM = permanent mold). [48] 33

Figure 2.17 (a) $L1_2$, (b) DO_{22}, and (c) DO_{23} structures.[83] 39

Figure 2.18 Al rich Al-Zr binary phase diagram (adapted from Murray[84] with metastable Al_3Zr ($L1_2$) solvus calculated by Liu *et al.*[85, 86] 40

Figure 2.19 Al-Ni binary phase diagram (from P. Nash *et al.*[90]) 42

Figure 2.20 A quality index chart for alloy 356. The dashed lines represent the quality index chart as determined using Equations 2.1 and 2.2, after Drouzy *et al.*,[80] in which the iso-YS lines are identified by the yield stress value, while the iso-Q lines are identified by the Q-value. The solid lines are flow curves identified by the n-value and iso-q lines identified by the q-value, having been calculated using Equations 2.5 and 2.7, respectively, assuming $K = 430$ MPa.[97] 44

Figure 2.21 Effects of overaging in tensile properties of a 201 alloy.[98] 45

Figure 2.22 Interpretation of the Quality Index Chart generated by the Cáceres model.[101] .48

Figure 3.1 Diagram showing an overview of the experimental procedures followed for this work. 52

Figure 3.2 Microstructure (200x) of Alloy 354 used as a base alloy in this study 55

Figure 3.3 Microstructure (200x) of the TiB_2 master alloy used for the addition of titanium as a grain refiner 56

Figure 3.4 Microstructure (200x) of the Al-10%Sr master alloy used for the addition of strontium as a modifier of the silicon structure. 56

Figure 3.5 Microstructure (200x) of the 6061Aluminum alloy-20%Al_2O_3 master alloy used for the addition of Al_2O_3. 57

Figure 3.6 Microstructure (200x) of the 356Alloy-20%SiC master alloy used for the addition of SiC. 57

Figure 3.7 Microstructure (200x) of the Al-20%Ni master alloy used for the addition of nickel. 58

Figure 3.8 Microstructure (200x) of the Al-15%Zr master alloy used for the addition of Zr. 58

Figure 3.9 Electrical resistance furnace. 59

Figure 3.10 Degassing system. 60

Figure 3.11 ASTM B108 metallic mold. 60

Figure 3.12 Lindberg Blue M electric furnace. 61

Figure 3.13 Measurements of the tensile test bars used in this study. 62

Figure 3.14 MTS Mechanical Testing machine. 63

Figure 3.15 Position of the extensometer used in the tensile tests. 63

Figure 3.16 Instron Universal Mechanical Testing machine. 65

Figure 3.17 Electrical resistance forced air box type furnace and extensometer cooled by circulating water 66

Figure 3.18 Electrical resistance furnaces and the graphite molds used in the thermal analysis experiments. 67

Figure 3.19 Diagram showing the sectioned area for analysis of tensile samples using optical microscopy. 68

Figure 3.20 Optical microscope - Image analysis setup. 69

Figure 3.21 Electron Probe Microanalyzer. 70

Figure 4.1 Diagram of an ideal solidification curve showing the parameters which characterize the cooling rates. 73

Figure 4.2 Plot correlating SDAS and cooling rates for alloy 354 in the experiments carried out for this thesis. 74

Figure 4.3 Temperature-time plot and first derivative from the thermal analysis of alloy A. 77

Figure 4.4 Microstructure at 200x magnification of alloy A from thermal analysis sample obtained at a low cooling rate of 0.35°C sec^{-1} 78

Figure 4.5 Backscattered image showing some of the phases observed in alloy A. 79

Figure 4.6 Temperature-time plot and first derivative from the thermal analysis of alloy D. 81

Figure 4.7 Microstructure at 200x magnification in alloy D from thermal analysis samples obtained at a low cooling rate of 0.35 °C sec^{-1} 82

Figure 4.8 Backscattered image of alloy D from thermal analysis sample obtained at a low cooling rate of 0.35 °C sec^{-1}. 83

Figure 4.9 Temperature-time plot and first derivative from the thermal analysis of alloy E. 85

Figure 4.10 Microstructure at 200x magnification in alloy E from thermal analysis sample obtained at a low cooling rate of 0.35 °C sec^{-1}. The black arrows point to the Al-Si-Zr-Ti phases observed in the alloy. 85

Figure 4.11 Backscattered image of alloy E from thermal analysis sample obtained at a low cooling rate of 0.35 °C sec^{-1}. 86

Figure 4.12 Temperature-time plot and first derivative from the thermal analysis of alloy F. 88

Figure 4.13 Microstructure at 200x magnification in alloy F from thermal analysis sample obtained at a low cooling rate of 0.35 °C sec^{-1}. The black arrows point to the Al-Si-Zr-Ti phases observed in the alloy. 88

Figure 4.14 Backscattered image of alloy F from thermal analysis sample obtained at a low cooling rate of 0.35 °C sec^{-1}. 89

Figure 4.15 Temperature-time plots and their first derivatives from the thermal analysis of alloy G. 89

Figure 4.16 Microstructure at 200x magnification in alloy G from thermal analysis samples obtained at a low cooling rate of 0.35 °C sec^{-1}. The black arrows point to the Zr-rich phases. 90

Figure 4.17 Backscattered image of alloy G from thermal analysis sample obtained at a low cooling rate of 0.35 °C sec^{-1}. 90

Figure 4.18 High-magnification backscattered image taken from alloy E showing the presence of both $(Al,Si)_2(Zr,Ti)$ and $(Al,Si)_3(Zr,Ti)$. 92

Figure 4.19 (a) EDX spectrum for $(Al,Si)_2(Zr,Ti)$, and (b) EDX spectrum for $(Al,Si)_3(Zr,Ti)$ phases. 92

Figure 4.20 X-ray images of (a) Al, (b) Si, (c) Ti, and (d) Zr corresponding to the $(Al,Si)_3(Zr,Ti)$ and $(Al,Si)_2(Zr,Ti)$ phases observed in the backscattered image of alloy E shown in Figure 4.18. 93

Figure 4.21 Backscattered image of alloy E (top right) showing the $(Al,Si)_2(Ti,Zr)$ and $(Al,Si)_3(Ti,Zr)$ phases and the corresponding X-ray images of Ti, Si, Zr, and Al. 94

Figure 4.22 Diagram of a hypothetical cooling curve showing recalescence. 95

Figure 4.23 Thermal analysis plots of the experimental alloys J1 to J4 (at $4°Cs^{-1}$). 98

Figure 4.24 Optical micrograph of alloy J1 taken at a magnification of 200x 101

Figure 4.25 Optical micrograph of alloy J2, taken at a magnification of 200x. The black arrows point to Zr-rich phases. 101

Figure 4.26 Optical micrograph of alloy J3, taken at a magnification of 200x. The black arrows point to Zr-rich phases. 102

Figure 4.27 Optical micrograph of alloy J4, taken at a magnification of 200x. The black arrows point to Zr-rich phases. 102

Figure 4.28 Optical micrograph of J4 alloy taken at a magnification of 500x, showing the presence of a Zr-Ti phase particle (thick, light grey particle) 103

Figure 4.29 Equilibrium Al-rich, Al-Zr binary phase diagram[125] showing the percentages of Zr used for this work. 106

Figure 4.30 Grain size plotted against recalescence, (ΔT_{R-U}), for a 356 alloy solidified at two cooling rates.[128] 108

Figure 5.1 Difference between the thermal analysis and tensile test samples for Grain Size and Secondary Dendrite Arm Spacing (SDAS). 113

Figure 5.2 Macrograph showing grain size in an as-cast tensile test sample of alloy A...114

Figure 5.3 Micrograph of a tensile test specimen of alloy A showing the microstructure in the as-cast condition.....115

Figure 5.4 Micrograph of a tensile test specimen of alloy A showing the microstructure after solution heat treatment.....115

Figure 5.5 Model of granulation of unmodified eutectic Si during heat treatment. [134] (a) Transport of Si with the cooperation of Al starts; (b) transport continues after fragmentation; (c) eutectic Si becomes spheroidized. 116

Figure 5.6 Grain size in Alloys A through G. 119

Figure 5.7 Microstructure of alloy B at 100x magnification showing the distribution of Al_2O_3 in the matrix.....122

Figure 5.8 Microstructure of alloy C at 100x magnification showing the distribution of SiC in the matrix. 122

Figure 5.9 Microstructure of alloy B at 100x magnification showing an aggregate of Al_2O_3 particles in the matrix.....123

Figure 5.10 Microstructure of alloy D (500x). 124

Figure 5.11 Microstructure of alloy E. The black arrows point to $(Al,Si)_3(Zr,Ti)$ phase particles (200x). 126

Figure 5.12 Microstructure of alloy E. The black arrows point to $(Al,Si)_3(Zr,Ti)$ phase particles (500x). 126

Figure 5.13 Microstructure of alloy F. The black arrows point to $(Al,Si)_3(Zr,Ti)$ phase particles (200x). 127

Figure 5.14 Microstructure of alloy F. The black arrows point to $(Al,Si)_3(Zr,Ti)$ phase particles (500x). 127

Figure 5.15 Microstructure of alloy G. The black arrows point to $(Al,Si)_3(Zr,Ti)$ phase particles (200x). 128

Figure 5.16 Microstructure of alloy G. The black arrows point to $(Al,Si)_3(Zr,Ti)$ phase particles (500x). 128

Figure 5.17 Ultimate Tensile Strength as a function of aging conditions in Alloy A. 131

Figure 5.18 Yield strength as a function of aging conditions in Alloy A. 131

Figure 5.19 Strain at fracture as a function of aging conditions in Alloy A. 133

Figure 5.20 Engineering stress-strain curve for Test 3 and corresponding UTS, YS, %Elongation (e_{Total}), $e_{plastic}$ and $e_{elastic}$ values. 136

Figure 5.21 True stress-true plastic strain flow curve for solution heat-treated Alloy A-Test 3, and the flow curve derived from the Holloman equation ($\sigma = K\varepsilon^n$) using K = 528 Mpa and n = 0.193. 138

Figure 5.22 Q and q values obtained from Equation 2.9 (Q) and Equation 2.6 (q). 143

Figure 5.23 Quality Index Chart for aging conditions corresponding to aging times of 2 hrs, 10 hrs, and 100 hrs at different aging temperatures. 144

Figure 5.24 Yield strength (YS) values and the strain-hardening exponent (n) plotted against the heat-treated condition in Alloy A. 146

Figure 5.25 Quality index chart for long exposure times at 190°C aging temperature. 149

Figure 5.26 Yield strength color-contour chart for alloy A corresponding to different aging conditions. 150

Figure 5.27 Yield strength color-contour chart for alloy B corresponding to different aging conditions. 151

Figure 5.28 Yield strength color-contour chart for alloy C corresponding to different aging conditions. 151

Figure 5.29 Quality color-contour chart for alloy A corresponding to different aging conditions; $Q=UTS + 0.4 \bullet K \bullet \log(\varepsilon_{plastic})$, where K=500MPa. 153

Figure 5.30 Quality color-contour chart for alloy B corresponding to different aging conditions; $Q=UTS + 0.4 \bullet K \bullet \log(\varepsilon_{plastic})$, where K=500MPa. 154

Figure 5.31 Quality color-contour chart for alloy C corresponding to different aging conditions; $Q=UTS + 0.4 \bullet K \bullet \log(\varepsilon_{plastic})$, where K=500MPa. 154

Figure 5.32 Quality index charts for alloy B. 156

Figure 5.33 Quality index charts for alloy C. 156

Figure 5.34 Quality index chart for long exposure times at 190°C aging temperature. 157

Figure 5.35 Mean standard deviation of the UTS values observed for the seven alloys studied, over the 13 aging conditions applied in this research. 159

Figure 5.36 Mean standard deviation of the %Elongation values observed for the seven alloys studied, over the 13 aging conditions applied in this research. 160

Figure 5.37 Yield Strength color-contour charts for alloys A and D corresponding to different aging conditions. 162

Figure 5.38 YS values plotted against aging time for aging temperatures of 155°C and 350°C for alloys A and D. 163

Figure 5.39 Quality index chart for alloy D corresponding to various heat treatment conditions. 165

Figure 5.40 Quality Index chart obtained for alloys D and A for long exposure times at 190°C aging-temperature. 166

Figure 5.41 YS color-contour charts for alloys A and E. 167

Figure 5.42 YS values plotted against aging time for aging temperatures of 155°C and 350°C for alloys A and E. 168

Figure 5.43 Strain color-contour charts for alloys A and E, showing the %El values obtained at various aging temperatures and times. 168

Figure 5.44 Percent elongation values plotted against aging time for aging temperatures of 155°C and 350°C for alloys A and E. 169

Figure 5.45 Quality index chart for alloy E corresponding to various heat treatment conditions. 170

Figure 5.46 Quality index chart obtained for alloys E and A for long-exposure times at 190°C aging temperature. 171

Figure 5.47 YS color-contour charts for alloys A and F. 173

Figure 5.48 YS values plotted against aging time for aging temperatures of 155°C and 350°C for alloys A and F. 173

Figure 5.49 Strain color-contour charts for alloys A and F, showing the %El values obtained at various aging temperatures and times. 175

Figure 5.50 Percent elongation values plotted against aging time for aging temperatures of 155°C and 350°C for alloys A and F. 175

Figure 5.51 Quality index chart for alloy F. 176

Figure 5.52 Quality index chart obtained for alloys F and A for long exposure times at 190°C aging-temperature. 177

Figure 5.53 YS color-contour charts for alloys A and G. 178

Figure 5.54 YS values plotted against aging time at aging temperatures of 155°C and 350°C for alloys A and G. 178

Figure 5.55 Quality index chart for alloy G. 180

Figure 5.56 Quality index chart obtained for alloys G and A for long exposure times at 190°C aging temperature. 181

Figure 5.57 Quality index chart for the alloys A, B, C, D, E, F, and G corresponding to as-cast and solution heat treated conditions. 183

Figure 5.58 Obtainable Q parameter (MPa) plotted against grain size (μm). 183

Figure 5.59 UTS values from experiments at ambient and at high temperature (Alloy A and Alloy 354 from Reference 88). 187

Figure 5.60 UTS values from experiments at ambient and at high temperatures for A through G alloys. 188

Figure 5.61 Vickers microhardness versus exposure time at 500°C in Al-Zr and Al-Zr-Ti alloys.[83] 189

CHAPTER 1

INTRODUCTION

CHAPTER 1

INTRODUCTION

1.1 Introduction

Cast aluminum alloys are an important group of materials which find wide application in the automotive industry. Current research efforts in this industry, based on the continued usage of traditional fuels such as oil or gasoline, are focused on reducing fuel consumption and decreasing fossil fuel emissions. Reduced fuel consumption and, consequently, lower emissions may be achieved either by significantly improving the efficiency of the car engine or by bringing about a sizeable reduction in total car weight. While some improvement in the efficiency of the car engine can be achieved by applying advanced materials and concepts, this may be unacceptable from an economic point of view. A reduction in the weight of key engine components together with higher service temperatures seems to allow for more efficient operation than hitherto. For these reasons, the aim of numerous research projects has always been to achieve a high output, in conjunction with outstanding efficiency of the designated alloys, making them applicable at higher temperatures. As may be seen in Figure 1.1, the ***customer voice***, or polled opinion, received from several automotive companies expressed an interest in exploring improvements related to high temperature performance, in this specific case, ones which would preserve the mechanical properties of cast aluminum alloys from 200°C to 300°C.

The task of improving the mechanical properties in an aluminum alloy at high temperatures should include the knowledge of several factors which are related principally to a decrease in the strength of the metal with increasing temperatures. This behavior is linked to the change or deterioration in the principal metallurgical parameters of the specific cast aluminum alloy during its performance at higher temperatures.

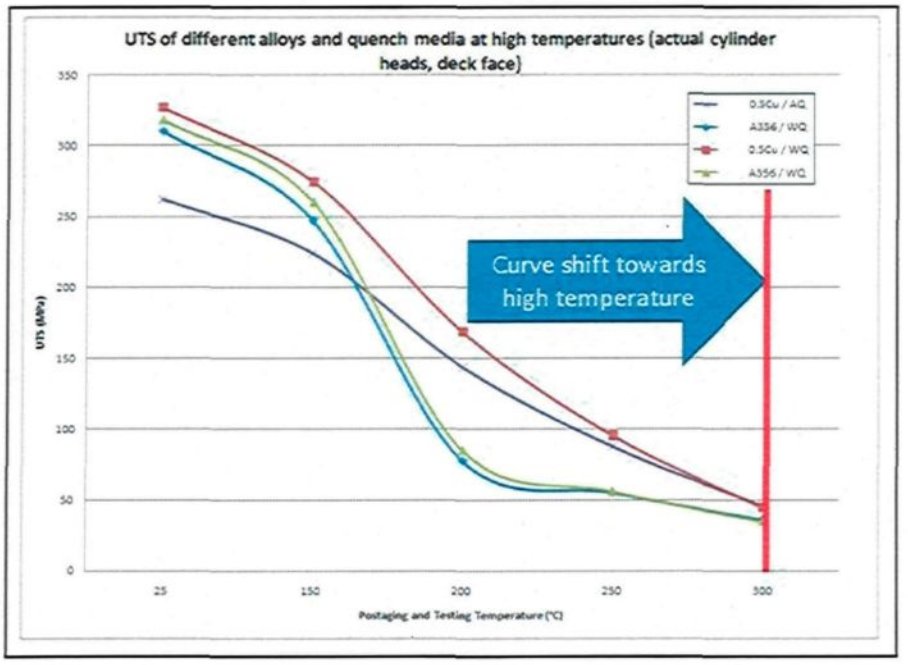

Figure 1.1 Plot from a presentation showing a particular requirement in the automotive market related to high temperature performance, as expressed by the *customer voice*.[1]

Aluminum silicon alloys are commonly used in the automotive industry principally because of their high-strength/low-weight relationship and their high castability. Such alloys are heat-treatable, *i.e.* their mechanical properties may be improved considerably following an appropriate heat treatment comprising solution heat treatment, quenching, and natural or artificial aging. Magnesium and/or copper may be added to these alloys where

they are responsible for the precipitation hardening which occurs during aging. For ideal strengthening, the second phase particles must be small and evenly distributed within the microstructure of the alloy. If the alloy is maintained at an elevated temperature for a certain period of time, however, the second phase particles Al_2Cu and Mg_2Si will dissolve or become larger in size, while a concurrent decrease in the mechanical properties of the alloy will also be observed.

The use of nickel and zirconium as additions to increase high temperature strength in aluminum alloys is based on the production of precipitates in the form of Al_3N and Al_3Zr, respectively; such particles are better able to support overaging at higher temperatures than precipitates normally present in cast aluminum alloys, *i.e.* Al_2Cu and Mg_2Si. The degree of strengthening is related to particle distribution in the ductile aluminum matrix. The volume fraction, the average particle diameter, and the mean interparticle spacing are the most important parameters in describing precipitation hardening. The presence of such coherent precipitates as Al_3Zr or Al_3Ni, which are essentially inert in the matrix, affects the strength of the material directly because they act as hard pinning points in the matrix inhibiting dislocation motion. The principal advantage of the precipitates formed is their stability at elevated temperatures; because of the low solubility of the finely dispersed second phase particles, these alloys can resist overaging and growth, thereby preserving their mechanical properties to a greater extent.

The strengthening of dispersoids in the form of the micro-oxides Al_2O_3 and SiC in aluminum occurs mainly as a result of the creation of dislocations resulting from differences in the coefficients of thermal expansion between the particles and the aluminum

matrix. While extremely low volume fractions are desirable in terms of ductility, dispersoid contents of as high as 15 volume percent have been used in applications requiring high temperature strength and creep resistance.

Insufficient studies have been carried out to date with regard to the mechanical performance of alloy 354 at room temperature and at high temperatures; nor has there been much research effectuated regarding the effects that small additions of elements or dispersoids tend to have on the mechanical properties of this alloy, again whether at room temperature or at elevated temperatures. Further research appears to be required in this respect with a view to acquiring greater detail concerning the mechanical behaviour of 354 alloys, whether in the presence or in the absence of minor additions of elements or dispersoids.

1.2 Objectives

The principal aim of the present research work is to investigate the effects of minor additions of the micro-ceramic dispersoids Al_2O_3 and SiC, as well as of nickel and zirconium, on the strength of the cast aluminum alloy 354 at high temperatures.

In order to meet this principal goal it is necessary to attain the following objectives:

(i) to acquire an understanding of the principal microstructural features of the alloys, such as phases, intermetallics, and precipitates, together with their identifying characteristics and evolution during controlled exposure at different temperatures and times;

(ii) to determine the tensile properties of the alloys studied, at room temperature, using the different aging conditions of temperature and time;

(iii) to obtain the high temperature tensile property values at different temperatures for the selected alloys or conditions based on the room temperature results of tensile testing.

(iv) to correlate the results obtained from the room temperature and high temperature tensile tests with the principal microstructural features observed in the corresponding alloy samples, in order to analyze and understand the major parameters involved in the strengthening of alloy 354 at high temperatures.

CHAPTER 2

REVIEW OF THE LITERATURE

CHAPTER 2

REVIEW OF THE LITERATURE

2.1 Introduction

This work is, on the whole, an attempt to investigate using minor additions of nickel, zirconium, and of the micro-ceramic particulates Al_2O_3 and SiC, as made to the cast aluminum alloy 354. The research also intends to examine the effects of these additions on the relevant mechanical properties at room temperature as well as at high temperatures.

The following sections refer to bibliographical research pertaining to the topics discussed in this work. The subjects addressed include (i) cast aluminum alloys and some of the melt treatments normally used in their fabrication process; (ii) heat treatment; (iii) the effects of temperature on aluminum casting alloys; (iv) the use of such dispersoids as Al_2O_3 and SiC in aluminum; (v) the effects of nickel and zirconium on aluminum alloys; and (vi) the use of Quality Index charts as a tool for evaluating the mechanical performance of different alloys.

2.2 Recycling and Cast Aluminum Alloys

Aluminum is the most abundant metallic element to be found in the earth's crust and, after oxygen and silicon, it is the third most abundant of all the elements. Because aluminum has the atomic number 13 with three electrons in its outer shell, it has a strong

affinity for bonding with other elements, particularly oxygen to form stable oxides, such as Al_2O_3, and silicates, such as Al_2SiO_5. This tendency is one of the reasons for which it is not found in its pure metallic form in nature, but in claylike material rich in aluminum oxide, usually in the form of bauxite. Bauxite deposits are found worldwide and have been used as the primary source for aluminum metal. The extraordinary quantity of energy required to produce aluminum from bauxite makes recycling this metal of great importance in the everyday life of modern society. It is estimated that to produce a given mass of aluminum from recycled scrap requires only 5% of the energy necessary to produce the same mass from virgin ore.[2] Recycled metal is a near perfect substitute for the primary metal given that the properties of metals, *i.e.* ductility and conductivity, are not lost when the metal is used and then ultimately scrapped.[2-7]

The use of cast aluminum alloys in the automotive market as a substitute for iron components, the density of aluminum being almost one-third that of iron, is put into effect principally to reduce the total weight of the manufactured vehicles. A lighter motor vehicle leads to the reduction of exhaust emissions as well as to improved crash characteristics by lowering the amount of kinetic energy involved; also, this improvement may be observed because certain light metals are able to perform better than steel in terms of energy absorption through plastic deformation in the event of a crash.[8-11]

The recycling of aluminum results in a more rational use of the non-renewable natural resources to save energy, thereby cutting down on waste disposal and reducing contaminant emissions.[12] The scrap material, mainly composed of secondary metals in processed form, is often cheap compared to the primary metal, since the costs for

exploration, mining, and the primary refining of aluminum oxides have already been deducted and the energy requirements are thus lower.[13] Cast aluminum alloys are produced almost in totality from recycled material; an extreme case of recyclability is the current use of alloy A319 in the automotive industries, often produced with a content of as much as 95% of secondary metal.[10, 14]

2.3 Al-Si Casting Alloys

Aluminum is a significant metal from an industrial viewpoint because of its technologically relevant qualities such as low density, regular mechanical properties, and good corrosion resistance; also, as was explained earlier, it is a material which is subject to a high percentage of recycling. Silicon may be used as a principal additive element since it is liable to improve certain qualities of the aluminum such as fluidity and mechanical resistance. Aluminum-silicon alloys are thus used extensively in the automotive industry for designated engine components including engine blocks, cylinder heads, pistons, intake manifolds, and brackets. These alloys are gradually replacing cast iron components because of their light weight.[15]

The excellent castability which is one of the main features of Al-Si alloys refers to the high fluidity of the molten alloy and its ability to flow and to fill all the areas of the mold before becoming too solid to flow any further. Alloying silicon into aluminum increases the heat which must be removed from the Al-Si alloy melt before it is able to solidify. Table 2.1 summarizes the most common aluminum casting alloys and their principal elements.

Table 2.1 Composition of common aluminum-silicon casting alloys (a) [16]

Alloy		Elements (wt. %)					
	Method (b)	Si	Cu	Mg	Fe	Zn	Others
319.0	S,P	6.0	3.5	< 0.10	< 1.0	< 1.0	
332.0	P	9.5	3.0	1.0	1.2	1.0	
355.0	S,P	5.0	1.25	0.5	< 0.06	< 0.35	
A356.0	S,P	7.0	< 0.20	0.35	< 0.2	< 0.1	0.05 Be
A357.0	S,P	7.0	< 0.20	0.55	< 0.2	< 0.1	
380.0	D	8.5	3.5	< 0.10	< 1.3	< 3.0	0.15 Sn
383.0	D	10.0	2.5	0.10	1.3	3.0	
384.0	D	11.0	2.0	< 0.3	< 1.3	< 3.0	0.35 Sn
390.0	D	17.0	4.5	0.55	< 1.3	< 0.1	< 0.10 Mg
413.0	D	12.0	< 0.1	< 0.10	< 2.0	-	
443.0	P	5.25	< 0.3	< 0.05	< 0.8	< 0.5	

(a) Remainder: Aluminum and other impurities
(b) S, Sand Casting; P, Permanent Mold Casting;
D, High Pressure Die Casting

Strengthening of Al-Si alloys may be obtained by adding small amounts of Cu and/or Mg. With regard to the hypoeutectic alloys, silicon provides satisfactory casting properties, while copper improves tensile strength, machinability, and thermal conductivity although this may occur at the expense of a reduction in ductility and corrosion resistance.[16]

The main feature of Al-Si casting alloys is that a eutectic is formed between aluminum and silicon at a Si-content of 11.5-12%, as illustrated in the portion of the phase diagram shown in Figure 2.1. Depending on the amount of silicon, the alloys are divided into three main groups: hypoeutectic alloys with a silicon content of between 5 and 10%; eutectic alloys with 11-13% Si; and hypereutectic alloys with a Si-content commonly between 14 and 20%.[16]

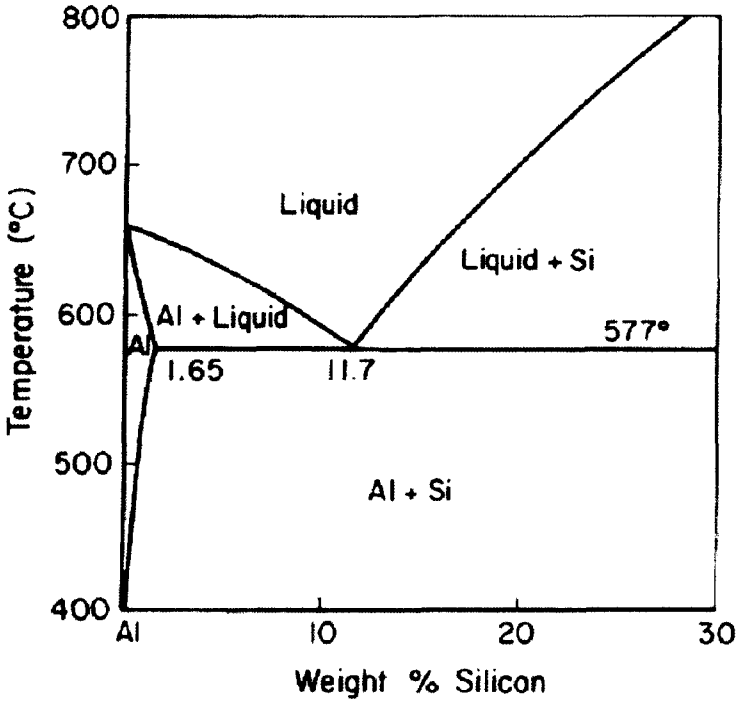

Figure 2.1 Portion of the equilibrium binary Al-Si phase diagram.

2.4 Al-Si-Cu and Al-Si-Cu-Mg Alloys

From Figure 2.1, it may be seen that the solidification process of Al-Si hypoeutectic alloys includes:

(i) the formation of the α-aluminum dendritic network;

(ii) the aluminum-silicon eutectic reaction to produce the Al-Si eutectic.[17]

In Al-Si alloys, magnesium and copper are the two most important alloying additions. Within Al-Si alloys, Al-Si-Mg, Al-Si-Cu, and Al-Si-Cu-Mg are the three major alloy systems in the 3XX series, of which A356, A319, and B319 are typical examples. The main function of Mg and Cu is to form the Mg_2Si and Al_2Cu precipitates, which are able to improve the mechanical properties upon heat treatment. At the same time, because of the

presence of certain impurity elements such as Fe and Mn, intermetallic phases also precipitate during solidification.

Among Al-Si alloys, hypoeutectic alloys such as 319 (Al-6.5%Si-3%Cu) and 356 (Al-7%Si-0.3%Mg) provide sound castability and good corrosion resistance, while the 380 alloy (Al-8.5%Si-3.5%Cu) is popularly used in die casting for its relatively high silicon percentage which provides good casting properties; also, the alloy can be strengthened by adding small amounts of Cu, Mg, or Ni if required.[16]

Eutectic alloys such as the 413, 443 and 444 alloys provide high corrosion resistance and satisfactory weldability while at the same time being possessed of low specific gravity. Hypereutectic alloys such as the 390 alloys which contain high silicon levels display significant wear resistance, a low thermal expansion coefficient, and excellent casting characteristics. Table 2.2 shows the characteristics of a number of major Al-Si alloys, where the characteristics are rated on a scale of 1 to 5, from best to least satisfactory.

Table 2.2 Characteristics of aluminum-silicon casting alloys[16]

Alloy	Casting Method	Resistance to Tearing	Pressure Toughness	Fluidity	Shrinkage Tendency	Corrosion Resistance	Machinability	Weldability
319.0	S,P	2	2	2	2	3	3	2
332.0	P	1	2	1	2	3	4	2
355.0	S,P	1	1	1	1	3	3	2
A356.0	S,P	1	1	1	1	2	3	2
A357.0	S,P	1	1	1	1	2	3	2
380.0	D	2	1	2	-	5	3	4
390.0	D	2	2	2	-	2	4	2
413.0	D	1	2	1	-	2	4	4
443.0	P	1	1	2	1	2	5	1

(1) Ratings: 1, best; 5, worst

2.5 Alloy 354

Aluminum-silicon-copper-magnesium alloys such as the 354 alloys show a greater response to heat treatment as a result of the presence of both Mg and Cu. These alloy types display excellent strength and hardness values although at some sacrifice of ductility and corrosion resistance. While the properties in the as-cast condition are acceptable for certain applications, the alloys are typically heat-treated for optimal properties. These alloys are then used for a wide range of applications, including the following non-exhaustive list: engine cooling fans, crankcases, high speed rotating parts (*e.g.* fans and impellers), structural aerospace components, air compressor pistons, fuel pumps, compressor cases, timing gears, rocker arms, machine parts, and so forth.[15, 18] The tensile properties and compressive yield stress for alloy 354 are shown in Table 2.3.

Table 2.3 Minimum mechanical properties[15] for casting alloy 354[a] (T6[b]) at room temperature.

UTS (MPa)	Tensile YS (MPa)	Elongation (%)	Compressive YS (MPa)
296	227	2	227

a.- Alloy 354 with a chemical composition (wt %): 9.1% Si, 1.8% Cu, 0.5% Mg, 0.1%Mn, 0.2% Fe maximum and 0.2% Ti maximum.
b.- T6 is a heat-treated condition corresponding to a solution heat treatment at 515° to 520 °C for 8 hours, followed by quenching in warm water (65° to 100°C) , and a subsequent aging treatment at 170° to 175°C for 12 to 26 hours.

2.6 Melt Treatment of Eutectic Al-Si Alloys

The interrelationships which exist between the mechanical properties, microstructure, and process in the metal itself make it essential to acquire a careful understanding of these three aspects of the subject since they ultimately prove to be of signal importance. The microstructure, and hence the mechanical properties of the Al-Si

alloys as well, are likely to be affected by the type of melt treatment applied in that they can be classified as either physical or chemical. A physical melt treatment may be interpreted as the application of rapid cooling rates, thereby transforming the microstructure into a fine eutectic structure, small dendritic arm spacing, and reduced grain size. When a melt is rapidly cooled (chilled), the rate of heat extraction can greatly exceed the rate of heat generated by the freezing process (latent heat of solidification). As a result, the liquid undercools when its temperature falls below the liquidus temperature. If this undercooling is sufficient, the full range of heterogeneous nucleants present in the liquid can become active. This multiple nucleation results in a fine eutectic microstructure.[16]

In view of the fact that it is not always possible to obtain rapid cooling during the process of solidification, a chemical melt treatment as an alternative can still be effective in obtaining these attributes. By chemical melt treatments is meant the inoculants added to the liquid metal as modifiers, including strontium or sodium, and chemical refiners such as titanium and/or boron.

2.6.1 Chemical Modification in Eutectic Al-Si Alloys

Modification in eutectic Al-Si alloys may be defined as the transformation of the eutectic silicon particles from coarse platelets to a fibrous, coral-like form. Chemical modification refers to the use of a chemical agent, such as Na or Sr, in order to change the morphology of the silicon phase from large acicular plate-like form into a fine branched globular morphology.[16] This change in the silicon particles from acicular to fibrous may be ascribed to a mechanism known as *impurity-induced twinning* in which a punctual defect is introduced into the solid liquid interface during solidification causing twins.[19]

The presence of twins is found to be higher by several orders of magnitude in modified silicon structures than it is in unmodified silicon structures. This type of twinning could explain the zig-zag growth of the silicon crystal during its solidification resulting in a bent fibrous structure.

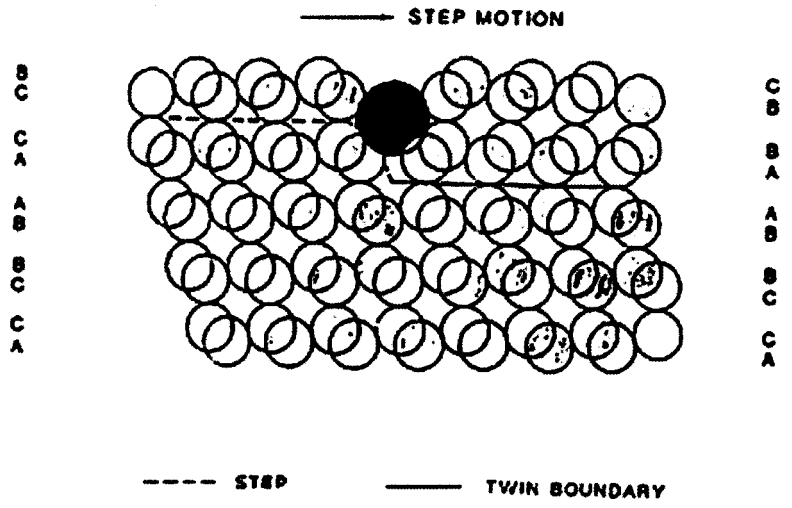

Figure 2.2 Schematic diagram of impurity induced twinning. A punctual defect (modifier atom in black) is presented during the solidification process causing twinning on the solidification front which crystallizes after the absorption of the modifier atom.[19]

Strontium is usually introduced directly into the melt in the form of an Al-10 wt% Sr master alloy.[16, 20] The amount of Sr necessary to achieve a degree of modification depends on the Si level, on the cooling rate, and on the concentration of other minor alloying elements. After modification, tensile properties are observably improved with the greatest improvement being evident in the elongation. Impact properties are highly sensitive to changes in the modification of Al-Si alloys.[21] The coarse silicon plates of unmodified acicular silicon structure act as internal stress raisers in the microstructure and

provide easy paths to fracture. With modification, the structure becomes finer and the silicon more rounded, both of which contribute to somewhat higher values of ultimate tensile strength as well as to greatly increased ductility values. Figure 2.3 shows the microstructures of alloy 319 (a) unmodified, and (b) modified with 0.012 wt% Sr.

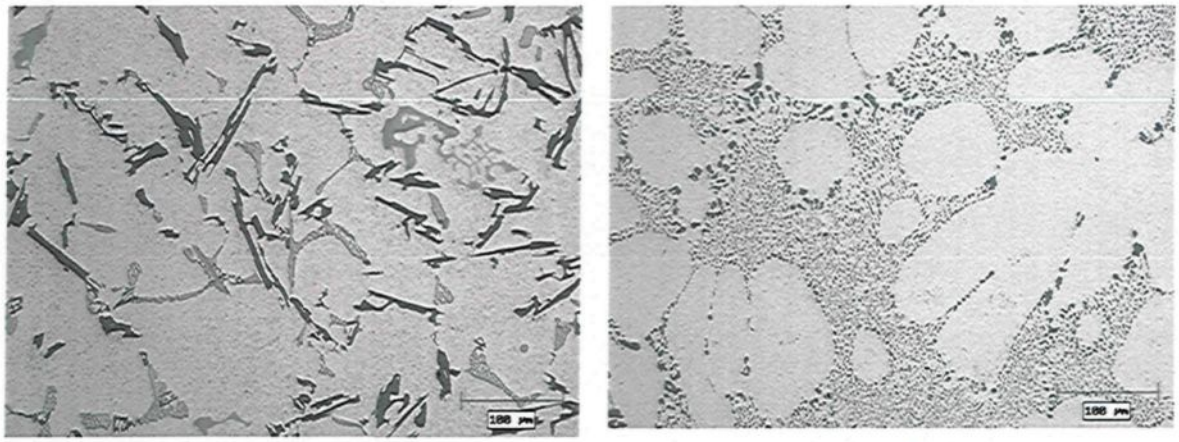

(a) (b)

Figure 2.3 Alloy 319 (a) unmodified, and (b) modified with 0.012 wt% Sr.

2.6.2 Chemical Grain Refinement in Eutectic Al-Si Alloys

Grain refinement refers to the reduction of the size of primary α-Al grains. Chemical refining is advantageous to mechanical properties, particularly those which are sensitive to hot-tearing and porosity. As is the case with modification, grain refinement can be achieved by rapid solidification and/or chemical additives. In most cases, it is not possible to remove the heat content rapidly. Medium to large size castings can not be significantly refined by means of chilling, and therefore other forms of grain refinement are required.

Chemical grain refinement involves the addition of special substrates to act as nucleating agents or to react with other elements in the melt thereby forming solid nucleant

particles. Hypothetically, every formed nucleus during the first stages of solidification will end as a whole grain after the process of solidification; therefore, a fine grain size is promoted by the presence of an augmented number of nuclei. As may be seen from the Al-Ti phase diagram shown in Figure 2.4, the peritectic reaction in the diagram is critical to the grain refinement of aluminum alloys. Particles of $TiAl_3$ will react with the liquid phase upon cooling to below 665°C according to the following peritectic reaction:

$$\textbf{Liquid} + TiAl_3 \rightarrow TiAl_3 + \alpha \textbf{ (solid)}$$

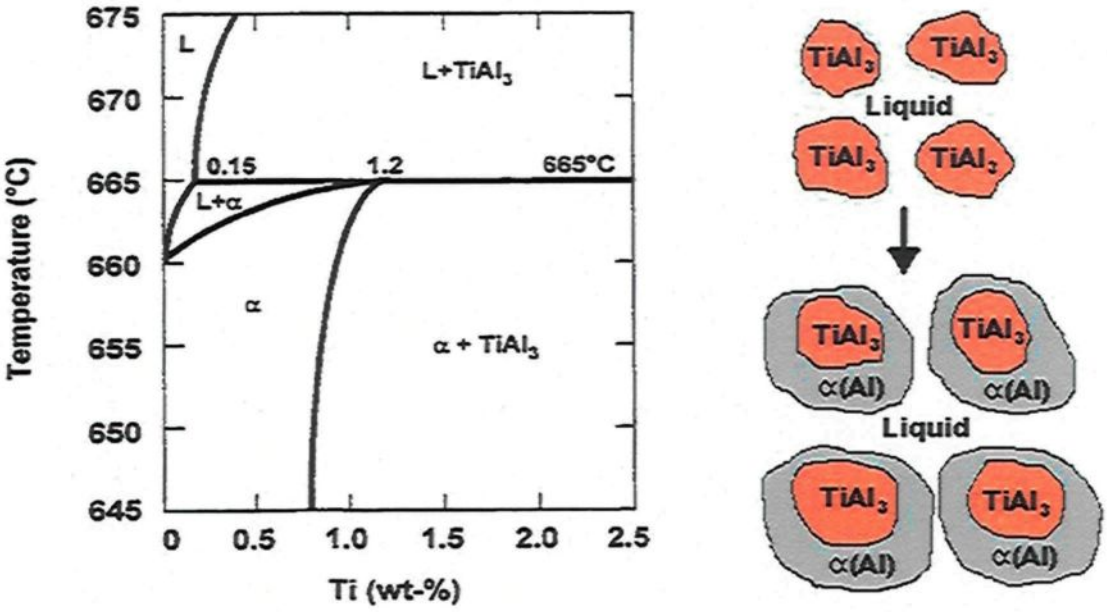

Figure 2.4 Portion of the Al-Ti phase diagram and a schematic representation of the nucleation of α (Al) through the peritectic reaction in the Al-Ti system.[22]

Shortly after the addition of a titanium master alloy to an aluminum melt, a $TiAl_3$ particle is placed in contact with either pure aluminum or a commercial alloy of low titanium content, a diffusion field will then be established in the vicinity of the $TiAl_3$ crystal. At the surface of $TiAl_3$, the titanium content in the liquid metal is about 0.15%

whereas the concentration away from the particle in the bulk of the metal phase is much higher. When the melt cools, solid aluminum will form at the surface of the $TiAl_3$ particle at temperatures above the melting point of the bulk metal mainly because titanium raises this melting point and because $TiAl_3$ is an extremely efficient nucleant. Once the solid has formed, however, the $TiAl_3$ particle becomes engulfed in the solid phase, and further growth becomes limited by the diffusion of Ti from Ti_3Al through the shell of solid aluminum. Normal dendritic growth cannot occur because the solid metal nucleus is still above the growth temperature of the bulk metal containing low levels of titanium, as may be observed from Figure 2.4.[23]

2.6.3 Titanium-Boron Refinement

It has been suggested by a number of researchers that Al-Ti-B master alloys perform better due to a shift in the onset of the peritectic reaction towards lower Ti values.[24-26] This shift may be observed in the Al-Ti phase diagram in the presence of boron (0.01%B) and, as a result, ensures the thermodynamic stability of Al_3Ti particles at low levels of titanium addition (0.05%Ti). This type of refinement is the one normally used in the automotive industry nowadays. Figure 2.5 shows some degree of refining effect as obtained through the addition of TiB_2 in the form of the master alloy Al-10%TiB_2.

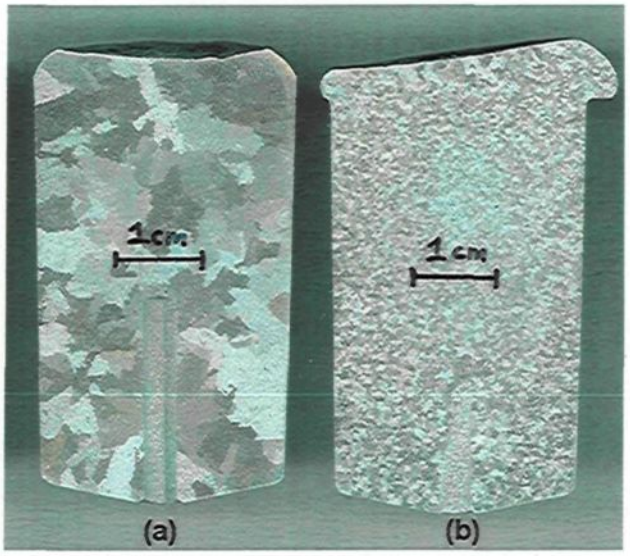

Figure 2.5 Macrographs of Alloy 319 (SDAS = 40μm); (a) not refined, and (b) refined with 0.01% of TiB_2.

2.7 Heat Treatment of Cast Aluminum Alloys

2.7.1 Age Hardening of Cast Aluminum Alloys

Generally speaking, heat treatment refers to any of the heating and cooling cycles which are applied with the purpose of modifying the mechanical properties, metallurgical structure, or residual stress state of any given metal.[27] Particularly for aluminum, heat treatment is more usually referred as the operations used with the aim of obtaining an increased strength and hardness. As is the case with other metals, however, heat treatment in cast aluminum alloys may be used to reduce the microstructural inhomogeneity originating in the solidification process,[28] so as to minimize the microsegregation and to change the form of the insoluble phases. Consequently, by affecting the susceptibility to corrosion and reducing the residual stresses, the machinability may be improved.

For cast aluminum alloys, the common heat treatment practices involve a three part sequence of treatment namely: solution heat treating, rapid cooling (quenching) in water

and precipitation hardening (artificial aging). This sequence of heat treatment which is normally applied to cast aluminum alloys is designated as a T6 treatment by the Aluminum Association of America.[29] The T6 treatment refers to a phase transformation process known as precipitation hardening because the small particles of a new phase which are formed may be termed precipitates. Age hardening is also used to designate precipitation hardening because the strength develops with the passage of time, or as the alloy ages. The basic requirement for an alloy to be amenable to age-hardening is a decrease in the solid solubility of one or more of the alloying elements present with decreasing temperature.[30]

2.7.2 Solution Heat Treatment

Solution heat treatment is the first step of the precipitation hardening process in which the solute atoms are dissolved to form a single phase in solid solution. Figure 2.6 shows the T_{SHT} temperature which is the temperature at which a supersaturated structure (α) is obtained for an alloy having a specific composition (C_{Alloy}) with hypothetical elements A and B.

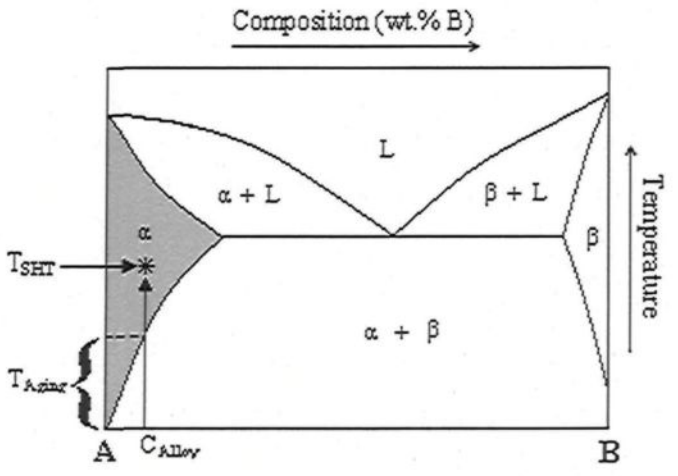

Figure 2.6 Hypothetical phase diagram.

Solution heat treatment must be applied for a sufficient length of time to obtain a homogeneous supersaturated structure, followed by the application of quenching with the aim of maintaining the supersaturated structure at ambient temperature. Figure 2.7 shows the major steps of the heat treatment which are normally used to improve the mechanical properties of aluminum. In Al-Si-Cu-Mg alloys, the primary purpose of solution heat treatment is to place the precipitation phases in solid solution and to alter the morphology of the eutectic Si particles.

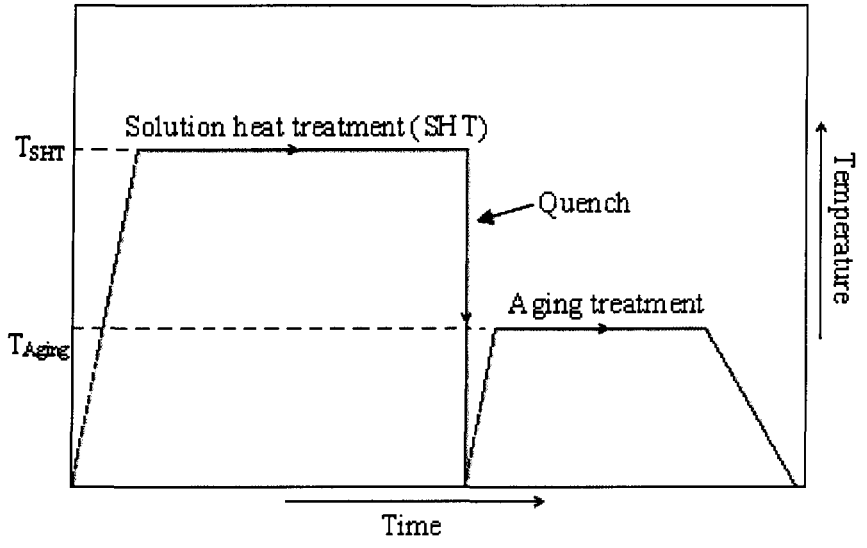

Figure 2.7 Diagram showing the three steps for precipitation hardening.

Solution heat treatment in Al-Si-Cu-Mg alloys is carried out to maximize the dissolution of Cu and Mg in the α-Al solid solution. The dissolution of these elements will cause precipitation hardening during the artificial aging treatment, or even in some cases, during natural aging. In order to reach the solid solution condition, the temperature should be maintained at a sufficiently high level, at which the solution and diffusion conditions are optimum. The selection of the solution heat treatment temperature for alloys of the Al-Si-

Cu system should be carried out with care. The temperature should be restricted to a range below the solidification point to avoid the melting of Cu-containing phases. Certain researchers suggest that the solution heat treatment temperature should be limited to 500°C in Al-Si alloys containing copper contents of more than 2%.[31, 32] Parallel research[33, 34, 35, 36] indicates that, at higher solution-heat-treatment temperatures, the melting of copper-containing phases occurs, thereby generating shrinkage porosity and a solidified structureless form of the copper phase which is detrimental to the mechanical properties of the alloys belonging to the Al-Si-Cu-Mg system.

Thermal analysis obtained during the solidification of 319 alloy, as can be observed in Figure 2.8, shows the presence of a Cu-rich phase eutectic reaction at approximately 495°C.[36] In order to dissolve the copper content of these alloys, as a solution treatment procedure the material should be heated at 490-500°C; overstepping this temperature would result in melting the Cu-rich phases. For this reason it is important to avoid an excessively high temperature in the solution heat treatment in order to prevent the occurrence of incipient melting. This type of melting results in the formation of shrinkage cavities when the alloy samples are quenched after solution heat treatment, thereby diminishing alloy soundness and mechanical properties to a great extent. In Al-Si-Cu alloys, with the segregation of the alloying elements, the composition may exceed the critical composition locally, in which case, incipient melting will occur. Samuel[37] noted that the incipient melting of Cu-rich phases in 319-type alloys took place when the high-Mg version of the alloy was solution-treated at temperatures above 505°C for sufficiently long periods.

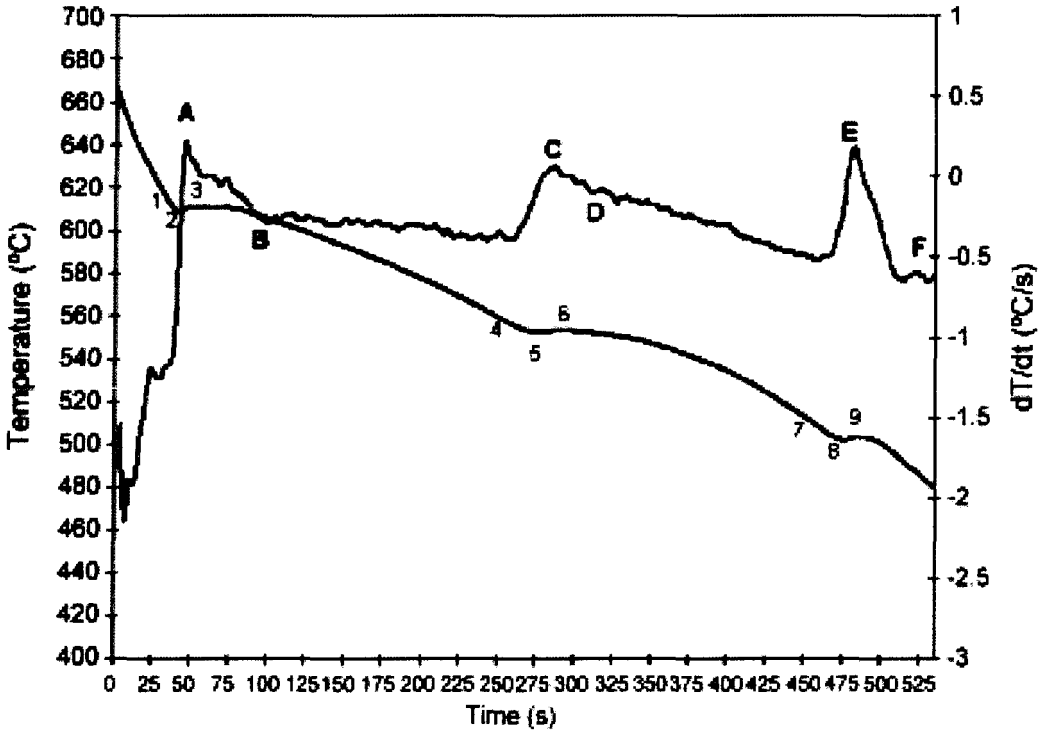

Figure 2.8 Cooling curve and its first derivative curve of the 319 alloy (0% wt Sr).

Other effects associated with the solution heat treatment stage are silicon spheroidization and coarsening of the silicon particles, which take place in an attempt to reduce the surface energy of the constituent phases in the alloy. The coarsening process, called Ostwald ripening, holds that larger particles grow at the expense of smaller ones. Solution treatment tends to spheroidize constituents which cannot be fully dissolved, as in the case of casting Al-Si alloys. At the beginning of the solution treatment, the acicular silicon platelets in the unmodified structure begin to break down into smaller fragments and gradually spheroidize. In modified structures[38] the spheroidization takes place at an early stage. Figure 10 shows a schematic representation of the spheroidization and coarsening process. [39]

Figure 2.10 shows a comparison between the microstructures of an as-cast Al-Si-Mg alloy and several samples which were solution heat treated at different temperatures for 5 hours. It is important to note the difference in the morphology of the eutectic silicon and how it becomes more rounded as the solution temperature increases.

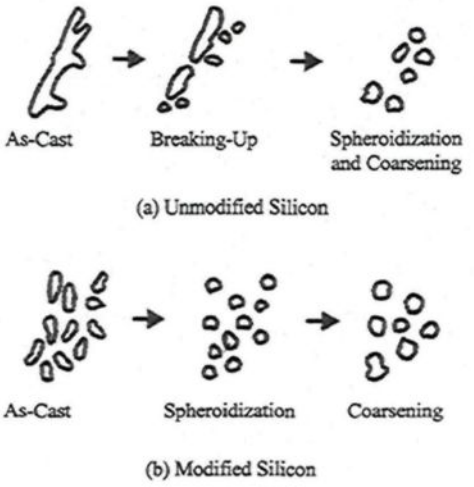

Figure 2.9 Schematic characterization of the three stages of spheroidization and coarsening of the eutectic silicon phase.

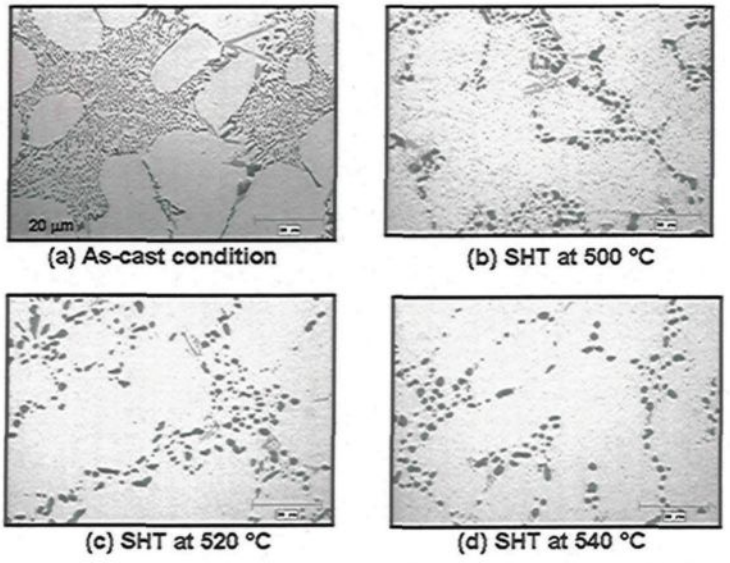

Figure 2.10 Optical micrographs of the microstructures of (a) as-cast, and (b) solution heat treated (SHT) samples of an Al-Si-Mg alloy.

2.7.3 Quenching

With the purpose of maintaining the highest possible degree of solution and amount of quenched-in vacancies, quenching is normally applied after solution heat treatment. Even if the quenching should be at its highest value in order to maintain the solid solution structure at room temperature, a large thermal gradient which arises during the quench operation induces large thermal-stresses. Thermal stresses, if they are sufficient, will cause inelastic yielding leading to differential strains within the component in the form of distortion or residual strains.[40] On the other hand, if the quenching in the solution heat treatment is too slow there is a possibility that a solid solution structure will not be present; a compromise between these factors is required to produce the optimal mechanical properties.

2.7.4 Artificial Aging

Generally speaking, precipitation hardening results from the development of particles (in size, form, and distribution) of a new phase within the metal matrices. In the case of hardenable aluminum alloys, the precipitation hardening is related to the nature of these precipitates and the way in which they are located within the matrix of the alloy, since it can be coherent or non-coherent with the matrix itself. The difference between a coherent precipitate and a non-coherent precipitate is principally the matching presented in the interface between matrix and precipitates, as is shown in the Figure 2.11, where the coherent precipitate has a continuous relationship with the matrix in its crystal structure and its atomic arrangement.[41]

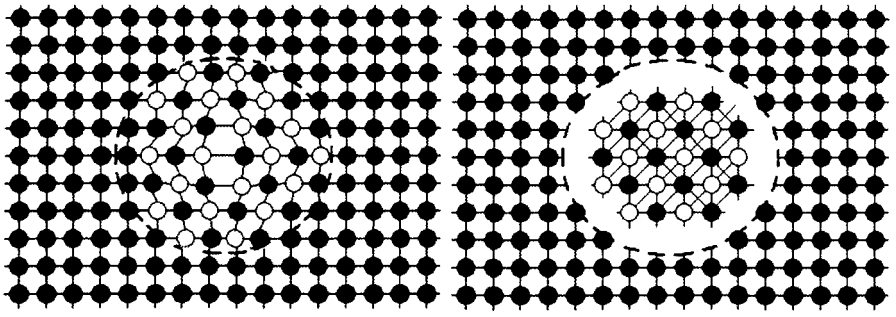

Figure 2.11 Schematic diagram showing: a) particle coherent with the matrix, and b) non-coherent particle within the matrix.

Figure 2.12 shows the different interactions between dislocations and precipitates depending on whether or not they are coherent or non-coherent. The coherent precipitates increase the strength of the alloy by distorting the crystal lattice and creating resistance to dislocation motion. The mechanism of the interaction between dislocation and precipitates would explain the mechanical behaviour showed by some metals, as in the case of strengthened aluminum alloys, where Figures 2.13 and 2.14 represent the strength behavior which is dependent on the level of coherency of such precipitates within the matrix.

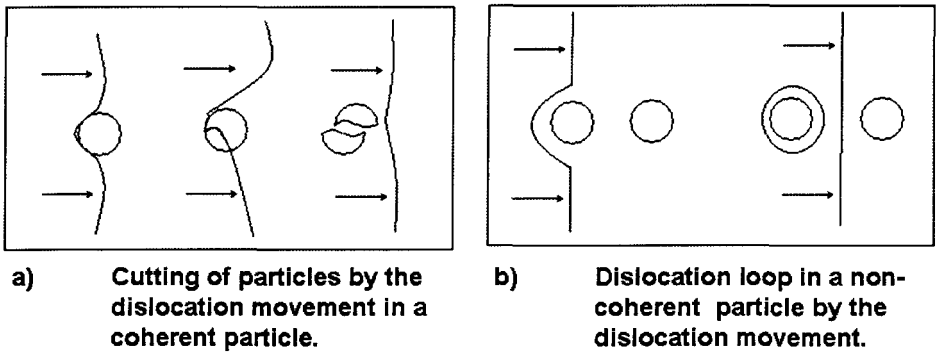

Figure 2.12 Schematic diagrams showing the Orowan dislocation process of interaction between dislocations and precipitates.

For cast aluminum alloys, copper and magnesium are the principal alloying elements which provide strength through natural or artificial aging. The generally accepted sequences of precipitation in Al-Cu-Mg alloys are: [42, 43]

$\alpha_{ss} \rightarrow$ GP zones $\rightarrow \theta'' \rightarrow \theta' \rightarrow \theta$-$Al_2Cu$

$\alpha_{ss} \rightarrow$ GPB zones $\rightarrow$ S'' $\rightarrow$S' $\rightarrow$ S- Al_2CuMg

where GP zones are the Guinier-Preston zones, θ'' and θ' are the metastable Al_2Cu phases, θ is the equilibrium Al_2Cu phase, GPB zones are the Cu/Mg Guinier-Preston-Bagariatsky zones, S'' and S' are the metastable Al_2CuMg phases, and S is the equilibrium Al_2CuMg phase.

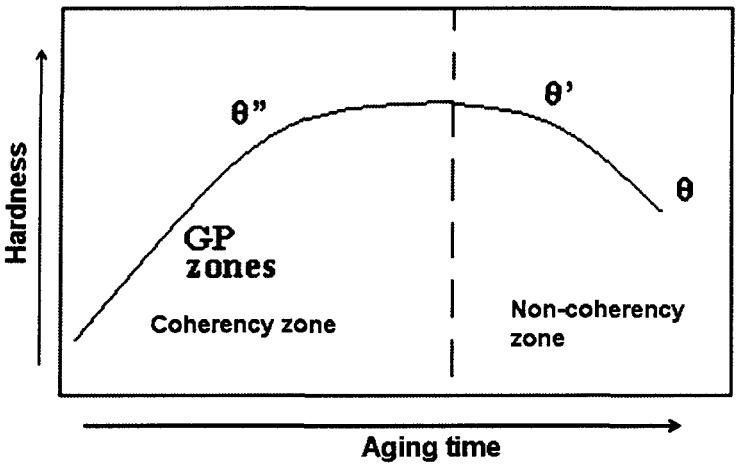

Figure 2.13 Schematic diagram showing the evolution of precipitates from a coherency zone to a non-coherency zone during the process of aging affecting the hardness of an aluminum alloy.

Depending on the alloy composition, the Cu content, and/or the Cu-to-Mg ratio, as well as the relevant aging parameters, a different phase distribution may be obtained and consequently different mechanical properties also. With regard to copper precipitates, Figure 15 shows the evolution of the θ precipitates during aging and its relationship to

hardness. Figures 2.13 and 2.14 show the different mechanical behavior existing in alloys depending on the coherency of their precipitates. The high values of yield strain and hardness, and the low rate of strain hardening observed in alloys with coherent precipitates, suggest that dislocations succeed in cutting the coherent particles once the stress reaches a high enough value, as is represented by Figure 2.12 (a). For the case of alloys containing non-coherent precipitates, which may be alloys in an overaged condition, the yield strength is low but the rate of strain hardening is high, as is shown in Figure 2.14. This behavior suggests that dislocations accumulate in tangles around precipitates in the process of passing between them, as shown in Figure 12 (b). High stresses from dislocation loops around precipitates produces incompatibilities because of the elastic deformation in the precipitate which tends to be equal to the plastic deformation in the matrix. High elastic strains are developed in the particles which would support a large fraction of the load by the mechanism of load-transfer[44] leading to a high strain hardening rate.

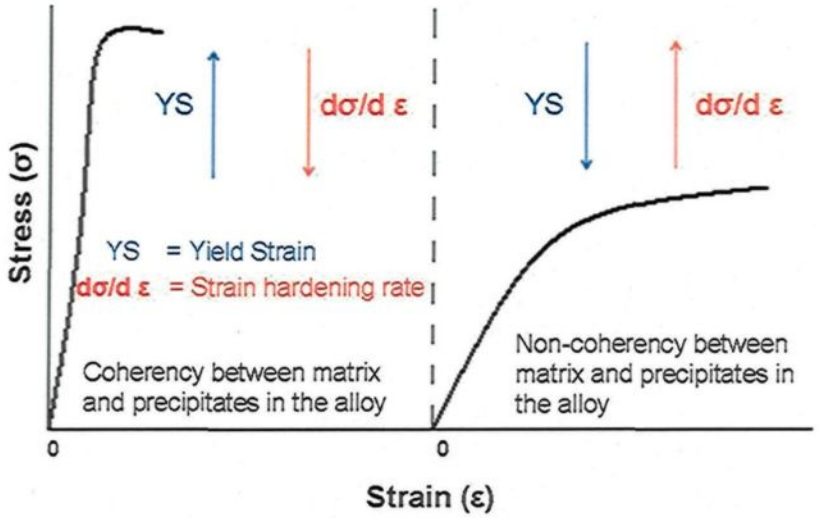

Figure 2.14 Schematic diagram showing the stress-strain flow curves in a hypothetical alloy where there exist different behaviors related to the coherency (or non-coherency) between matrix and precipitates.

2.8 Effects of Temperature on Cast Aluminum Alloys

In Al-Si casting alloys, applications are generally to be carried out at temperatures of no more than 230°C.[45] This recommendation is made in view of the fact that, for certain applications such as those required by the automotive industry, these alloys must operate over a wide range of temperatures and stress conditions where temperatures are liable to rise even higher than 230°C.[46] Alloying elements such as copper and magnesium are often added to improve alloy strength at room temperature as well as at higher temperatures. When they are affected by temperatures above 190°C, the major alloy strengthening phases which include the θ'(Al_2Cu) and S'(Al_2CuMg) phases will tend to become unstable, coarsen rapidly, and then dissolve, leading to the production of an alloy which has an undesirable microstructure for high temperature applications. Apart from these phases, when a casting is produced, there are other microstructural features which contribute to strength, ductility, and durability; these include secondary dendrite arm spacing, grain size, and interdendritic Si particles. [18, 46, 47]

The mechanical properties of most Al-Si cast alloys are not severely affected by temperatures of up to 100°C, particularly those related to the tension test. Since most castings are used in the underaged condition, prolonged exposure to temperatures of the order of 100°C leads to additional precipitation-hardening. As a result, the strength increases, and the ductility decreases slightly. At temperatures higher than 150°C, increasing temperatures and exposure time lead to an appreciable reduction in strength and an increase in ductility, as may be observed in Figure 2.15. The reduction in strength can be ascribed to overaging which may occur suddenly at temperatures close to the GP zone

solvus temperature; this parameter has been measured and recorded as being of the order of 190°C.[48]

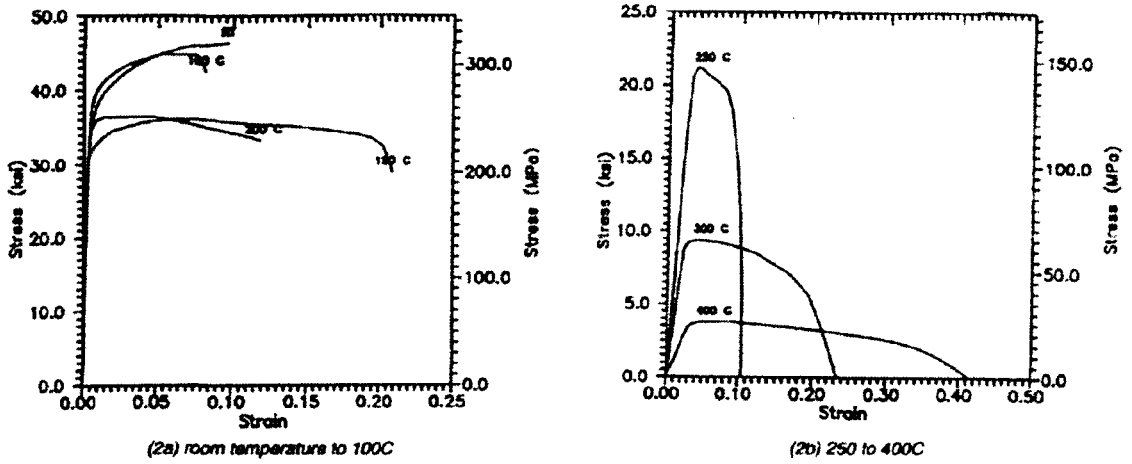

Figure 2.15 Typical stress-strain curves for permanent-mold A356-T6 castings at various temperatures (exposure time = 1hr).[17]

Fracture is essentially transgranular and interdendritic up to about 200°C. It should also be kept in mind that the mechanical properties and fracture behavior of these alloys may depend on such macrodefects as internal oxide layers and shrinkage macroporosity,[49, 50]on microporosity,[51] and on the size and shape of the Si-particles present in the interdendritic regions. The fracture and debonding of silicon particles is a major aspect of damage evolution in these alloys.[52] Such fracturing, or debonding, together with the formation and growth of voids around the particles, and the subsequent interlinkage of the voids, all lead to crack propagation in the interdendritic regions.[47]

The amount and the number of pores on the fracture surface of a sand casting increase with exposure to temperature and time. Furthermore, modified castings contain a significantly larger number of pores than do unmodified castings. It appears that the initial

pore structure in the casting is enlarged during matrix deformation at elevated temperatures. Hence, the pore characteristics in the casting may be a significant factor affecting elevated temperature properties.[47, 48, 53, 54, 55]

The variation in mechanical properties resulting from exposure to high temperatures may be analyzed on the basis of the fracture behavior of the cast Al-Si alloys. The fractures are classified into two categories as follows:[48]

(i) fractures occurring at temperatures lower than 0.3 Tm (where Tm is the melting temperature of the alloy); and

(ii) fractures occurring at temperatures higher than 0.3 Tm.

The fracture behavior of Al-Si alloys has been studied by several investigators, and it has been shown that fracture occurs in three stages:[47, 48, 55]

(i) initiation of cracks in the Si particles;

(ii) growth of these cracks into cavities; and

(iii) rupture of the aluminum matrix separating the cavities.

The principal changes in the microstructural features of Al-Si alloys according to temperature are summarized in Table 2.4.[48]

Table 2.4 Summary of Elevated-Temperature Fracture Behavior[48]

Low Temperature (T<0.3Tm)	High Temperature (T>0.3Tm)
Coherent precipitates in matrix may control the strength.	Precipitates may lose coherency and strength decreases.
Dendrite arm spacing and second phase particle morphology are significant parameters.	Dendrite arm spacing and grain size are significant parameters.
Particle cracking significant.	Both particle cracking and void growth significant.
Relaxation processes not operative.	Relaxation processes become significant. Fracture postponed to higher strains.
Void nucleation mainly caused by fracture of Si particles. Dislocation storage and work-hardening build up internal stresses.	Void nucleation difficult because of low stress levels due to high dislocation mobility and climb within the matrix.
Void growth difficult.	Void growth aided by dislocation slip.
Fracture is transgranular and interdendritic.	Fracture may be intergranular if grain boundary slip occurs.

When void nucleation can occur easily, the fracture properties are regulated by the growth and coalescence of voids. Growing voids reach a critical size, relative to the spacing, and local plastic instabilities develop between voids, resulting in failure.[56] Under such conditions, and as shown in Figure 2.16, four types of fracture may be observed in the case of A356 alloy castings exposed to various temperatures for short and extended periods of time.[48]

These fracture types indicate the following details:

Type I: Low levels of plastic strain which result in a macroscopically flat surface. Below 200°C, the material fractures without extensive strain, the dislocation pile-ups are minimal, and the particle breaks are due to fiber loading. After the Si particles fracture, the

cross-sectional load-bearing area is reduced. If the specimen has exhausted its ability to strain-harden, instabilities arise in the remaining ligaments, resulting in rupture.[48]

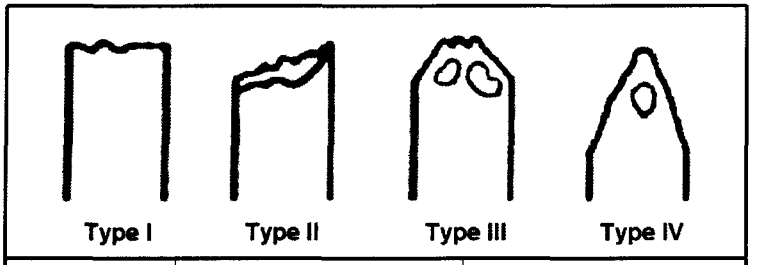

Temperature (°C)	1 hr Exposure			1000 hr exposure		
	SCU	SCM	PM	SCU	SCM	PM
100	I	I	I	I	I	I
150	I	I	I	I	I	II
200	I	I	II	II	II	II
250	II	II	III	II	II	III
300	II	II	IV	III	III	IV
400			IV			IV

Figure 2.16 Schematic showing classification of the type of fracture at different test temperatures for the study of an A356 alloy (SCU = sand cast, unmodified; SCM = sand cast, modified; PM = permanent mold).[48]

Type II: Intermediate degrees of plastic strain result in a sheared fracture surface. Above 200°C, Si particles exhibit random multiple cracking. At these temperatures, the samples yield at low stresses. As the stress increases, plastic flow of the matrix relieves the stresses experienced by the Si particles. With continued strain, a buildup of local stresses eventually causes the Si particles to fracture. In samples which experience large amounts of plastic deformation, cavity initiation is not determined by the magnitude of the applied stress but rather by the local state of deformation.[56] Fracture of this type occurs by means of blocked slip and pile-up mechanisms.[30, 57] As the plastic deformation and shearing continues, the voids eventually coalesce, and failure then occurs. Because relaxation

processes are operative, the specimens exhibit significant ductility, and a slight degree of necking is observed on the fracture surface, as may be seen in Figure 2.16.

Type III: High levels of plastic strain result in a necked fracture surface. Increasing stress relief and relaxation at elevated temperatures postpone the breaking of Si particles and lead to a noticeable degree of necking. The Si particles fracture with increasing amounts of plastic strain. With continued strain, voids coalesce and lead to the fracture of the specimen. Several macroscopic coalesced voids were also observed below the fracture surface. [47, 48]

Type IV: Extreme amounts of plastic strain result in a severe reduction of the cross-sectional area as well as to a large void in the center of the fracture surface. At very high temperatures, fracture of Si particles becomes difficult. Continuous stress relaxation occurs and the samples exhibit a high degree of ductility. As the specimen begins to neck, a triaxial state of stress is produced, thereby promoting void nucleation and growth on large particles. With further strain, the voids coalesce and produce a circular flaw.[47, 48]

2.9 Effects of Micro-Ceramic Particulates (Al_2O_3 and SiC) on Mechanical Properties in Cast Aluminum Alloys

Even if the development of metal matrix composites (MMCs) has been one of the major innovations in the production of technological materials over the past thirty years,[58, 59] there exists a gap in the theoretical survey concerning the addition of low percentages, namely < 2%, of particulates such as Al_2O_3 and SiC to metals. This drawback may cause even more concern when viewed in the light of the effects of minor additions of such particulates on the mechanical properties of aluminum alloys at high temperatures. The

promotion of MMCs in the automotive market has been held up by the low volume usage of these materials, caused mainly by their high cost which is about three times higher than that of the unreinforced alloy.[58]

An acceptable definition for an MMC is that it can be identified by the following characteristics:[38]

- it must be man-made;
- it must be a combination of at least two chemically distinct materials, one of them being a metal with a distinct interface separating the constituents;
- the separate materials must be combined three-dimensionally;
- it should create properties which could not be obtained by any of the individual constituents alone.

This definition differentiates aluminum matrix composites from aluminum alloys, which are achieved via control of naturally occurring phase transformations during solidification or thermo-mechanical processing.[44]

In view of the minimal percentage of particulates used for the purposes of this study, namely 0.5 wt%, it is not entirely appropriate to refer to the alloy compositions studied as metal matrix composites. Because of the lack of available literature regarding lower percentages (< 2%) of dispersoids, however, it would be useful to acquire an understanding of some of the principal aspects related to the addition of these particulates to aluminum alloys covered in the numerous studies on MMCs as reported in the literature.[60, 61, 62] Even if dispersoids are added in the form of master alloys, *e.g.* alloys 6061-20%Al_2O_3 and 359-20%SiC, it is necessary to consider the main difficulties

frequently encountered in the production and remelting of certain MMC casting alloys.[60, 63, 64, 65] These difficulties are related to:

(i) the absence of wetting between the molten metal aluminum and the ceramic particles (*i.e.* oxides and carbides) at the temperatures used in conventional foundry practice.[66, 67] This lack of wetting leads to the rejection of the ceramic particles when they are added to the melt.

(ii) the segregation of dispersed particles in the melt due to the difference in density between the aluminum matrix and the ceramic particles.

The same importance must be accorded to the influence that these particles could have on the effects of the heat treatment applied to the material; this influence could alter the precipitation behavior[50] and/or accelerate precipitation kinetics.[68, 69, 70] There is even the added possibility of a harmful chemical reaction being caused by such products as MgO, $MgAl_2O_4$, or Al_4C_3.[71] One way of contemplating possible strengthening mechanisms through the addition of minor additions of micro-particulates to cast alloys would be to carry out a detailed study of the literature available on aluminum *MMCs*, and to attempt to harness certain principles which are potentially applicable to this work. The basic strengthening mechanisms involved in *MMCs*, where the volume fraction of reinforcement is high, namely 5-40%, derive principally from the following:[69, 72, 73, 74, 75, 76]

- high dislocation densities due to dislocation generation resulting from differences in the coefficients of thermal expansion between metal matrix and dispersoids;
- small subgrain size resulting from the generation of high dislocation density;
- residual elastic stresses;

- differences in texture between metal matrix and dispersoids;
- classical composite strengthening or load transfer;
- dispersion strengthening.

The tensile strength of the MMCs is dependent on achieving a strong interfacial bond between the matrix and the composite.[62] When the strength and stiffness of the reinforcement are greater than those of the matrix, mechanical properties will be influenced mostly by load transfer from the soft matrix to the micro-particulates which act as rigid reinforcement.[66] The increase in dislocation density is due to the mismatch of the coefficient of thermal expansion (*CTE*) between matrix and reinforcement.[77]

The behavior of MMCs is often sensitive to changes in temperature. This behavior arises for two reasons: firstly, because the response of the metal to an applied load is itself temperature-dependent and secondly, because changes in temperature can cause internal stresses to be set up as a result of differential thermal contraction between the phases. Thus, metals generally have larger thermal expansion coefficients (α) than do ceramics.

2.10 Effects of Zirconium on Cast Aluminum Alloys

Minor additions of zirconium are often made to high strength wrought aluminum alloys for the purpose of regulating grain structure and inhibiting recrystallization during heat treatment, which occurs as a result of the obstructive action of coherent particles with dislocations.[78] According to the literature,[79] it would be necessary to obtain a microstructure containing thermally stable and coarsening-resistant dispersoids in order to improve mechanical properties at high temperatures in an aluminum alloy. These dispersoids or particles will be resistant to coarsening if the energy of their interface with

the matrix is low, and if the diffusivity and solubility of the rate-controlling element are both minimal. Zirconium has the smallest diffusion flux in aluminum of all the transition metals,[80] and its addition to aluminum base alloys results in the formation of the Al_3Zr phase, which precipitates out during the initial solution heat treatment in the form of metastable $L1_2$ Al_3Zr particles, as shown in Figure 2.17. These particles are resistant to dissolution and coarsening; they can also control the evolution of the grain and subgrain structure, thereby making it possible to increase strength and ductility in the precipitation-hardened T6 condition[46] or during subsequent processing operations, such as the hot rolling of wrought alloys. The addition of small amounts of Zr to wrought aluminum alloys has been widely studied, although the effects of the Zr *per se* on cast aluminum alloys is a topic which has been infrequently discussed in the literature to date.[79, 80]

The effectiveness of the dispersoids will depend on their size, spacing, and distribution. In direct-chill cast alloys, the alloying elements are highly segregated following solidification. The Al_3Zr particles precipitate from this segregated structure, leading to an inhomogeneous distribution of the dispersoids which is not optimal for inhibiting recrystallization.[81, 82]

Proof stress, tensile strength, and the elongation to failure are all improved by the addition of Zr to cast aluminum alloys. It should be noted that, in this case, there is an additive strengthening effect combined with the strengthening produced by the aging process. Such improvements in strength and ductility lead to an enhancement of the quality index of the material.[79] Minor additions of Zr to A319 aluminum casting alloys improve the hardness of the material. This is believed to be a direct result of the precipitation of the

Al_3Zr phase, which not only induces an increase in the hardness of the alloy but also increases the wear resistance of the material to an appreciable extent.[80]

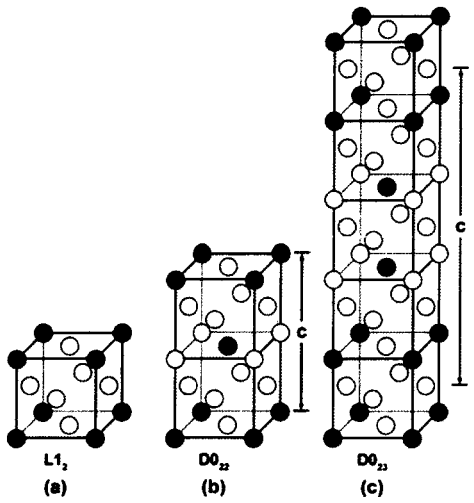

Figure 2.17 (a) $L1_2$, (b) DO_{22}, and (c) DO_{23} structures.[83]

According to the binary Al-Zr phase diagram shown in Figure 2.18, dispersoid precipitation can only be thermodynamically possible if the Zr concentration is higher than 0.08% at temperatures approaching 500°C. Precipitation will thus occur at the dendrite cores with Zr concentrations of more than 0.15% and will continue until the concentration is reduced to 0.08 wt%, which is the minimum required limit for precipitation at or near 500°C.

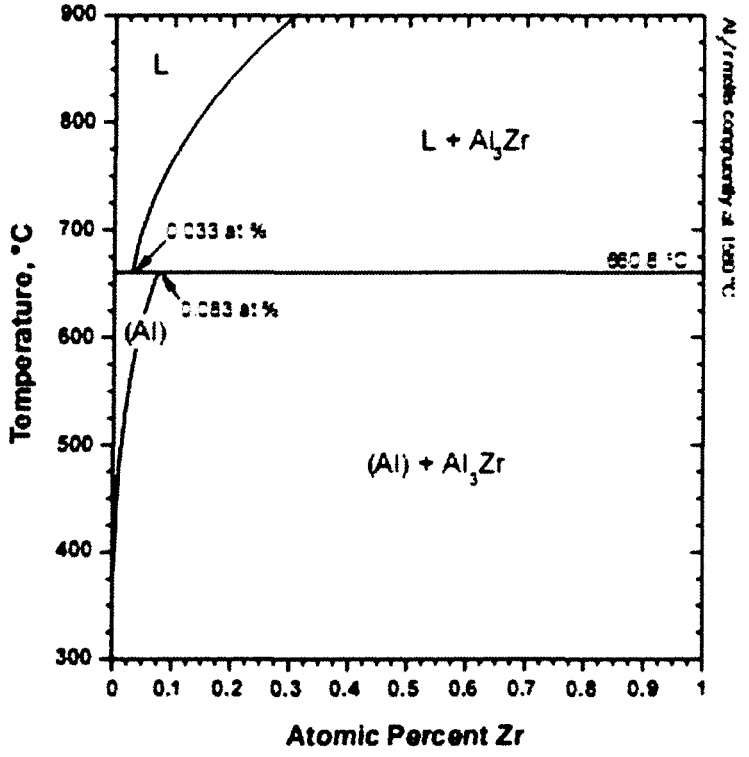

Figure 2.18 Al rich Al-Zr binary phase diagram (adapted from Murray[84] with metastable Al_3Zr ($L1_2$) solvus calculated by Liu *et al.*[85, 86]

2.11 Effects of Nickel on Cast Aluminum Alloys

Aluminum acts as a solid solution hardener in nickel. Lattice expansion associated with atomic diameter oversize can be related to the hardening observed in nickel base alloys using additions of Al. The precipitation of γ', Ni_3Al, in a high nickel matrix provides significant strengthening to the nickel base alloys. This unique intermetallic phase has a face-centered cubic structure similar to that of the matrix, and a lattice constant with a mismatch of 1% or less with the γ matrix. In nickel base alloys, the volume percent of γ' precipitated is also of significance since high temperature strength increases with the amount of the phase present. In order to retard coarsening, the alloy designer can add

elements with a view to increasing the volume percent of γ' which has a face-centered cubic structure with an ordered $L1_2$ form.[87]

Based on the details discussed above, there exists the possibility that a similar trend has been explored by a number of researchers with regard to using the Al_3Ni phase as a strengthener for high temperature applications in aluminum alloys instead of the Ni_3Al phase in the nickel phase alloys. The capacity of nickel for improving the strength of wrought aluminum alloys at high temperatures has already been established; nickel is thus used in combination with copper to enhance high temperature properties.[88] The solid solubility of nickel in aluminum cannot exceed 0.04%. If this amount is exceeded, then it is present as an insoluble intermetallic, usually in combination with iron. Nickel content of up to 2% increases the strength of high-purity aluminum but reduces its ductility. Binary aluminum-nickel alloys are no longer in use, but nickel is added to aluminum-copper and aluminum-silicon alloys to improve both hardness and strength parameters at elevated temperatures as well as to reduce the coefficient of thermal expansion.[89]

In a number of studies on Al-Si casting alloys, it was shown that Ni contents of less than 2% do not affect the mechanical properties, whereas nickel variations of up to 2-3% affect only the specific gravity from among the usual physical properties. Nickel is present largely as a relatively massive acicular dispersion of Al_3Ni and the amount of this compound has been shown to increase with increasing nickel content. Effective strengthening would thus necessitate a much finer dispersion of Al_3Ni or a much higher volume fraction of the coarse compound, leading to the view that much larger amounts of nickel would be necessary for any useful improvement in strength. With regard to

aluminum casting alloys, a high percentage of Ni seems not to be practical, mainly because it would increase the cost of the alloy.[78, 79]

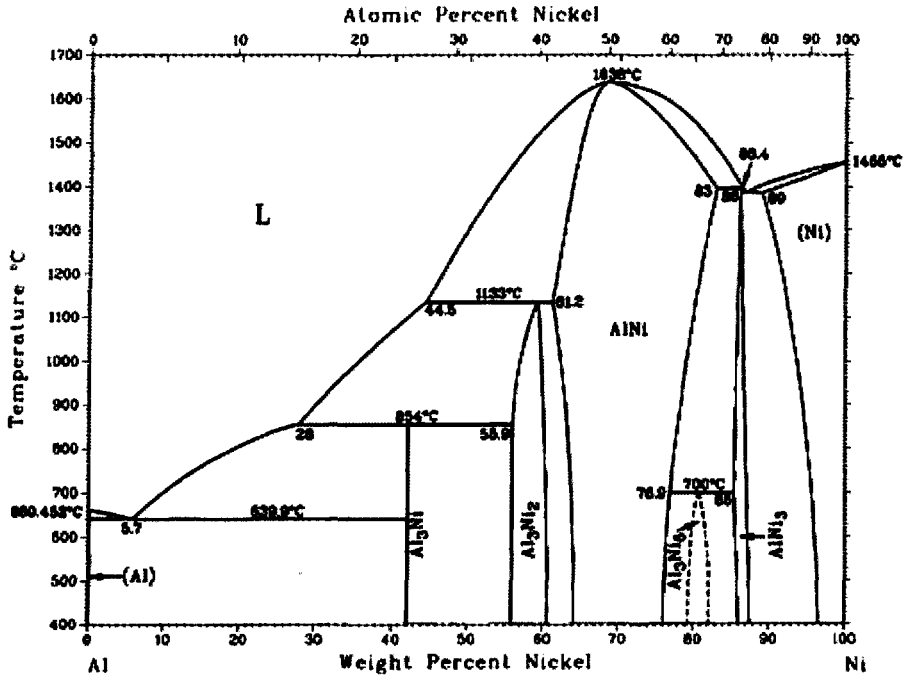

Figure 2.19 Al-Ni binary phase diagram (from P. Nash *et al.*[90])

2.12 Quality Index Charts

Quality Index is a pivotal concept originally developed by Drouzy, Jacob and Richard[93] who introduced an empirical parameter Q, or quality index, to characterize the mechanical performance of Al-7%Si-Mg casting alloys. They related the quality index, Q, to the tensile strength, UTS, and the plastic strain of the material to fracture, s_f, as represented by the following equation:

$$\mathbf{Q = UTS + d \log (s_f)} \qquad \textbf{Equation 2.1}$$

With reference to Figure 2.20, the dashed lines generated by applying Equation 2.1 represent lines of constant alloy "quality" and are called *iso-Q lines*, the Q-value being

defined as the y-intercept at s_f=1%. Samples having the same Mg content and similar aging conditions but different ductility values resulting from different dendrite arm spacings, and iron or porosity content, were observed to have the same yield stress, YS, which then relates to the UTS and s_f as:

$$\mathbf{YS = a\ UTS - b\ log\ (}s_f\mathbf{) - c} \qquad \textbf{Equation 2.2}$$

where for the Al-7Si-0.4Mg alloy,[93] a=1, b=60 MPa, c=13 Mpa, and d=150 MPa. The dashed lines generated by applying Equation 2.2 are called *iso-YS lines*, as shown in Figure 2.20.

If the tensile strength of a batch of samples of an Al-7Si-Mg alloy for a given Mg content, aged for different durations of time, is plotted against the tensile ductility, the experimental points tend to follow one of the iso-Q lines, or dashed lines, shown in Figure 2.20, *i.e.* the "quality" of the alloy does not change with the aging. This behavior has been observed for underaged and up to moderately overaged material;[93, 94, 95] it also constitutes one of the basic observations which ultimately led to the development of the quality index concept.[93]

Although the concept was developed specifically for alloys 356 and 357, it has occasionally been applied to other alloy systems as well.[95, 96, 97, 98, 99] A number of studies on Al-Cu-Mg-Ag alloys,[77, 100] however, showed that in contrast with the linear behavior of alloy 356, a plot of UTS *vs* s_f describes a curvilinear contour if the material has undergone aging, as was the case for alloy 201 and shown in Figure 2.21. Furthermore, the parameters involved in Equations 2.1 and 2.2 displayed different numerical values and varied with the prevailing aging condition.

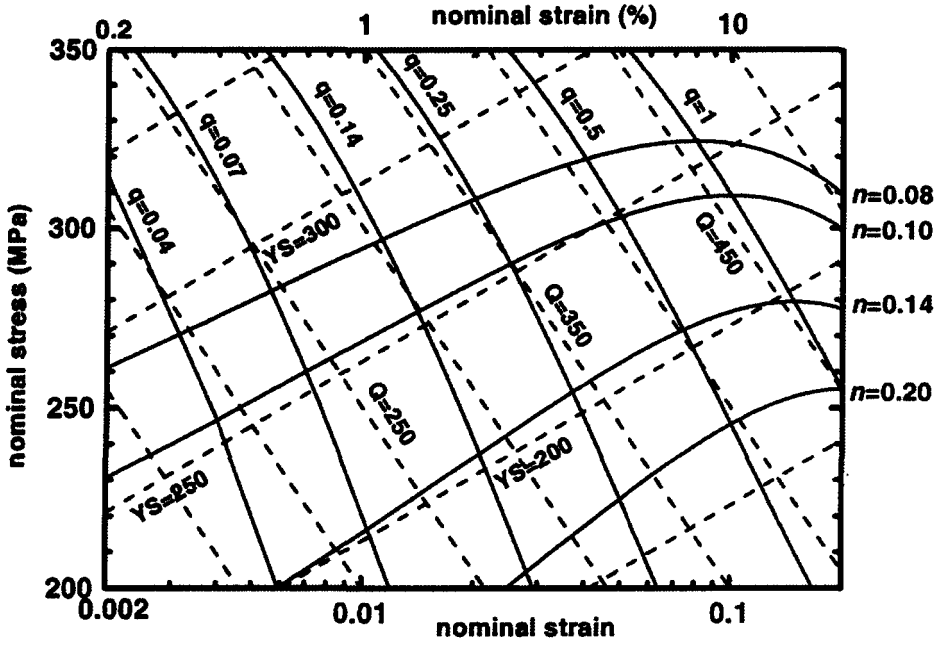

Figure 2.20 A quality index chart for alloy 356. The dashed lines represent the quality index chart as determined using Equations 2.1 and 2.2, after Drouzy *et al.*,[80] in which the iso-YS lines are identified by the yield stress value, while the iso-Q lines are identified by the Q-value. The solid lines are flow curves identified by the n-value and iso-q lines identified by the q-value, having been calculated using Equations 2.5 and 2.7, respectively, assuming $K = 430$ MPa.[97]

The curvilinear contour in the plots **UTS vs s_f** when the material has undergone aging,[96, 101] which is present in the aluminum alloys containing copper, implies that extending the quality index concept to systems other than the Al-Si-Mg casting alloys requires determining the behavior of the strength-ductility relationship as the material undergoes the aging process. These behaviors suggest that the curvilinear pattern may be a characteristic of Cu-containing aluminum alloys.

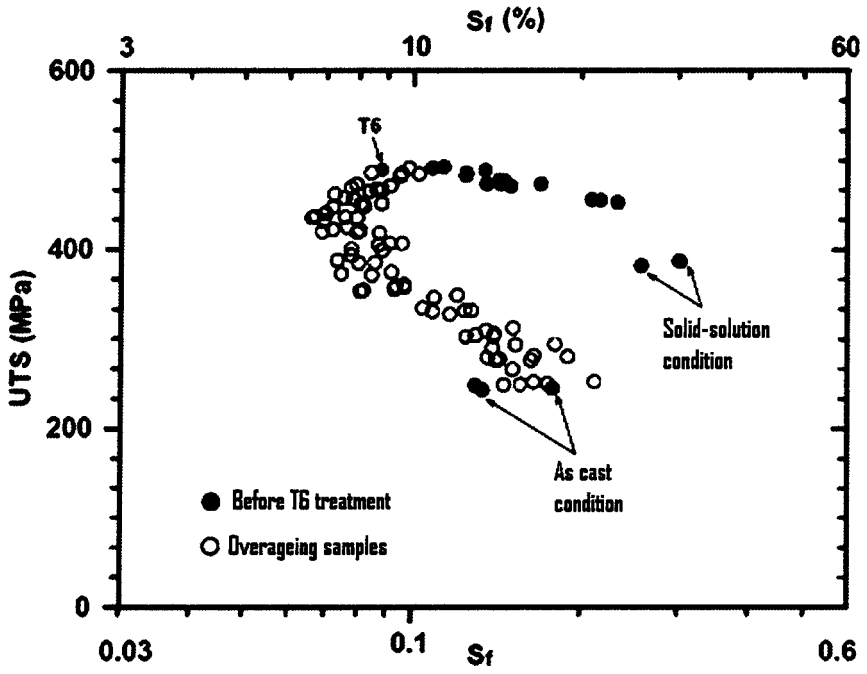

Figure 2.21 Effects of overaging in tensile properties of a 201 alloy.[98]

A model developed by Cáceres[97] shows that the *iso-Q* lines in Figure 2.20 (dashed lines) represent contours of constant relative ductility, the latter thus providing a simple physical rationale for the Q parameter. The Cáceres model assumes that the material can be described with a constitutive equation of the form:

$$\sigma = K\varepsilon^n \qquad \textbf{Equation 2.3}$$

where σ is the true flow stress, K is the strength coefficient, n is the strain-hardening exponent, and ε is the true plastic strain. The parameter n relates to the strain-hardening rate, $d\sigma/d\varepsilon$, through the equation[102]

$$n = \varepsilon/\sigma \; d\sigma/d\varepsilon \qquad \textbf{Equation 2.4}$$

The engineering stress-strain curve may be obtained from Equation 2.3 by relating the true values of the stress and strain, σ and ε, and the corresponding engineering values, P

and s, by $\varepsilon = ln(1+s)$ and $P = \sigma/(1+s)$, respectively.[103] If the elastic component of the strain is disregarded and assuming that true and nominal strain are equivalent (*i.e.* $s \approx \varepsilon$), which is a reasonable assumption for casting alloys due to their limited ductility, then the nominal stress-strain curve can be approximated by

$$P = K[ln(1+s)]^n e^{-ln(1+s)} \approx Ks^n e^{-s} \qquad \textbf{Equation 2.5}$$

Equation 2.5 was used to generate the flow curves in Figure 2.20 in which the solid lines are identified by the n-value, setting $K = 430$ MPa and varying n between 0.08 and 0.2 to represent different aging conditions.[75]

The iso-quality lines in Figure 2.21 can also be generated using Equation 2.5 by introducing the relative ductility parameter, q, defined as the ratio between the strain-hardening exponent of the material and the elongation to fracture, s_f,

$$q = s_f / n \qquad \textbf{Equation 2.6}$$

where $q = 1$ when the samples reach necking (*i.e.* the most ductile samples), while $q<1$ identifies progressively less ductile samples. Thus, $q = 0.5, 0.2, 0.1$ identifies samples which fail at 50, 20, or 10% of their necking onset strain, respectively. Solving Equation 2.6 for n and substituting in Equation 2.5, gives

$$P = Ks^{s/q} e^{-s} \qquad \textbf{Equation 2.7}$$

Equation 2.7 was used to generate the set of constant relative ductility contour lines, or *iso-q* (solid lines in Figure 2.20), each identified by a q-value. It will be observed that the *iso-q* lines are nearly parallel to the empirically determined *iso-Q* lines. The correlation between *iso-q* lines and *iso-Q* lines provides a straightforward physical meaning for the quality index in terms of the relative ductility parameter; a constant Q-value implies

constant relative ductility, q. The maximum quality corresponds to samples which reach necking and thus display the maximum relative ductility, as is indicated in Figure 2.20 by the line $q = 1$.

Differentiation of Equation 2.7 with respect to strain, s, taking into account the semi-logarithmic scale of Figure 2.20, relates the slope of the *iso-Q* lines, which is the parameter d in Equation 2.1, to k and q as follows:

$$d = -dP/ds = -(s/mq)\,P\,[1 + \ln(s) - q\,]$$

$$= -(s/mq)\,K\,s^{s/q}\,e^{-s}\,[1 + \ln(s) - q] \qquad \textbf{Equation 2.8}$$

where $m = 0.434$. The negative sign has been added to keep this formulation consistent with Equation 2.1. Equation 2.8 was solved for the ratio d/K and plotted in Figure 2.20 as a function of s for a range of q-values. It will be seen that for $q \rightarrow 1$ the following is a reasonable approximation

$$d \approx 0.4\,K \qquad (q = 1) \qquad \textbf{Equation 2.8-a}$$

By combining Equations 2.1, 2.5, 2.6, and 2.8-a, the quality index becomes a function of the parameters of the flow curve:

$$\mathbf{Q = K\,[(qn)^n\,e^{-qn} + 0.4\,\log\,(100\,qn)]} \qquad \textbf{Equation 2.9}$$

An approximation of Equation 2.8 could be Equation 2.10 which may arise as a result of combining Equations 2.1 and 2.7, considering that Equation 2.7 is a valid equation for whatever the value of q might be. Equation 2.10 makes it possible to calculate the Quality Index from the tensile test results based solely on the knowledge of the value of K.[104]

$$\mathbf{Q = UTS + 0.4\,K\,\log\,(s_f)} \qquad \textbf{Equation 2.10}$$

Quality Index charts are thus a viable option for presenting results obtained from tensile tests considering that the UTS, YS (intersection of the flow curves at a plastic strain of 0.2%), and plastic strain % may be read in one and the same plot. Additionally, the relative ductility, as well as the quality index which corresponds to these same properties, may also be observed in the graph.[72] Using the model developed by Cáceres, it is possible to design a quality index chart for any alloy, comparing different alloys in one single plot in such a way that it becomes possible to define the effects related to changes occurring in chemical composition, microstructure, and heat treatments within the mechanical properties under study.[72, 98] Figure 2.22 shows the Quality Index chart generated by the Cáceres model.

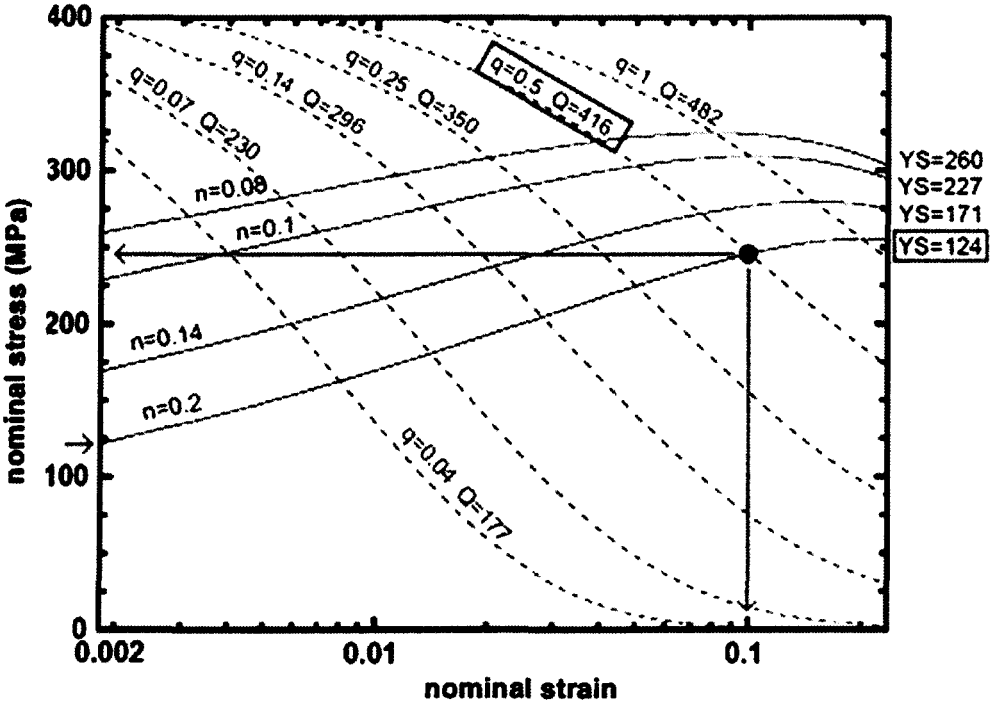

Figure 2.22 Interpretation of the Quality Index Chart generated by the Cáceres model.[101]

CHAPTER 3

EXPERIMENTAL PROCEDURES

CHAPTER 3

EXPERIMENTAL PROCEDURES

3.1 Introduction

The main aim of the experimental procedure for this research work is to investigate the effects of temperature on the mechanical properties within the alloys studied. The term "temperature" here refers to both the temperatures used for aging as applied to the samples tested at room temperature, as well as those used for conducting the mechanical tests at elevated temperatures.

The aging parameters used in this experimental procedure involve aging temperatures ranging from 155°C to 350°C, and aging times from 2 to 100 hours each; subsequently, tensile tests at room temperature are applied to the aged samples. Based on a knowledge of the values of these tensile tests applied at room temperature, one temperature may be selected by means of which it becomes possible to observe the effects of such a temperature for a period of up to 1000 hours with the aim of analyzing the further effects of increased aging time on the mechanical properties at room temperature. With all these values available, it will be possible to select at least two temperatures for high temperature tensile tests which will be useful in describing the mechanical behaviour of the alloys at high temperatures. One of the purposes of these experiments is to find out with precision what the limits of strength and ductility are with regard to the alloys in question.

This process will be analyzed in detail in the relevant discussion chapters so as to shed light on the effects which additions of elements like Ni or Zr or micro-particulates like Al_2O_3 or SiC have on the alloys with respect to aging behaviour; these data will subsequently provide the initial mechanical values which characterize the thermal history of the alloys at the very instant that the high temperature tensile tests are applied. The effects of the additives (Al_2O_3, SiC, Ni and Zr) on the mechanical properties at high temperatures will thus be revealed.

Apart from the analysis of microstructures obtained from tensile test samples, further description of the microstructure involves thermal analysis, which is a method for identifying the main phase reactions related to the solidification of the alloys studied. This characterization may be carried out by means of the analysis of Time-Temperature plotted graphs (T *vs* t) and their first derivatives dT/dt, which will reveal the main sequence of precipitation during solidification as well as the temperature of the corresponding phase reactions. The microstructure of the samples obtained from these experiments will be analyzed by means of optical microscopy and electron probe microanalysis (EPMA) so as to distinguish the main phases involved in the solidification of the alloys. Figure 3.1 shows a schematic diagram of the experimental procedures applied in this research.

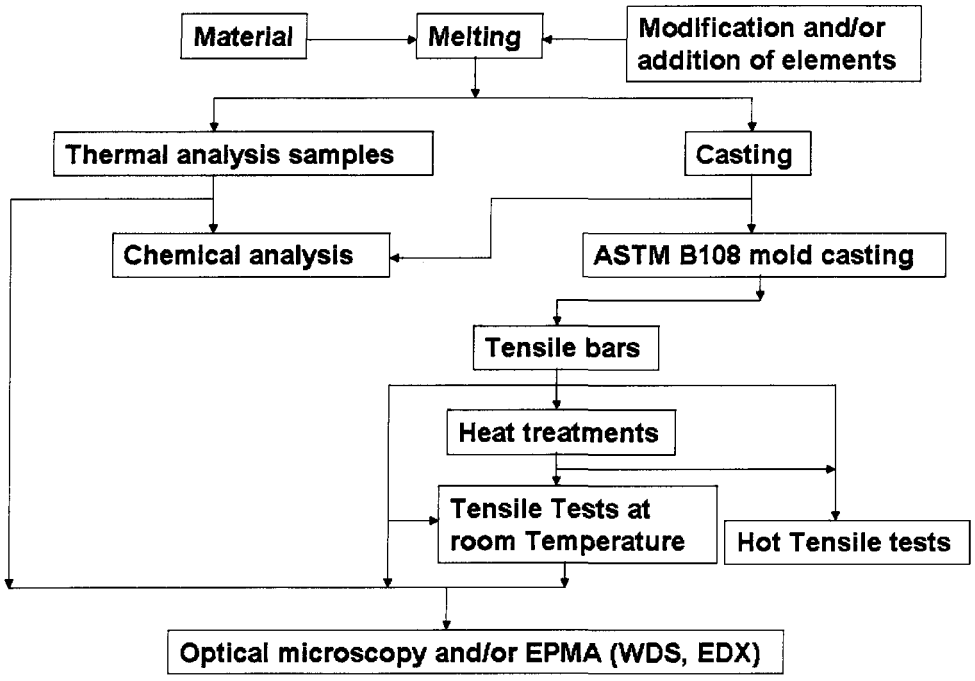

Figure 3.1 Diagram showing an overview of the experimental procedures followed for this work.

3.2 Schedule for Experimental Procedures

In order to attain the objectives outlined previously, an experimental work plan will be developed and executed in three successive stages:

Stage I

(i) Castings to be made so as to obtain tensile test bars for the 7 alloys investigated;

(ii) Heat treatment of all test bars produced as follows:

1. Solution heat treatment for 8 hours at 495°C;
2. Quenching in warm water at 60°C;
3. Artificial aging at 6 temperatures for times ranging from 2 hours to 100 hours, as shown in Table 3.1; and

(iii) Tensile testing of the heat-treated test bars.

Table 3.1 Artificial aging conditions used for room temperature tensile tests

Temperature(°C)	Aging Time (h) and Aging Condition Codes												
	2	**4**	**6**	**8**	**10**	**12**	**16**	**20**	**24**	**36**	**48**	**72**	**100**
155	1	2	3	4	5	6	7	8	9	10	11	12	13
170	14	15	16	17	18	19	20	21	22	23	24	25	26
190	27	28	29	30	31	32	33	34	35	36	37	38	39
240	40	41	42	43	44	45	46	47	48	49	50	51	52
300	53	54	55	56	57	58	59	60	61	62	63	64	65
350	66	67	68	69	70	71	72	73	74	75	76	77	78

Stage II

(i) Artificial aging for over 1000 hours at one single temperature to be selected out of the experimental data obtained from work carried out in Stage I;

(ii) High temperature tensile tests to be applied at different temperatures for selecting aged specimens, based on data previously obtained.

Stage III

Applying microstructural characterization using optical microscopy, electron probe microanalysis (EPMA), and thermal analysis, with a view to identifying and quantifying the principal microstructural features observed in the alloy samples already studied.

3.3 Materials and Procedures

3.3.1 Materials

Alloys

The following alloys will be used in this study:

1. Alloy A (Alloy 354 + 200 ppm Sr + 0.25 wt% Ti);
2. Alloy B (Alloy A + 0.5 wt% Al_2O_3);
3. Alloy C (Alloy A + 0.5 wt% SiC);
4. Alloy D (Alloy A + 0.4 wt% Ni);
5. Alloy E (Alloy A + 0.4 wt% Zr);
6. Alloy F (Alloy A + 0.4 wt% Ni + 0.4 wt% Zr);
7. Alloy G (Alloy A + 0.2 wt % Ni + 0.2 wt% Zr).

Alloy 354 modified with 200 ppm of strontium and grain refined using 0.25wt% Ti (Al-5%Ti-1%B) will be used as the base alloy (alloy A). The chemical composition in wt pct of the as-received 354 alloy is listed in Table 3.2.

Table 3.2 Chemical composition of the as-received 354 alloy

Element (wt %)					
Si	**Fe**	**Cu**	**Mn**	**Mg**	**Al**
9.1	**0.12**	**1.8**	**0.0085**	**0.6**	**87.6**

Additions

(i) The addition of Al_2O_3 will be carried out using a metal matrix composite comprised of a 6061 wrought aluminum alloy containing 20 vol % Al_2O_3 having a 2-to-30 μm particle size.

(ii) The addition of SiC will be carried out using a MMC comprised of a 359 cast aluminum alloy containing 20 vol % SiC having a 2-to-30 μm particle size.

(iii and iv) The addition of zirconium and nickel will be carried out using Al-20 wt% Zr and Al-20 wt% Ni master alloys, respectively.

The microstructures of the 354 base alloy and the master alloys used for the addition of elements and/or micro-particles are shown in Figures 3.2 to 3.8.

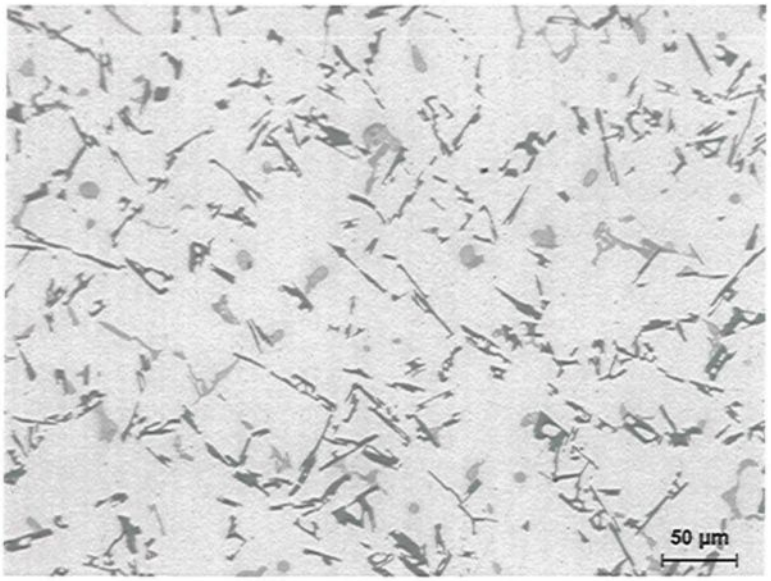

Figure 3.2 Microstructure (200x) of Alloy 354 used as a base alloy in this study.

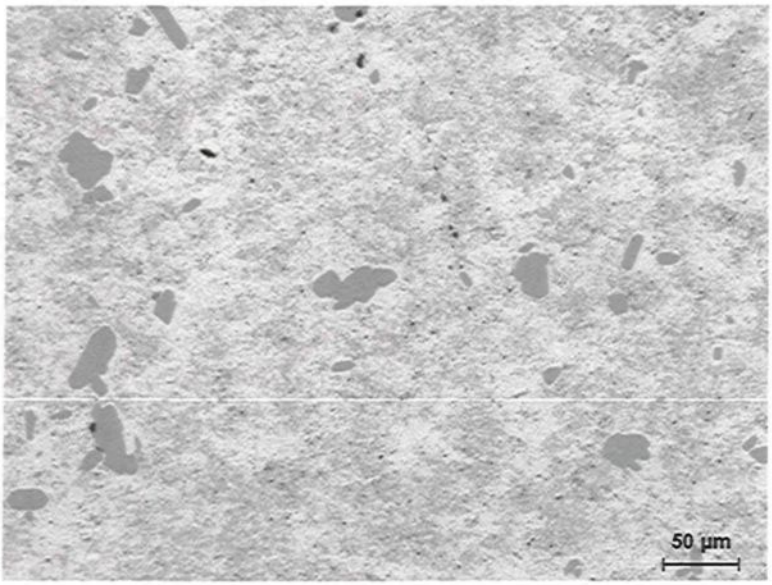

Figure 3.3 Microstructure (200x) of the TiB_2 master alloy used for the addition of titanium as a grain refiner.

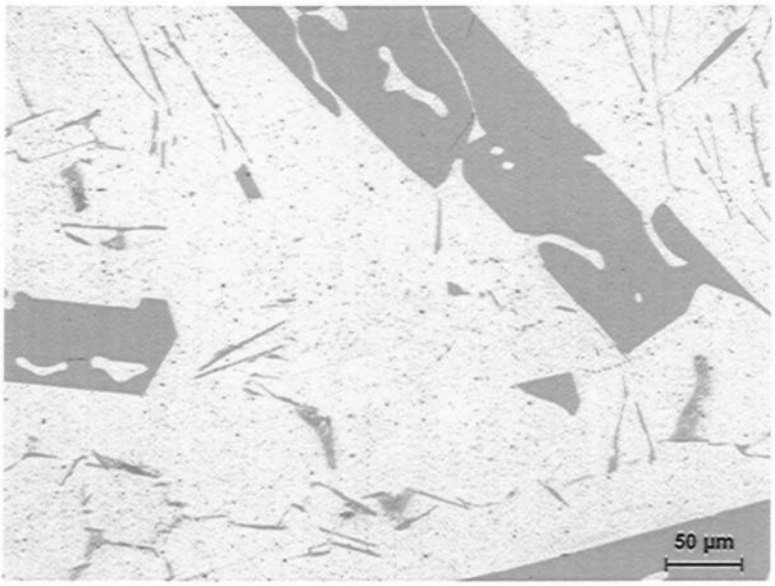

Figure 3.4 Microstructure (200x) of the Al-10%Sr master alloy used for the addition of strontium as a modifier of the silicon structure.

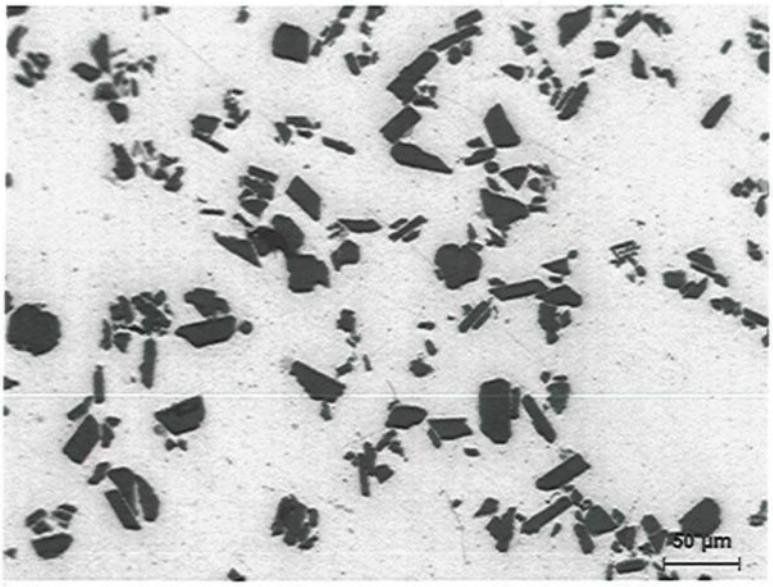

Figure 3.5 Microstructure (200x) of the 6061Aluminum alloy-20%Al_2O_3 master alloy used for the addition of Al_2O_3.

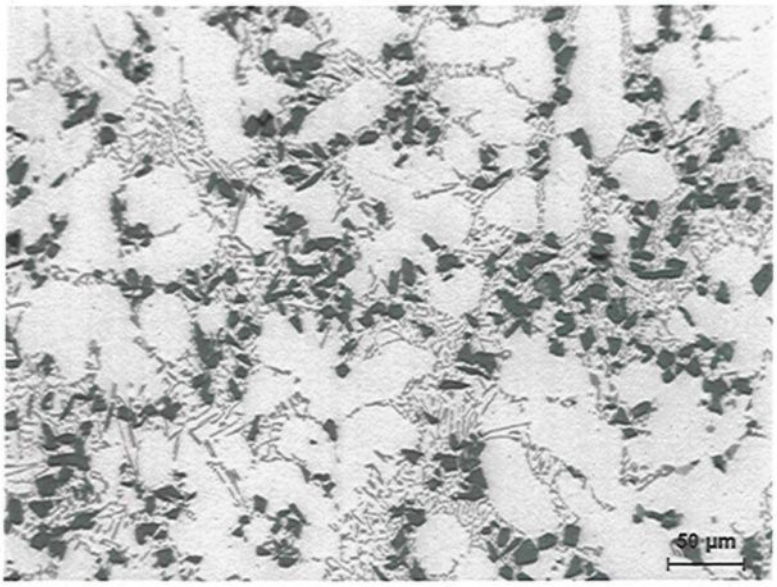

Figure 3.6 Microstructure (200x) of the 356Alloy-20%SiC master alloy used for the addition of SiC.

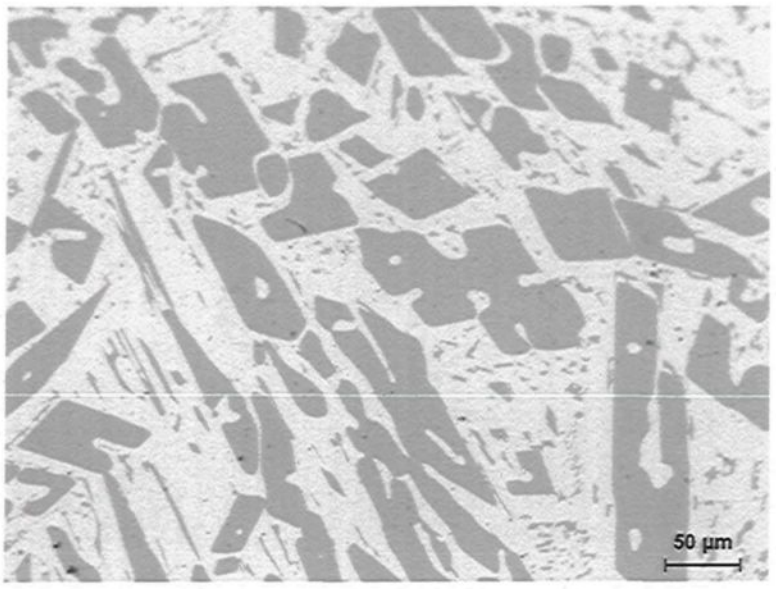

Figure 3.7 Microstructure (200x) of the Al-20%Ni master alloy used for the addition of nickel.

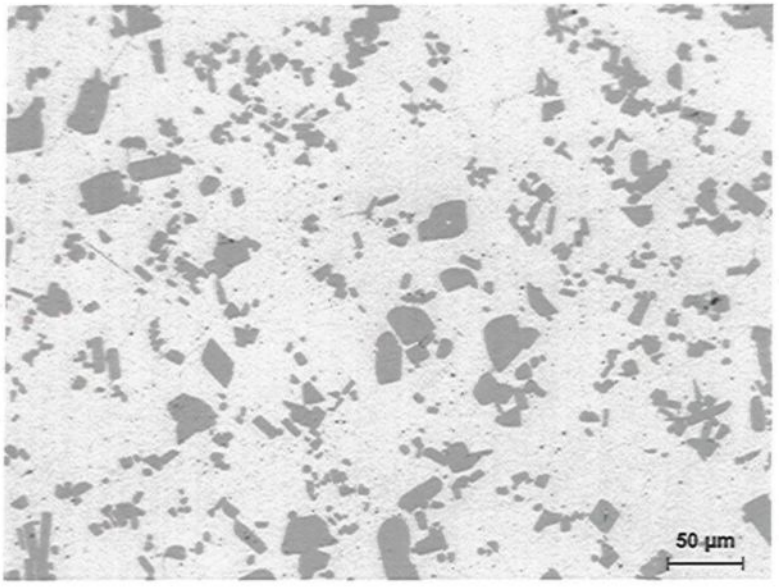

Figure 3.8 Microstructure (200x) of the Al-15%Zr master alloy used for the addition of Zr.

3.3.2 Castings

The experimental 354 base alloy, coded A, with a chemical composition as shown in Table 3.2 was used for this work. The material used to obtain alloy A was cut into smaller pieces, then dried and melted in a 120-kg capacity SiC crucible, using an electrical resistance furnace, as shown in Figure 3.9. The metal temperature was maintained at 780°C, while the melt was degassed using pure, dry argon injected into the melt for 20 min by means of a rotating graphite impeller at 200 rpm, as shown in Figure 3.10. Grain refining and modification of the melt were carried out using Al-5% Ti-1% B and Al-10% Sr master alloys, respectively, to obtain levels of 0.25% Ti and 200 ppm Sr in the melt.

Figure 3.9 Electrical resistance furnace.

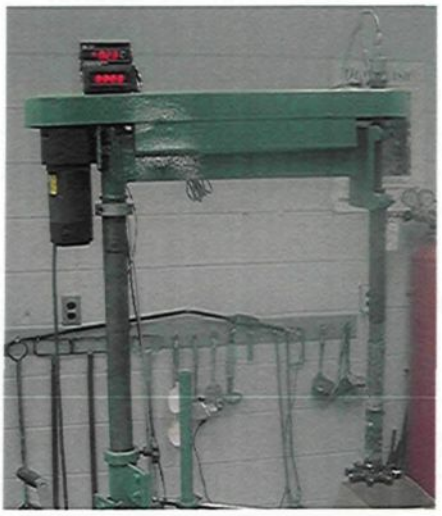

Figure 3.10 Degassing system.

For the remaining six alloys, the master alloys used as additives were aggregated in order to build up the programmed chemical specification. The master alloys were cut into smaller pieces, dried and then added to the melted base alloy. Master alloys were added only instants before degassing to ensure homogeneous mixing of the additives together with the degassing. The humidity varied between 10 and 14% when preparing these melts.

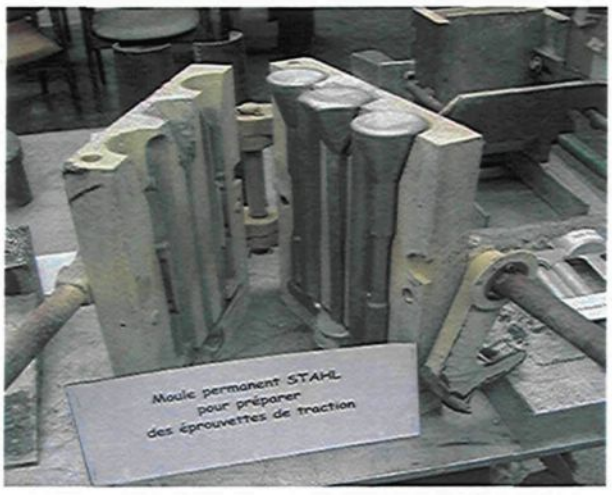

Figure 3.11 ASTM B108 metallic mold.

The melt was poured into a preheated ASTM B-108 permanent mold (preheated to 460°C), shown in Figure 3.11, to prepare test bars for the tensile tests. Three samples for chemical analysis were also taken at the time of the casting; this was done at the beginning, in the middle, and at the end of the casting process to ascertain the exact chemical composition of each alloy.

3.3.3 Heat Treatment

As will be mentioned in a later subsection, heat treatment of the test bars used for tensile testing involves solution heat treating them at 495°C for 8 hours, followed by quenching in warm water at 60°C, after which artificial aging is applied according to the plan established in Table 3.1. After aging, the test bars are allowed to cool naturally at room temperature (25°C). All heat treatments are carried out in a Lindberg Blue M electrical resistance furnace, shown in Figure 3.12.

Figure 3.12 Lindberg Blue M electric furnace.

3.4 Mechanical Tests

3.4.1 Tensile Tests at Room Temperature

All of the samples, whether as-cast, solution heat-treated, or aged, were tested to the point of fracture using an MTS servo-hydraulic mechanical testing machine at a strain rate of 4×10^{-4} s^{-1}, as shown in Figure 3.14. Tensile test bars were produced using the ASTM B-108 mold, shown in Figure 3.11. Each mold casting provides two tensile bars, each with a gauge length of 70 mm and a cross-sectional diameter of 12.7 mm, as shown in Figure 3.13.

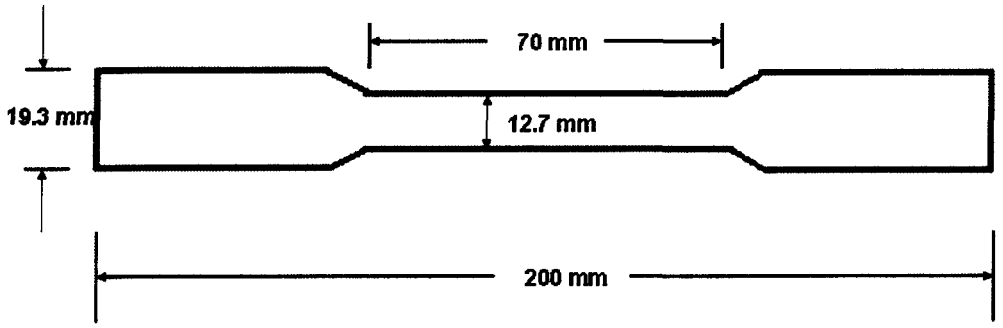

Figure 3.13 Measurements of the tensile test bars used in this study.

The yield strength (YS) was calculated according to the standard 0.2% offset strain, and the fracture elongation was calculated as the percent elongation (%El) over 50mm gauge length, as recorded by the extensometer. The ultimate tensile strength (UTS) was also obtained from the data acquisition system of the MTS machine. This machine was calibrated anew each time any testing was carried out. The average %El, YS, or UTS value obtained from the five samples tested was considered to be the value representing a specific condition. An extensometer, or strain gage, shown in Figure 3.15 was used in the tests to measure the extent of deformation in the samples.

Figure 3.14 MTS Mechanical Testing machine.

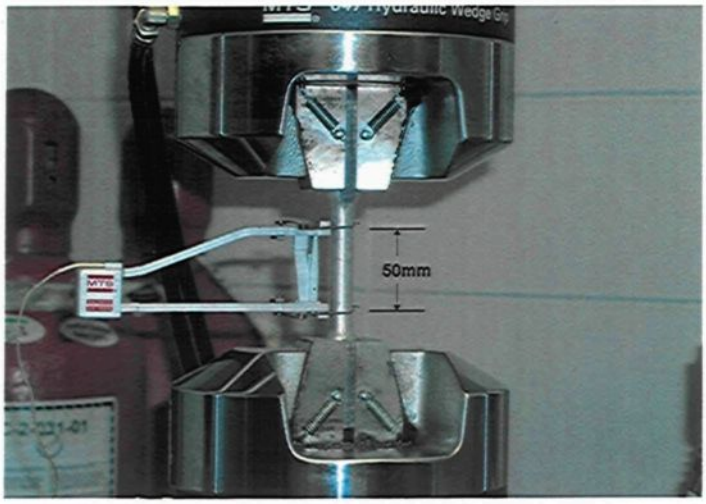

Figure 3.15 Position of the extensometer used in the tensile tests.

Five samples from each condition were tested, for a total of 80 conditions for each alloy in Stage I of the experimental procedure plan. The remaining three conditions were tested for each alloy corresponding to 200 hours, 600 hours, and 1000 hours from which would be selected one specific aging temperature (190°C); this will be explained in greater detail further on in the text. The values for the mechanical properties, namely, UTS, YS, and % El, were gathered from the computerized system of the MTS machine.

3.4.2 High Temperature Tensile Tests

For the high temperature tensile tests, samples from selected conditions were tested to the point of fracture using an Instron Universal Mechanical Testing machine at a strain rate of 4×10^{-4} s^{-1}, as shown in Figure 3.16. The heating furnace installed on the testing machine is an electrical resistance forced air box type furnace having the dimensions 30cm x 43cm x 30cm. The extensometer, which is cooled by circulated water, was used in the tests to measure the extent of deformation in the samples. Both the extensometer and the heating furnace are shown in Figure 3.17. The yield strength (YS) was calculated according to the standard 0.2% offset strain, and the fracture elongation was calculated as the percent elongation (%El) over the 25.4mm gauge length as recorded by the extensometer. The ultimate tensile strength (UTS) was obtained from the data acquisition system of the Universal Testing machine.

In order to reach and stabilize the intended test temperature during the tests, at the time that the samples were mounted in the tensile testing machine, the furnace was already pre-set at the required temperature; also, these samples were kept mounted in the furnace of the tensile testing machine for 30 minutes before the start of every test.

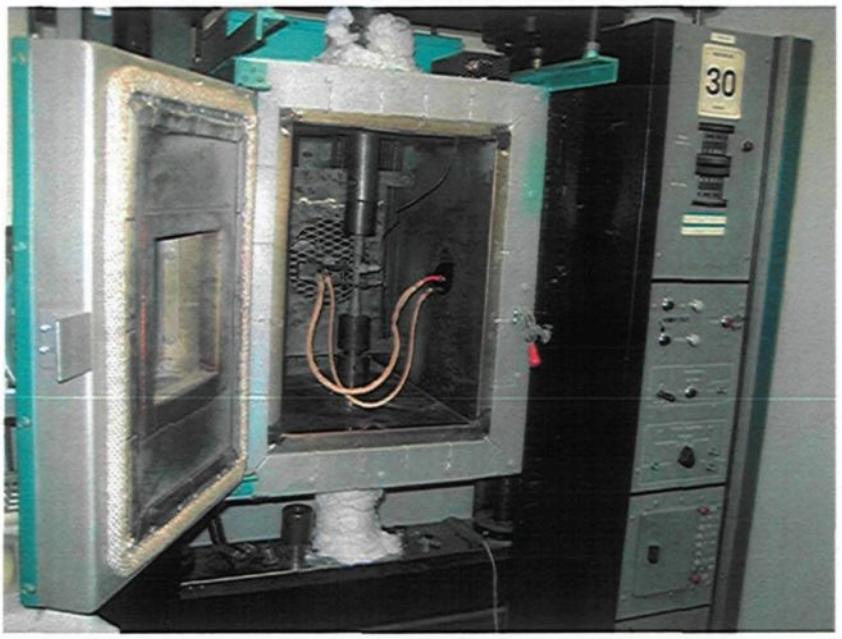

Figure 3.16 Instron Universal Mechanical Testing machine.

The conditions selected for use in the high temperature tensile testing were the as-cast condition in conjunction with 190°C/2hours aging for the A, D, E, F, and G alloys. The temperatures at which high temperature testing was carried out were 25°C (room temperature), 190°C, 250°C, and 350°C. Five samples from each condition were submitted to testing. The average %E1, YS, or UTS values obtained from the five samples tested per condition were considered as the values representing that specific condition.

Figure 3.17 Electrical resistance forced air box type furnace and extensometer cooled by circulating water.

3.5 Characterization of the Microstructure

3.5.1 Thermal Analysis

Ingots of the as-received commercial 354 alloy were cut into smaller pieces, cleaned, and then dried to prepare the required alloys. The melting process was carried out in a graphite crucible of 2 kg capacity, using an electrical resistance furnace; the melting temperature was maintained at 780 °C, while the alloys were grain-refined by adding 0.2 wt% Ti as Al-5wt%Ti-1wt%B master alloy in rod form and modified by adding 150 ppm Sr in the form of an Al-10wt%Sr master alloy. Taking the grain-refined and modified alloy "A" as the base alloy, additions of Zr and Ni were made in order to study the effects of these elements on the phase formation and microstructure of these alloys. Nickel and zirconium were added to the alloys in the form of master alloys containing Al-20wt%Ni

and Al-15wt%Zr, respectively, as was the case with the casting of the tensile samples. The chemical analysis was carried out using an ASPAC® spectrometer.

For the purposes of determining the reactions taking place during solidification, part of the molten metal was also poured into an 800 grams capacity graphite mold preheated to 650°C so as to obtain close-to-equilibrium solidification conditions at a cooling rate of 0.35°Cs^{1}. Thermal analysis was carried out using a chromel/alumel Type K thermocouple inserted into the crucible through a hole in the bottom, and linked to a computer system to record the temperature-time data every 0.1 second. The cooling curve and first derivative curve were plotted from this data to determine the reactions taking place during the solidification of the alloy.

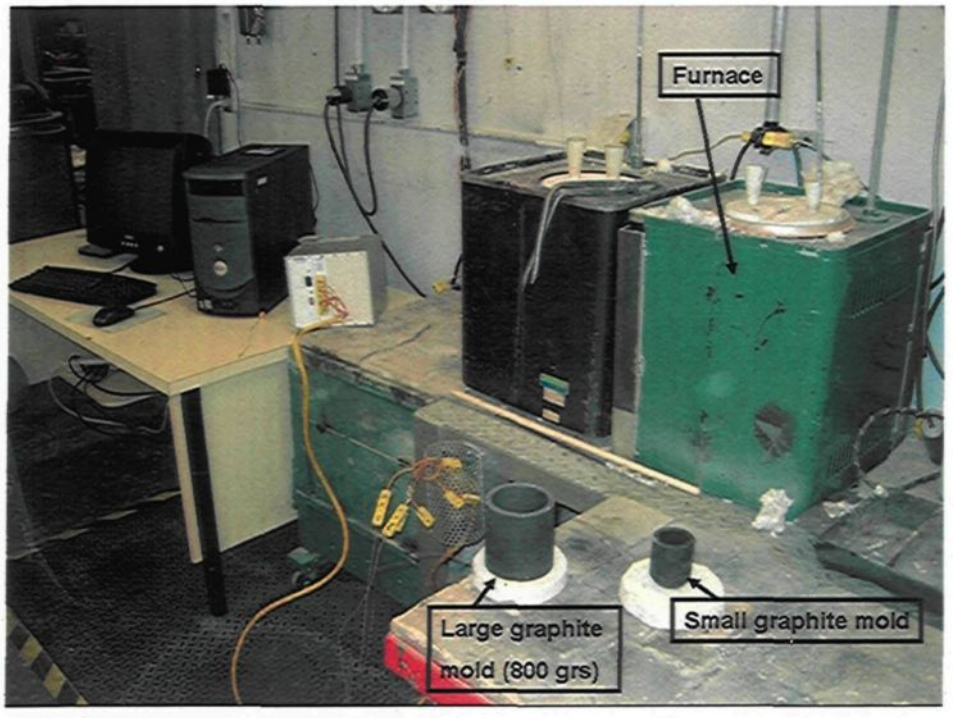

Figure 3.18 Electrical resistance furnaces and the graphite molds used in the thermal analysis experiments.

As will be seen later in the discussion of this research work, it became necessary to conduct a further set of thermal analysis experiments at a higher cooling rate in an attempt to observe the phase-forming reactions of Zr-rich phases which were not detected earlier when using the lower cooling rate. The higher cooling rate was achieved with the use of the smaller graphite mold seen to the right of the large mold in Figure 3.18.

3.5.2 Optical Microstructure

Samples for metallography were sectioned from the tensile-tested bars of all the alloys studied, about 10 mm below the fracture surface, as shown in Figure 3.17; they were then individually mounted in bakelite, and subsequently polished to a fine finish using 1μm diamond suspension. The percentage porosity and eutectic Si-particle characteristics were measured and quantified using an Olympus PMG3 optical microscope linked to a Clemex image analysis system. The microstructures of the polished sample surfaces were examined using the set-up shown in Figure 3.20.

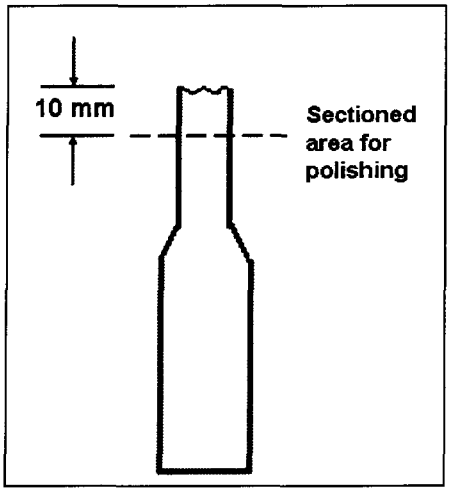

Figure 3.19 Diagram showing the sectioned area for analysis of tensile samples using optical microscopy.

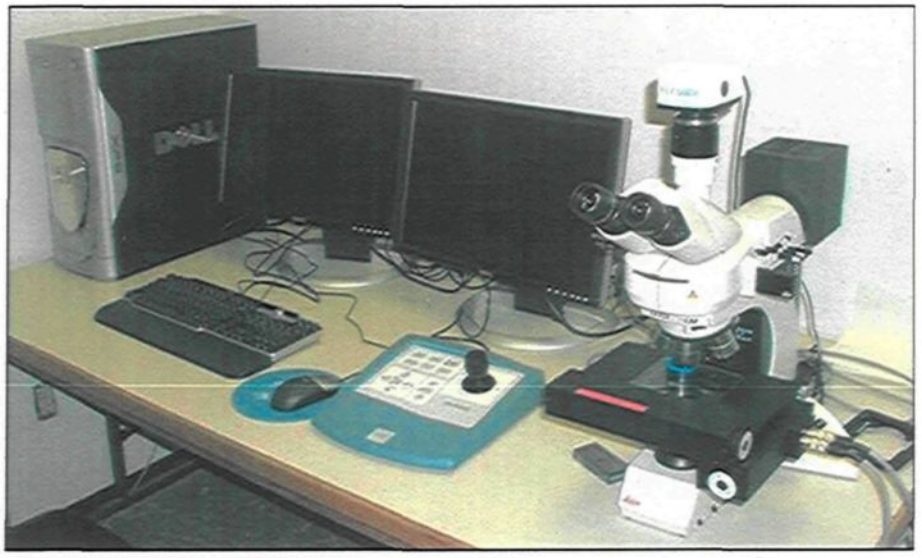

Figure 3.20 Optical microscope - Image analysis setup.

3.5.3 Electron Probe Microanalysis.

Phase identification was carried out using electron probe microanalysis (EPMA) in conjunction with wavelength dispersive spectroscopic (WDS) analysis, using a JEOL JXA-889001WD/ED combined microanalyzer as shown in Figure 3.21, operating at 20 kV and 30 nA, where the electron beam size was ~2 μm. Mapping of certain specific areas of the polished sample surfaces was also carried out where required, so as to show the distribution of different elements within the phases.

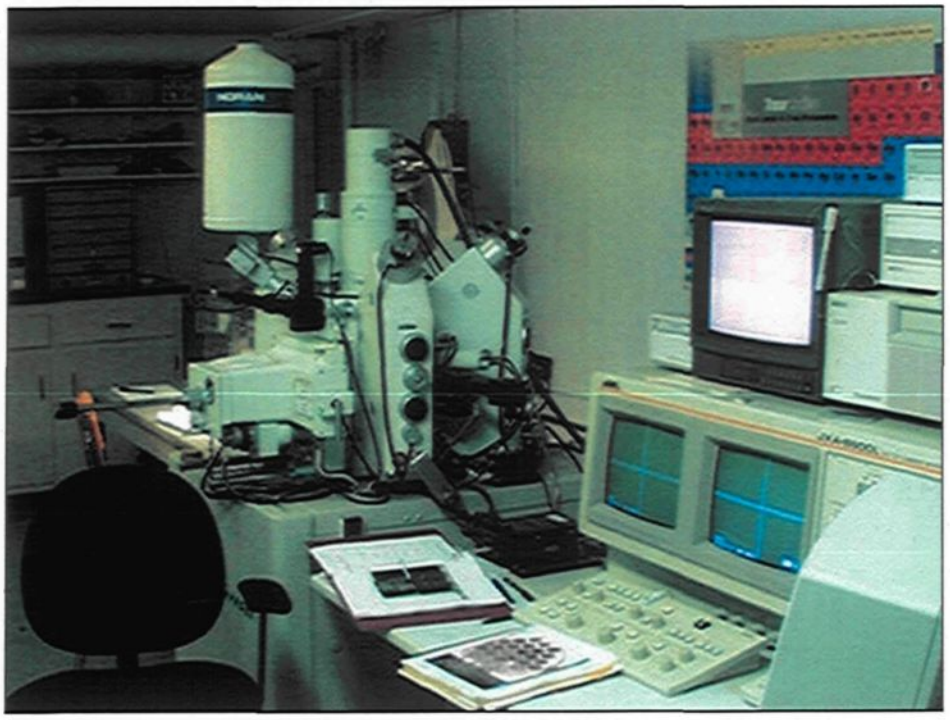

Figure 3.21 Electron Probe Microanalyzer.

CHAPTER 4

MICROSTRUCTURE OF THERMAL ANALYSIS SAMPLES

CHAPTER 4

MICROSTRUCTURE OF THERMAL ANALYSIS SAMPLES

4.1 Introduction

This chapter will present the plotted graphs of the thermal analysis and the microstructures obtained by making use of an optical microscope and an electron probe microanalyzer (EPMA) to investigate the relevant alloys. For the sake of simplicity, the main analysis was carried out using alloy A, which is the base alloy. With regard to the other alloys, D, E, F and G, the only observable difference with respect to alloy A, is the addition of various elements, particularly nickel and zirconium. The principal differences in the microstructure of the thermal analysis samples, as well as in the thermal analysis plots, between the base alloy and the alloys with additions of Zr and Ni, may be seen in the upcoming pages.

For the purposes of this research, the cooling rate is calculated by taking into consideration the temperature and time at which the first and the last reaction was observed on a cooling curve; this implies that it would be correct to consider this cooling rate a *solidification rate* because it includes a greater part of the solidification.

Most of the work carried out in thermal analysis involves following Bäckerud's criterion.[102] Bäckerud's cooling rate considers only the first slope on the temperature-time plot during solidification. The reason for which he applied this criterion as it is nowadays

used is explained by Tamminen[103] in his doctoral Thesis; in their work, two samples were used for every thermal analysis experiment, with, however, the same chemical composition and heat extraction conditions applied to each sample, although it was only for one of these two samples that complete solidification was recorded, implying that the thermocouple remained inserted in place throughout the duration of the whole transformation. The second sample, where the thermocouple was removed from the melt just before the start of solidification, is used to analyze microstructure. As a means of being certain that both cooling rates are the same for both samples, the cooling rate taken was measured on the undisturbed portion of the cooling curves just before the start of solidification. Figure 4.1 represents a schematic example of how the cooling rate values are calculated according to Bäckerud *et al.*[102] and in the present study.

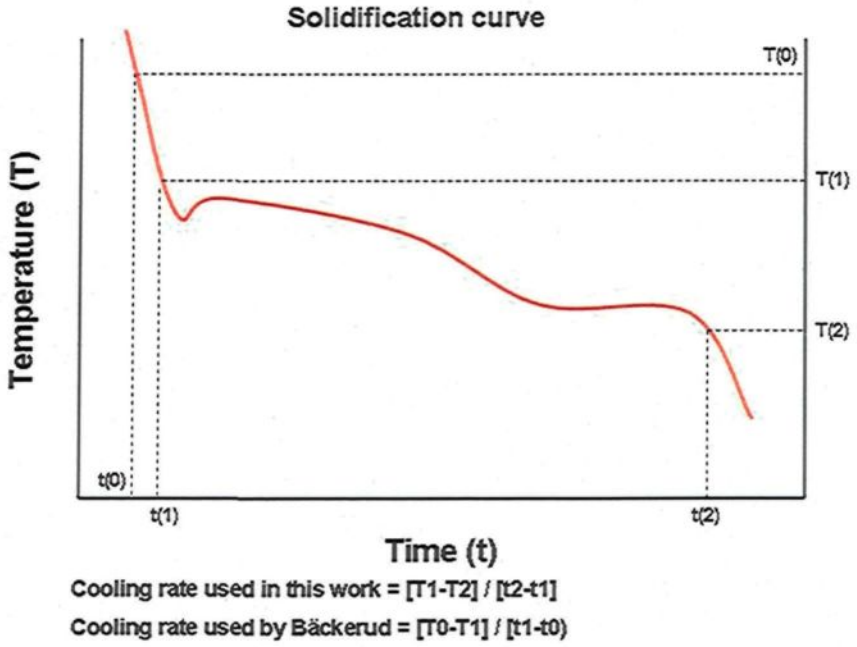

Figure 4.1 Diagram of an ideal solidification curve showing the parameters which characterize the cooling rates.

For this research work, however, it will be necessary to show the secondary dendrite arm spacing value which is a referent for estimating the magnitude of the cooling rate in aluminum-silicon alloys. Figure 4.2 shows the secondary dendrite arm spacing plotted against the cooling rates obtained from the thermal analysis experiments carried out for this work with alloy 354 taking both criteria into consideration.

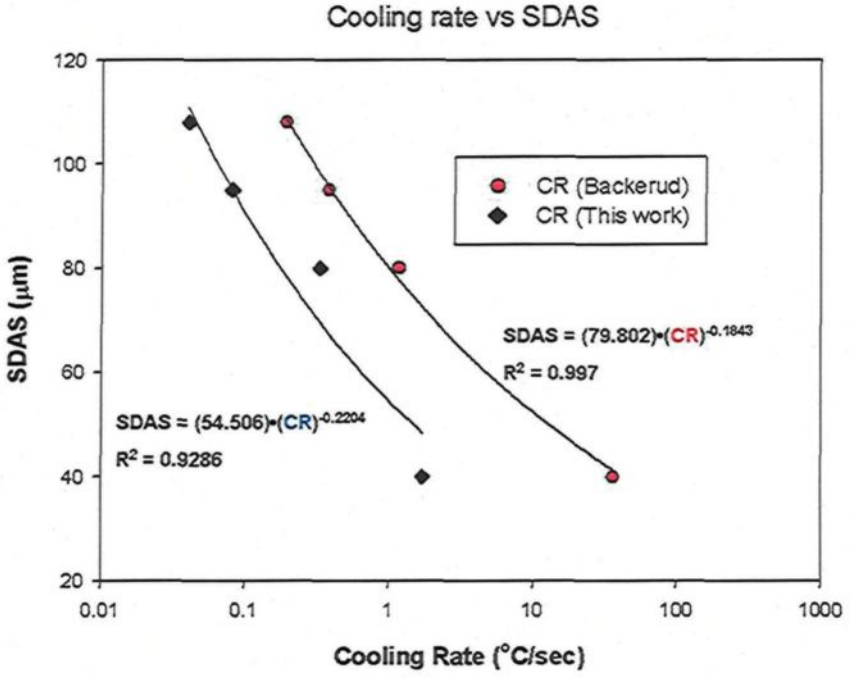

Figure 4.2 Plot correlating SDAS and cooling rates for alloy 354 in the experiments carried out for this thesis.

4.2 Chemical Analysis and Volume Fraction

Table 4.1 lists the chemical analysis of the various alloys studied together with their respective codes, as obtained from samplings taken for this purpose from the corresponding melts used in this work.

Table 4.1 Chemical composition of the alloys used in this work (wt%)

Alloy/Element	Si	Fe	Cu	Mn	Mg	Ti	Sr	Ni	Zr	Al
A	9.43	0.08	1.85	0.01	0.49	0.22	0.0150	~	~	87.5
D	9.16	0.08	1.84	0.01	0.49	0.22	0.0149	**0.46**	~	87.7
E	9.10	0.07	1.83	0.00	0.45	0.21	0.0145	~	**0.39**	87.7
F	9.10	0.08	1.86	0.00	0.46	0.22	0.0122	**0.40**	**0.39**	87.5
G	9.01	0.08	1.85	0.00	0.45	0.21	0.0127	**0.21**	**0.190**	87.8

The volume fraction of the undissolved phases in the matrix was measured using EPMA analysis. For this purpose, a JEOL JX-8900 N WD/RD combined microanalyzer operating at 20 KV and 30 nA was used. In each case, ten fields were measured over the entire sample surface to determine the volume fraction of the undissolved phases. In Table 4.2, samples in the as-cast condition are identified as AC, while samples which have been solution heat-treated at 495°C for 8 hours followed by quenching in warm water at 60°C are identified as SHT.

Table 4.2 Volume fraction of undissolved phases observed in the matrix of alloys A through G used for this research.

Volume Fraction (%)	A	D	E	F	G
AC Condition - Average	3.09	4.87	3.47	6.48	4.42
AC Condition - Std. Deviation	0.32	0.60	0.35	0.31	0.65
SHT Condition - Average	2.05	3.37	2.26	4.50	3.39
SHT Condition - Std. Deviation	0.42	0.56	0.39	0.44	0.81

As may be seen from Table 4.2, the volume fraction increases as the percentage of such additives as Ni and Zr increases. The highest volume fraction is present in alloy F, which is the alloy containing higher levels of zirconium and nickel; taking into consideration the volume fraction in alloy A, the volume fraction in alloy F is superior to the sum of the volume fractions of both alloy D containing nickel plus alloy E containing

zirconium. From these comparisons in volume fraction values it may be deduced that the elements Zr and Ni must interact between themselves, or with other elements contained in the base alloy, in order to form new phases. Such new phases would thus increase the value of the volume fraction of intermetallics, as is observed to be the case with alloy F. Interactions between Zr and Ni with different elements to form Zr-Ni-Al-Cu, Zr-Ni-Al, and Zr-Ti-Si phases have been reported by several researchers studying these systems.[104-107]

Table 4.3 shows the secondary dendrite arm spacing values and grain sizes observed in the samples obtained from the thermal analysis experiments. The SDAS value of ~80 μm is an expected value based on the low cooling rates obtained with the preheated graphite mold used for these thermal analysis experiments, *i.e.* the larger mold shown in Figure 3.10.

Table 4.3 Grain Size and SDAS values observed in the alloys studied

Parameter (μm)	A	D	E	F	G
SDAS	78	80	85	76	73
Grain size	345	270	300	260	265

4.3 Thermal Analysis: Alloys A, D, E, F, and G

4.3.1 Alloy A

The cooling curve for alloy A, obtained from its time-temperature data and its first derivative plot, are provided in Figure 4.3. The temperatures at which the main reactions take place during solidification were determined from the first derivative curve and are listed in Table 4.4 for all the alloys. In Figure 4.3, these reactions are marked by numbers

on the first derivative curve. Similarly, the reactions observed in the other alloys, are numbered on their first derivative curves shown later on in Figures 4.6, 4.9, 4.12, and 4.15.

Table 4.4 Proposed main reactions occurring during solidification of alloys A, D, E, F, and G [29,102,108,109]

Reaction #	Suggested Temperature Range (°C)	Suggested Precipitated Phase
1	600-597	α-aluminum dendritic network
2	560-558	Eutectic Al-Si
3	555-556	Al_9FeNi
4	540-538	Mg_2Si
5	525-523	$Al_8Mg_3FeSi_6$
6	523-520	Al_3CuNi
7	500-496	Eutectic Al-Al_2Cu
8	485-489	$Al_5Mg_8Cu_2Si_6$

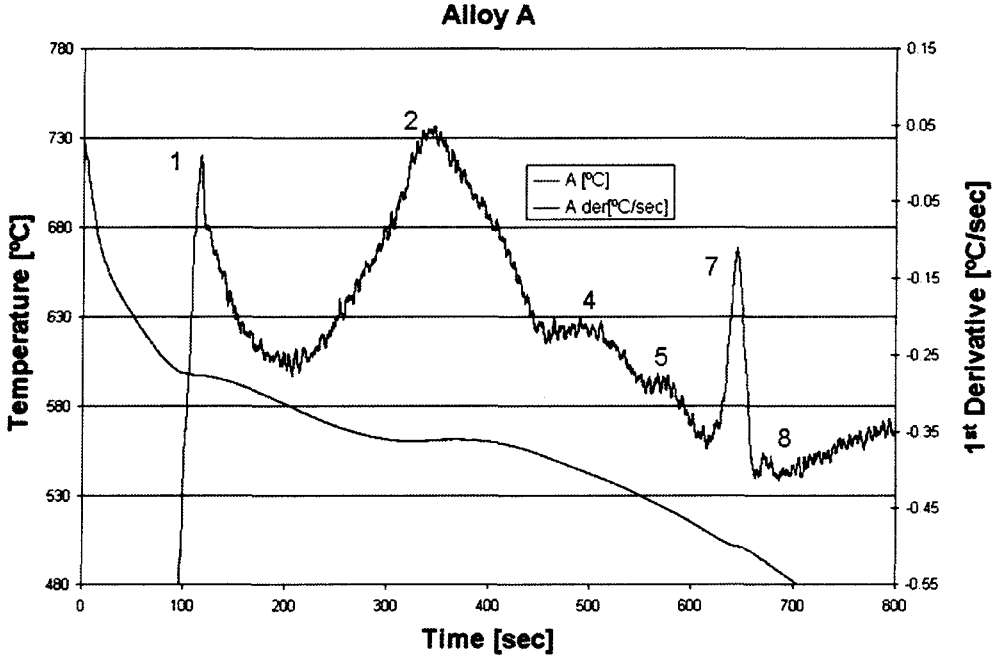

Figure 4.3 Temperature-time plot and first derivative from the thermal analysis of alloy A.

Figure 4.4 Microstructure at 200x magnification of alloy A from thermal analysis sample obtained at a low cooling rate of 0.35°C sec^{-1}.

The optical micrograph shown in Figure 4.4 for alloy A illustrates prominent phases such as the α-Al dendrites and eutectic silicon in the interdendritic regions. Some of the other phases observed in this alloy appear in the backscattered image presented in Figure 4.5; these phases were identified by WDS, as shown in Table 4.5 and are those typically observed in the Al-Si-Cu-Mg system.[102, 110, 111] With regard to alloy A, even if the $Al_5Mg_8Cu_2Si_6$ phase reaction may only barely be perceived at 485°C, the solidification range is still one of 115°C, *i.e.* from 600°C to 485°C; this is similar to the solidification range observed for the 319 alloy.[108, 112]

Tables 4.5 through 4.9 present the chemical composition of the phases examined in alloys A, D, E, F, and G as recorded by means of WDS analysis of samples obtained from the graphite mold used for the thermal analysis experiments at low cooling rates. For the

sake of simplicity, Tables 4.6 to 4.9 show only the WDS analysis of those phases which are not shared with the base alloy A.

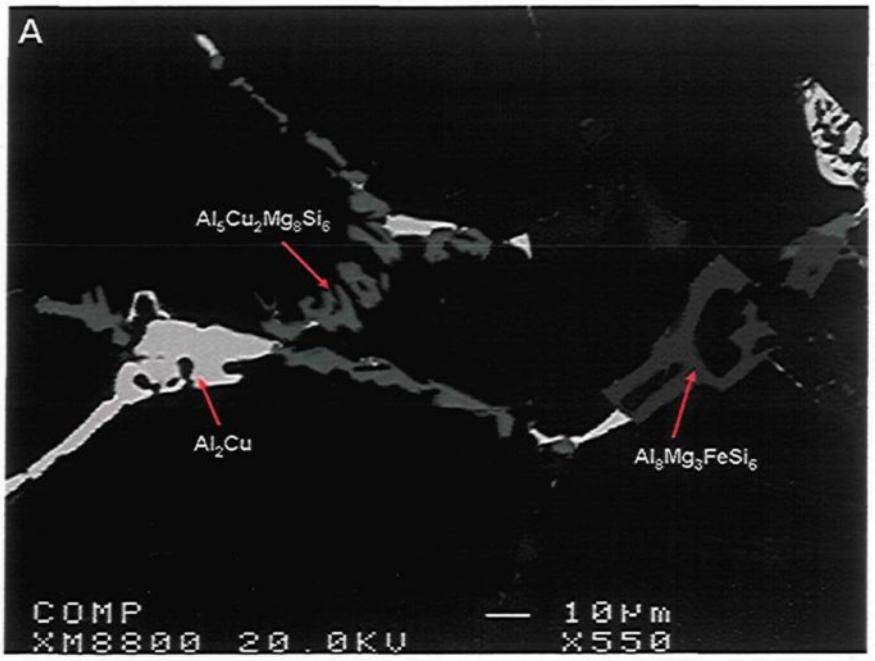

Figure 4.5 Backscattered image showing some of the phases observed in alloy A.

A further similarity between the thermal analysis of the 319 and 354 alloys may be observed at 500°C where the copper phase reaction appears clearly; this observation reveals that the solution heat treatment temperature should be less than 500°C in order to avoid risking the incipient melting of the Al_2Cu phase. This similarity between the solidification of alloys 319 and 354 should be considered for future analysis in relation to the heat treatment of the 354 alloys since most of the literature recommends a solution temperature which is higher than 515°C for this particular alloy.[112-115]

Table 4.5 WDS analysis of phases observed in Alloy A

Alloy Code	Element	Wt %	At %	Calculated Formula	Shape and Color	Suggested Formula
A	Al	48.5	68.1	$Al_{2.12}Cu$	Blocklike, white	Al_2Cu
	Cu	50.7	32.1			
	Total	99.2	100.2			
	Al	45.9	47.8	$Al_{8.6}FeMg_{3.4}Si_{4.8}$	Small particles, brown	$Al_8FeMg_3Si_6$
	Fe	10.9	5.6			
	Mg	16.6	19.2			
	Si	26.8	26.3			
	Total	100.2	98.9			
	Al	16.9	17.7	$Al_{3.9}Cu_2Mg_{9.2}Si_{6.9}$	Small particles, grey	$Al_5Cu_2Mg_8Si_6$
	Cu	19.8	9.0			
	Mg	34.8	41.8			
	Si	30.5	31.4			
	Total	102.0	99.9			
	Mg	63.4	67.9	$Mg_{2.13}Si$	Small particles, black	Mg_2Si
	Si	36.8	31.9			
	Total	100.2	99.8			

4.3.2 Alloy D

The optical micrographs obtained from the low cooling rate thermal analysis samples of alloys D, E, F, and G are shown in Figures 4.7, 4.10, 4.13, and 4.16. Apart from the α-Al dendrites and the eutectic Si particles observed in the interdendritic regions, other phases may also be observed, as denoted by the arrows in each micrograph. The irregular shaped plate-like particles correspond to Al-Si-Zr-Ti phases, as was determined from the WDS analysis of these particles which were observed in alloys containing Zr, namely Alloys E, F, and G. It is interesting to note that the eutectic Si particles in these micrographs, as well as those shown in Figure 4.4 for alloy A, appear to be only partially modified even though the alloys contained over 120 ppm Sr, as may be seen from Table

4.1. The incomplete modification of the eutectic silicon structure may be attributed to the slow cooling rate used in the thermal analysis experiments.

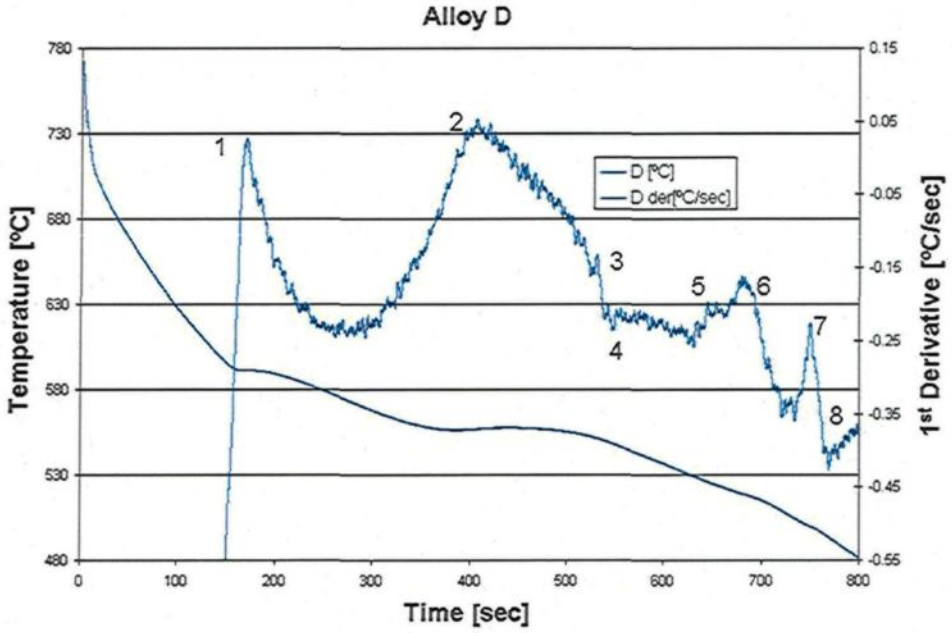

Figure 4.6 Temperature-time plot and first derivative from the thermal analysis of alloy D.

The copper phase is seen mainly as small pockets of the blocklike Al_2Cu; presumably the low cooling rate used in this work, the relatively high percentage of magnesium, and the strontium content, all lead to an increase in the tendency of this phase to segregate to the limits of the α-Al dendrites.

Based on the absence of Reactions 3 and 6 in the thermal analysis curves shown in Figures 4.3 and 4.6, for alloys A and E, respectively, that is to say in alloys containing no nickel, it is possible to deduce that such reactions must correspond to the precipitation of nickel-rich phases. As may be observed from Table 4.4 and Figure 4.6, Reaction 3 is present at 556°C following the Al-Si eutectic reaction, while Reaction 6 is close to Reaction

7 involving precipitation of the Al_2Cu phase. Both Reactions 3 and 6 have been reported in the literature for the Al-Si-Cu-Mg-Ni alloy systems normally used in the manufacture of automotive pistons, for which the reaction temperature, chemical composition in atomic percent, and the form of the precipitates appear similar to those observed in this study.[116]

Figures 4.8, 4.11, 4.14, and 4.17 show the backscattered images obtained from the thermal analysis samples of Alloys D, E, F, and G, respectively, showing the different phases observed for these alloys. From these images, it will be observed that among the phases whose reactions were listed in Table 4.4, those specifically corresponding to reactions 1, 2, 4, 5, 7, and 8, are common to all the alloys.

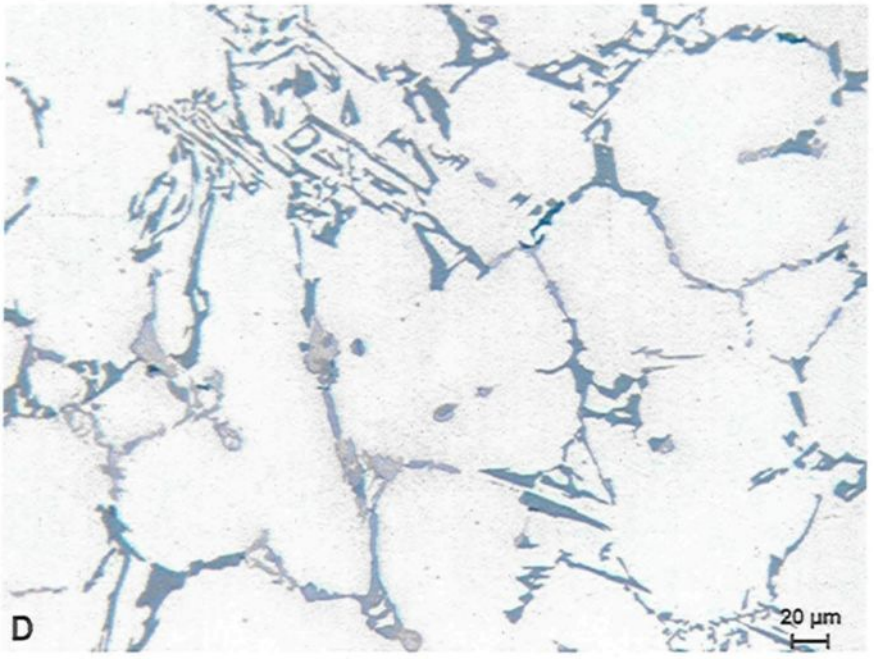

Figure 4.7 Microstructure at 200x magnification in alloy D from thermal analysis samples obtained at a low cooling rate of 0.35 °C sec^{-1}.

The β-iron phase, Al_5FeSi, was not in evidence, possibly due to the relatively low Fe-content present in alloy A. In conjunction with the segregation of the copper phases, the

presence of the β-iron phase is known to have a negative effect on the mechanical properties of Al-Si-Cu-Mg alloys.[117]

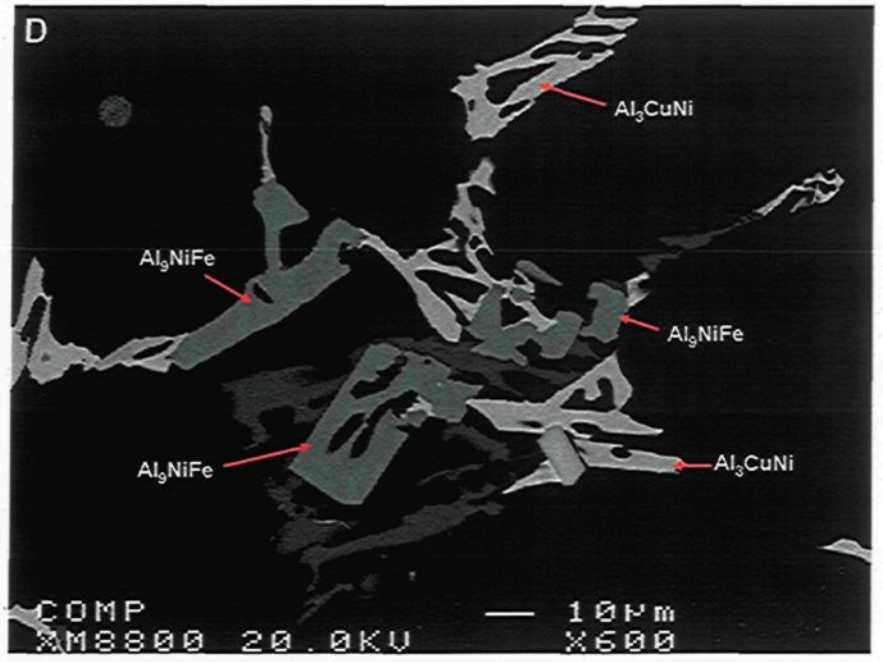

Figure 4.8 Backscattered image of alloy D from thermal analysis sample obtained at a low cooling rate of 0.35 °C sec^{-1}.

Table 4.6 WDS analysis of phases observed in Alloy D

Alloy Code	Element	Wt%	At%	Calculated Formula	Shape and Color	Suggested Formula
D	Al	64.4	79.18	$Al_{10.1}Ni_{1.6}Fe$	Irregular form, dark grey	Al_9NiFe + AlNi
	Ni	22.5	12.86			
	Fe	10.1	7.87			
	Total	97.00	99.91			
	Al	40.8	61.26	$Al_{3.3}Cu_{1.1}Ni$	Irregular, white	Al_3CuNi
	Cu	30.8	19.9			
	Ni	26.8	18.4			
	Total	98.40	100.01			

The mechanism involved in Al_2Cu precipitation was proposed by Samuel[118] as follows: (a) during the first stages of solid fraction, the formation of the α-Al dendritic network is associated with the segregation of Si and Cu in the melt, ahead of the progressing dendrites; (b) when the solidification temperature approaches the eutectic temperature, Si particles precipitate, leading to a local concentration of Cu in the remaining areas, and because of this segregation, the Al_2Cu phase more often than not precipitates in the blocklike form rather than in the fine eutectic form. In the alloys containing nickel, the Al_3CuNi phase is observed situated adjacent to the Al_2Cu phase and both phases are located at the limits of the dendritic α-Al phase; this observation is in concordance with the fact that the reactions noted in the thermal analysis curves, namely Reaction 6 and Reaction 7, are contiguous to one another.

4.3.3 Alloy E

As in the previous section pertaining to alloy D, relevant data for alloy E are presented in this section.

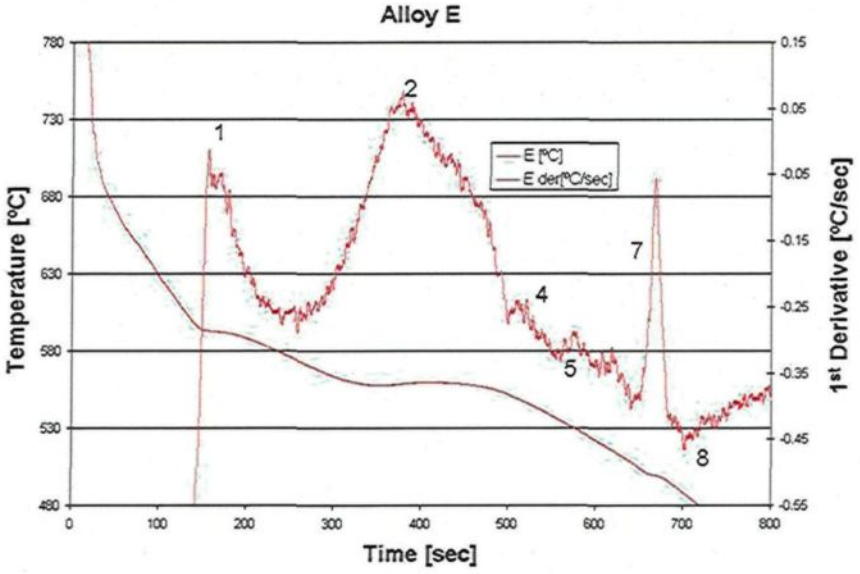

Figure 4.9 Temperature-time plot and first derivative from the thermal analysis of alloy E.

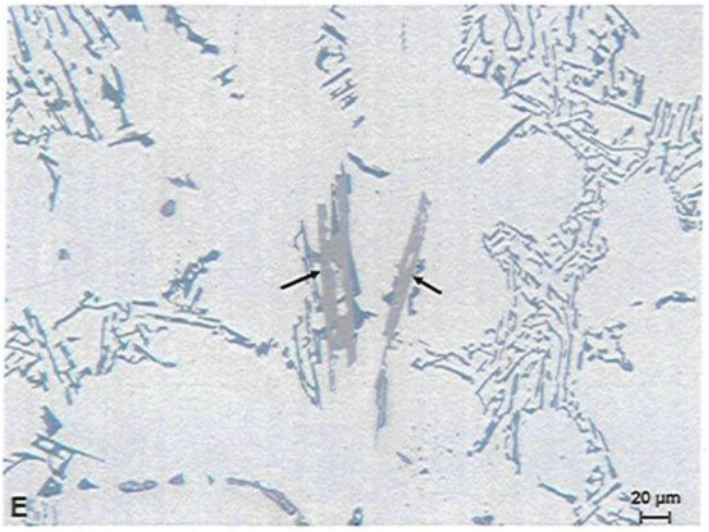

Figure 4.10 Microstructure at 200x magnification in alloy E from thermal analysis sample obtained at a low cooling rate of 0.35 °C sec^{-1}. The black arrows point to the Al-Si-Zr-Ti phases observed in the alloy.

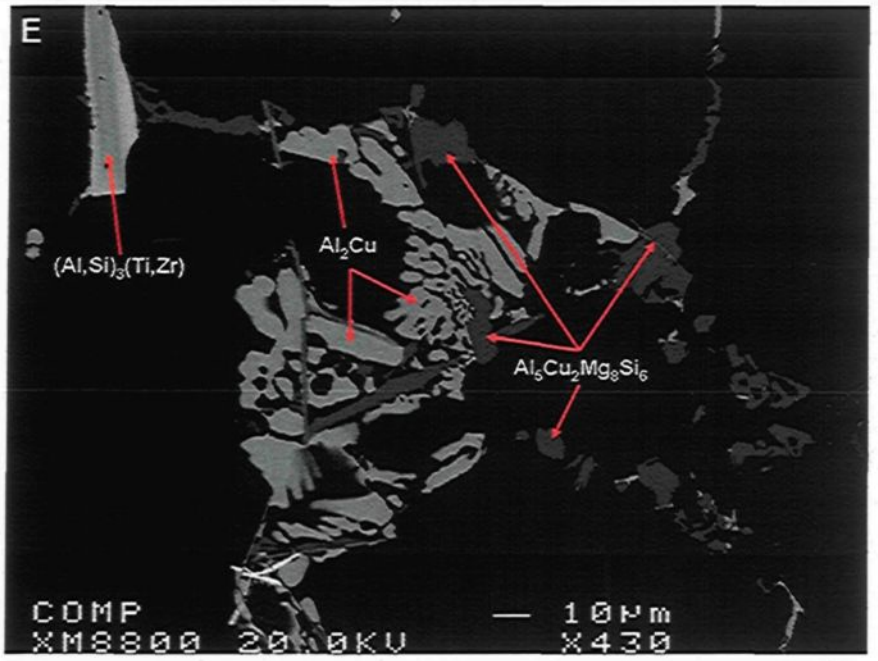

Figure 4.11 Backscattered image of alloy E from thermal analysis sample obtained at a low cooling rate of 0.35 °C sec^{-1}.

Table 4.7 WDS analysis of phases observed in Alloy E

Alloy Code	Element	Wt%	At%	Calculated Formula	Shape and Color	Suggested Formula
E	Al	5.26	8.59	$AlSi_{6.87}Ti_{1.56}Zr_{2.16}$	Blocklike, white	$(Al,Si)_2(Ti,Zr)$
	Si	37.63	59.06			
	Ti	14.59	13.42			
	Zr	38.51	18.62			
	Total	96.00	99.69			
	Al	43.82	62.92	$Al_{6.4}Si_{1.33}TiZr_{1.41}$	Needlelike, grey	$(Al,Si)_3(Ti,Zr)$
	Si	9.54	13.16			
	Ti	12.19	9.85			
	Zr	32.74	13.92			
	Total	98.29	99.85			

4.3.4 Alloy F

Relevant data for alloy F are presented in this section.

Table 4.8 WDS analysis of phases observed in Alloy F

Alloy Code	Element	wt.%	At.%	Calculated Formula	Shape and Color	Suggested Formula
F	Al	40.7	61.53	$Al_{3.2}Cu_{1.1}Ni$	Irregular form, white	Al_3CuNi
	Cu	49.1	31.48			
	Ni	9.5	6.6			
	Total	99.3	99.61			
	Al	64.3	79.2	$Al_{16.2}Ni_{2.6}Fe$	Irregular form, dark grey	$Al_9NiFe + Al_3Ni_2 + Al$
	Ni	22.73	12.9			
	Fe	8.2	4.9			
	Total	95.2	97			
	Al	5.41	8.6	$AlSi_{6.7}Ti_2Zr_{1.9}$	Blocklike, white	$(Al,Si)_2(Ti,Zr)$
	Si	38.1	57.86			
	Zr	34.81	16.3			
	Ti	18.93	16.88			
	Total	97.2	99.6			
	Al	41.25	60.6	$Al_{5.3}Si_{1.2}TiZr_{1.3}$	Needlelike, white	$(Al,Si)_3(Ti,Zr)$
	Si	9.57	13.5			
	Zr	32.92	14.3			
	Ti	13.74	11.37			
	Total	97.4	99.8			

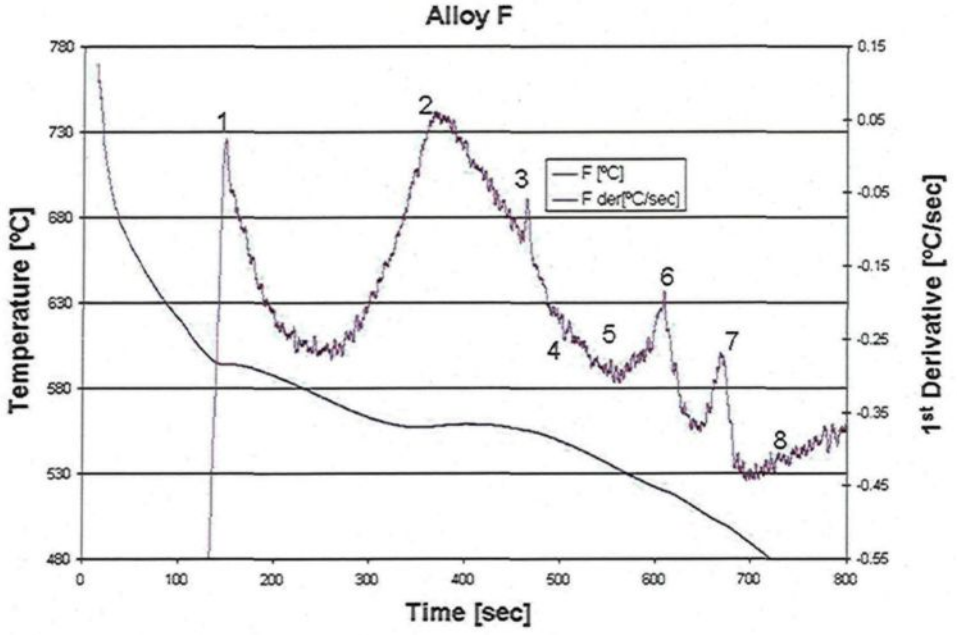

Figure 4.12 Temperature-time plot and first derivative from the thermal analysis of alloy F.

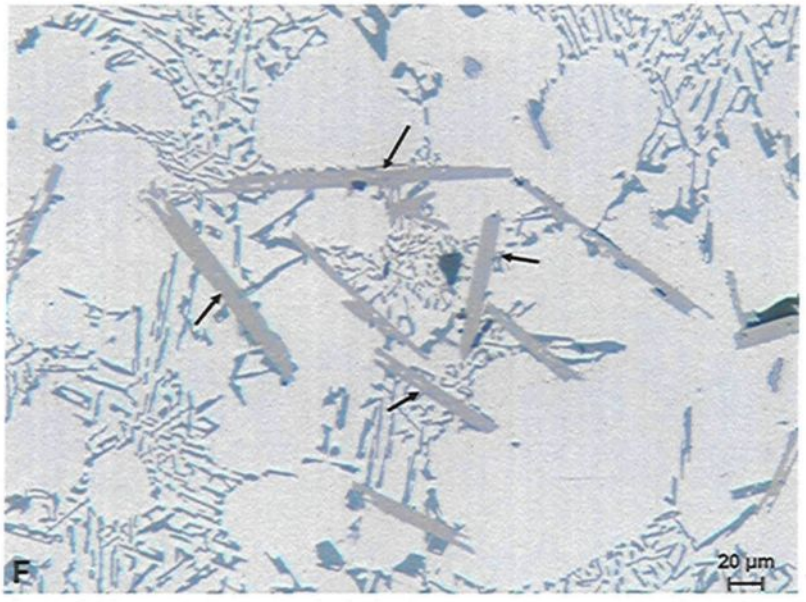

Figure 4.13 Microstructure at 200x magnification in alloy F from thermal analysis sample obtained at a low cooling rate of 0.35 °C sec^{-1}. The black arrows point to the Al-Si-Zr-Ti phases observed in the alloy.

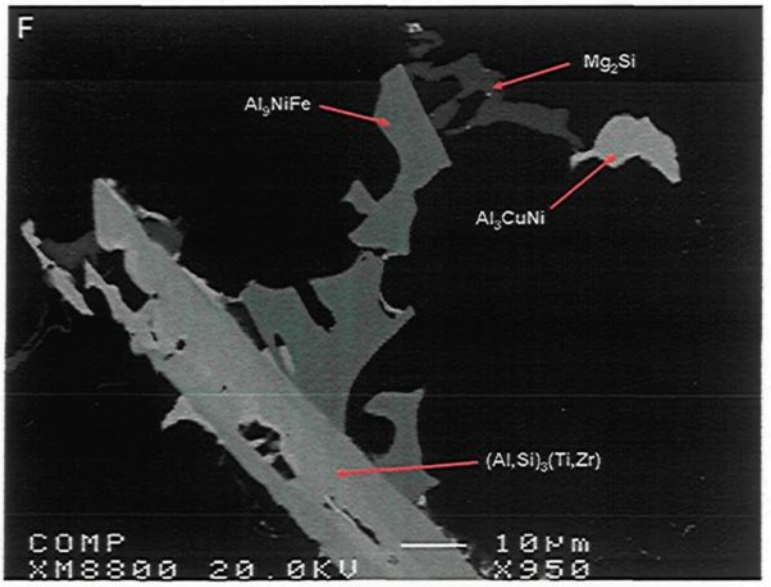

Figure 4.14 Backscattered image of alloy F from thermal analysis sample obtained at a low cooling rate of 0.35 °C sec^{-1}.

4.3.5 Alloy G

Relevant data for alloy G presented in this section.

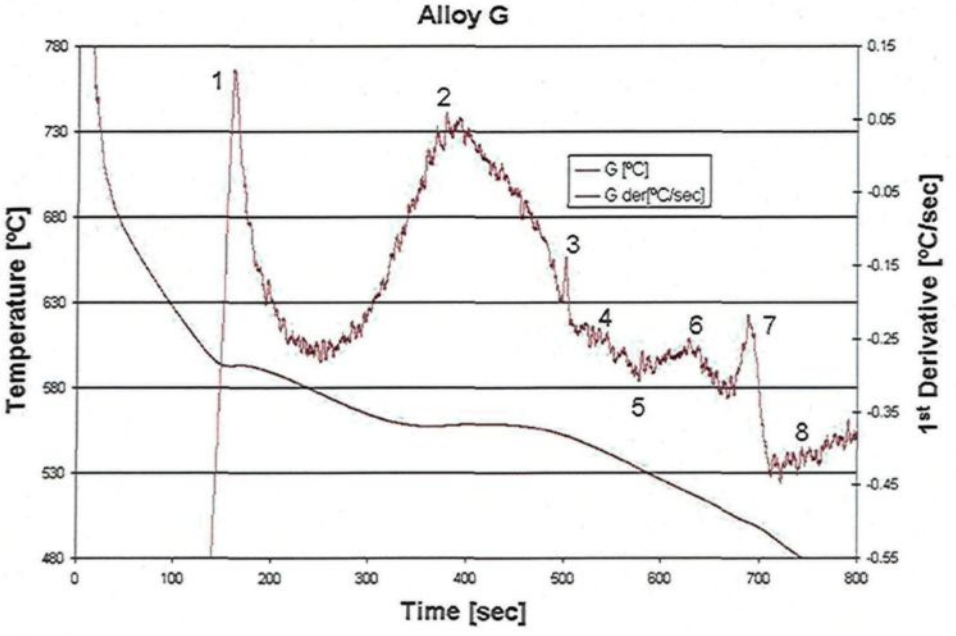

Figure 4.15 Temperature-time plots and their first derivatives from the thermal analysis of alloy G.

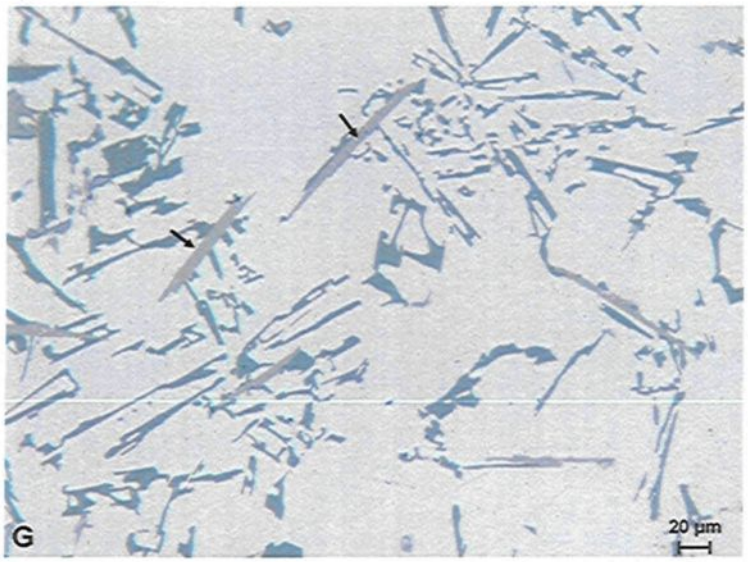

Figure 4.16 Microstructure at 200x magnification in alloy G from thermal analysis samples obtained at a low cooling rate of 0.35 °C sec^{-1}. The black arrows point to the Zr-rich phases.

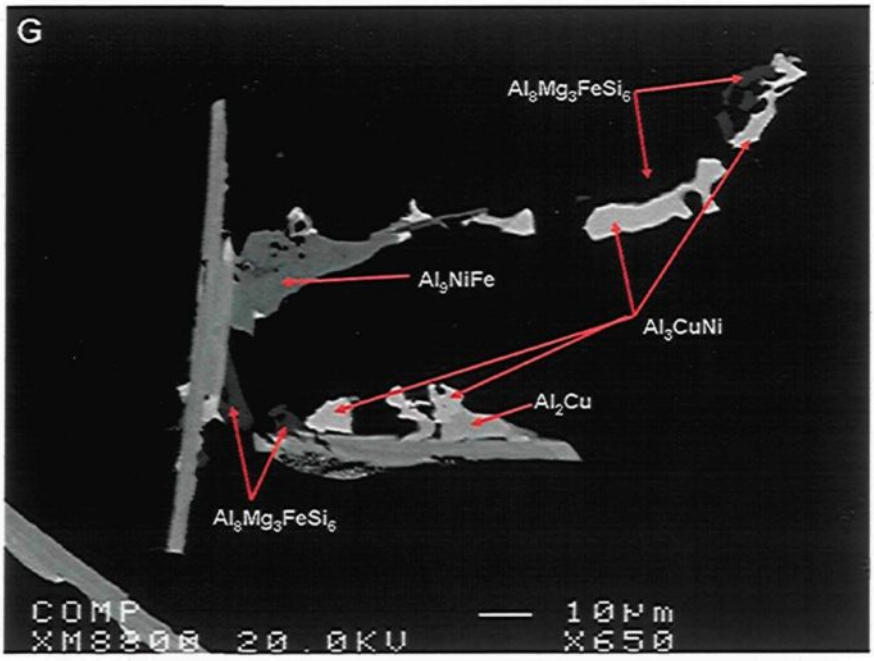

Figure 4.17 Backscattered image of alloy G from thermal analysis sample obtained at a low cooling rate of 0.35 °C sec^{-1}.

Table 4.9 WDS analysis of phases observed in Alloy G.

Alloy Code	Element	wt.%	At.%	Calculated formula	Shape and Color	Suggested Formula
G	Al	40.19	60.6	$Al_{3.5}Cu_{1.2}Ni$	Irregular form, white	Al_3CuNi
	Cu	32.9	21.06			
	Ni	25.46	17.64			
	Total	98.55	99.3			
	Al	65.67	80.1	$Al_{17}Ni_{2.8}Fe$	Irregular form dark grey,	$Al_9NiFe + Al_3Ni_2 + Al$
	Ni	23.08	13			
	Fe	8.1	4.5			
	Total	96.8	97.6			
	Al	44.3	60.7	$Al_{6.9}Si_{1.6}Ti_{1.9}Zr$	Needlelike, white	$(Al,Si)_3(Ti,Zr)$
	Si	10.35	13.68			
	Zr	21.5	8.75			
	Ti	21.23	16.45			
	Total	97.4	99.6			

Figure 4.18 shows a high-magnification backscattered image of alloy E showing the morphology of the Al-Si-Zr-Ti phases which were revealed by this investigation. The corresponding EDX spectra, displayed in Figure 4.19, show that the strongest reflections are those of Al and Si; depending on the phase in question, and as seen from the WDS analysis of Table 4.7, the EDX spectrum of $(Al,Si)_2(Zr,Ti)$ which is a Si-rich phase has a stronger Si peak while that of $(Al,Si)_3(Zr,Ti)$ which is an Al-rich phase, shows a stronger Al peak.

The EDX spectra for the $(Al,Si)_2(Zr,Ti)$ and $(Al,Si)_3(Zr,Ti)$ phases in Figure 4.19, as well as the X-ray images in Figure 4.20, in which the different element concentrations may be seen, are all in keeping with the WDS analysis shown in Tables 4.7 to 4.9: each of the two phases differs in its silicon and aluminum content.

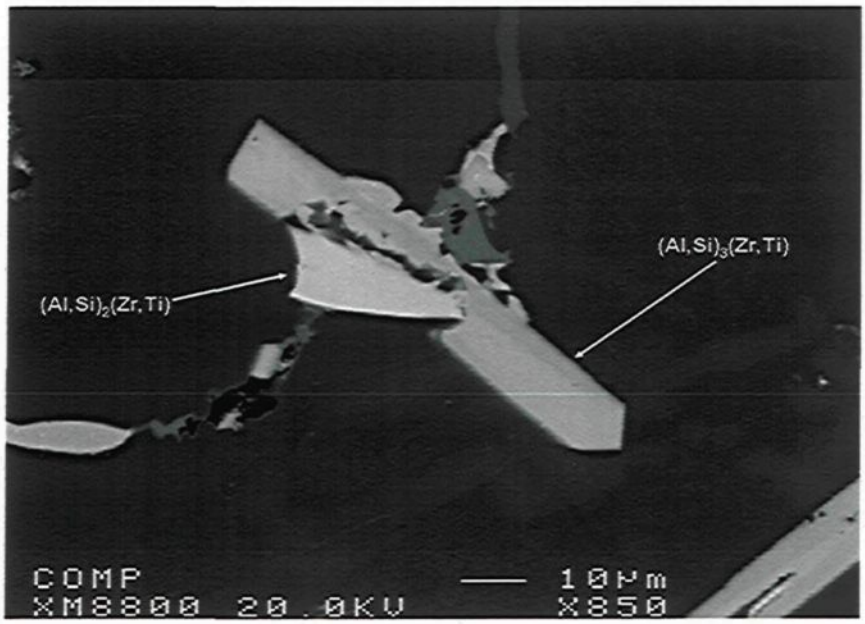

Figure 4.18 High-magnification backscattered image taken from alloy E showing the presence of both $(Al,Si)_2(Zr,Ti)$ and $(Al,Si)_3(Zr,Ti)$.

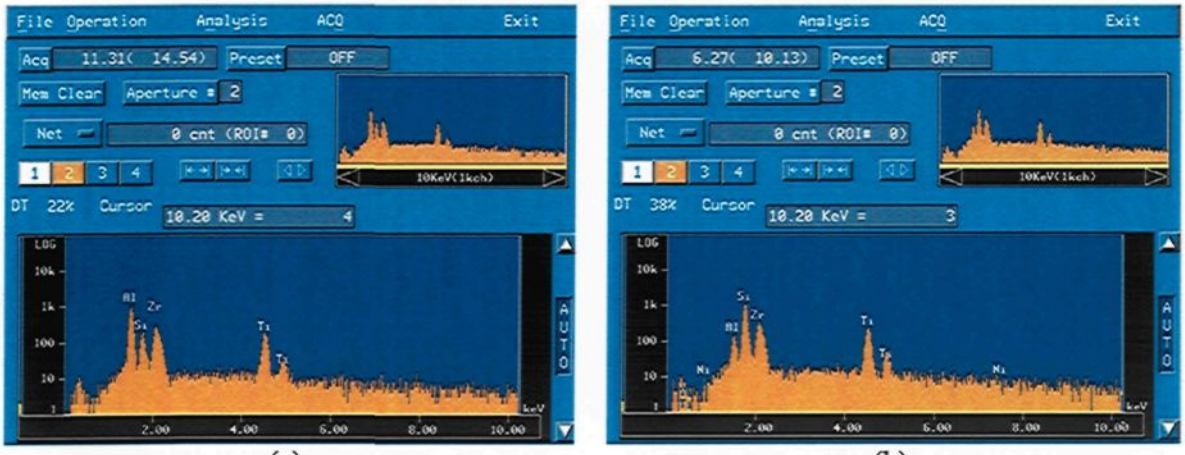

(a) (b)

Figure 4.19 (a) EDX spectrum for $(Al,Si)_2(Zr,Ti)$, and (b) EDX spectrum for $(Al,Si)_3(Zr,Ti)$ phases.

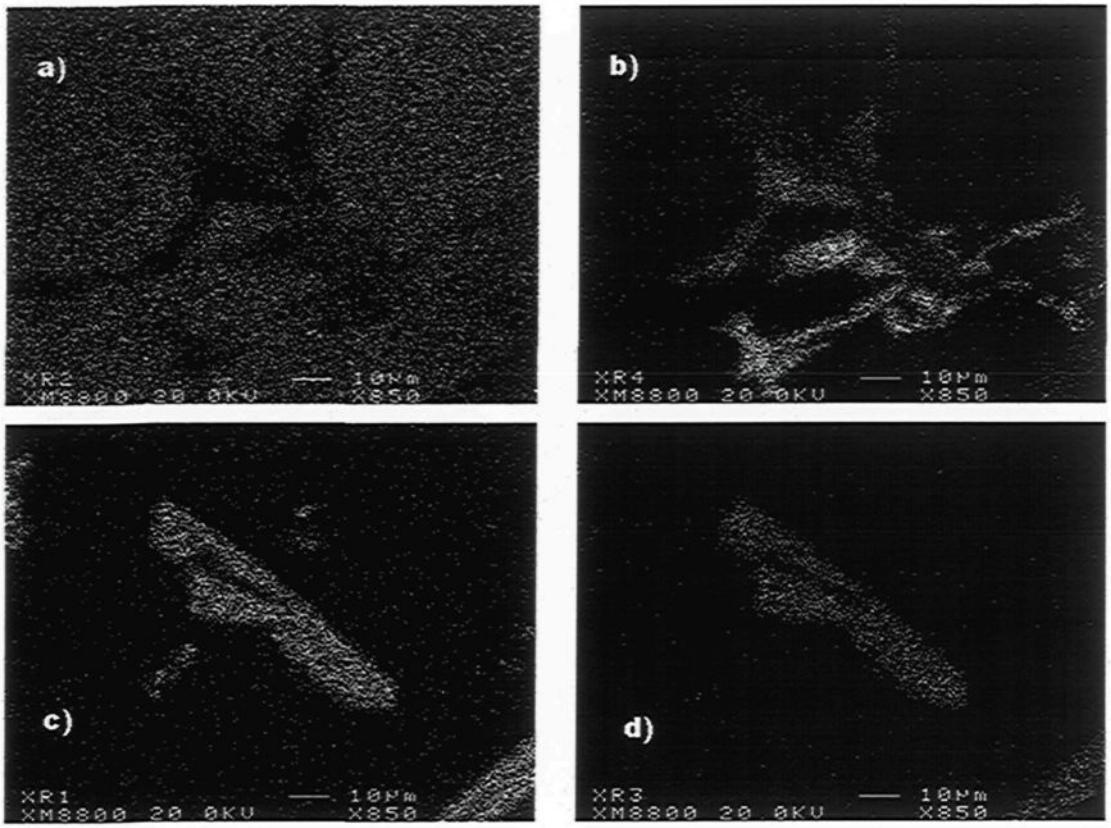

Figure 4.20 X-ray images of (a) Al, (b) Si, (c) Ti, and (d) Zr corresponding to the $(Al,Si)_3(Zr,Ti)$ and $(Al,Si)_2(Zr,Ti)$ phases observed in the backscattered image of alloy E shown in Figure 4.18.

For the purposes of further investigation, X-ray mapping of the $(Al,Si)_2(Zr,Ti)$ and $(Al,Si)_3(Zr,Ti)$ phases was carried out to determine the distribution of Al, Si, Ti, and Zr within these phases. The results are displayed in Figure 4.21. The maps correspond to the backscattered image shown at the top right hand side of the figure, in which the particles of these two phases may clearly be observed.

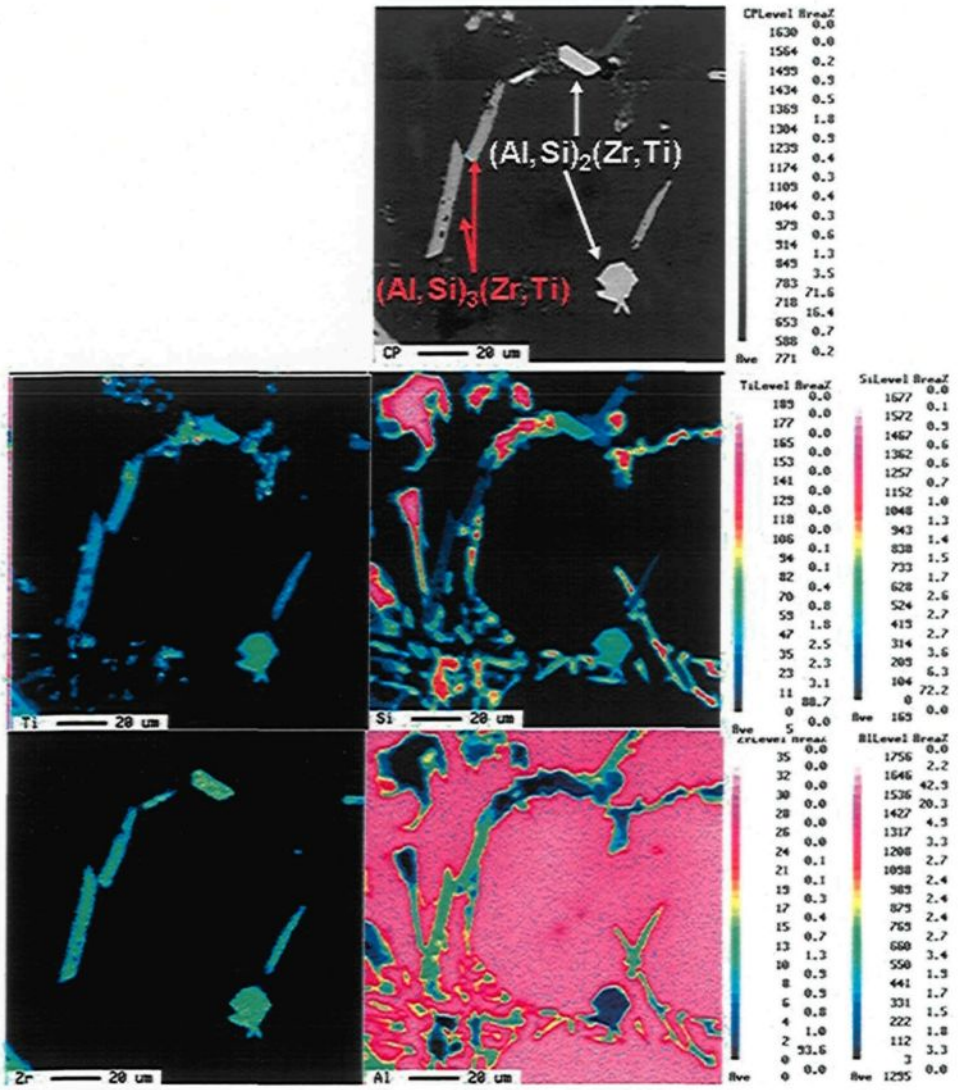

Figure 4.21 Backscattered image of alloy E (top right) showing the $(Al,Si)_2(Ti,Zr)$ and $(Al,Si)_3(Ti,Zr)$ phases and the corresponding X-ray images of Ti, Si, Zr, and Al.

In spite of the fact that the thermal analysis curves did not detect any Zr-rich phase reaction, the EPMA, WDS, and EDX results clearly indicate that while there is no reaction of Zr with nickel, copper, strontium, reacts with Ti, Si, and Al to form both the block-like $(Al,Si)_2(Ti,Zr)$ phase with a high silicon content, and the needle-like $(Al,Si)_3(Ti,Zr)$ phase with a high Al content.

4.4 Thermal Analysis for Detection of Zr-rich Phases

It is interesting to note that the Zr-rich phases present in the alloys containing Zr did not produce any characteristic thermal analysis peak related to the precipitation of these phases during the solidification of Alloys E, F, and G. In an attempt to investigate the reaction temperature of the Zr-rich phases observed in this work, it was necessary to consider modifying the thermal analysis experiments.

Figure 4.22 shows a diagram representing recalescence (ΔT) which is defined[119] as the heat generated during solidification relating to the nucleation and growth of a new phase.

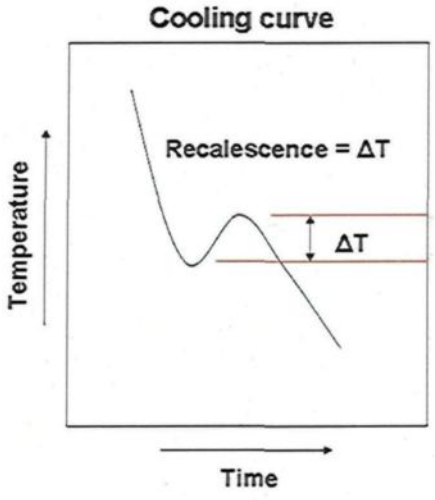

Figure 4.22 Diagram of a hypothetical cooling curve showing recalescence.

Without intending to make an in-depth approach to the mathematics of solidification, but rather to understand the constituent parts governing the solidification process itself, Equation 4.1 provides a basic mathematical formula[119] which introduces the principal parameters of recalescence.

$$\Delta T = [(\Delta hf/cp)(\delta fs/\delta t)] - [(q_e/cp)(A/V)] \qquad \textbf{Equation 4.1}$$

As will be observed from Equation 4.1, Δhf is the latent heat of fusion denoting a decrease in enthalpy due to the transformation from liquid to solid; cp is the specific heat per unit volume; q_e is the heat flux; A and V are area and volume, respectively, of the solidifying sample; and fs is the solid fraction. The first term on the right-hand side of Equation 4.1 takes into account the continuing evolution of the latent heat of fusion during solidification. The second term reflects principally the effects of casting geometry, area, and volume of the solidifying samples. Regarding this equation, recalescence will occur when the first term on the right-hand side of Equation 4.1 becomes greater than the second one.

As may be deduced from Equation 4.1, the heat extraction of the samples in thermal analysis plays an essential role in perceiving recalescence based on solidification data, in the eventuality that there is a high discrepancy between both terms of this equation; for example, if the second term is much higher than the first term, the perception of the recalescence may remain concealed, and as a result, the thermal analysis data will not reveal any noticeable reaction. Generally speaking, throughout the course of thermal analysis experiments at slow cooling rates, the heat loss from the surrounding environment exceeds the heat generated by nascent, or incipient, phase reactions to a great extent, specifically during the initial solidification period, making it impossible to detect their appearance on the cooling curve, *i.e.* to perceive the recalescence.[120] Therefore, by modifying the parameters involving Equation 4.1, it would be possible to perceive the recalescence, which should be present at temperatures higher than 650°C during thermal

analysis, located on the initial solidification curve, as the phase diagram predicts for the binary Al-Zr system.

Discerning the reactions involved in the solidification of alloys containing zirconium leads us to take two aspects into consideration: (a) reducing the number of reactions to simplify the analysis by using a binary Al-9 wt. pct Si alloy, coded J1, and (b) applying a higher cooling rate by reducing the volume of the sample in the thermal analysis.

The chemical composition of the alloys used for thermal analysis at higher cooling rates is provided in Table 4.10. As may be seen from this table, J2 was selected as a composition containing 0.4 wt% Zr in an attempt to differentiate between possible Zr-rich and Zr-Ti rich reactions. The materials used for the preparation of the binary alloy were 99.99% pure aluminum and 99.99% pure silicon.

The use of a higher cooling rate applied here is a consequence of reducing the volume of the samples from the thermal analysis experiments, with a view to pinpointing small reactions, or at least, those reactions which occur at the beginning of solidification. The cooling rate used in these thermal analysis experiments was $4°Cs^{-1}$. The cooling curves for Alloys J1 through J4 are shown in Figure 4.23. The first reaction observed in J2, J3, and J4 alloys is presented in every plot as an enlarged inset showing the value of the recalescence, ΔT, associated with this reaction in each case.

Table 4.10 Chemical composition of the alloys used for thermal analysis at $4°Cs^{-1}$

Identification	Composition (wt%)
J1	Al-9Si
J2	Al-9Si-0.4Zr
J3	Al-9Si-0.22Ti-0.2Zr
J4	Al-9Si-0.22Ti-0.4Zr

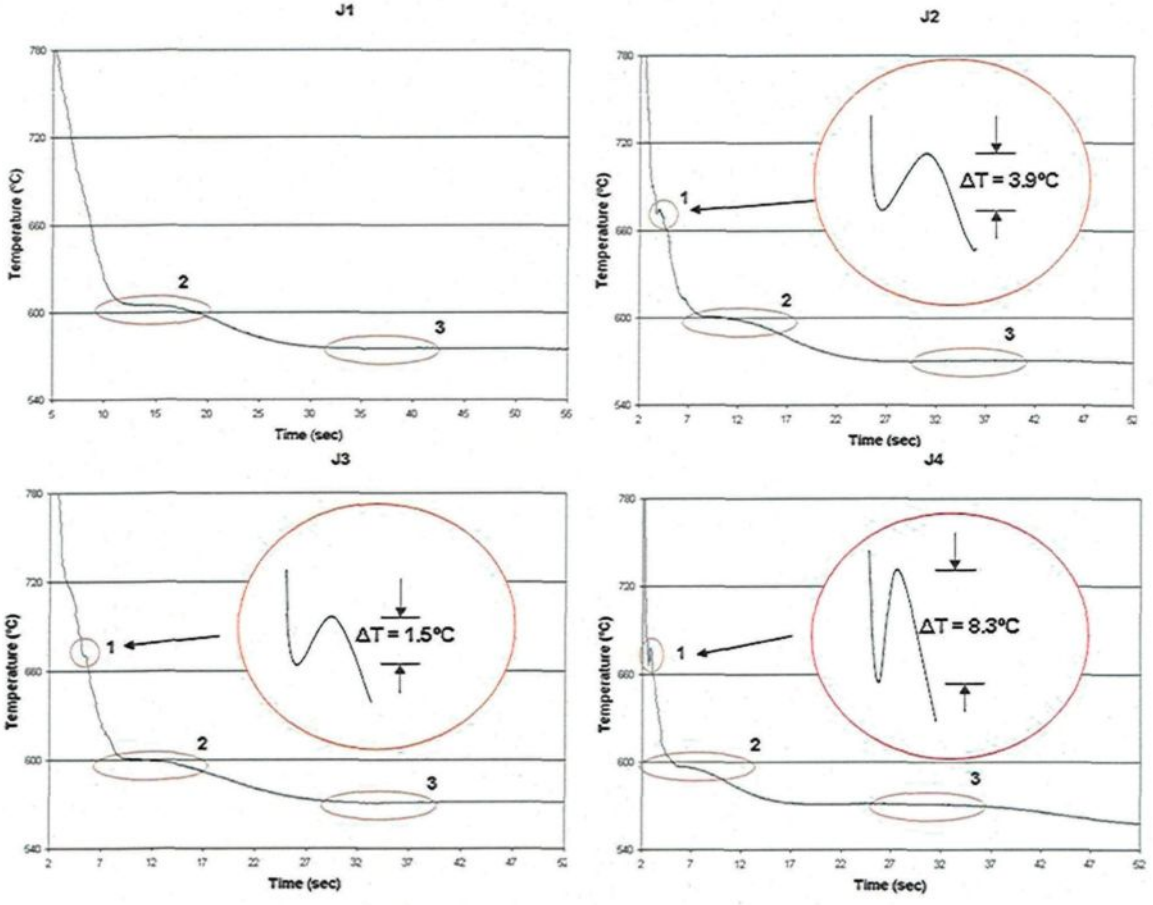

Figure 4.23 Thermal analysis plots of the experimental alloys J1 to J4 (at $4°Cs^{-1}$).

As may be seen from Figure 4.23 and Table 4.11, the first reaction is not present in alloy J1, which suggests that there must be a Zr-rich phase reaction which is present in J2, J3, and J4 alloys at temperatures of the order of 667° to 671°C. Recalescence is higher for the J4 alloy, a fact which may be associated particularly with the higher Zr and Ti content.

The principal problems arising from the use of higher cooling rates in thermal analysis are related to the impossibility of reaching thermal balance before the inception of solidification, which would imply that it is not feasible to carry out realistic calculations based on the cooling curve. Even if the first reaction seems clearly perceived, the absence of thermal balance leads to fluctuations in the cooling curve which in turn creates problems in the interpretation of these curves, thereby making it difficult to calculate the first derivative curves. As mentioned in studies carried out by Tamminen,[103] when the metal is poured into a cold crucible with a pre-mounted thermocouple, nucleation and some solidification will be likely to occur upon first contact with the crucible. If the superheat is high enough, however, some part of the solidified metal will remelt; on the other hand, some of these nuclei or phases might persist, implying that growth could continue out of these particles, which would make it difficult to discern which kind of nucleus or phase is related to the initial undercooling.

In spite of the complications related to the lack of heat balance, however, the first reaction in the cooling curves of J2, J3, and J4 alloys is well-defined, and the phases shown in Figures 4.24 and 4.25 look similar to those shown earlier for the Zr-Ti phases observed in the microstructures of the thermal analysis samples of alloys E, F and G obtained at low cooling rates.

According to Table 4.11, the grain size diminishes as the Zr-Ti content increases for alloys J1 to J4. These results suggest that there is no observable poisoning effect in the grain refining as a result of Zr-Ti interactions, even though it has been suggested that Zr-Ti

phases are discernible in the microstructures shown for alloys J2, J3, and J4 in Figures 4.25 through 4.28.

Table 4.11 Suggested precipitated phases for thermal analysis peaks observed during solidification of experimental alloys J1 to J4

Alloy Code	Grain Size (μm)	SDAS (μm)	Reaction #	Temperature (°C)	Phase Precipitated
J1	245	38	1	~	Not observed
			2	605	α- Aluminum dendritic network
			3	574	Eutectic Al-Si
J2	170	38	1	671	Suggested Zr-rich phase
			2	600	α- Aluminum dendritic network
			3	571	Eutectic Al-Si
J3	134	40	1	670	Suggested Zr-rich phase
			2	600	α- Aluminum dendritic network
			3	571	Eutectic Al-Si
J4	128	35	1	667	Suggested Zr-rich phase
			2	597	α- Aluminum dendritic network
			3	571	Eutectic Al-Si

The microstructures of alloys J1 to J4 in Figures 4.24 to 4.28 show that the principal phases, apart from the α-Al and the eutectic silicon phases, seem to be the Zr-rich phases; this is because the form of these phases may resemble the Zr-Ti-rich phases, which were observed in the E, F, and G alloys with regard to the thermal analysis experiments carried out at low cooling rates.

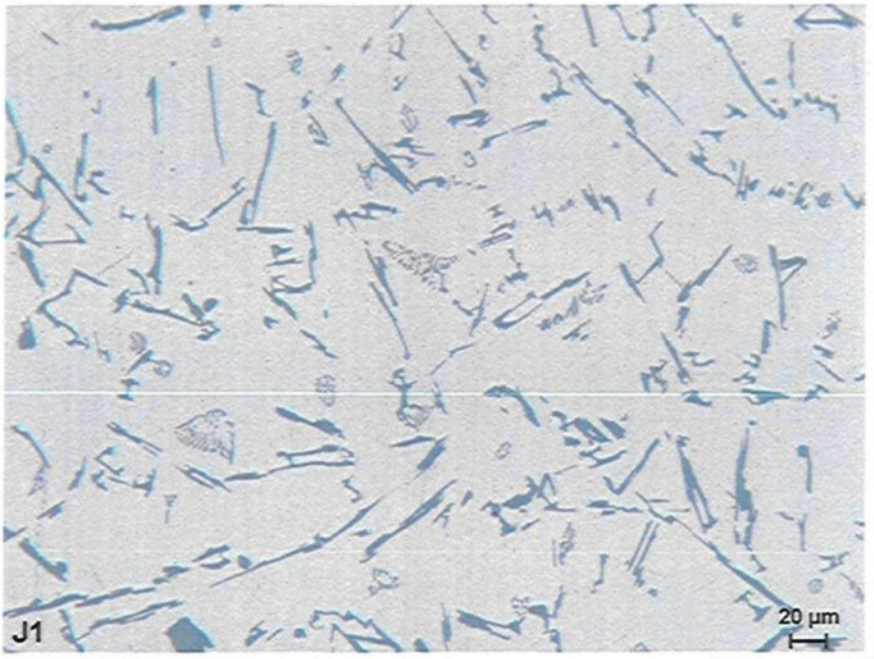

Figure 4.24 Optical micrograph of alloy **J1** taken at a magnification of 200x.

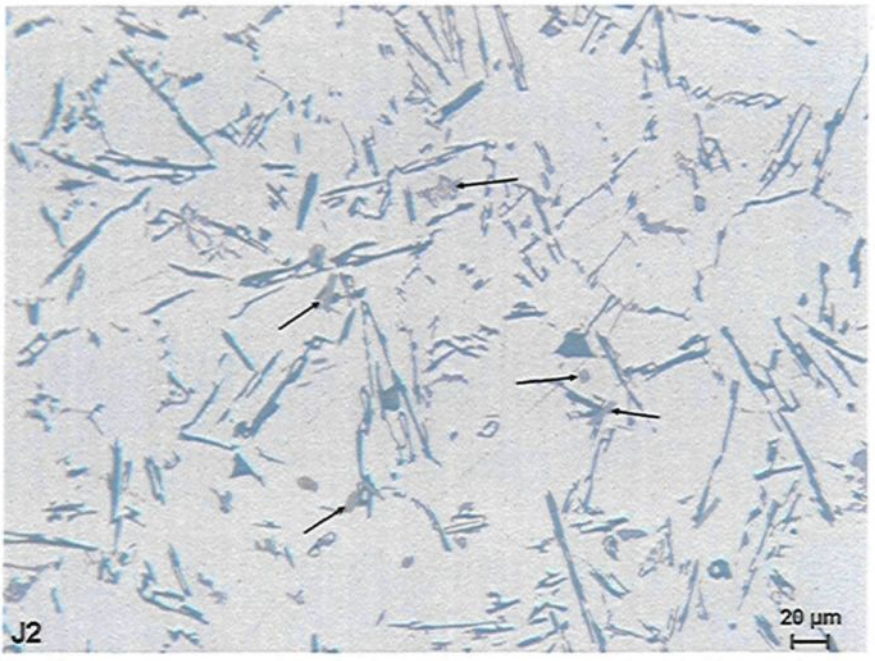

Figure 4.25 Optical micrograph of alloy J2, taken at a magnification of 200x. The black arrows point to Zr-rich phases.

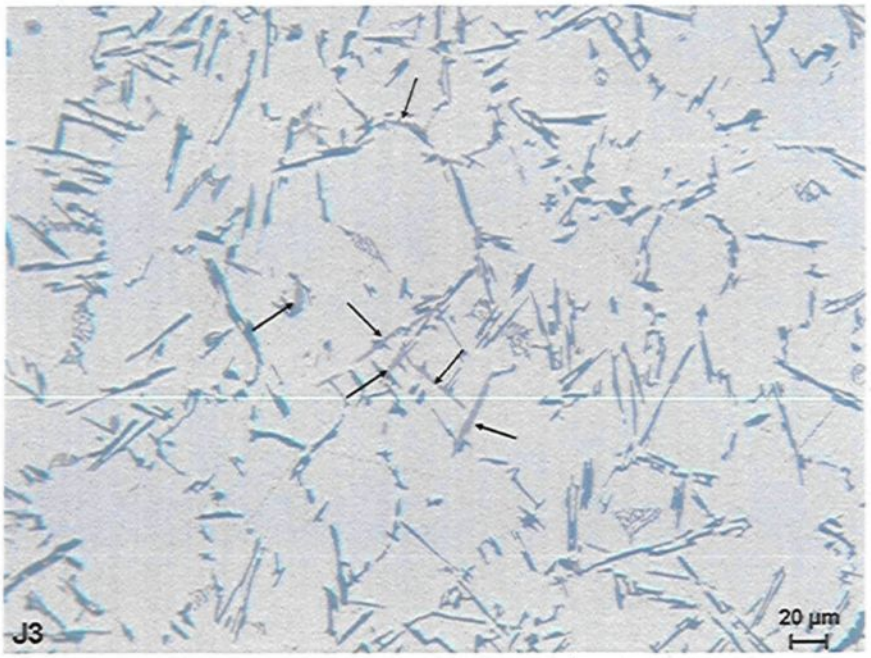

Figure 4.26 Optical micrograph of alloy **J3**, taken at a magnification of 200x. The black arrows point to Zr-rich phases.

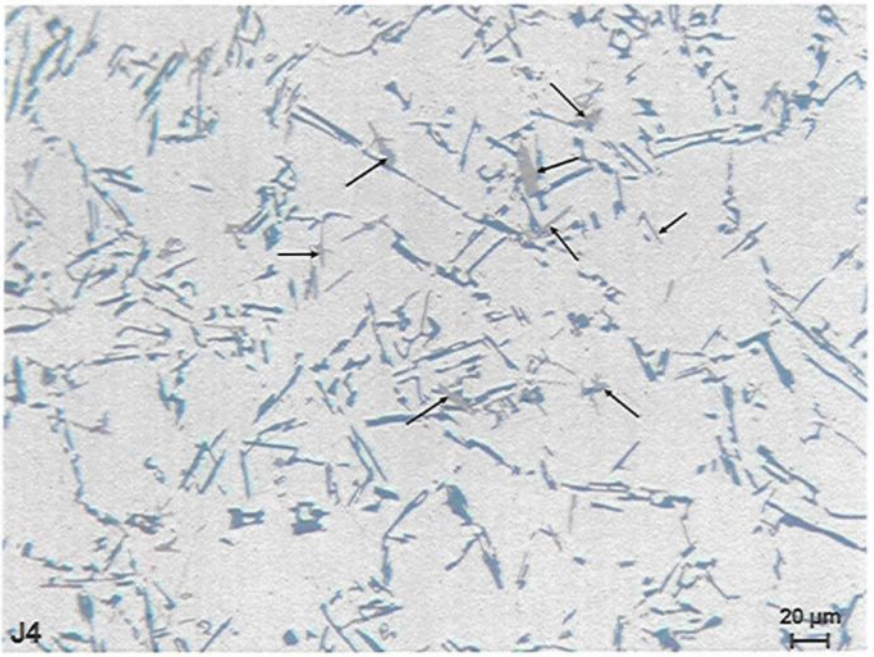

Figure 4.27 Optical micrograph of alloy J4, taken at a magnification of 200x. The black arrows point to Zr-rich phases.

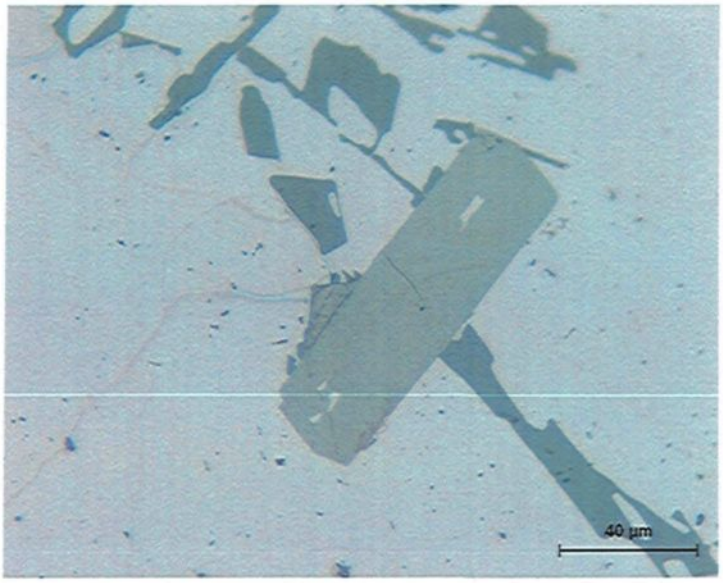

Figure 4.28 Optical micrograph of **J4** alloy taken at a magnification of 500x, showing the presence of a Zr-Ti phase particle (thick, light grey particle).

The WDS analyses shown in Tables 4.12 through 4.14 present the average chemical composition of the Zr-rich particles analyzed from alloy samples J2, J3, and J4.

Table 4.12 WDS Analysis of the Phases Observed in Alloy J2

Alloy Code	Element	wt.%	At.%	Calculated Formula	Shape and Color	Suggested Formula
J2	Al	38.7	61.9	$Al_{4.5}SiZr_{1.7}$	Blocklike, white	$(Al,Si)_3Zr$
	Si	9.01	13.9			
	Zr	49.7	23.6			
	Total	98.1	99.5			

The atomic composition of the Zr-rich particles shown in Table 4.12 is similar to that of the Zr-rich phases discussed in the work of Sato;[121] on the basis of this work, an aluminum alloy was used to analyze formed precipitates having a different chemical composition ranging from 0.34 to 0.64 wt% Zr, 0.0 to 0.28 wt% Ti, and 0.01 to 0.56 wt%

Si, with the rest balancing out the aluminum. It was found that additions of Si to Al-Zr alloys would subsequently suppress the discontinuous precipitation of Al_3Zr particles.[122-124]

Silicon as well as titanium would enhance the continuous precipitation of spherical particles with crystal $L1_2$-type structures, namely, $(Al,Si)_3Zr$ and $(Al,Si)_3(Zr,Ti)$. The enhanced precipitation of the Al-Zr-Ti-Si particles which accompanies the addition of silicon or titanium may be a result of these elements affecting either the interfacial energy, or the misfit strain energy of the nucleation process, or the interaction with vacancies to form heterogeneous nucleation sites. The strong binding energy between Si and vacancies in aluminum could explain the fact that quenched-in excess vacancies and Si or Ti atoms are able to form clusters which act as nucleation sites for the Al-Si-Zr-Ti phases. [121] Simultaneous additions of silicon and titanium would tend to enhance the formation of the $(Al,Si)_3Zr$ and $(Al,Si)_3(Ti,Zr)$; these phases are reported by Sato[121] as metastable phases with a DO_{22}-type crystal structure.

Table 4.13 WDS Analysis of the Phases Observed in Alloy J3

Alloy Code	Element	wt.%	At.%	Calculated Formula	Shape and Color	Suggested Formula
J3	Al	43.46	62.6	$Al_{6.3}Si_{4.7}TiZr_{1.4}$	Needlelike, white	$(Al,Si)_3(Ti,Zr)$
	Si	9.61	13.3			
	Zr	33.04	14.1			
	Ti	12.14	9.9			
	Total	98.3	99.8			

Expressly regarding the atomic composition of the $(Al,Si)_3(Ti,Zr)$ phases, it would be possible to infer that this was the phase reported on by Sato;[121] it is important to notice that, in the present work, the silicon content is much higher than it is in the work of Sato[121]

and could thus change not only the form of the particulates but also their crystal structure, even if the atomic composition seems similar with regard to the particles found in both research projects. Unlike the $(Al,Si)_3(Ti,Zr)$ phases which were reported on in Sato's work, the $(Al,Si)_2(Ti,Zr)$ phases, at least with regard to their atomic composition, appear to constitute an unknown phase, taking into consideration the fact that a most recently updated bibliography was consulted for the present work.

Table 4.14 WDS Analysis of the Phases Observed in Alloy J4

Alloy Code	Element	wt.%	At.%	Calculated Formula	Shape and Color	Suggested Formula
J4	Al	5.53	9.32	$Al_{1.1}Si_{7.0}TiZr_{2.9}$	Blocklike, white	$(Al,Si)_2(Ti,Zr)$
	Si	35.67	58.1			
	Zr	48.37	24.3			
	Ti	8.66	8.29			
	Total	98.27	99.9			
	Al	40.8	61.7	$Al_{9.4}Si_{2.1}TiZr_{2.7}$	Needlelike, white	$(Al,Si)_3(Ti,Zr)$
	Si	9.6	13.9			
	Zr	39.8	17.8			
	Ti	7.7	6.6			
	Total	97.9	99.9			

To summarize the Zr-rich phases observed from the thermal analysis results, using high and low cooling rates, alloys with 0.4 wt pct Zr show the $(Al,Si)_2(Zr,Ti)$, $(Al,Si)_3(Zr,Ti)$ and $(Al,Si)_3Zr$ phases. In alloys containing 0.2 wt. pct Zr, only the $(Al,Si)_3(Zr,Ti)$ phase is observed.

As may be seen from Tables 4.12 through 4.15, the unknown $(Al,Si)_2(Zr,Ti)$ high-silicon phase, characterized as a blocklike white phase, was not discernible in the microstructures of alloys containing 0.2 wt. pct Zr. According to the Al-Zr binary

equilibrium phase diagram shown in Figure 4.29, there exists a peritectic reaction at 660.8°C which should be related to the reaction observed in the thermal analysis at high cooling rates. This peritectic reaction is represented by:

$$L + Al_3Zr \rightarrow Al + Al_3Zr$$

Since the Al_3Zr precipitate must be present before the peritectic reaction, the formation of the Al_3Zr from liquid is called a pro-peritectic reaction.[124] In accordance with the Zr concentration used for this work, 0.2 wt pct and 0.4 wt pct, for alloys G and E-F, respectively, as shown in Figure 4.29, the *liquidus* temperature should be 718°C and 780°C, respectively. During the preparation of the casting, the melt was maintained at 780°C, which should be indicative of the fact that most of the Zr was dissolved in the melt.

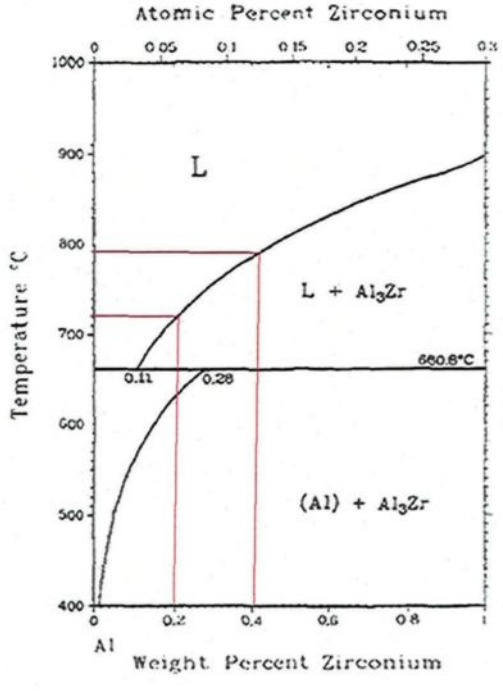

Figure 4.29 Equilibrium Al-rich, Al-Zr binary phase diagram[125] showing the percentages of Zr used for this work.

Taking into consideration the thermodynamic diagram shown in Figure 4.29, the pro-peritectic reaction from the liquid should appear[125] at *liquidus* temperatures indicating the formation of the Al_3Zr phase, sometimes called the β phase.[126, 127] For any peritectic reaction,[83] the amount of the pro-peritectic precipitated in the alloy decreases with increasing solidification rate and/or decreasing solute content; for sufficient rapid cooling, it is possible for the formation of the pro-peritectic Al_3Zr phase to be suppressed completely, resulting in the solidification of the peritectic α-Al phase directly from the liquid.

The only reactions which seem to be clearly perceived are located above the peritectic arrest at 660.6°C. By means of these reactions, the solidification of the α-aluminum phase in the alloys J2, J3 and J4 would be initiated. The equilibrium diagram, however, should be used with discretion for the analysis of solidification in this project, as was done for the work carried out by Sato,[121] because of the fact that the chemical composition diverges widely with respect to the binary alloy, specifically regarding the silicon content, which would better represent the solidification behavior expected of the equilibrium Al-Zr diagram, shown in Figure 4.29.

A relationship between grain size and the recalescence in some Al-Si-Cu-Mg systems has been observed, as shown in Figure 4.30 where recalescence values display an increase as the grain size increases.[128, 129]

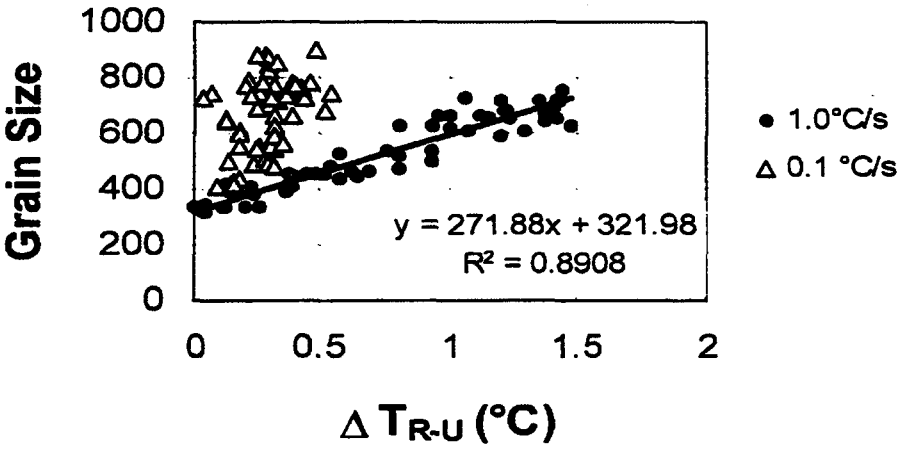

Figure 4.30 Grain size plotted against recalescence, (ΔT_{R-U}), for a 356 alloy solidified at two cooling rates.[128]

In the thermal analysis results for this research, the recalescence values increased as the Zr-Ti content was increased, resulting in a decrease in the grain size. This observation is contrary to the expected results which are based on the decrease in grain size as recalescence diminishes. Such non-congruous results open up the possibility that the reactions observed between 667°C and 671°C, which are located above the peritectic arrest of 660°C, were not in fact derived from the nucleation of the α-Al phase, but rather occurred as a result of pro-peritectic reactions. In this context, the conclusion may be drawn that the $(Al,Si)_3(Zr,Ti)$ phases observed in the alloys E, F, G, J3, and J4, as well as the $(Al,Si)_3Zr$ phases observed in the J2 alloy, are pro-peritectic phases.

Also, taking into consideration that the $(Al,Si)_2(Zr,Ti)$ phase appears only in the hyper-peritectic alloys containing 0.4 wt. pct Zr, and where the temperature of the liquid metal should be at least 780°C so as to dissolve the Al_3Zr phase completely, it is possible that the $(Al,Si)_2(Zr,Ti)$ phase is part of a non-dissolved Al_3Zr phase, which derives originally from the Al-Zr master alloy and which had been added during the prior casting

procedures. On the other hand, it should be noted that the hypo-peritectic alloys, namely G and J2, containing 0.2 wt. pct Zr, and registering a *liquidus* temperature of 720°C, did not show any trace of the $(Al,Si)_2(Zr,Ti)$ phase in their microstructure, even from the thermal analysis experiments carried out at low cooling rates.

CHAPTER 5

AMBIENT AND HIGH TEMPERATURE TENSILE PROPERTIES

CHAPTER 5

AMBIENT AND HIGH TEMPERATURE TENSILE PROPERTIES

5.1 Introduction

This chapter will document and analyze the tensile test results for the alloys studied in this work together with their microstructures. Major microstructural features such as SDAS, porosity, modification level, grain size, volume fraction of intermetallic phases, and silicon-particle characteristics were all analyzed in order to acquire an understanding of the relationship between the microstructure and the mechanical properties of the alloys studied.

The thermal analysis experiments described in Chapter 4 provided evidence of the solidification sequence in which phases appeared during solidification at low cooling rates. Since the cooling rate for the tensile test samples is higher than it is for that obtained with the thermal analysis experiments, certain differences between the precipitated phases may be possible since the precipitation kinetics would be different in the two cases. The thermal analysis results are, however, of primary importance in this chapter because they are used as a reference for identifying the phases appearing in the microstructure of the tensile test samples.

The analysis and discussion of tensile test results will be carried out with the emphasis placed on fulfilling the two major aims of this research work: firstly, to acquire detailed information regarding the mechanical limits of alloy 354 after it has been submitted to extreme aging treatments, and secondly, to obtain an understanding of the effects of the addition of nickel and/or zirconium, Al_2O_3, and SiC, on alloy 354, namely, the base alloy A, with respect to the mechanical properties and the aging treatments applied.

Quality index charts will be used with the purpose of setting the limits of the tensile properties, as well as to compare the mechanical behavior of the alloys studied, to delineate the effects of the additions with respect to the aging treatments applied.

The tensile test data are provided in the form of tables and graphs in the sections that follow. For the sake of simplicity, only selected data have been highlighted in this chapter; results from Quality index charts are provided in the appendix at the end of the thesis.

5.2 Microstructure of Tensile Test Samples

5.2.1 Difference between Thermal Analysis and Tensile Test Samples

The major difference between the thermal analysis samples analyzed in Chapter 4 and the tensile test samples is related to the cooling rate prevalent during the casting procedure of such samples. Figure 5.1 shows the grain size and secondary dendrite arm spacing (SDAS) values for both thermal analysis and tensile test samples for alloy A.

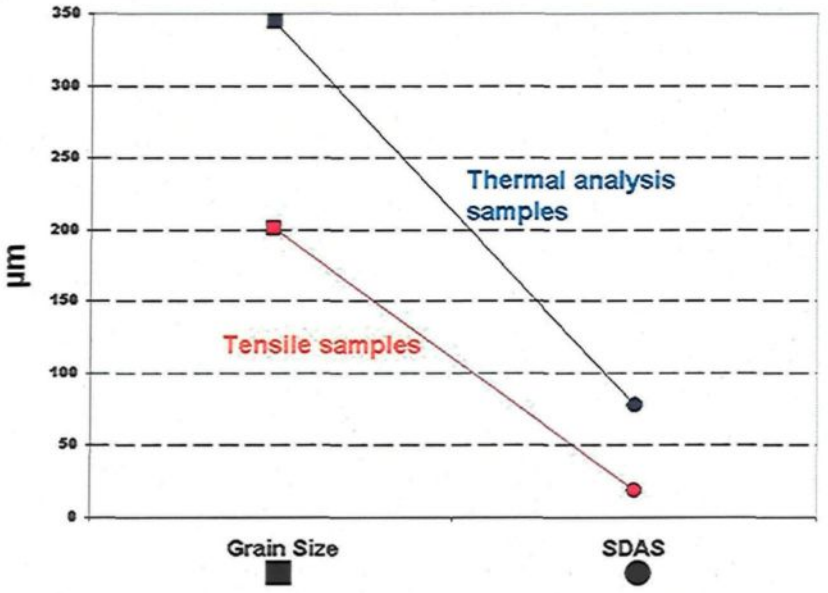

Figure 5.1 Difference between the thermal analysis and tensile test samples for Grain Size and Secondary Dendrite Arm Spacing (SDAS).

As was mentioned in the previous chapter, the solidification rate for the tensile test samples is higher than it is for the thermal analysis samples, while quantitative measurement of the microstructures revealed that the samples exhibit secondary dendrite arm spacings (SDAS) of 19 and 78 microns, respectively. A finer structure resulting from a higher cooling rate will produce a smaller SDAS value and *vice versa*. The higher solidification rate effect will be observed in the improved modification and more refined phases and grain structures than those appearing in the thermal analysis samples.[130-133]

5.2.2 Alloy A

Figure 5.2 shows the microstructure illustrating the grain size for alloy A having an approximate value of about 200 µm. A complete modification of the silicon particles in the microstructure of alloy A in the as-cast condition may be observed in Figure 5.3. As may

be observed in Figures 5.3 and 5.4 for alloy A, solution heat treatment has the effect of changing the morphology of the silicon particles from faceted to globular; together with this change, which occurs as a consequence of solution heat treatment, there may also be observed a reduction in the number of silicon particles and a reduction in the density of the silicon phase from 14 to 10% as a result of the diffusion of silicon into the aluminum matrix.

Figure 5.2 Macrograph showing grain size in an as-cast tensile test sample of alloy A.

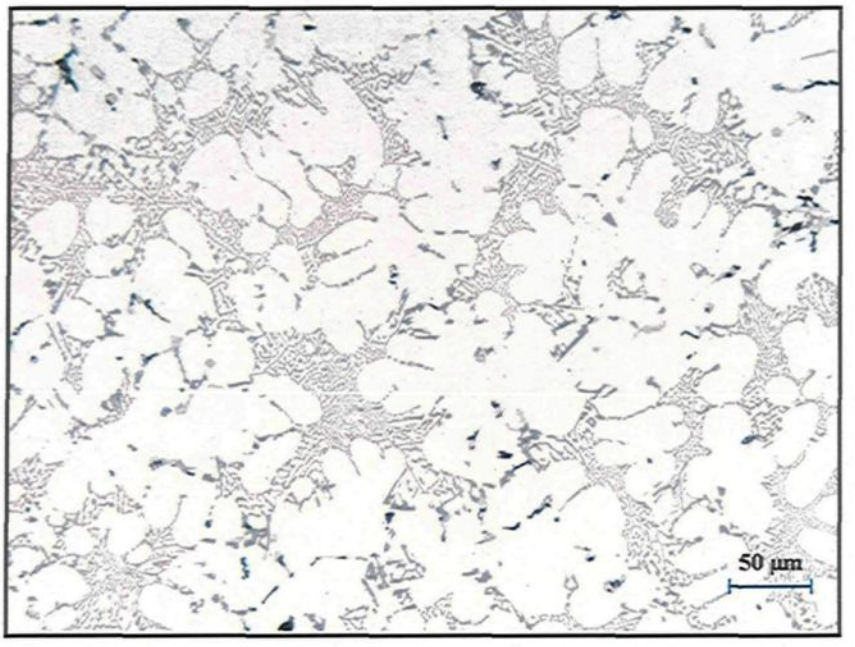

Figure 5.3 Micrograph of a tensile test specimen of alloy A showing the microstructure in the as-cast condition.

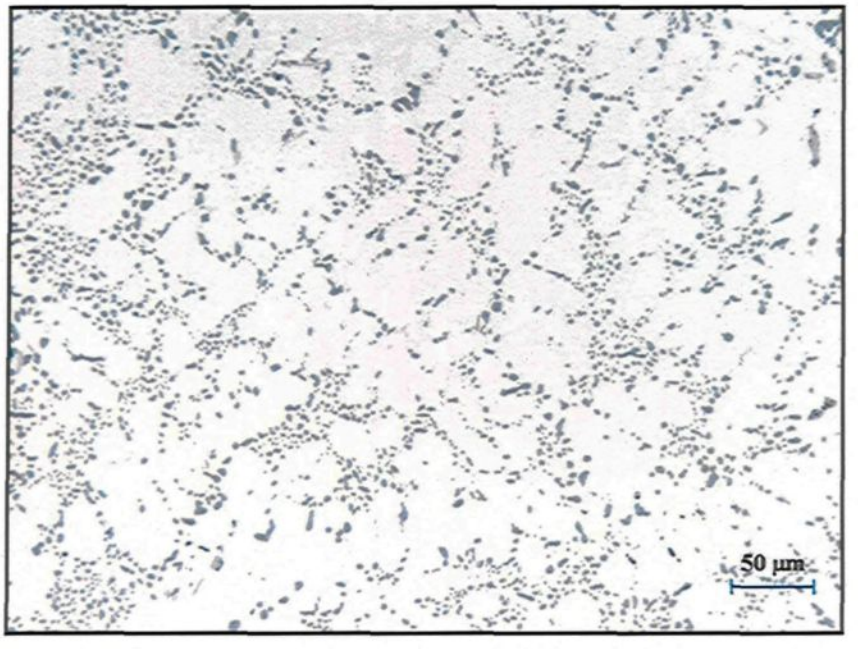

Figure 5.4 Micrograph of a tensile test specimen of alloy A showing the microstructure after solution heat treatment.

Eutectic silicon is the discontinuous eutectic phase in Al-Si alloys. The common feature of eutectic alloys is that there exists a degree of solubility of the discontinuous phase in the matrix at a certain temperature below the eutectic point. The solubility of practical Al-Si alloys, however, is not constant because eutectic silicon has a different surface curvature and is an imperfect crystal having a different lattice deformation energy which affects solubility. In general, the energy state, *i.e.* the surface curvature and the lattice deformation energy of the discontinuous eutectic phase, is inhomogeneous. Figure 5.5 shows a model of the granulation of unmodified eutectic Si illustrating three major stages during heat treatment: (a) the mass transport of solute which occurs from areas of intensified high energy state to areas of low energy state; (b) a discontinuous phase fragmentation, and lastly, (c) spheroidization when the inhomogeneity of energy conditions is sufficiently high.

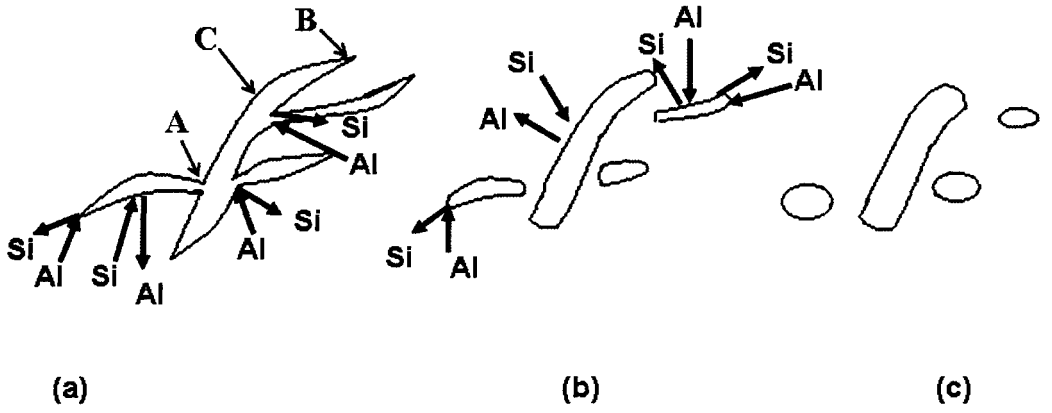

Figure 5.5 Model of granulation of unmodified eutectic Si during heat treatment. [134] (a) Transport of Si with the cooperation of Al starts; (b) transport continues after fragmentation; (c) eutectic Si becomes spheroidized.

Based on this model of the granulation of silicon particles, the solubility of silicon particles is different from point to point depending on the surface morphology of such

particles, for example, the surface curvature or lattice deformation energy of eutectic silicon is greater at the roots of branches (A), and at the tips (B), than on the flat faces (C), as can be observed in Figure 5.5. The solubility of silicon in the matrix at locations A and B is thus larger than it is at location C. During heat treatment, the silicon atoms in the matrix at locations A and B diffuse to location C, resulting in the dissolution of eutectic silicon at A and B, and the precipitation of silicon on the eutectic silicon at C. This transport of silicon ultimately causes the fragmentation and spheroidization of eutectic silicon.

5.2.3 Microstructural Features of Tensile Test Samples.

Tables 5.1 and 5.2 show the values of such microstructural features as secondary dendrite arm spacing (SDAS), porosity, modification level, and grain size for both the as cast (AC) and solution heat-treated (SHT) conditions for the seven alloys used in this work. It was observed that silicon particle characterization, SDAS, and the modification level did not show any significant difference among the alloys studied.

Figure 5.6 shows macrographs of the grain size in the tensile test samples in the as-cast condition for alloys B through G. As may be observed in both Figure 5.6 and Table 5.1, while alloys A, B, and C have approximately the same grain size, alloys containing additions of zirconium, namely, alloys E, F, and G, display a sharp decrease in grain size.

Table 5.1 SDAS, Porosity %, Grain Size, Level of Modification, and Volume Fraction of Intermetallics for Alloys A through G

Alloy Code Condition	SDAS (μm)	Modification Level	Grain Size (μm)	Porosity (%)		Volume Fraction of Intermetallics (%) EPMA	
	Av	Av		Av	SD	Av	SD
A-AC	19.3	Modified	201	0.135	0.06	3.08	0.32
A-SHT	23.1	Modified	192	0.12	0.05	1.27	0.13
B-AC	18.6	Modified	198	0.21	0.12	2.95	0.33
B-SHT	18.2	Modified	212	0.18	0.13	1.78	0.16
C-AC	18.1	Modified	200	0.16	0.11	3.05	0.41
C-SHT	21.2	Modified	196	0.161	0.15	1.86	0.13
D-AC	18.2	Modified	186	0.121	0.07	4.22	0.35
D-SHT	18.6	Modified	184	0.122	0.06	2.76	0.47
E-AC	18.9	Modified	122	0.11	0.05	4.23	0.40
E-SHT	19.9	Modified	116	0.108	0.04	2.86	0.43
F-AC	19	Modified	94	0.11	0.05	5.02	0.43
F-SHT	21	Modified	96	0.111	0.06	3.74	0.31
G-AC	25.3	Modified	125	0.12	0.03	3.57	0.23
G-SHT	21.2	Modified	111	0.13	0.04	2.03	0.34

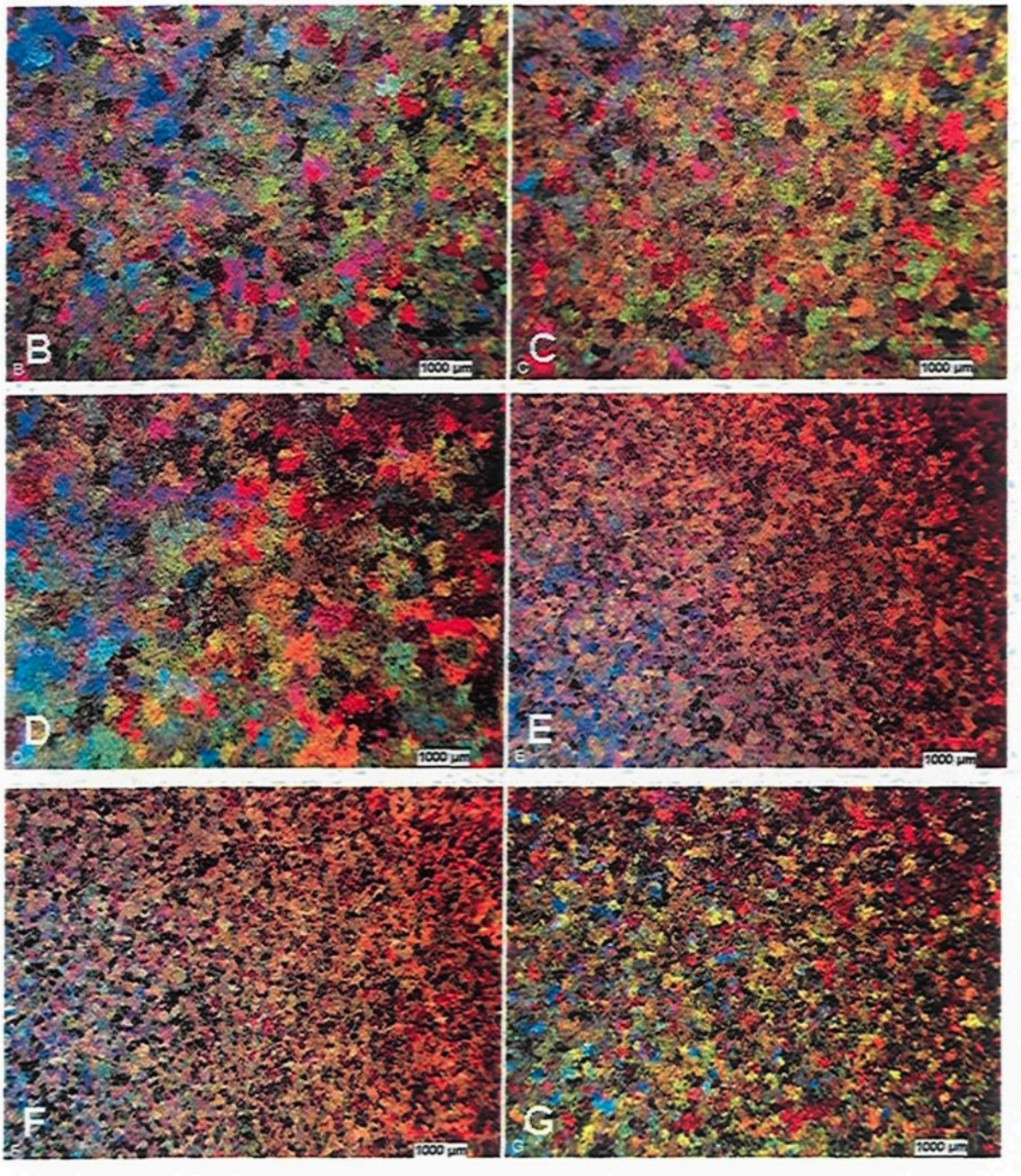

Figure 5.6 Grain size in Alloys A through G.

Table 5.2 Silicon Particle Characteristics for Alloys A through G.

Alloy Code Condition	Area (%)	Particle length (μm)		Roundness ratio (%)		Aspect ratio		Density (particles/mm^2)
	Av	Av	SD	Av	SD	Av	SD	
A-AC	14.58	3.522	3.94	0.4302	0.181	2.033	0.8609	39110
A-SHT	10.868	4.286	3.144	0.554	0.1547	1.641	0.5429	12080
B-AC	12.87	3.572	3.246	0.4075	0.1672	2.016	0.7466	31121
B-SHT	11.062	3.604	2.588	0.5592	0.1542	1.61	0.5162	11062
C-AC	15.078	3.453	3.365	0.407	0.1655	1.956	0.685	32143
C-SHT	11.296	3.4	2.293	0.5804	0.1535	1.618	0.523	16833
D-AC	13.908	4.288	4.6	0.4212	0.1698	1.97	0.747	22333
D-SHT	11.686	3.694	2.702	0.5546	0.1528	1.644	0.5114	17853
E-AC	13.71	3.525	3.618	0.4176	0.1718	2.053	0.822	31333
E-SHT	11.12	3.298	2.55	0.554	0.15	1.63	0.5078	21132
F-AC	15.405	2.858	3.208	0.4544	0.1722	1.913	0.67	46166
F-SHT	12.568	3.82	3.465	0.553	0.166	1.68	0.5798	17543
G-AC	13.618	6.278	6.728	0.361	0.1878	2.346	1.186	33480
G-SHT	12.618	5.96	5.01	0.4498	0.1773	2.171	1.113	14350

5.2.4 Micro-particulates Al_2O_3 and SiC in the microstructure of tensile test samples of alloys B and C

As may be observed from Table 5.1, porosity is greater in the alloys containing micro-particulates than it is in the other alloys. This observation may be ascribed to a procedure followed during casting, and which will be explained further on in the text. The characterization of the micro-particulates Al_2O_3 and SiC in alloys B and C is provided in Table 5.3. Also, as may be observed from the microstructures of alloys B and C shown in Figures 5.2 and 5.3, respectively, the micro-particulates have an irregular shape and, instead of the relatively high standard deviation shown in Table 5.3, they appear to be well

distributed in the matrix in both cases. The SDAS in the microstructure of alloys B and C is 25 μm, indicating a high cooling rate. Such high cooling rates (small SDASs) imply a better distribution of the micro-particulates, since during solidification micro-particulates are pushed into the interdendritic regions as shown in Figures 5.7 and 5.8; it will be important to note, however, that the use of micro-particulates in certain of the automotive applications involves a risk, since micro-particulates are capable of segregating and forming aggregates of particles which are liable to act as stress concentrators. Figure 5.9 shows a cumulus zone of micro-particulates which interferes with solidification feeding and, as a consequence, creates the potential for porosity to increase.

Table 5.3 Characterization of Micro-Oxides in Tensile Test Samples

Alloy	Type of μ-particulate	Area (%)		Size (μm)		Aspect ratio		Density (particles/mm^2)	
		Av.	SD	Av.	SD	Av.	SD	Av.	SD
B	Al_2O_3	0.65	0.448	23.2	15.3	2.01	0.95	46.5	26.5
C	SiC	0.59	0.478	13.6	5.8	1.55	0.53	74.3	36.4

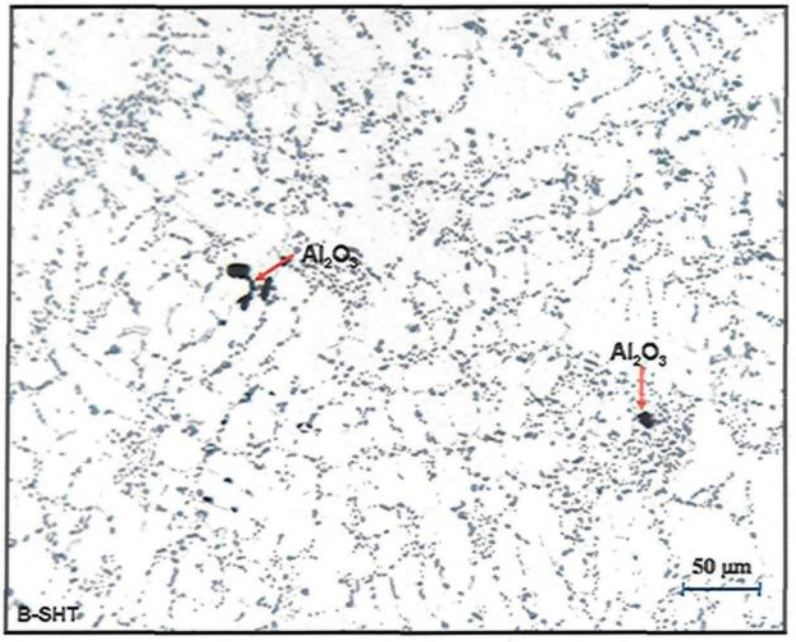

Figure 5.7 Microstructure of alloy B at 100x magnification showing the distribution of Al_2O_3 in the matrix.

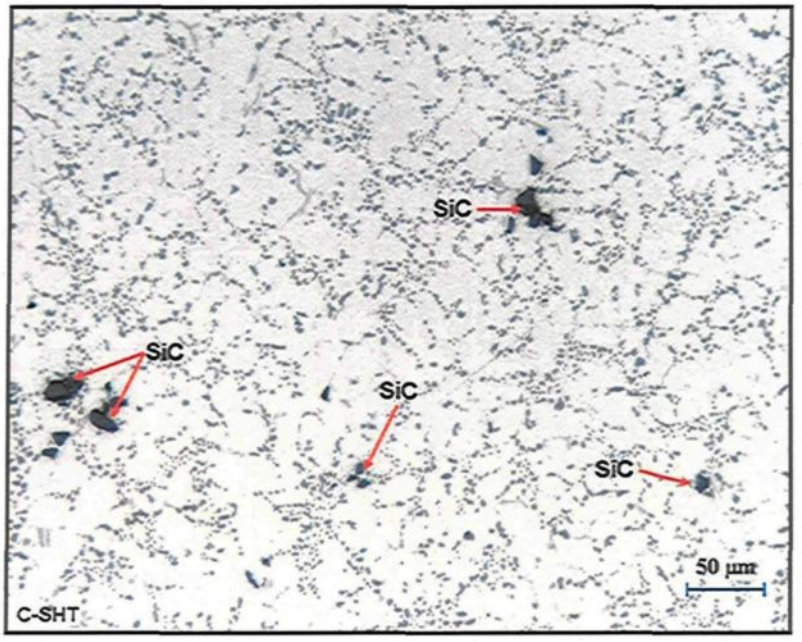

Figure 5.8 Microstructure of alloy C at 100x magnification showing the distribution of SiC in the matrix.

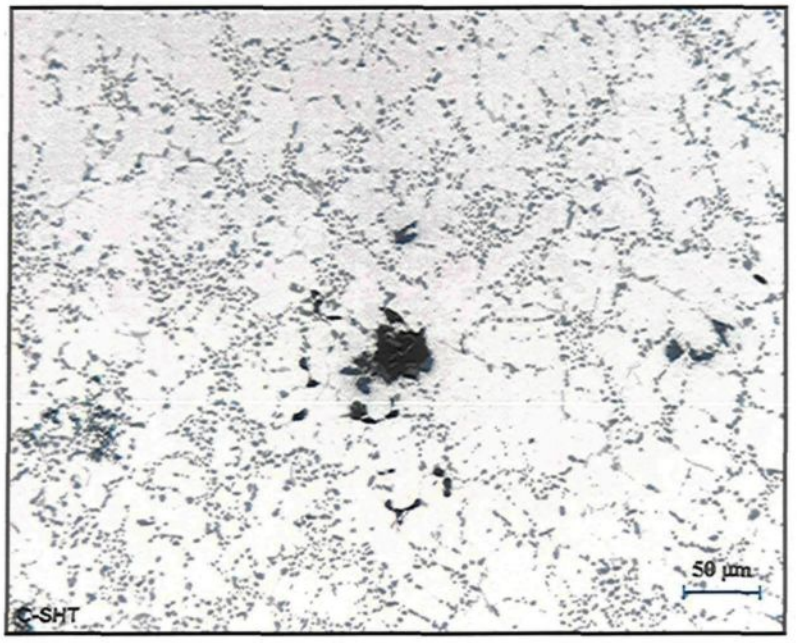

Figure 5.9 Microstructure of alloy B at 100x magnification showing an aggregate of Al_2O_3 particles in the matrix.

5.2.5 Alloy D

A number of particular phases such as Al_3CuNi and Al_9NiFe observed in the microstructure of tensile test specimens of alloy D is shown in Figure 5.10. These particles were identified using an electron microprobe analyzer and employing wavelength dispersive spectroscopic (WDS) analysis.

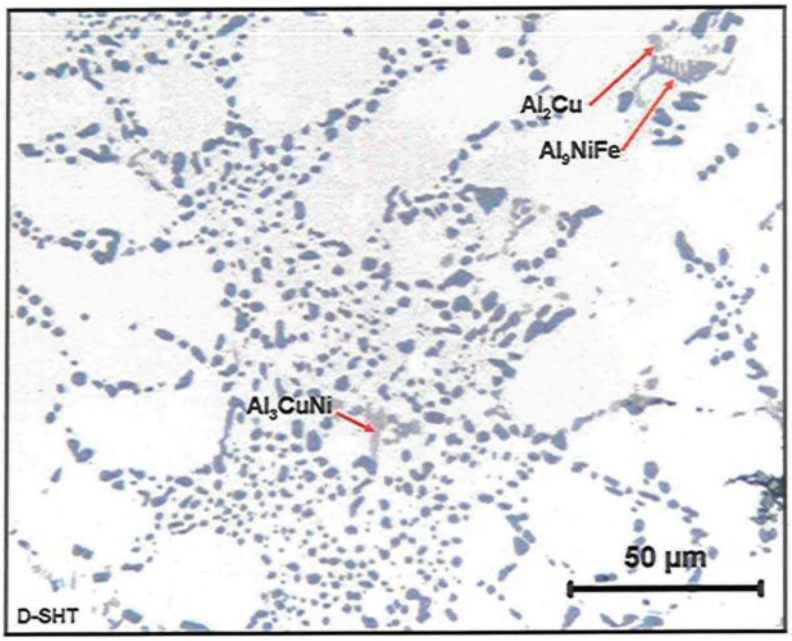

Figure 5.10 Microstructure of alloy D (500x).

5.2.6 Alloys with Zr (Alloys E, F, and G)

Figures 5.11 through 5.16 show the $(Al,Si)_3(Zr,Ti)$ phase present in the microstructures of alloys containing Zr which is a needle-like Zr-rich phase, already identified previously in the chapter on thermal analysis experiments. It is important to mention that the blocklike form $(Al,Si)_2(Zr,Ti)$ was not observed in the microstructure of the tensile samples. In Figure 5.12, it will be observed that the Zr-rich particles display different sizes and that a number of these particles seem to be segregated. These

observations, with regard to the size and segregation of the abovementioned particles present in the microstructures of tensile samples, may be understood from the fact that in the thermal analysis experiments at 4°C/sec, a presumably Zr-rich phase reaction was perceived at 660°C; since α-Al is known to start to solidify at approximately 605°C, the alloy is then completely liquid at 660°C, implying that the major nucleation and growth of the Zr-rich phases would occur between 660°C and 605°C thereby explaining the presence of the large Zr-rich particles observed in the microstructures. Once the Zr-rich particles were formed, therefore, some of these particles could sediment due to density differences between the Zr-rich particles and the remaining liquid alloy, before the start of solidification of the α-Al, which would explain the segregation of the Zr-rich phases observed in the microstructure of Figure 5.16. The major phases of the base alloy A, Al_2Cu, eutectic-Si, and α-Al were observed to adhere to the needle-like Zr-rich phases; this fact suggests that such phases could nucleate from the Zr-rich phases formed at the start of solidification.

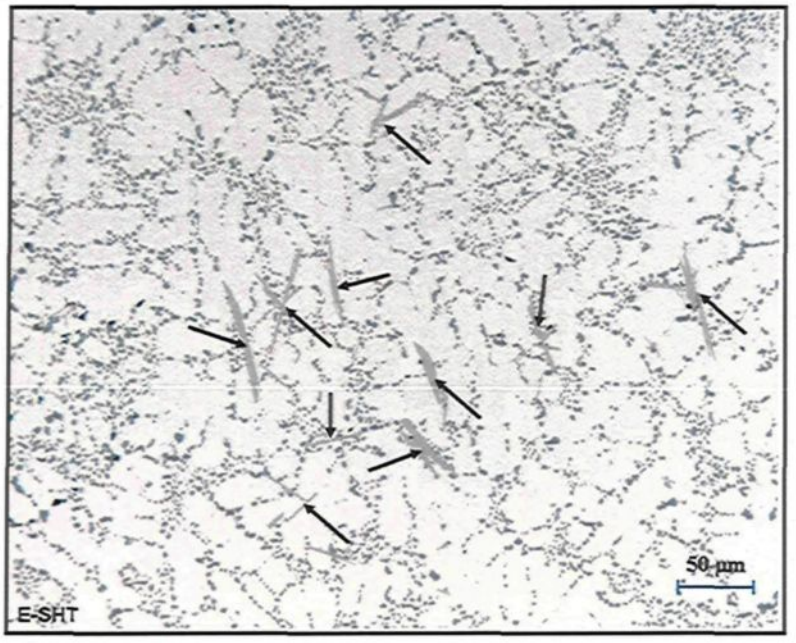

Figure 5.11 Microstructure of alloy E. The black arrows point to $(Al,Si)_3(Zr,Ti)$ phase particles (200x).

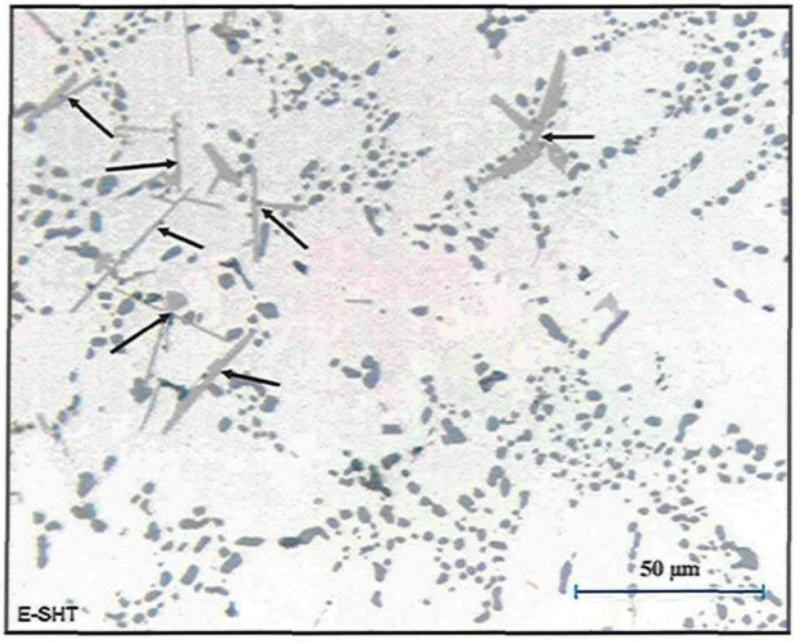

Figure 5.12 Microstructure of alloy E. The black arrows point to $(Al,Si)_3(Zr,Ti)$ phase particles (500x).

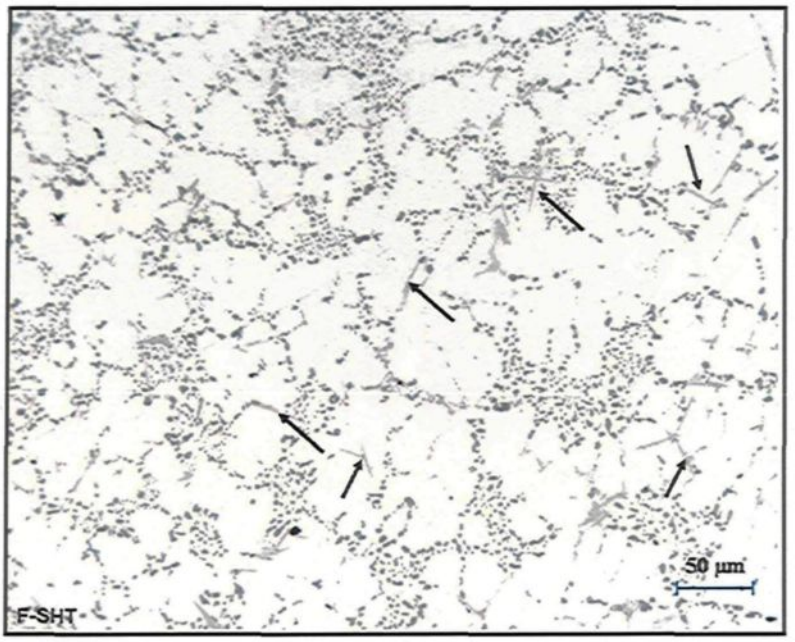

Figure 5.13 Microstructure of alloy F. The black arrows point to $(Al,Si)_3(Zr,Ti)$ phase particles (200x).

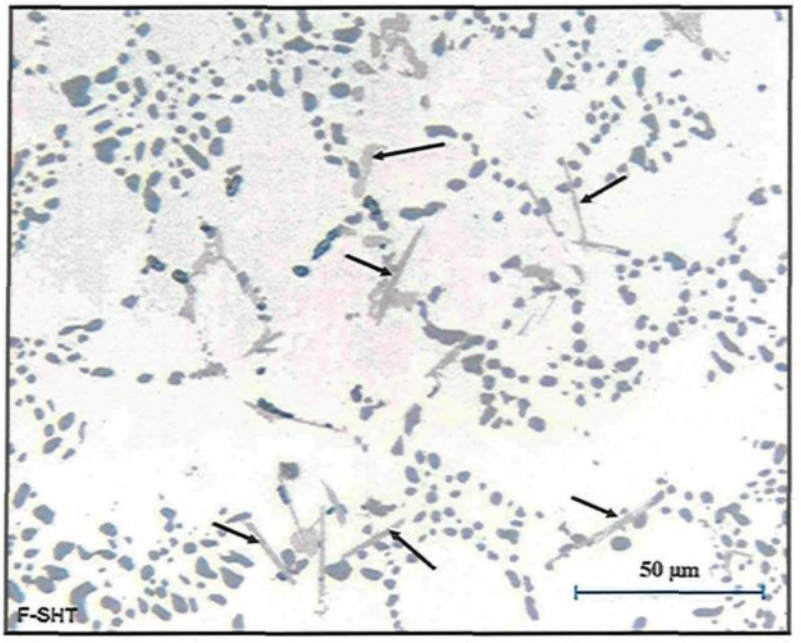

Figure 5.14 Microstructure of alloy F. The black arrows point to $(Al,Si)_3(Zr,Ti)$ phase particles (500x).

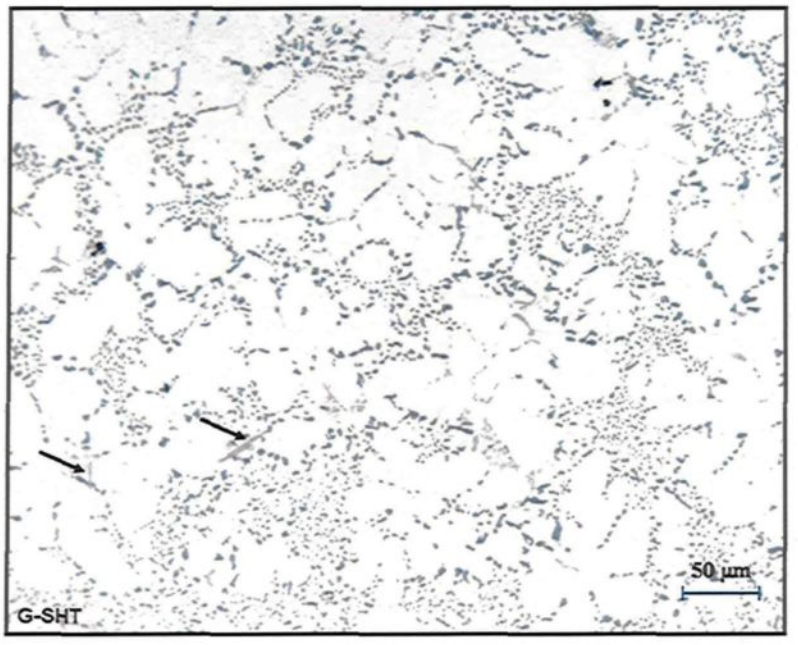

Figure 5.15 Microstructure of alloy G. The black arrows point to $(Al,Si)_3(Zr,Ti)$ phase particles (200x).

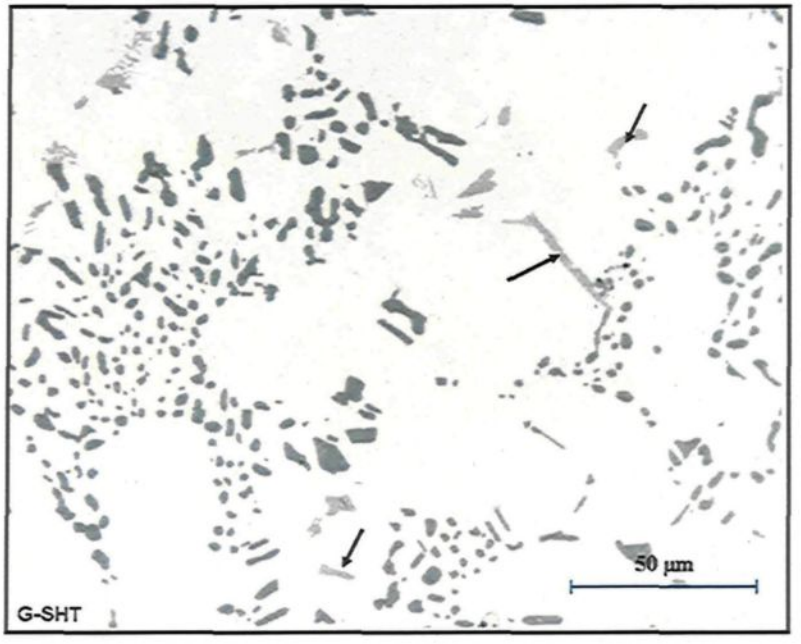

Figure 5.16 Microstructure of alloy G. The black arrows point to $(Al,Si)_3(Zr,Ti)$ phase particles (500x).

5.3 Tensile Results for Alloy A

Table 5.4 presents the UTS, YS and %Elongation values for the as-cast (AC) and solution heat-treated (SHT) conditions.

Table 5.4 Mechanical Values, UTS, YS and %Elongation for Alloy A

Condition	UTS	YS	%El
AC	235	154	1.63
SHT	305	161	6.36

In spite of the relatively low solution heat treatment temperature of 495°C used for the purposes of this work, increased strength after the treatment is normally to be observed in similar 354 alloys which use a solution heat treatment temperature of 525°C over a 2-3 hour period, in conjunction with analogous aging treatments.[113, 135] It was mentioned in a previous chapter that the solution heat treatment temperature of 495°C was selected only after corroboration with the thermal analysis curve shown in Figure 4.3. Even if the copper content of the alloy does not exceed 2%, this thermal analysis curve shows that the temperature at which the reaction of copper phases seems to appear during solidification is at ~500°C. This selected temperature for the solution heat treatment might appear to be over-conservative, but it was deemed necessary to avoid the risk of any incipient melting of the copper phases, which could have the potential for deteriorating the mechanical properties of the alloys to a great extent. The strength values, particularly the UTS, increased by as much as 30 pct between the as-cast (AC) and the solution heat-treated (SHT) conditions. This increase in the mechanical properties is related to the changes occurring in the form of the silicon particles which become more rounded, decreasing their

aspect-ratio and density, as may be seen in Table 5.2. The changes in the morphology of the silicon particles during solution heat treatment may be observed principally in the increase of the ductility values rather than in that of the strength values; with regard to both the as-cast and solution-treated conditions, the difference in yield strength is no more than 5 pct whereas it is over 290 pct for elongation.

The increase in ductility may be explained as follows: the silicon particles act as stress concentrators since they are harder than the matrix; serving as stress concentration sites, such particles tend to promote crack propagation during load application thereby principally decreasing the ductility of the alloy.

The effects of solution heat treatment on the spheroidization of such particles tends to decrease the stress concentration as the silicon particles become increasingly more rounded with the progress of solution treatment at the specified solution temperature. Figures 5.17 through 5.19 show the tensile properties of alloy A for the several aging times and temperatures applied during the heat treatment. Through solution heat treatment and artificial aging, the strength of alloy A was increased by ~64 pct over its as-cast strength. From the tensile properties listed in Tables I1 through I3, to be found in the appendix section, and as shown in Figure 5.18, the maximum value for UTS of ~386 MPa may be obtained with three different sets of aging conditions, *i.e.* 155°C/100hrs, 170°C/10hrs, and 190°C/2hrs. The greatest mechanical stability for the aging treatments was to be observed at 155°C and the second greatest at 170°C.

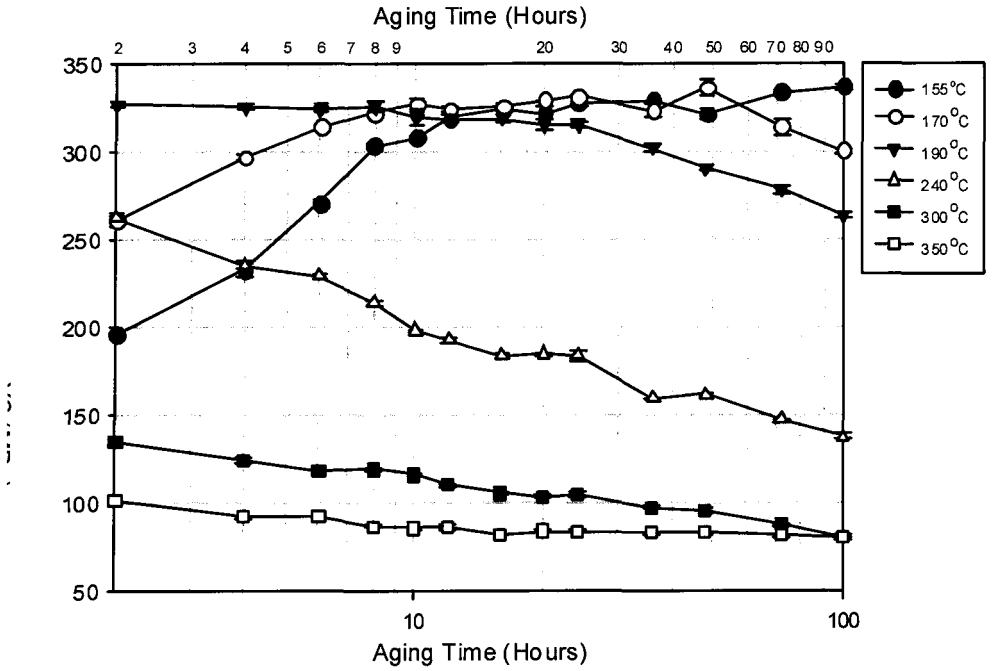

Figure 5.17 Ultimate Tensile Strength as a function of aging conditions in Alloy A.

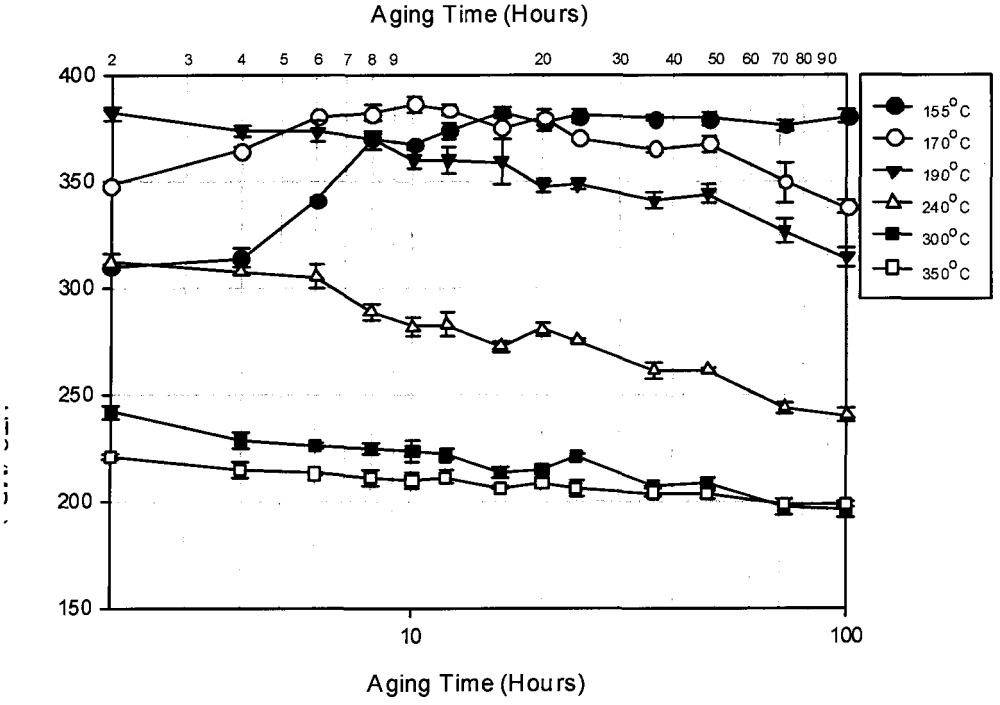

Figure 5.18 Yield strength as a function of aging conditions in Alloy A.

Considering the yield strength value in the solution heat-treated condition, in conjunction with the artificial aging conditions used, it was possible to increase the yield strength value by more than 100 pct. The maximum yield strength was reached after 100 hours at the aging temperature of 155°C, after 48 hours at 170°C, and after 2 hours at 190°C.

When considering the whole range of aging treatments applied in this work, the greatest decrease in tensile strength may be observed at 240°C, going from 312 MPa at 2 hours to 240 MPa at 100 hours. In the same way, a significant decrease in strength going from 382 MPa at 2 hours to 314 MPa at 100 hours is also to be observed at 190°C. Even though a significant decrease in the alloy strength is not in evidence from 2 to 100 hours at 300°C and 350°C, nonetheless, the greatest mechanical deterioration is expected to be observed after less than 2 hours of aging treatment. This assumption is based on a consideration of the tensile properties of the material upon solution heat treatment, namely, UTS = 305 MPa and YS = 161 MPa, implying that the over-aged samples tended to lose between 15% and 40% of their original strength within the first 2 hours of being subjected to aging at temperatures of 300°C and 350°C.

As will be observed in Table 5.4 and Figure 5.19, ductility displays values ranging from 1 to 6 pct, in which any value greater than 3 pct is considered a high ductility value when considering the hypoeutectic Al-Si alloys.[136]

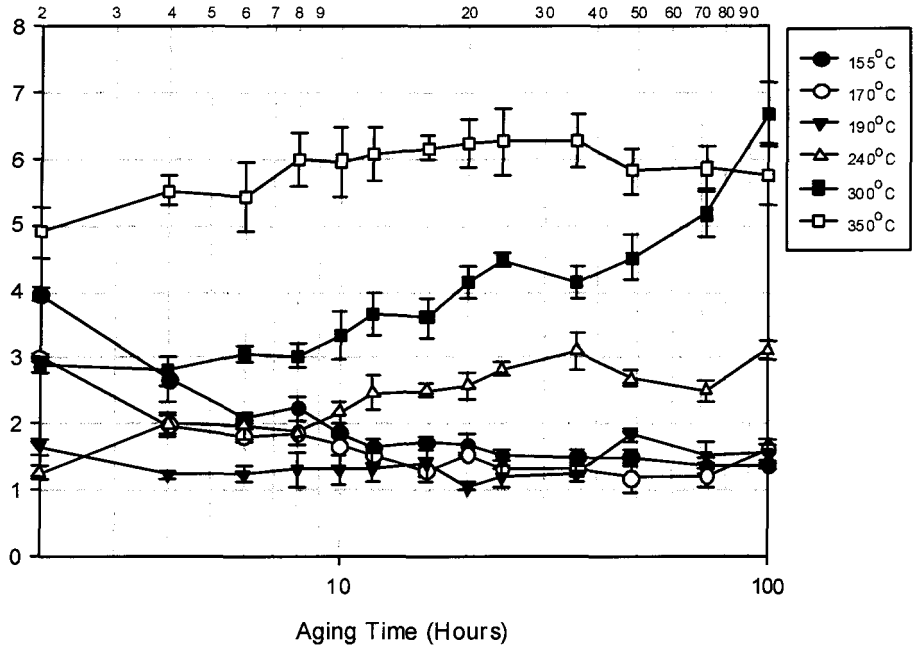

Figure 5.19 Strain at fracture as a function of aging conditions in Alloy A.

The high silicon content of the base alloy, which is 9 pct, seems to be part of this behavior with respect to elongation. With low silicon content, namely 5 to 7 pct in hypoeutectic Al-Si alloys, the eutectic liquid solidifies in narrow bands surrounding the Al grains, and therefore the intermetallics which precipitate out of this liquid are observed to form along these narrow bands as entwined clusters. Contrary behavior occurs in the case of high silicon alloys, with a greater volume fraction of eutectic liquid, but rather than just forming wider bands of particles around the grains, they form within the complex networks of interdendritic and intergranular liquid pools; these are bounded by the more orthogonal dendritic Al grains, and ultimately lead to the formation of more uniformly dispersed intermetallic phases.[137]

The general behavior of Alloy A with regard to ductility displays a decrease from 155°C to 190°C, as shown in Figure 5.19. A lower ductility value is observed for the condition involving 190°C for 12 hours in the experimental alloy test samples. Increased ductility may be observed above 190°C as the aging temperature increases. The greatest ductility values may be observed for aging at 350°C, although none of the aging conditions reaches the higher ductility values shown in the solution heat-treated condition. This observation may be considered evidence that the mechanical behaviour displayed by alloy A is common to that of the Al-Si-Cu-Mg alloys whose strength is obtained at the expense of ductility.[33, 136-138]

In comparison to the ascendant and steady strength curves displayed in Figures 5.17 and 5.18 corresponding to aging temperatures of 155°C and 170°C, fluctuations in the strength curves were observed at aging temperatures of 190°C and over; this behaviour is similar to that reported in a study carried out by Reif [138] where a similar alloy was used and an ascendant monotonic strength curve was observed at an aging temperature of 155°C.

After 2 hours of aging at 190°C, the tensile properties attain the highest strength values while exhibiting the lowest ductility of all the aging conditions applied. The yield strength behavior appears to be the most stable at 190°C aging temperature, showing a variation of 50 MPa in yield strength values for aging times between 2 and 100 hours. These observations were taken into account for the selection of this specific temperature for experiments designed to investigate how the mechanical properties may be affected by long exposure times.

The next subsection deals with the construction of the quality index charts which will be used to illustrate the long-exposure-time experiments at 190°C together with selected conditions for the general mechanical behaviour of the alloys at the aging conditions used throughout this investigation.

The fulfilment of the objectives of this research relies strongly on the use of Quality index charts as a useful tool for illustrating, in an accessible way, the general behaviour of the alloys with respect to tensile properties as the aging temperatures and times increase.

The Quality index charts presented here are explained for a single specific condition with regard to Alloy A, namely the solution-heat-treated condition. Five test bars were used for each alloy/heat treatment condition studied. For explicative details regarding the construction of the Quality index charts, the values corresponding to the five tests for the solution heat-treated condition and their averages as well as the standard deviations are presented in Table 5.5.

The first step is to select one flow curve out of the five available curves per condition. The criterion for selecting this particular curve involved choosing the sample whose UTS was the closest to the average UTS, or otherwise, the one displaying a ductility value which was the closest to the average ductility of the entire batch. In this case, the selection would be Test 3, as delineated by the colored rows in Table 5.5. Figure 5.20 shows the engineering stress-strain flow curve for the solution heat treated condition - Test 3 relating to Alloy A. It ought to be mentioned here that the average and standard deviations of the tensile properties for all aging conditions were calculated in a similar

manner and are summarized in Tables I1 to I4 in the Appendix section at the end of the thesis.

Table 5.5 Tensile test results for Alloy A, solution heat-treated condition

Test	UTS (MPa)	YS (MPa)	El.(%)
1	307.2	163	6.4
2	302.67	160.99	6.08
3	306.94	162.54	6.39
4	299.66	158.04	6.49
5	308.66	164.42	6.47
Average	305.03	161.8	6.37
Std.Dev.	3.74	2.43	0.167

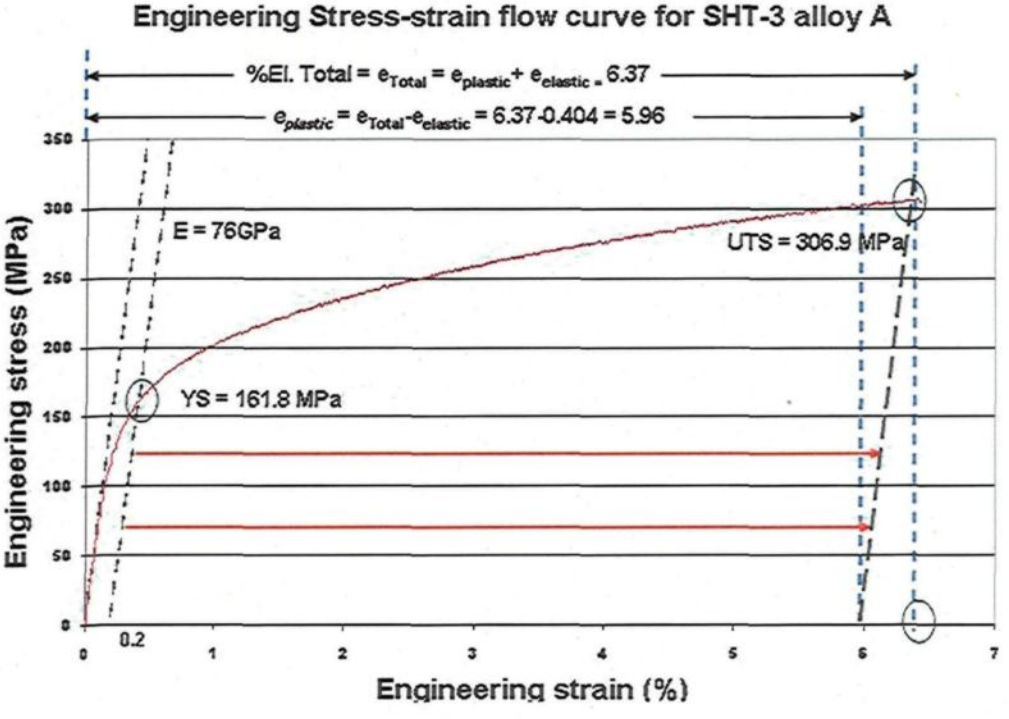

Figure 5.20 Engineering stress-strain curve for Test 3 and corresponding UTS, YS, %Elongation (e_{Total}), $e_{plastic}$ and $e_{elastic}$ values.

The next step is to convert the engineering stress-strain data obtained to true stress-strain data. The conversion from engineering stress-strain curve to true stress-strain curve may be obtained from the relationship between the formulae 5.1 and 5.2.[146]

$\sigma = (P/A_0)\ (e_{plastic} + 1) = s\ (e_{plastic} + 1)$ Equation 5.1

$\varepsilon_{plastic} = ln\ (e_{plastic} + 1)$ Equation 5.2

where P is the load applied over the original cross-sectional area, A, of the tensile sample, σ is the true-stress, ε is the true-strain, s is the engineering stress, and e is the engineering strain. Figure 5.21 shows the true stress-true strain flow curve.

The third step is to obtain the strain-hardening exponent (n) and the strength coefficient (K) over the entire plastic stress-strain flow curve. An overview of the method to calculate n and K from the real-stress-real-strain curve may be found in Reference [147]. Figure 5.21 shows a comparison of two curves, a black curve which is the flow curve corresponding to the example shown in and a red curve which follows the values obtained using Holloman's equation $\sigma = K\varepsilon^n$ and using the values of n = 0.193 and K = 528 obtained from the Test 3 data. The same procedure was repeated for the different heat treatment conditions applied to Alloy A. The results are presented in Table 5.6.

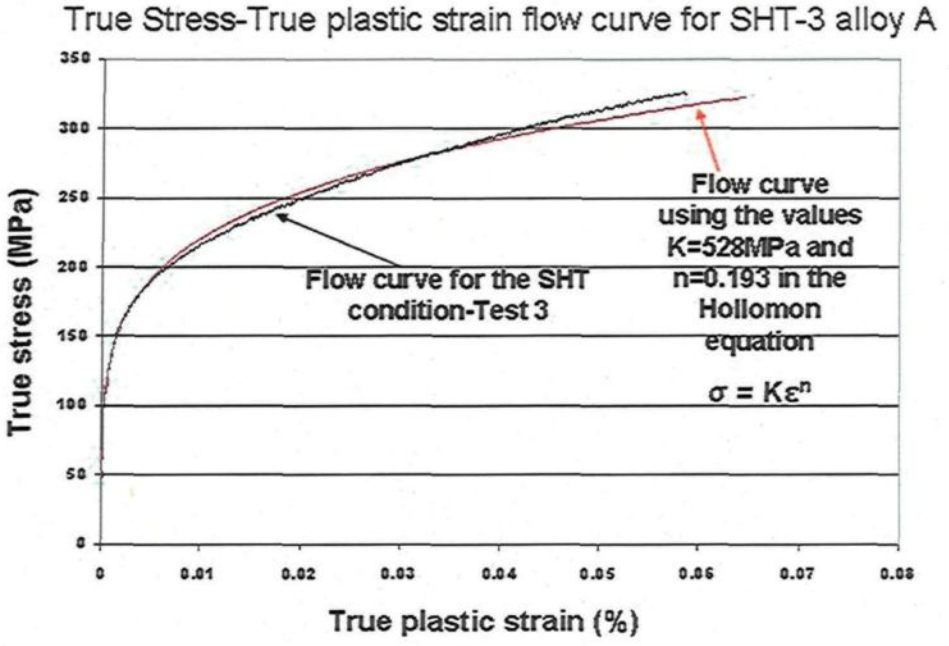

Figure 5.21 True stress-true plastic strain flow curve for solution heat-treated Alloy A-Test 3, and the flow curve derived from the Holloman equation ($\sigma = K\varepsilon^n$) using $K = 528$ Mpa and $n = 0.193$.

The Cáceres method which is used here for constructing the quality index charts involves the use of a single value of the strength coefficient (K) for all the conditions appearing in the charts. The value K = 500 MPa was taken as the average K value for constructing the quality index (QI) charts with regard to all the conditions covering the seven alloys studied (see Tables I-4 to I-8 in the appendix I), where Equation 2.10 was used to obtain the Quality Index (Q).

One way of verifying whether or not the K value selected for the model is adequate might be to compare the values of the quality index (Q) obtained from Equation 2.10 with those obtained from Equation 2.9. The reason for this recommendation is that Equation 2.9 uses the parameters q, n, and K from the individual true-stress/true-strain flow curves,

which should thus be more realistic than Equation 2.10.[142] Table 5.7 presents a comparison of the Q values obtained from Equations 2.9 and 2.10.

The average value of the strength coefficient ($\boldsymbol{K}$) is K = 502 as used in the Quality Index charts for all the conditions applied in relation to the seven alloys studied, that is to say, 161 conditions in total. The value of K was rounded to 500 and used to represent the average value for all conditions when the quality index was calculated.

Returning to the example of Test 3, the error percentage is calculated as 1.32% which appears to be a satisfactory approximation for this specific condition. This type of comparison provides a means for quantifying the percentage of error persisting in the model for the quality index charts as used in this research. Thus, using K = 500 MPa to construct the Quality Index charts for the alloys used in this work may be deemed a reasonable proposition.

Table 5.6 Mean values of UTS, YS, Total and Plastic Strain obtained for Alloy A subjected to different heat treatment conditions; Q values obtained with Eq. 2.10.

$Q = UTS + 0.4K \cdot \log (S_f)$								Equation 2.10
Identification	UTS (MPa)		YS (MPa)		Total Strain S_T (%)		Plastic Strain S_f (%)	Q (MPa) (Eq.2.10)
	AV	SD	AV	SD	AV	SD	AV	AV
A-AC	235	5.8	154	4.8	1.63	0.24	1.32	259
A-SHT	304	3.7	161	2.4	6.36	0.17	5.96	459
A1-155°C-2hrs	309	2.7	196	1.9	3.96	0.19	3.58	420
A5-155°C-10hrs	367	0.4	308	1.7	1.86	0.11	1.40	397
A13-155°C-100hrs	380	7.0	336	3.5	1.38	0.10	0.92	373
A14-170°C-2hrs	348	3.2	261	5.8	3.01	0.13	2.60	431
A18-170°C-10hrs	386	7.6	327	7.5	1.67	0.31	1.20	402
A26-170°C-100hrs	337	6.1	300	2.7	1.62	0.32	1.20	354
A27-190°C-2hrs	381	6.7	327	4.3	1.66	0.24	1.21	399
A31-190°C-10hrs	360	9.4	319	7.9	1.32	0.44	0.87	348
A39-190°C-100hrs	314	9.0	263	3.5	1.56	0.28	1.18	328
A40-240°C-2hrs	312	7.8	262	4.5	1.25	0.20	0.87	300
A44-240°C-10hrs	281	7.9	198	1.8	2.17	0.32	1.79	332
A52-240°C-100hrs	240	5.6	137	3.1	3.12	0.28	2.80	329
A53-300°C-2hrs	241	7.1	134	3.7	2.89	0.27	2.56	323
A57-300°C-10hrs	223	9.8	116	1.1	3.33	0.72	2.99	318
A65-300°C-100hrs	195	6.8	80	1.8	6.70	0.93	6.32	356
A66-350°C-2hrs	221	3.0	101	1.7	4.90	0.76	4.53	352
A70-350°C-10hrs	209	7.1	86	2.3	5.98	1.04	5.64	360
A78-350°C-100hrs	198	3.1	81	1.1	5.76	0.88	5.37	344

Table 5.7 **K** and **n** values obtained for Alloy A from single sample **σ-ε** plots; **Q** values obtained from Equation 2.9

$Q = K\,[(qn)^n e^{-qn} + 0.4 \log (100\,qn)]$				Equation 2.9	
$\%Error = [(Q_{Eq.2.10} - Q_{Eq.2.9})/Q_{Eq.2.9}] \cdot 100$				Equation 5.1	
$q = s_f/n$				Equation 2.6	
Identification	K	n	q	Q (MPa) (Eq. 2.9)	%Error (Eq. 5.1)
A-AC	586	0.207	0.070	278	6.83
A-SHT	528	0.193	0.309	453	1.32
A1-155°C-2hrs	512	0.1472	0.243	416	1.01
A5-155°C-10hrs	515	0.0776	0.180	395	0.45
A13-155°C-100hrs	476	0.0499	0.184	366	1.80
A14-170°C-2hrs	497	0.0982	0.264	421	2.44
A18-170°C-10hrs	552	0.0803	0.150	400	0.51
A26-170°C-100hrs	467	0.0559	0.215	375	5.74
A27-190°C-2hrs	552	0.0803	0.151	401	0.65
A31-190°C-10hrs	525	0.0713	0.122	359	2.93
A39-190°C-100hrs	530	0.1062	0.111	342	3.99
A40-240°C-2hrs	579	0.128	0.068	298	0.45
A44-240°C-10hrs	570	0.1674	0.107	344	3.22
A52-240°C-100hrs	490	0.199	0.141	322	2.47
A53-300°C-2hrs	505	0.199	0.128	320	1.12
A57-300°C-10hrs	501	0.2299	0.130	312	1.94
A65-300°C-100hrs	449	0.278	0.227	340	4.82
A66-350°C-2hrs	538	0.2784	0.163	359	1.70
A70-350°C-10hrs	493	0.2815	0.200	355	1.27
A78-350°C-100hrs	539	0.3163	0.170	360	4.29

The ***q*** values used in the Cáceres model for the Quality Index charts makes use of Equation 2.3, $q = \varepsilon_{plastic} / n$, involving the application of Considère's criterion of instability, in view of the fact that necking or localized deformation begins at maximum load, where the increase in stress due to a decrease in the cross-sectional area of the tensile specimen becomes greater than the increase in the load-carrying ability of the metal as a result of strain-hardening.

The condition of instability leading to localized deformation is defined by the conditions:

$dP = 0$

$P = \sigma A$

$dP = \sigma dA + A d\sigma = 0$

$-d\sigma/\sigma = dA/A$ **Equation 5.3**

From the constancy of volume relationship:

$dL/L = -dA/A = d\varepsilon$

Since $-dA/A = d\varepsilon = d\sigma/\sigma$,

$\sigma = d\sigma/d\varepsilon$, which is the equation of maximum true-stress.

Considering the definition of ***n*** (reference 146) given in Chapter 2,

$n = d(\log\sigma)/d(\log\varepsilon) = d(\ln\sigma)/d(\ln\varepsilon) = (\varepsilon/\sigma)(d\sigma/d\varepsilon)$

or $d\sigma/d\varepsilon = n(\sigma/\varepsilon)$ **Equation 2.4**

Combining Equations 5.3 and 2.4,

$\sigma = d\sigma/d\varepsilon = n(\sigma/\varepsilon)$

$\sigma = n(\sigma/\varepsilon)$

$\varepsilon = n$

Since $q = \varepsilon/n$ which implies that $q = 1$.

As the necking stage is reached, which presupposes a fairly ductile material, the quality Q displays the greatest possible values. It is important to mention here that even if the q used by Cáceres is not the same Q as the one used in Equation 2.10, the correlation between q and Q as may be observed in the plot of Figure 5.22, using the q-values obtained with Equation 2.6 and the Q-values obtained with Equation 2.10 from Tables 5.6 and 5.7 for alloy A.

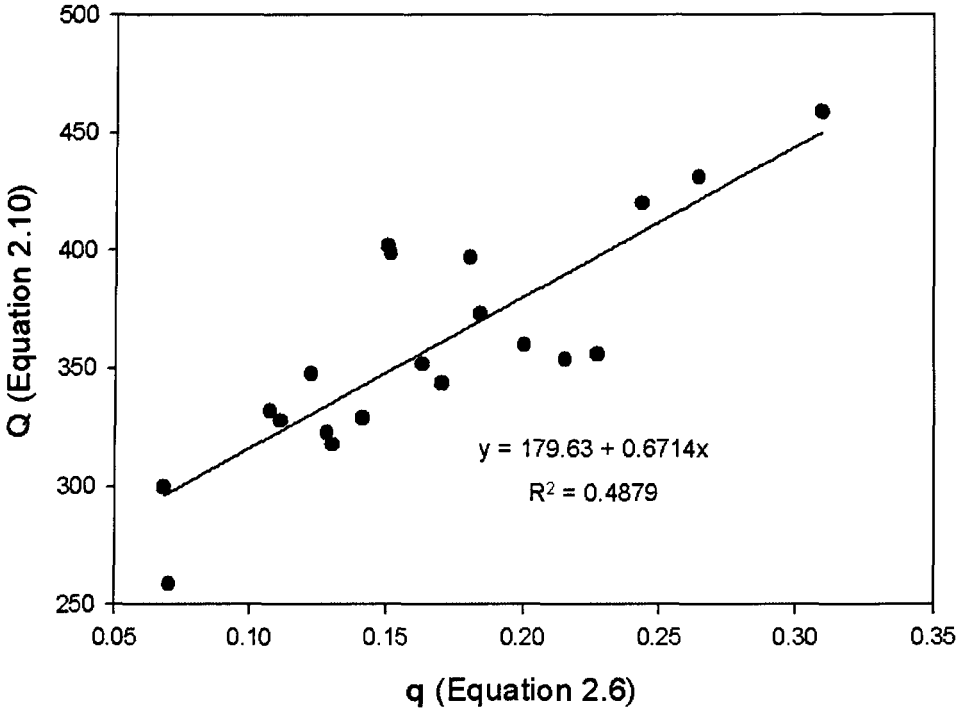

Figure 5.22 Q and q values obtained from Equation 2.9 (Q) and Equation 2.6 (q).

In Figure 5.23 is presented a Quality Index chart showing the lowest and highest mechanical quality occurring in the as-cast (AC) and solution heat-treated (SHT)

conditions, respectively. Between each one of these conditions there exists a difference of nearly 70 MPa in UTS, while for both cases the YS is virtually similar, as may be corroborated by Table 5.4 and Figure 5.23. In order to analyze mechanical quality by means of the Quality Index charts, 20 conditions per alloy were selected from among all the conditions used; such conditions are the as-cast and the solution heat-treated conditions plus 18 aging conditions per alloy; the 18 conditions are 2, 10, and 100 hours for every aging temperature of 155°C, 170°C, 190°C, 240°C, 300°C, and 350°C. The reason for taking only 20 conditions out of a total of 80 per alloy was principally to avoid an overcrowded Quality Index chart in which it would not be possible either to discern or to show the general mechanical behaviour covering all of the experiments carried out for this research.

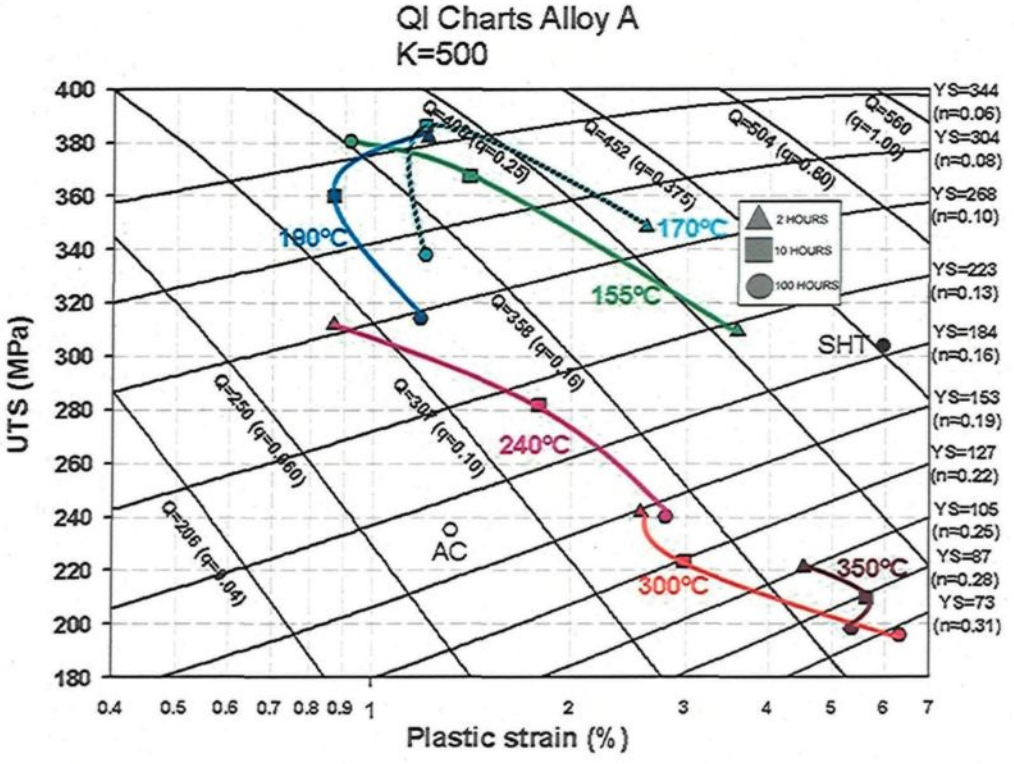

Figure 5.23 Quality Index Chart for aging conditions corresponding to aging times of 2 hrs, 10 hrs, and 100 hrs at different aging temperatures.

The criterion applied for using these 20 conditions (including the as-cast and SHT conditions) was to take into consideration the extreme values, particularly those regarding the pct elongation and yield strength values. As was observed in Figures 5.17 to 5.19, these 20 values show the maximum and minimum mechanical properties out of the whole set of experiments carried out for the purposes of this research.

The plastic strain and the quality index (Q) both display a significant increase upon solution heat treatment, in spite of the fact that the relative ductility (q) attains a value of 0.31 implying that Alloy A in its solution-treated condition has reached 31% of its maximum quality index value (Q). The usefulness of q as a complementary parameter expresses how far a particular sample is from its maximum possible ductility q = 1; even though, a q-value <1 indicates that it would be possible to manipulate the microstructure, for instance, by reducing the SDAS, or the porosity, or the Fe-level to increase the ductility and hence, ultimately, the quality index, Q. When the ductility increases sharply from the as-cast to the solution heat-treated condition, such changes can be related to the spheroidization of silicon particles and to the uniformity of the microstructure in the solution heat-treated condition, as shown in Figures 5.3 and 5.4.

The greater part of the behavior of Alloy A under different heat-treatment conditions illustrated in Figures 5.17, 5.18, and 5.19 is displayed through the quality index chart provided in Figure 5.23. Furthermore, by taking into consideration all the aging temperatures listed in this same figure, it becomes possible to detect mechanical behavior which is similar to that displayed by alloy 319 as evidenced by the curvilinear aspect of the quality index as it emerges throughout the aging process of the material.[98, 137]

The contour curve observed in the quality index chart can be related to changes in the yield strain and strain-hardening which are principally due to the effects of aging time and temperature on the precipitation-hardening of copper phase particles. Figure 5.24 shows the values of the strain-hardening exponent and the yield strength under different conditions of artificial aging.

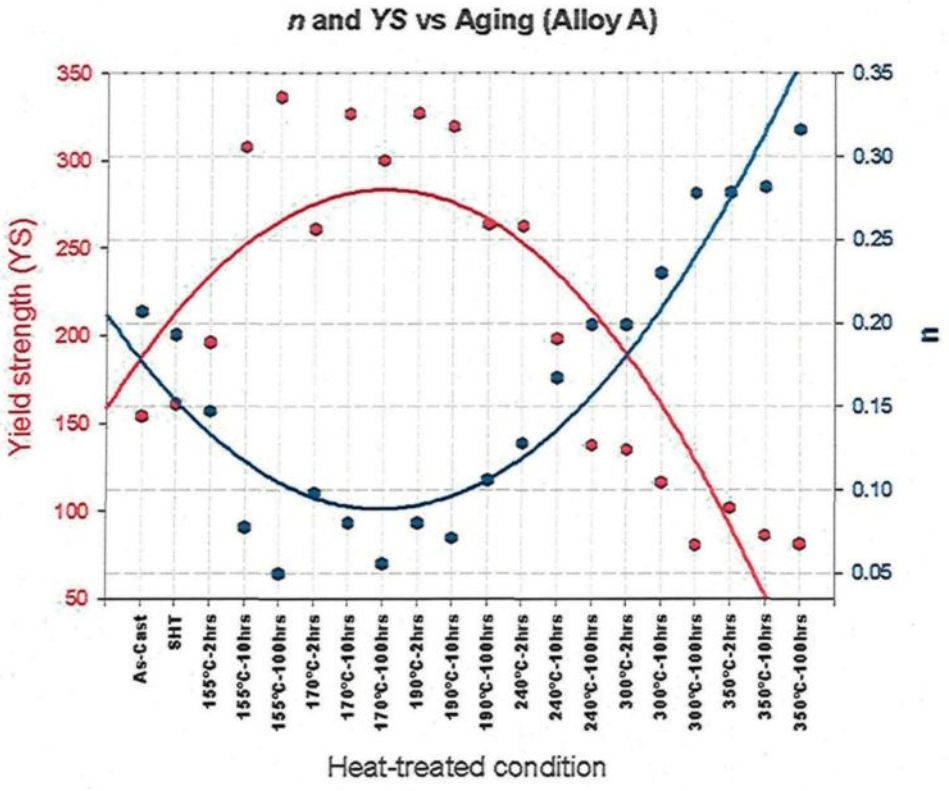

Figure 5.24 Yield strength (*YS*) values and the strain-hardening exponent (*n*) plotted against the heat-treated condition in Alloy A.

A contrary relationship may be observed between *n* and *YS* in view of the fact that artificial aging increases both temperature and time. The form of these two plots in Figure 5.24 is related to the contour curve observed in the Quality Index chart shown in Figure 5.23; the YS reaches a maximum and then decreases after the 190°C/2hr condition when

the strain-hardening coefficient reaches a minimum followed by an increase in value as either the temperature or the time, or both, are increased. Below the 190°C/2hr condition, GP zones and θ' precipitates develop such that they are coherent with the matrix;[33, 137] YS is thus increased because of the strain fields associated with these precipitates, which are sheared by the dislocations and subsequently lead to a low strain-hardening rate.

It may be deduced from parallel research that the θ-$CuAl_2$ precipitates form at temperatures of 190°C and higher.[139] These particles are incoherent with the matrix and cannot be cut by dislocations,[33] thereby promoting lower strength values and a high strain-hardening rate resulting from the accumulation of Orowan loops around the copper phase particles. As the strain is increased, however, the gradual development of primary shear loops generates intense stress fields around the strengthening precipitates, which are in themselves limited[137] by the activation of a secondary dislocation cross-slip process, thus reducing the strain-hardening ability of the material.

The experiments involving long exposure times consisted of three conditions, namely, 200, 600, and 1000 hours aging at 190°C. The solution heat-treated conditions including 2, 10, and 100 hours at 190°C were added to the plot in order to amplify the perspective of the effects of time exposure during aging at such temperature. The same contour curve observed in Figure 5.23 may be observed in Figure 5.25 which shows the Quality Index chart pertaining to the 190°C aging temperature for long exposure times. Tables 5.8 and 5.9 show the values of the principal parameters of the Quality Index chart of Figure 5.25.

Table 5.8 Mean values of UTS, YS, and Plastic Strain; Q values obtained using Equation 2.10 applying a single K=500 MPa for Alloy A at 190°C.

$Q = UTS + 0.4K \cdot \log(S_f)$ Equation 2.10								
Identification	UTS (MPa)		YS (MPa)		Total Strain S_T (%)		Plastic Strain S_f (%)	Q (MPa) (Eq.2.10)
	AV	SD	AV	SD	AV	SD	AV	AV
A-200hrs	283	4.5	229	3.9	1.92	0.31	1.54	321
A-600hrs	263	3.5	195	2.9	2.41	0.35	2.03	324
A-1000hrs	243	3.4	164	3.1	3.06	0.21	2.69	329

Table 5.9 K and n values obtained for Alloy A from the single sample σ-ε plots; Q values obtained from Equation 2.9

$Q = K[(qn)^n e^{-qn} + 0.4 \log(100\ qn)]$ Equation 2.9 $\%Error = ([Q_{Eq.2.10} - Q_{Eq.2.9}]/Q_{Eq.2.9}) \cdot 100$ Equation 5.1 **$q = s_f/n$** Equation 2.6					
Identification	K	n	q	Q (MPa) (Eq. 2.9)	% Error (Eq. 5.1)
A-200hrs	496	0.1234	0.125	329	2.45
A-600hrs	457	0.1369	0.148	319	1.65
A-1000hrs	444	0.1634	0.165	316	4.10

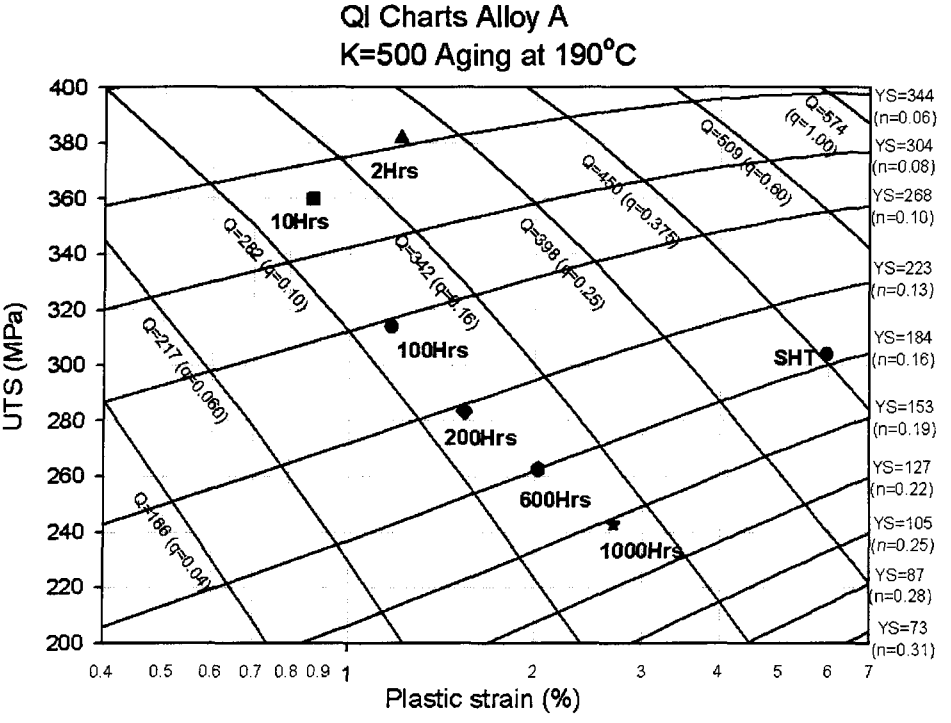

Figure 5.25 Quality index chart for long exposure times at 190°C aging temperature.

As may be observed from Figure 5.25, beyond 2 hours, aging time appears to have little or no effect on the mechanical quality of the alloy at 100, 200, 600 and 1000 hours, as the quality index value remains situated between 315 and 350 MPa, despite the increase in ductility from 1.15% to 2.69% when exposure time is increased from 100 to 1000 hours. The compromise between strength and ductility in Alloy A is evident from the figure.

The yield strength is most affected since it decreases by 60 pct, whereas the UTS decreases by only 22 pct over the aging times studied. The tensile properties after a long exposure time at 190°C are comparable to those observed after artificial aging at 240°C from 10 to 100 hours of exposure. The results discussed here are integral evidence that the mechanical properties obtained for Alloy A depend strongly on its thermal history.

5.4 Mechanical Properties of Alloys A, B, and C (Effects of micro-particulates)

Figure 5.26, 5.27 and 5.28 show the yield strength (YS) color-contour maps for alloys A, B, and C, respectively. These figures reveal that the strength, particularly the yield strength, does not change to any great extent with progress in aging time compared with that of the base alloy.

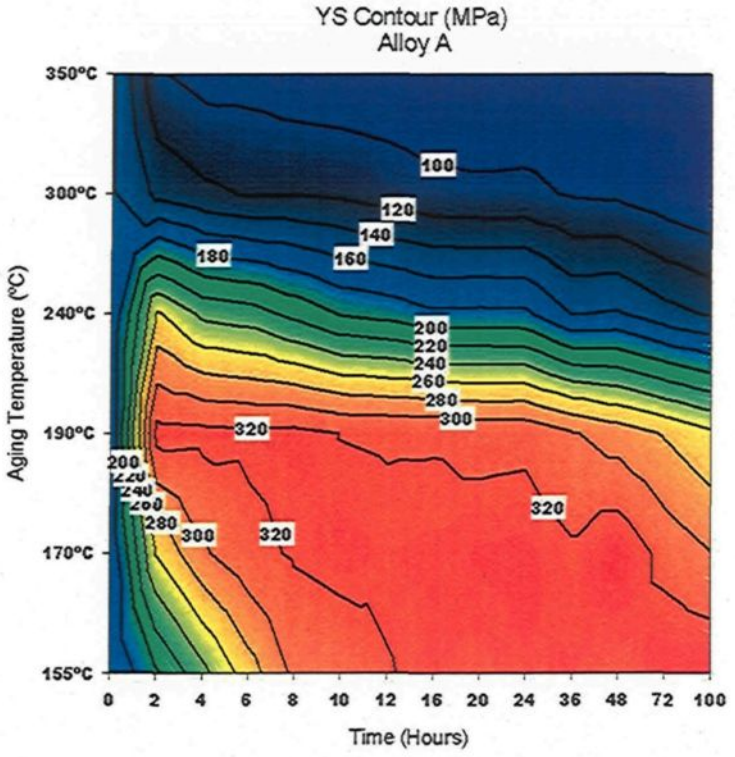

Figure 5.26 Yield strength color-contour chart for alloy A corresponding to different aging conditions.

While only selected diagrams are presented here to show evidence of some particular behavior, the appendix section provides all the diagrams, tables, and contour-maps showing the UTS, YS, %Elongation, and quality index (Q) values for the different aging conditions and alloys used in this research work.

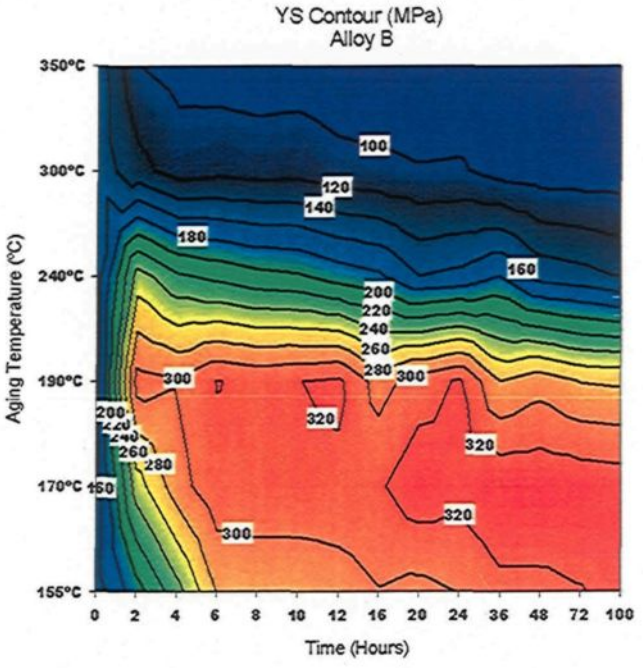

Figure 5.27 Yield strength color-contour chart for alloy B corresponding to different aging conditions.

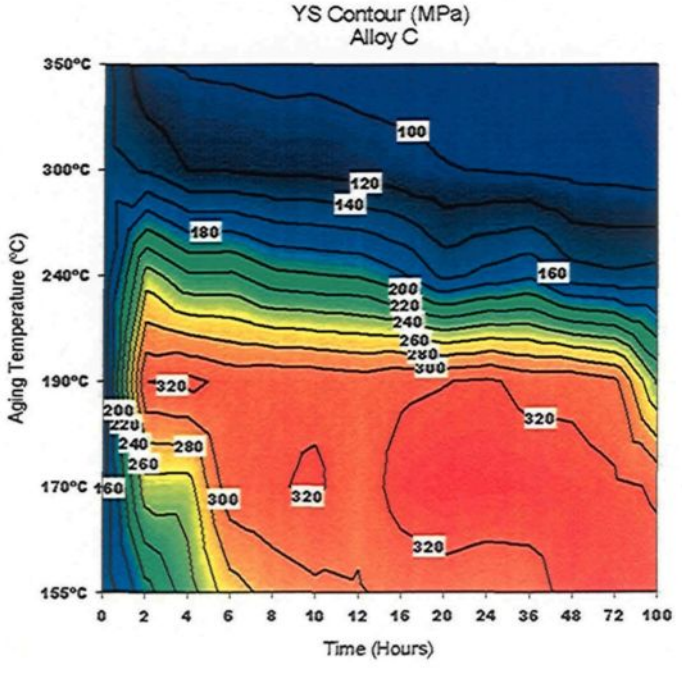

Figure 5.28 Yield strength color-contour chart for alloy C corresponding to different aging conditions.

It has been observed that ceramic reinforcement possesses the capacity to affect the age-hardening behavior of alloy matrices by significantly accelerating the kinetics of precipitation. This acceleration is related to an increase in the precipitate growth rate. The kinetics of hardening is normally enhanced either by micro-oxides or carbides, Al_2O_3 or SiC, since hardening precipitates develop preferentially along the dislocation lines which increase, as a result of a mismatch between the coefficient of thermal expansion of the matrix and the reinforcement, without any alteration in the precipitation sequence.[140] The relative amounts of age-hardened precipitates are also observed to be affected by the addition of reinforcements.[71] These mechanical behaviors have been observed in metal-matrix composites, where the amount (pct) of micro-oxide/carbide added exceeds by one order of magnitude or more the amount added to alloys B and C as was used in this thesis; this low micro-particulate content showed no significant augmentation of or acceleration in strength when compared to the base alloy, as may be observed from Figures 5.26 to 5.28.

As opposed to the behavior of the YS values observed in alloys containing micro-particulates, which are similar to the base alloy, the quality index for alloys B and C did not display the same behavior as alloy A, as will be observed in the color-contour maps shown in Figures 5.29 to 5.31. In these figures, the quality index (Q) obtained by applying Equation 2.10 and using K=500MPa is plotted as a function of aging time and aging temperature. Compared to the base alloy, the quality indices for alloys B and C decrease by approximately 10 pct at different zones of the color-contour maps from Figures 5.30 to 5.31. The more colorful charts for alloys B and C are indicative of the fact that the mechanical quality shows not only a decrease in the range of values but also that it

fluctuates more than it does in the base alloy. The elevated fluctuations of the quality index values, which depend on the UTS and strain values, may be viewed as the occurrence of such defects as segregation of the micro-oxides/carbides limiting the plastic flow, and as a decrease in both UTS and strain during the tensile tests. As mentioned earlier in a previous subsection, segregation was observed in some microstructures of the B and C alloy samples.

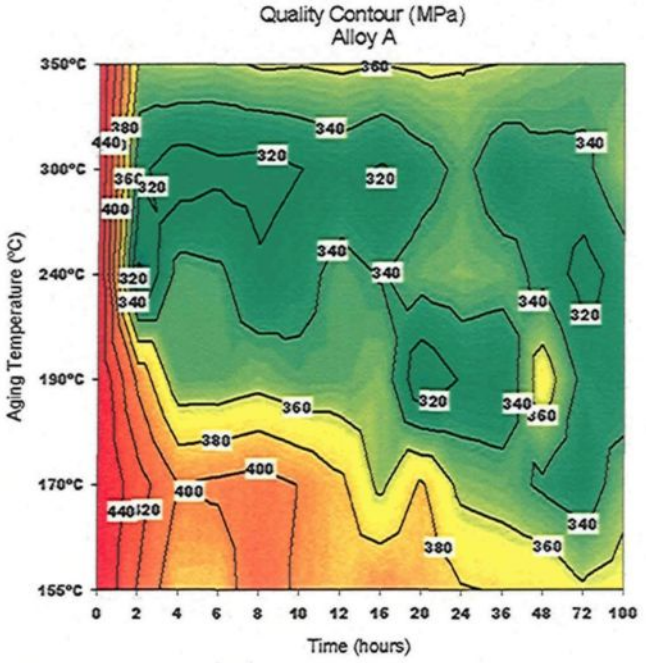

Figure 5.29 Quality color-contour chart for alloy A corresponding to different aging conditions; $Q=UTS + 0.4 \bullet K \bullet \log(\varepsilon_{plastic})$, where K=500MPa.

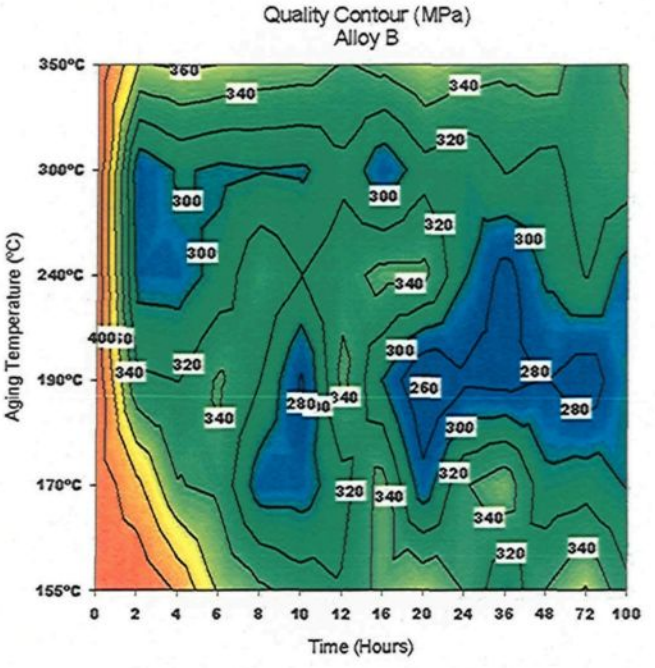

Figure 5.30 Quality color-contour chart for alloy B corresponding to different aging conditions; $Q=UTS + 0.4 \bullet K \bullet \log(\varepsilon_{plastic})$, where K=500MPa.

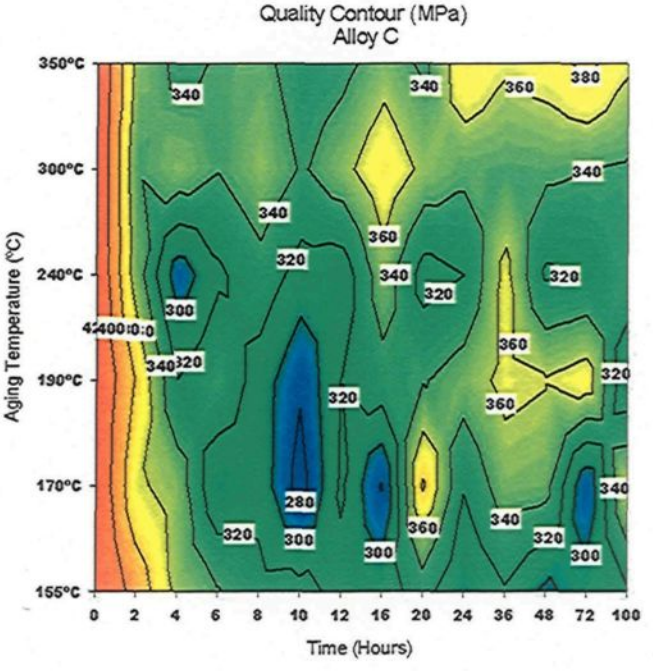

Figure 5.31 Quality color-contour chart for alloy C corresponding to different aging conditions; $Q=UTS + 0.4 \bullet K \bullet \log(\varepsilon_{plastic})$, where K=500MPa.

Figures 5.32 and 5.33 show the quality index charts for 20 selected conditions for alloys B and C. The use of quality index charts makes it possible to observe the general behavior tendencies of both alloys B and C with respect to the tensile test results. The same behavior may be observed in the color-contour maps shown in Figures 5.28, 5.29 and 5.30, compared to the base alloy. In the charts shown in Figures 5.32 and 5.33, the data points are more dispersed, moving towards the left of the chart, indicating a decrease in ductility and quality. Even if both of these alloys never attain the higher mechanical properties of alloy A, there occurs a great loss in ductility which is more evident in some aging conditions than in others, such as at 190°C for 10 hours, at 300°C for 100 hours, at 170°C for 10 hours, and at 170°C for 100 hours. The decrease in ductility in alloy C is not so evident as it is in alloy B; alloy C, however, never attains the higher quality index values obtained for the base alloy A.

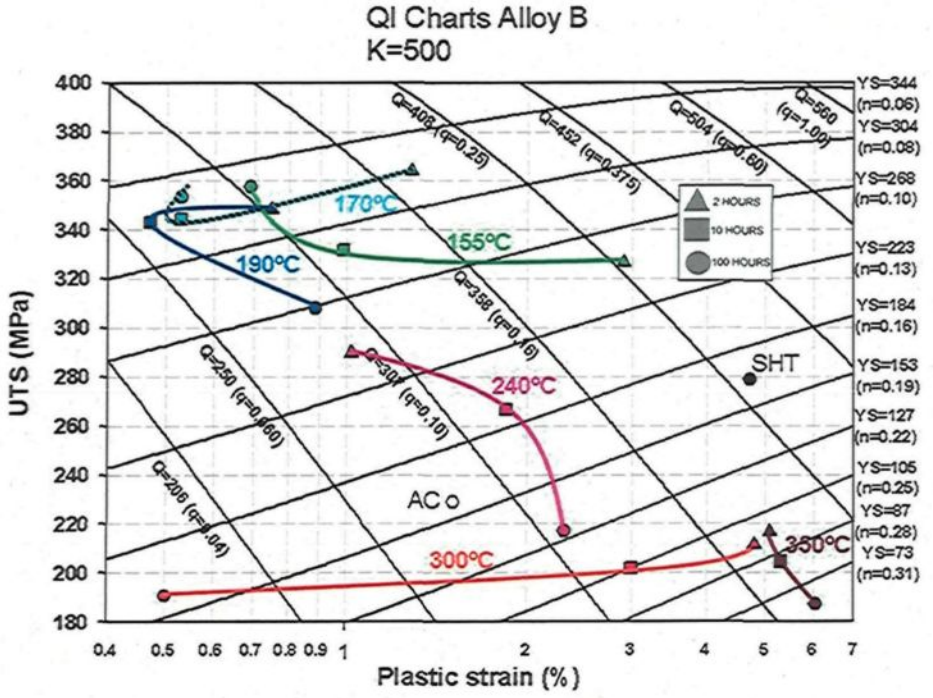

Figure 5.32 Quality index charts for alloy B.

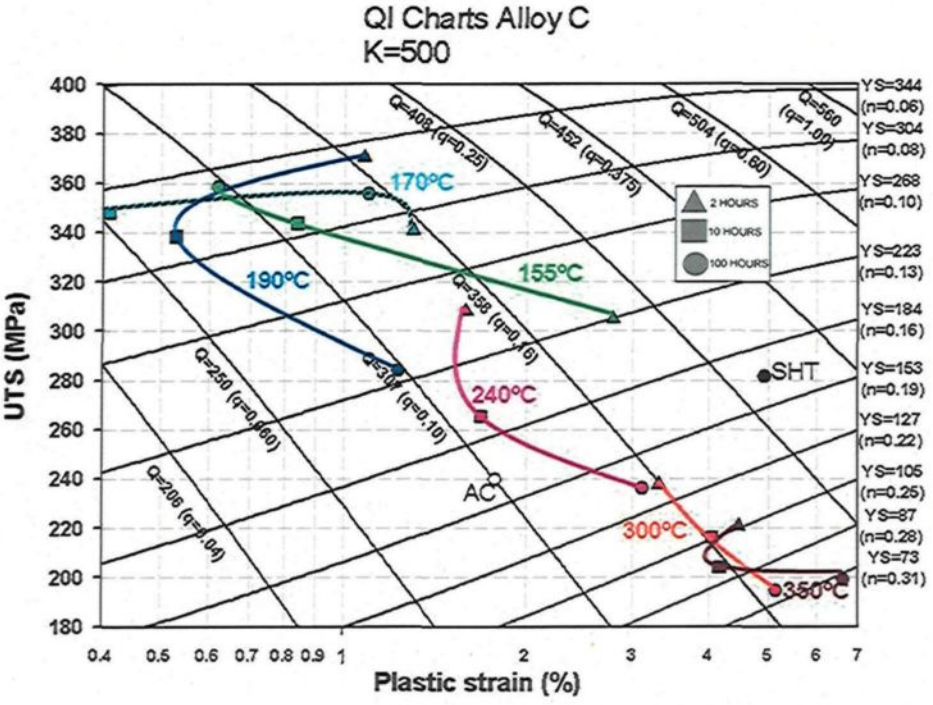

Figure 5.33 Quality index charts for alloy C.

Taking into consideration the quality index charts for alloys A, B, and C corresponding to Figures 5.31 to 5.33, it is observed that the maximum relative ductility (q), and consequently the highest mechanical quality, appears to correspond to the solution-heat-treated condition. The variability shown by the tensile test data of alloys B and C, compared to alloys A, D, E, F, and G, will be observed when the standard deviation values of the UTS, YS, and %Elongation of these two alloys are compared.

Figure 5.34 shows the quality index charts for alloys B and C pertaining to the extended exposure/aging time experiments carried out at 190°C. In this figure, the values of alloy A have been added to the chart, where, in addition to the extended aging time conditions, the solution treated condition and the 2-hr, 10-hr, and 100-hr aging time conditions have also been included for comparison purposes.

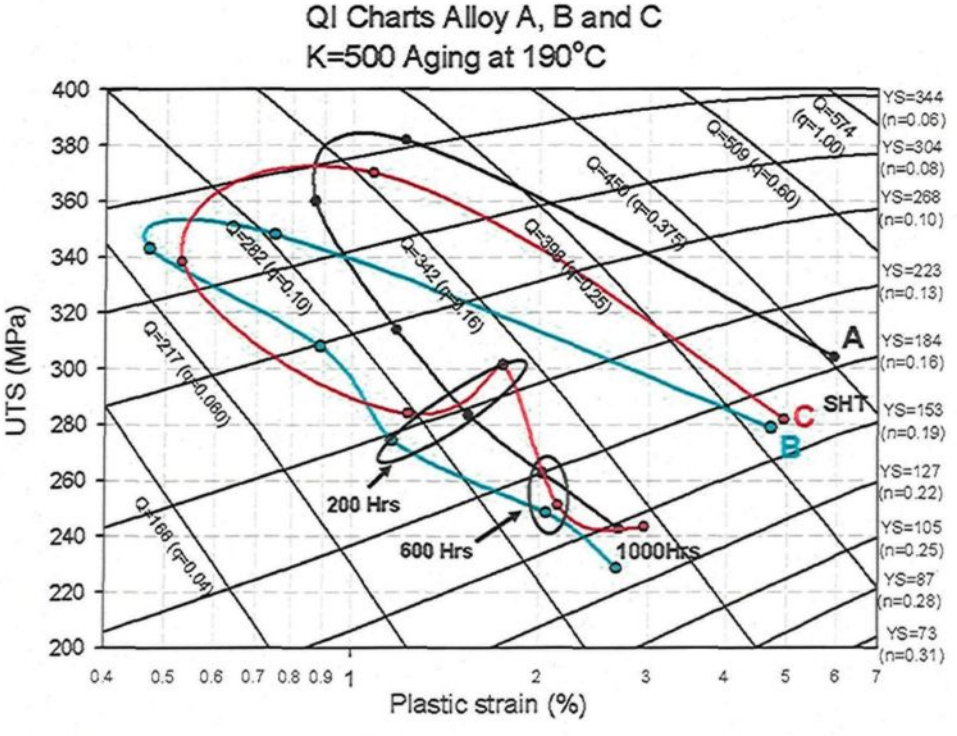

Figure 5.34 Quality index chart for long exposure times at 190°C aging temperature.

Figures 5.35 and 5.36 show the mean standard deviations for the tensile strength and percent elongation values of the seven alloys studied over the 13 aging times employed for every aging temperature. Thus, each point on these two plots represents the average of the standard deviation (SD) values obtained at the corresponding aging temperature over the 13 aging conditions investigated; it is understood that the standard deviation at a particular aging temperature/time condition corresponds to the average UTS and %El values obtained over the five tensile tests carried out per condition. An example of how these standard deviation values were calculated is demonstrated through Table 5.10 for Alloy A for the 170°C aging temperature, the 13 aging times ranging from 2 hours to 100 hours.

Table 5.10 Standard deviation calculation from the UTS values obtained for Alloy A at 170°C aging temperature and different aging times

Aging time (h)	**2**	**4**	**6**	**8**	**10**	**12**	**16**	**20**	**24**	**36**	**48**	**72**	**100**	**Av. SD**
SD*	3.2	3.0	2.7	7.3	7.6	3.9	1.5	6.8	0.4	3.4	7.9	18.8	6.1	**5.58**

*SD obtained over the 5 tensile tests carried out per aging condition (temp/time)

The table is self explanatory and the average SD value of 5.58 is that shown in Figure 5.35 by the white dot for Alloy A at the 170°C aging temperature. It should be noted here that the UTS, YS and %El values obtained for each aging condition and their respective standard deviations are shown individually for each aging time/temperature condition studied.

As will be observed from Figure 5.35, the greatest standard deviations with respect to UTS are exhibited by the alloys containing micro-particulates; also, the variations are more accentuated for the temperatures where the maximum strength values were observed, i.e. at 155°C, 170°C, and 190°C. This behavior can be corroborated by comparing the tables and diagrams in the appendix section showing the average mechanical properties and standard deviation values for all alloys studied, where the higher standard deviation values may be observed for the properties pertaining to alloys B and C.

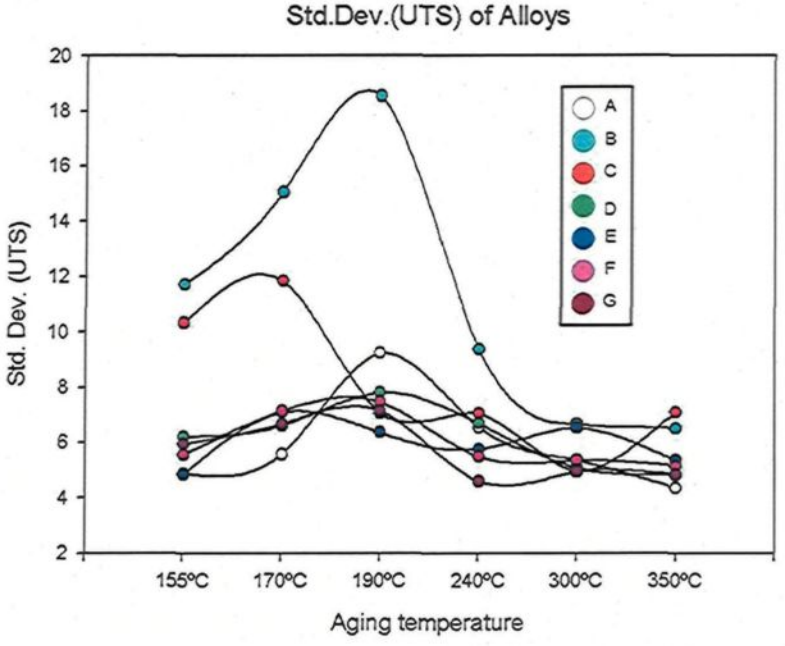

Figure 5.35 Mean standard deviation of the UTS values observed for the seven alloys studied, over the 13 aging conditions applied in this research.

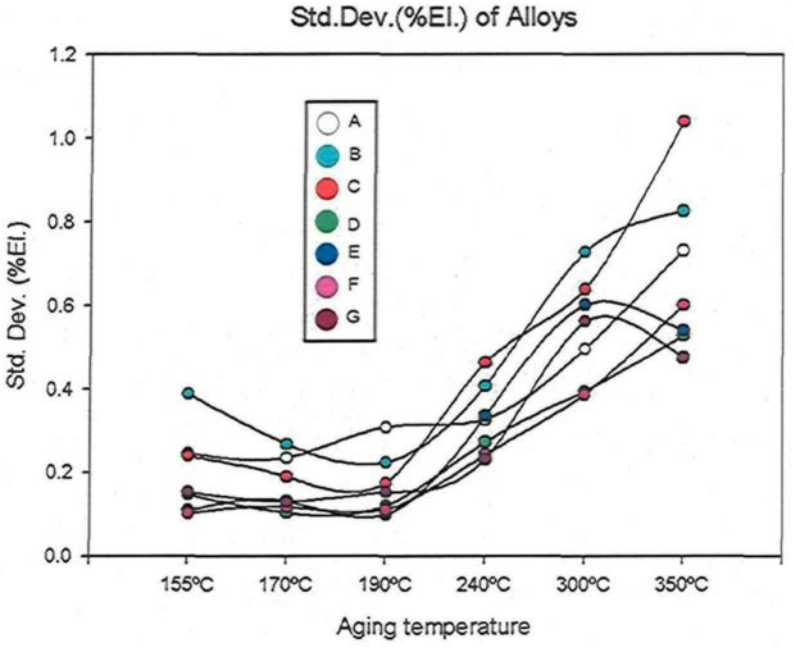

Figure 5.36 Mean standard deviation of the %Elongation values observed for the seven alloys studied, over the 13 aging conditions applied in this research.

In Figure 5.36, the maximum standard deviations correspond to the maximum ductility values, observed at 155°C and 350°C for alloys containing micro-oxides/carbides. In both Figures 5.35 and 5.36, the tensile test values corresponding to these two temperatures show the highest standard deviations, particularly for alloys B and C, when the seven alloys used in this study are subjected to comparison.

All the diagrams of alloys containing the micro-particulates Al_2O_3 and SiC show abrupt changes in their tensile test results and their standard deviations as the aging times and aging temperatures vary. These fluctuations, observed mainly in relation to the UTS and %Elongation values, are due principally to the occurrence of such defects as porosity and segregation. As was shown in Figure 5.9, segregation of particulates was observed in a number of analyzed samples. This segregation has the potential for creating unstable plastic

zones thereby reducing ductility, and contributing to an increase in porosity. The increase in the porosity of alloys B and C was observed to be approximately 20 pct more than it was for the base alloy, which may be the result of an artifact of the casting procedures.

During the melt treatment procedures, the addition of the particulates Al_2O_3 and SiC was effectuated with master alloys whose microstructures are illustrated in Figures 3.5 and 3.6. Settling or *sedimentation* of the micro-oxides/carbides to the bottom of the melt normally occurs during the remelting stage once the melt material from the master alloys reaches the mushy zone.[59,63-69,71,141] As the temperature rises, the sedimentation increases with the increasing fluidity of the molten metal; the upper regions of the melt may became denuded of microparticles, which could then lead to a wide disparity in melt viscosity and temperature in various parts of the melt. It was thus essential that mechanical stirring be commenced as soon as the master alloy was incorporated into the melt, with manual stirring being carried out for very short periods of times both prior to and after casting, when no mechanical stirring was done. During the casting procedures, manual stirring was carried out only on alloys B and C; it is clear that this factor contributed to the increased porosity observed in the microstructures.

The SDAS of 25 μm obtained for the microstructures of the tensile test samples is an indication of the high solidification rate obtained when the permanent mold was used for casting. The cooling rate for a SDAS value of 25 μm can be calculated by applying the equations to be found in Figure 4.3, giving a value of $34°Csec^{-1}$ for the cooling rate, which may be considered a high cooling rate. Higher cooling rates promote the homogeneous distribution of the SiC/Al_2O_3 particles which then subsequently results in higher strength

parameters, particularly in the case of such particulate reinforced Al-Si-Mg composites.[63,66-71,73]

In spite of applying manual and mechanical stirring techniques, and the high solidification rate provided by the permanent mold, it was difficult to control the homogeneous distribution of the micro-oxides/carbides, namely Al_2O_3 and SiC, as evidenced by the high standard deviation observed for the percentage area values of these particulates listed in Table 5.3.

5.5 Alloy D (Effects of 0.4 wt. pct. Ni)

Figure 5.37 shows the color-contour chart of the yield strengths exhibited by alloys A and D as a function of aging temperature and time.

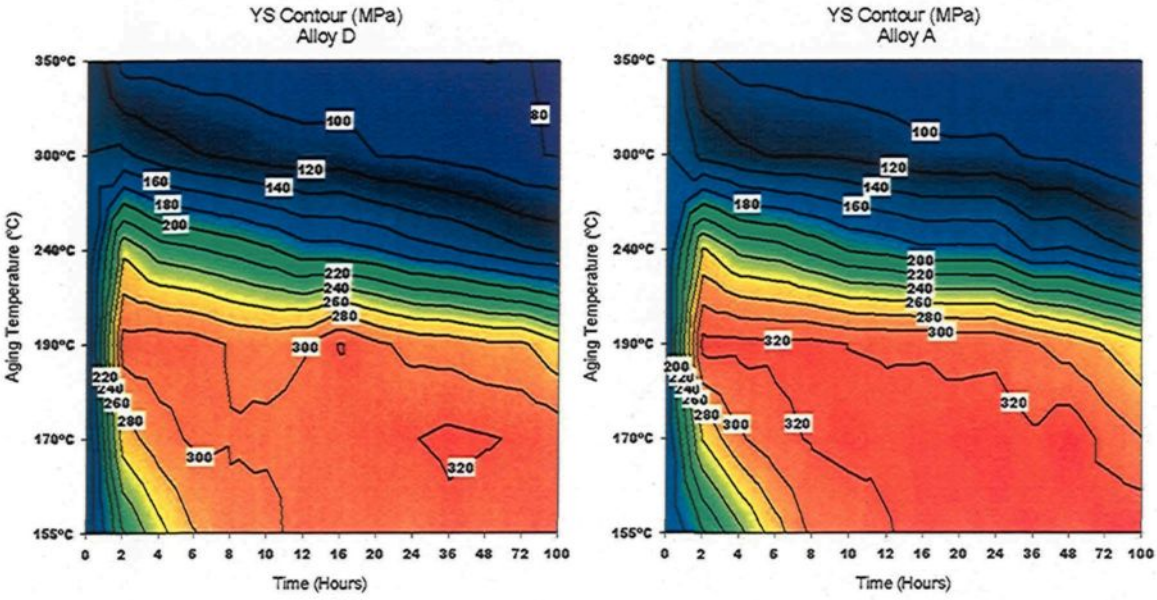

Figure 5.37 Yield Strength color-contour charts for alloys A and D corresponding to different aging conditions.

On comparing the two color-contour charts shown in the figure, a loss of strength in alloy D will be observed, as indicated by the lower intensity of color of the chart to the right. The magnitude of the decrease in strength is approximately 20 MPa in some areas of the chart.

Figure 5.38 shows the YS values for alloys A and D at aging temperatures of 155°C and 350°C, which represent the extreme ends of the range of aging temperatures used for these alloys. A decrease in yield strength as a result of the addition of nickel is noted at the aging temperature of 155°C, of the order of 20 MPa. In contrast, no appreciable difference in the YS values is observed between alloys D and A at the 350°C aging temperature.

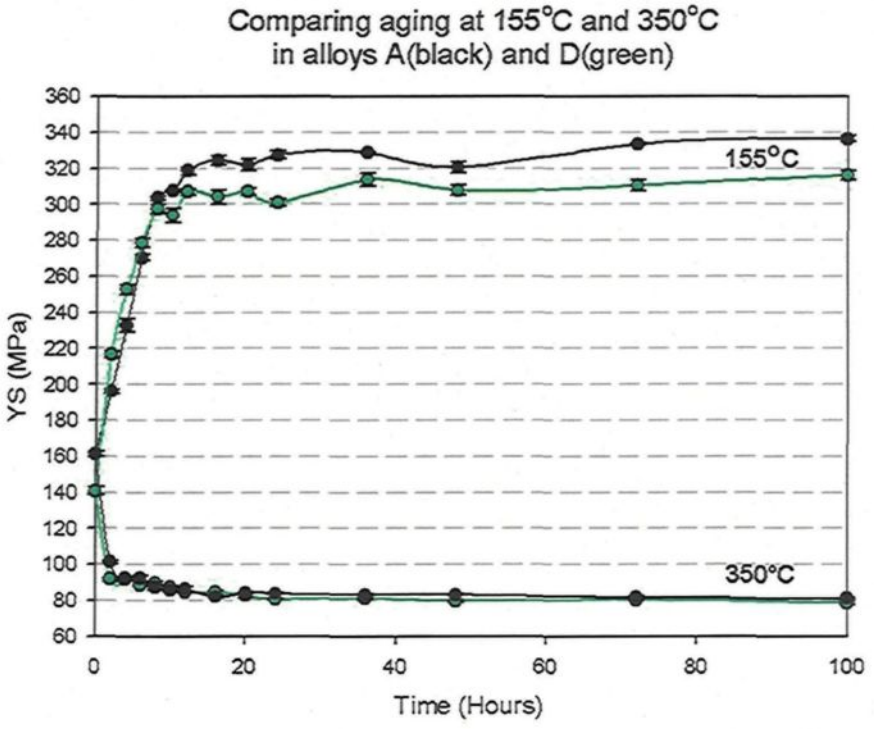

Figure 5.38 YS values plotted against aging time for aging temperatures of 155°C and 350°C for alloys A and D.

A decrease in the tensile properties of Al-Si-Cu alloys upon the addition of increasing amounts of Ni has been noted in the related literature.[91, 92, 116, 143] This decrease in strength through the addition of nickel is related to the interaction between copper and nickel to form precipitates of Al_3CuNi in the microstructure. The Al_3CuNi phase was detected in the thermal analysis experiments which were carried out on alloys containing nickel, namely alloys D, F, and G. Since copper, as well as magnesium, determine the precipitation strengthening of Al-Si-Cu-Mg alloys, the available copper would form Al_2Cu precipitates through the solution heat treatment/quenching/aging process, thereby strengthening the cast alloys. The formation of Al-Cu-Ni precipitates would thus subtract part of the copper content available for strengthening; this is the principal reason for which a slight decrease in YS is observed with the addition of 0.4 wt. pct nickel.

Figure 5.39 shows the quality index chart for 20 selected heat-treatment conditions for alloy D.

Upon comparing the tensile test results of alloy D with those of the base alloy, the Quality index chart in Figure 5.39 shows a decrease in UTS values in the order of 20-35 MPa as the principal effect of nickel addition, followed by a decrease in ductility for the *low* aging-temperatures of 155°C, 170°C, and 190°C.

As was shown in the thermal analysis experiments discussed in Chapter 4, nickel interacts with iron and copper forming the Al_9NiFe and Al_3CuNi phases; such phases would then act as stress concentrators provoking instability in the flow strain, thereby reducing ductility. As was also shown in Table 5.1, the percentage of intermetallic phases

containing nickel, from alloy A to alloy D, displayed an increase in the percentage of insoluble phases from 1.27 pct to 2.76 pct, respectively.

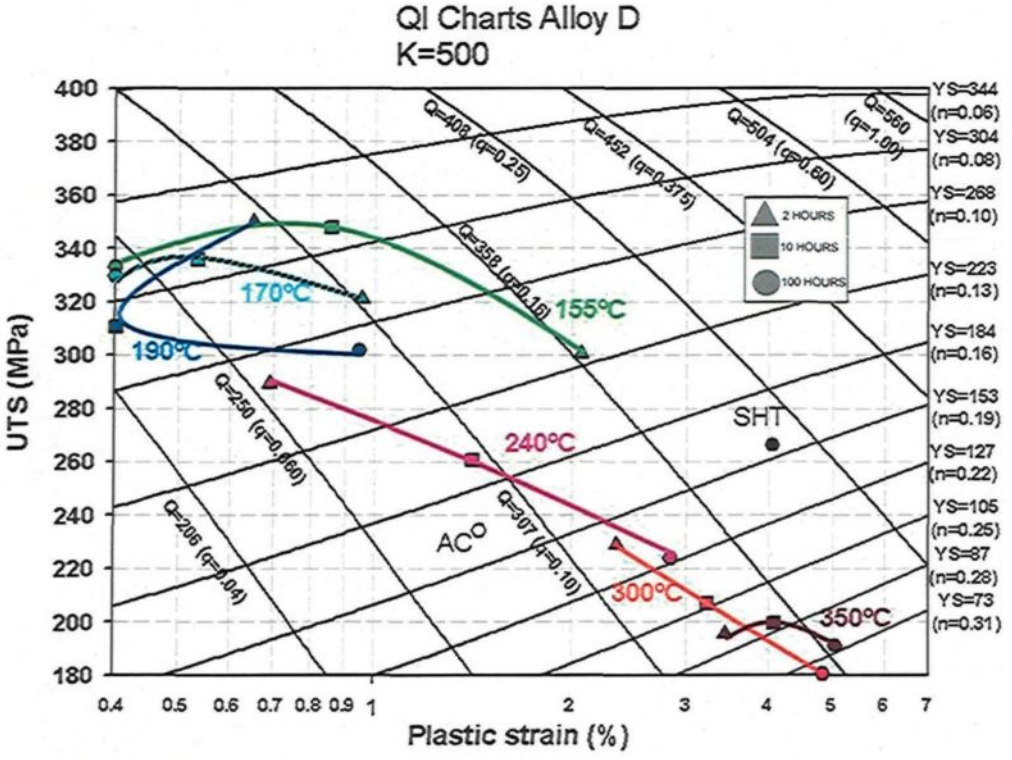

Figure 5.39 Quality index chart for alloy D corresponding to various heat treatment conditions.

With regard to the base alloy, as well as alloys B, C, and D, the maximum strength is reached at *low* aging-temperatures ranging from 155°C to 190°C, showing a decrease in ductility with the increase in strength; it should be noted that this is the expected behavior for Al-Si-Cu-Mg alloys. [33, 34, 95, 113, 137] It will also be observed that, at *low* aging-temperatures, the effect of intermetallics on the reduction of ductility is more pronounced than it is at the *high* aging-temperatures of 240°C, 300°C, and 350°C. The increase in ductility at an aging-temperature of 190°C, or more, becomes evident since the alloy softens and the effect of the intermetallics on ductility seems attenuated.

These comparisons, as drawn between alloy D and alloy A, may be seen more clearly in the tensile strength values of the quality index chart shown in Figure 5.40 illustrating the long-exposure-time experiments. Figure 5.40, as well as Figures 5.37 through 5.39, summarize the effects of 0.4 wt. pct nickel on the mechanical properties of the 354 alloy. The reduction in strength occurs principally due to the decrease in the available copper for precipitation strengthening in relation to the formation of Al_3CuNi, while an increase of the intermetallics Al_3CuNi and Al_9NiFe is responsible for the reduction in ductility.

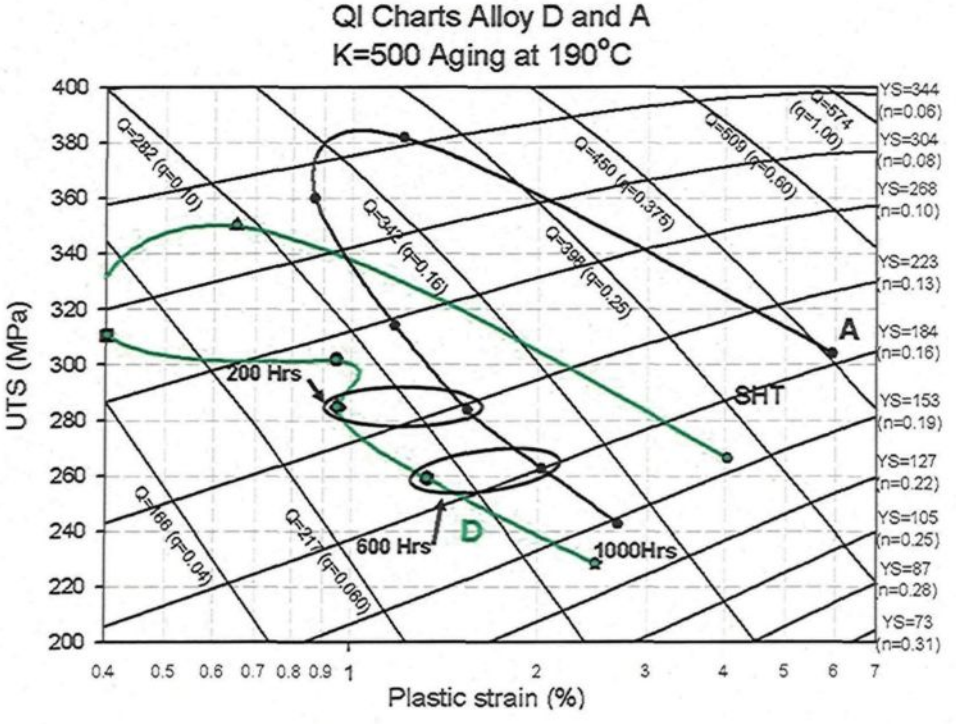

Figure 5.40 Quality Index chart obtained for alloys D and A for long exposure times at 190°C aging-temperature.

5.6 Alloy E (Effects of 0.4 wt. pct. Zirconium)

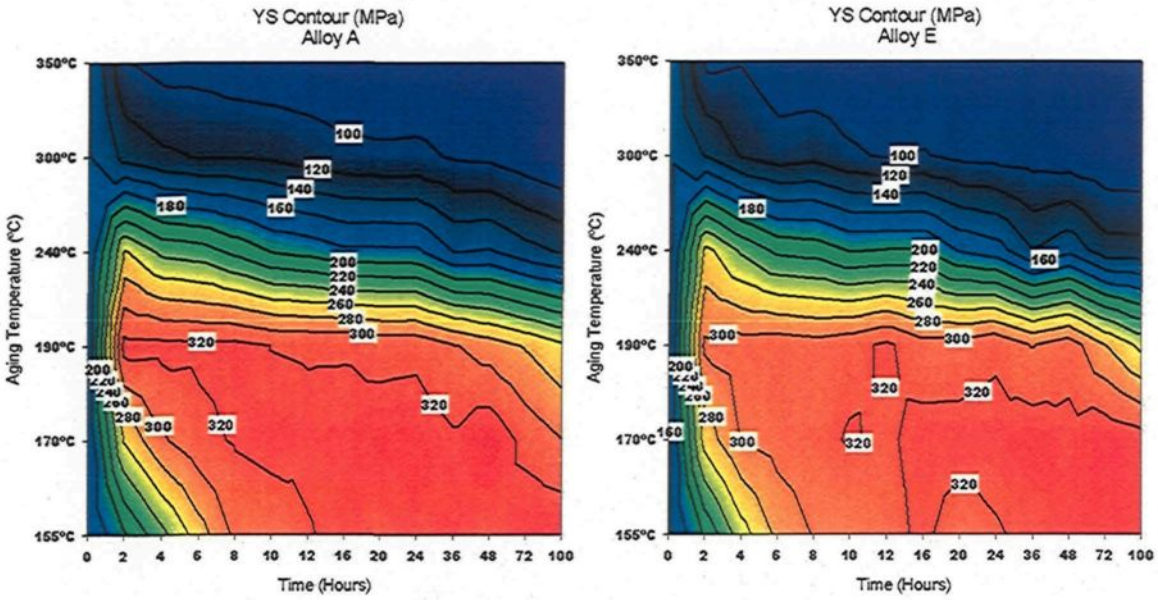

Figure 5.41 YS color-contour charts for alloys A and E.

Figure 5.41 shows the color-contour charts of yield strength as a function of aging time and aging temperature for alloys A and E.

Figure 5.42 shows the variation in YS values for alloys A and E as a function of aging time at the aging temperatures of 155°C and 350°C, the solution heat treatment condition corresponding to zero aging time.

From Figures 5.41 and 5.42 it is observed that alloy E, containing 0.4 wt pct Zr, does not show any significant change in YS, when compared to the base alloy. The strain contour charts in Figure 5.43 show the percentage elongation values exhibited by alloy A and alloy E at the aging temperatures and aging times studied.

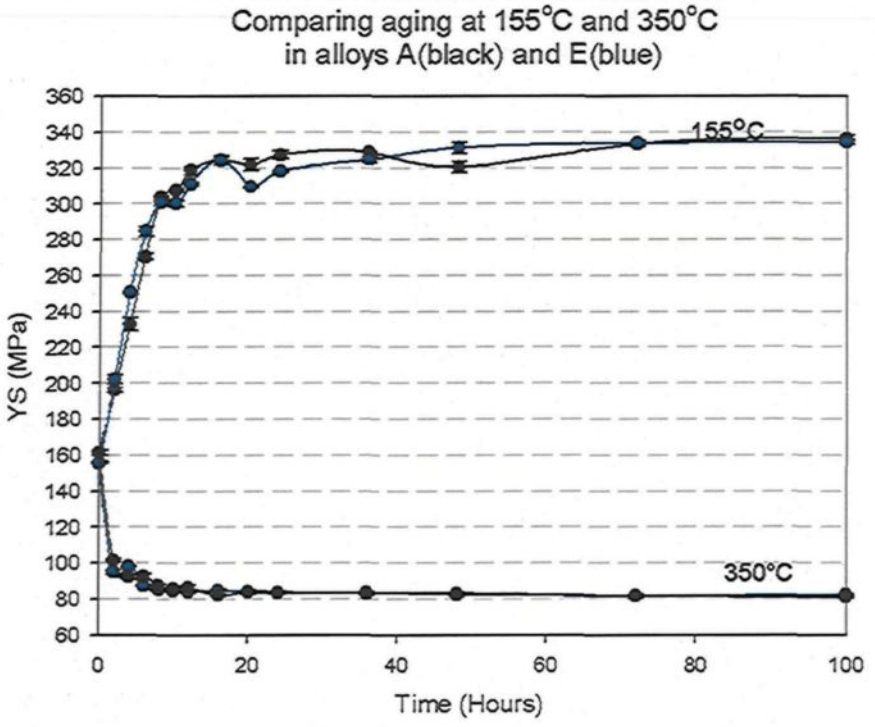

Figure 5.42 YS values plotted against aging time for aging temperatures of 155°C and 350°C for alloys A and E.

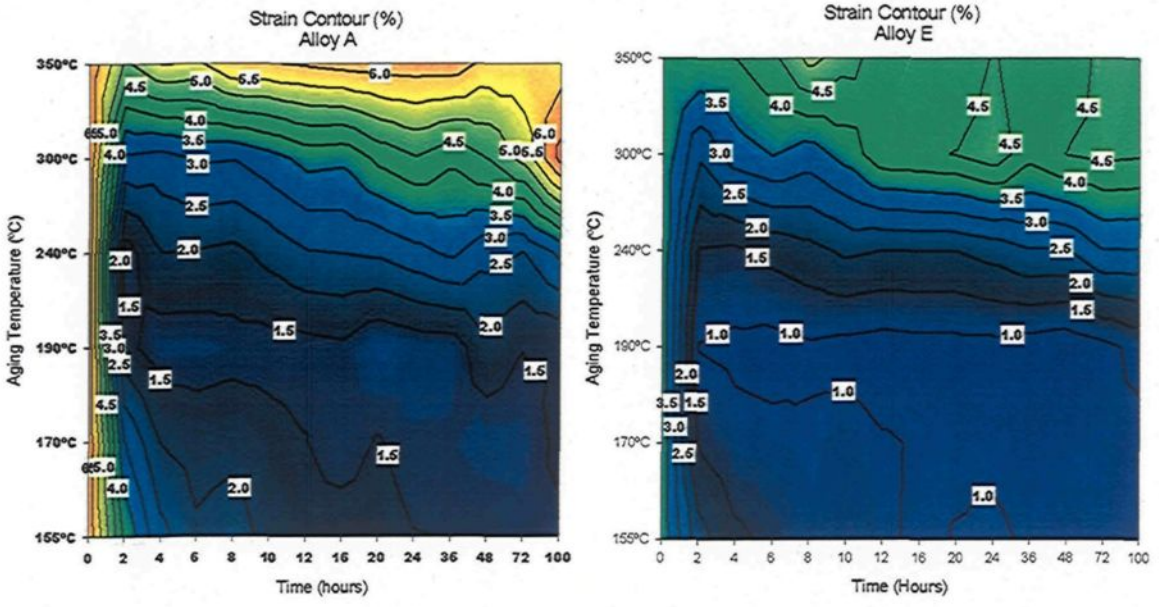

Figure 5.43 Strain color-contour charts for alloys A and E, showing the %El values obtained at various aging temperatures and times.

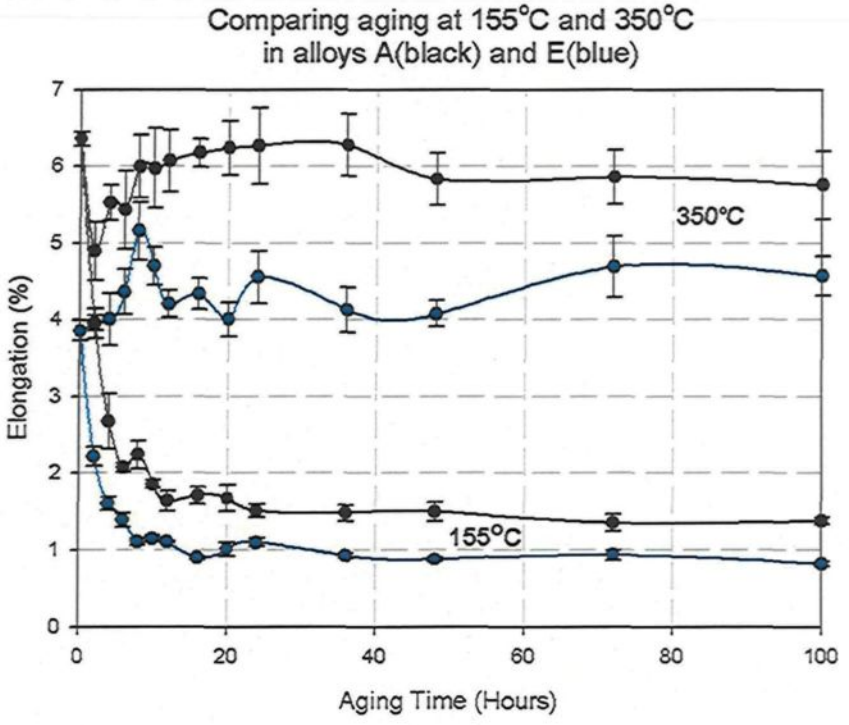

Figure 5.44 Percent elongation values plotted against aging time for aging temperatures of 155°C and 350°C for alloys A and E.

Contrary to the behavior displayed by the YS for alloy E, Figures 5.43 and 5.44 show notable differences displayed by the strain with regard to the base alloy. Since ductility as well as UTS decreases, the quality index also decreases, particularly at the *low* aging-temperatures of 155°C through 190°C, as may be observed in the quality index chart shown below in Figure 5.45 for alloy E for the 20 selected aging conditions. Even if the strength displayed by alloy E did not show any significant difference during aging with respect to the base alloy, ductility and quality index values were reduced principally at the *low* aging temperatures.

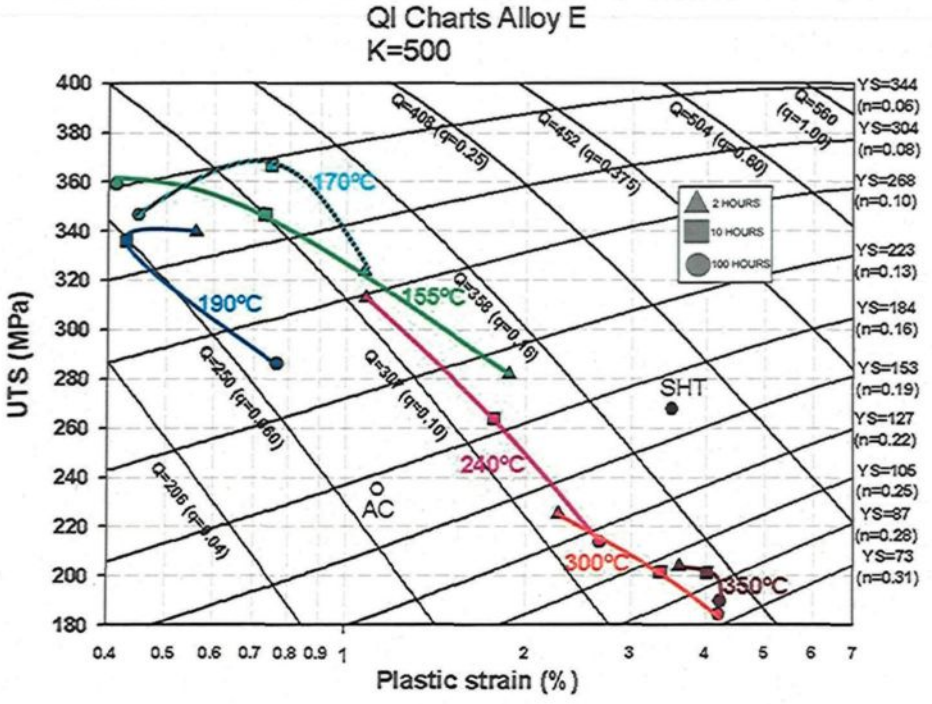

Figure 5.45 Quality index chart for alloy E corresponding to various heat treatment conditions.

The decrease in the ductility of alloy E with respect to alloy A may be assimilated by observing Table 5.1 where the level of insoluble intermetallics increases from 1.27 to 2.86 pct, between the base alloy and alloy E, respectively. This behavior may also be seen in Figure 5.46 for the long-exposure-time experiments at the aging temperature of 190°C.

In general terms, and as shown in Figures 5.41 through 5.45, there is no appreciable increase in strength (UTS and YS) to be observed in alloy E containing 0.4 wt. pct. zirconium, although there is, however, a visible decrease in ductility which is greater than 20 pct. for nearly all of the tests performed.

Figure 5.46 shows the quality index chart for the long-exposure-time experiments at 190°C aging temperature, illustrating the major effects of adding 0.4 wt. pct. Zr to the 354

alloy. The results of the addition involved a loss of ductility due to an increase in the intermetallics affecting the quality index values principally at low aging-temperatures, although there was no concomitant increase in strength observed in this case.

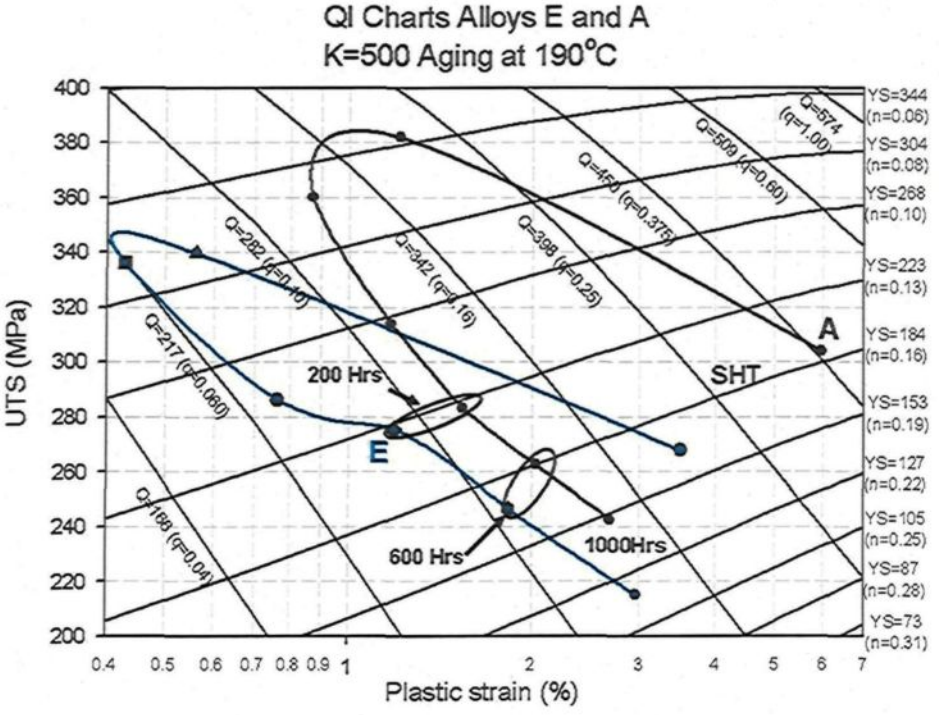

Figure 5.46 Quality index chart obtained for alloys E and A for long-exposure times at 190°C aging temperature.

The limited amount of research work which has been carried out on the casting of aluminum alloys with zirconium additions shows that a reduction of the grain size as well as an increase in the strength of alloy E with respect to the base alloy is to be expected.[78-80, 82, 83] While the addition of 0.4 wt. pct. Zr did indeed reduce the grain size, no increase in the resistance of alloy E was to be observed.

To understand the latter observation, it is necessary to consider three characteristics observed from the microstructural analysis of alloy E. Firstly, the amount of insoluble

intermetallic phases increased from 1.27 pct in the base alloy to 2. 86 pct. in alloy E. Secondly, grain size was reduced from 200 μm in alloy A to 120 μm in alloy E. Both arguments could indicate that the Zr available for strengthening was used to form large intermetallics in the form of $(Al,Si)_3(Zr,Ti)$ phases, as well as to reduce the grain size. Finally, a third aspect which should be taken into consideration is that during the casting procedures, the temperature of the melt was maintained at 760°C, implying that Zr added in the form of Al-20%Zr master alloy was not capable of dissolving completely; this is due to the fact that, at 0.4 wt. pct. zirconium, the Al-Zr phase diagram indicates the *liquidus* temperature at 780°C.[125]

5.7 Alloy F (Effects of 0.4 wt. pct. Zr + 0.4 wt. pct. Ni)

Figure 5.47 shows the color-contour charts of the yield strengths exhibited by alloys A and F as a function of aging temperature and time, while Figure 5.48 compares the variation in YS with aging time at 155°C and 350°C aging temperatures for the two alloys.

As may be observed from Figures 5.47 and 5.48, there are no discernible changes in yield strength for alloys A and F. This behavior is different from that displayed by alloy E containing 0.4 wt. pct. Ni. As was mentioned earlier in Chapter 4, part of the copper available for the strengthening of alloy E interacted with the nickel forming the Al_3CuNi phase, as was observed in the thermal analysis experiments; because of this, alloy E revealed a slight decrease in yield strength values when compared to those shown by the base alloy.

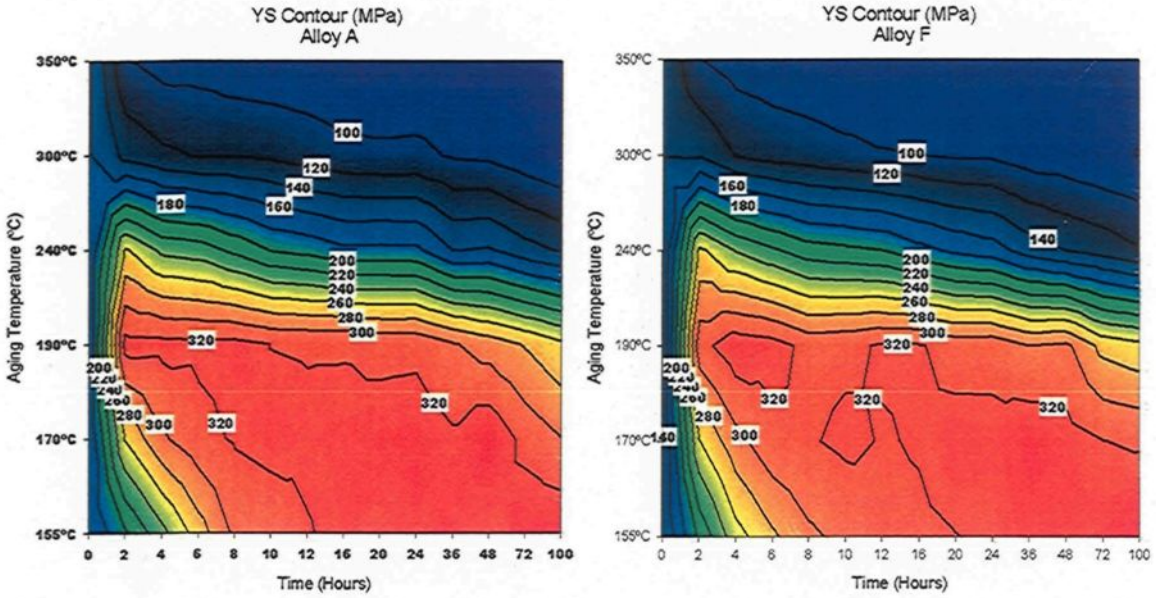

Figure 5.47 YS color-contour charts for alloys A and F.

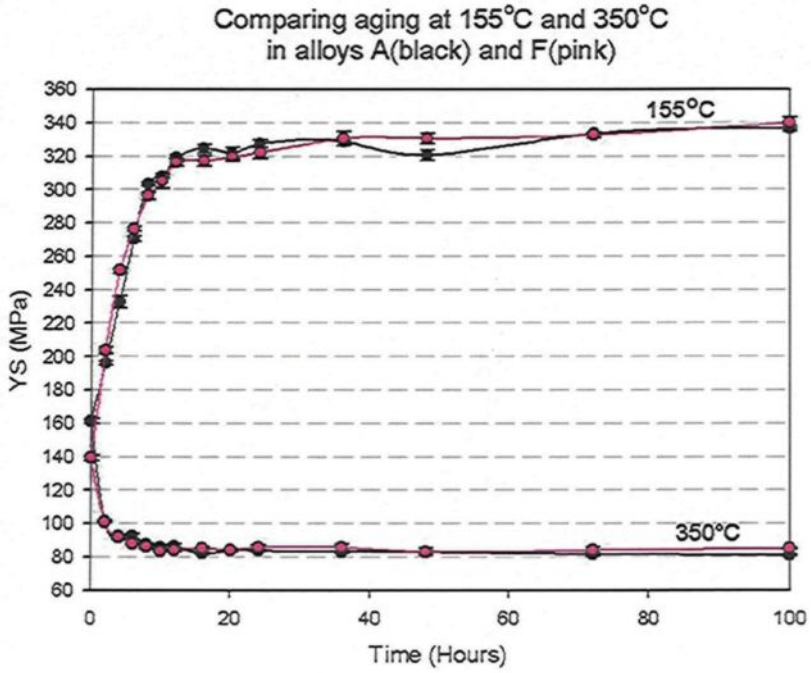

Figure 5.48 YS values plotted against aging time for aging temperatures of 155°C and 350°C for alloys A and F.

As a result of examining the negative effects of nickel on the strength of alloy E, it becomes relevant to discuss why the addition of nickel did not reduce the yield strength in alloy F which contains 0.4 wt. pct. nickel plus 0.4 wt. pct. Zr. With regard to the thermal analysis investigations described in Chapter 4, Figure 4.14 shows the $(Al,Si)_3(Zr,Ti)$ phase with the Ni-rich phase Al_9NiFe adhering to it. Such Al_9NiFe phase particles were observed in the microstructure of tensile samples, as well as phases which appeared similar to the Ni-rich phase were observed to adhere to the Zr-rich phases in the microstructures of the tensile samples of alloy F. This type of Ni-rich phase resembles the Ni-rich phases of the master alloy Al-20%Ni, as used in this work and shown in Figure 3.7. These observations suggest that the copper did not interact with the nickel to form Al_3CuNi phases, and as a result, the copper was free to strengthen alloy F, in the same way as the copper was able to strengthen alloy A.

Figure 5.49 shows the strain color-contour charts exhibited by alloys A and F, while Figure 50 compares the variation in percent elongation with aging time at 155°C and 350°C aging temperatures. As may be seen, the ductility seems to be affected principally at the *low* aging temperatures of 155°C through 190°C. This decrease in ductility may be interpreted by noting that alloy F had the greatest amount of insoluble phases as listed in Table 5.1; these would then act as stress concentrators during flow stress, thereby limiting the ductility in alloy F.[144, 145]

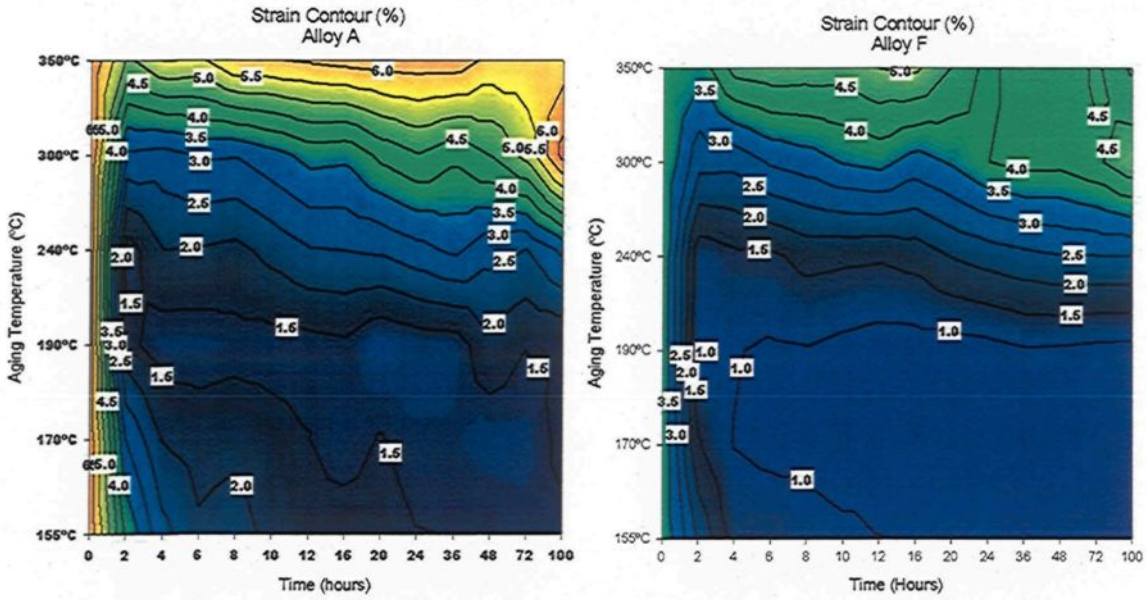

Figure 5.49 Strain color-contour charts for alloys A and F, showing the %El values obtained at various aging temperatures and times.

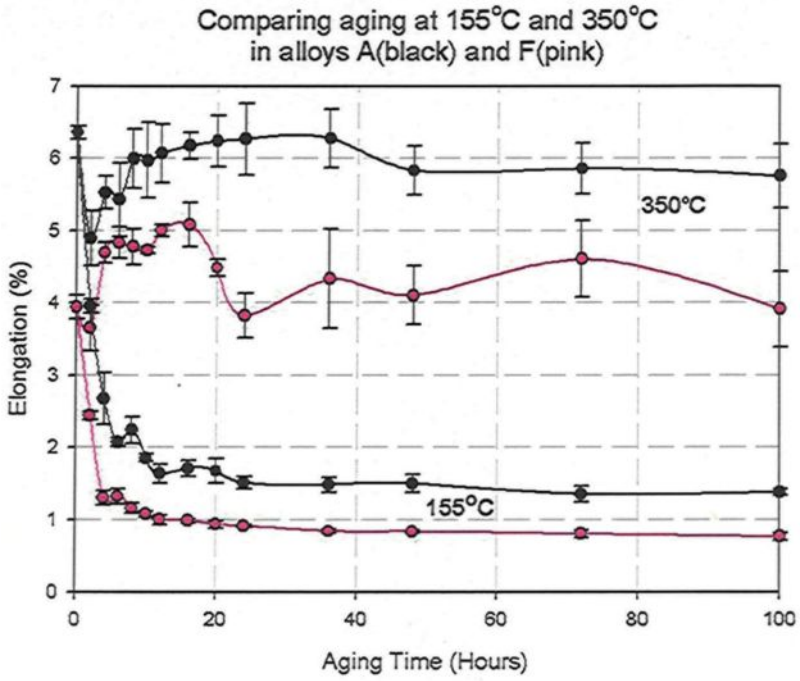

Figure 5.50 Percent elongation values plotted against aging time for aging temperatures of 155°C and 350°C for alloys A and F.

Figure 5.51 shows the quality index chart for alloy F obtained for various aging temperatures and aging times of 2, 10, and 100 hours. It is observed in this figure that the decrease in ductility affects the quality index principally at *low* aging temperatures where alloy F performs at maximum strength. In Figure 5.52, which compares the quality index values of alloys A and F, it is observed that while the tensile strength values of alloy A follow a progressive "contour" curve, which seems to be uniform up to the point where there is an increase in aging time, alloy F values, on the other hand, display an abrupt decrease in UTS beyond 200 hours at 190°C.

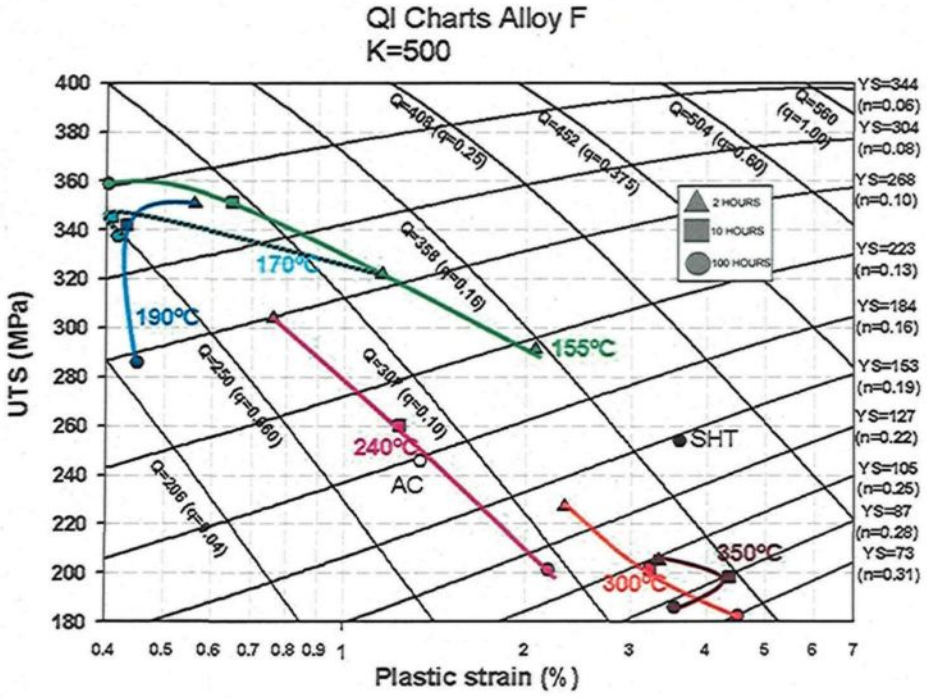

Figure 5.51 Quality index chart for alloy F.

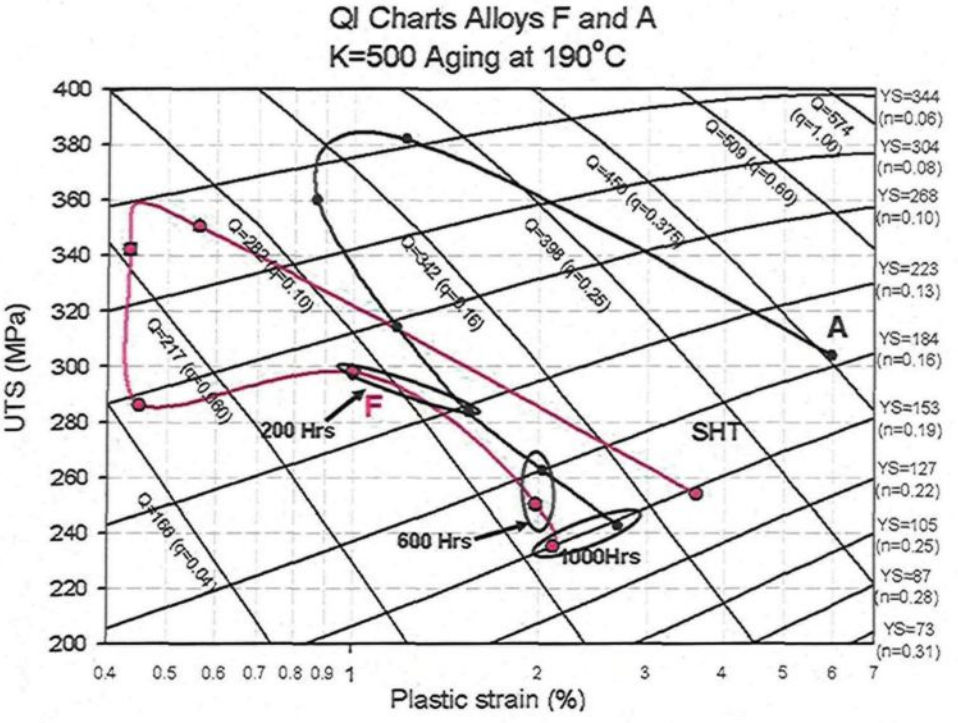

Figure 5.52 Quality index chart obtained for alloys F and A for long exposure times at 190°C aging-temperature.

5.8 Alloy G (Effects of 0.2 wt. pct. Zr + 0.2 wt. pct. Ni)

Figure 5.53 shows the color-contour chart of the yield strengths exhibited by alloys A and F as a function of aging temperature and time, while Figure 5.54 compares the variation in YS with aging time at 155°C and 350°C aging temperatures for the two alloys. Yield strength values display a slight increase of approximately 20 MPa, as will be observed in particular zones of the YS color-contour charts in Figure 5.53, taking the mechanical values of the base alloy as a reference. As may be seen from Figure 5.54, Alloy G is the only alloy in this research which shows an increase in strength in comparison with alloy A. In fact, even at the aging temperature of 350°C, the strength values are observed to be greater than those obtained with the base alloy.

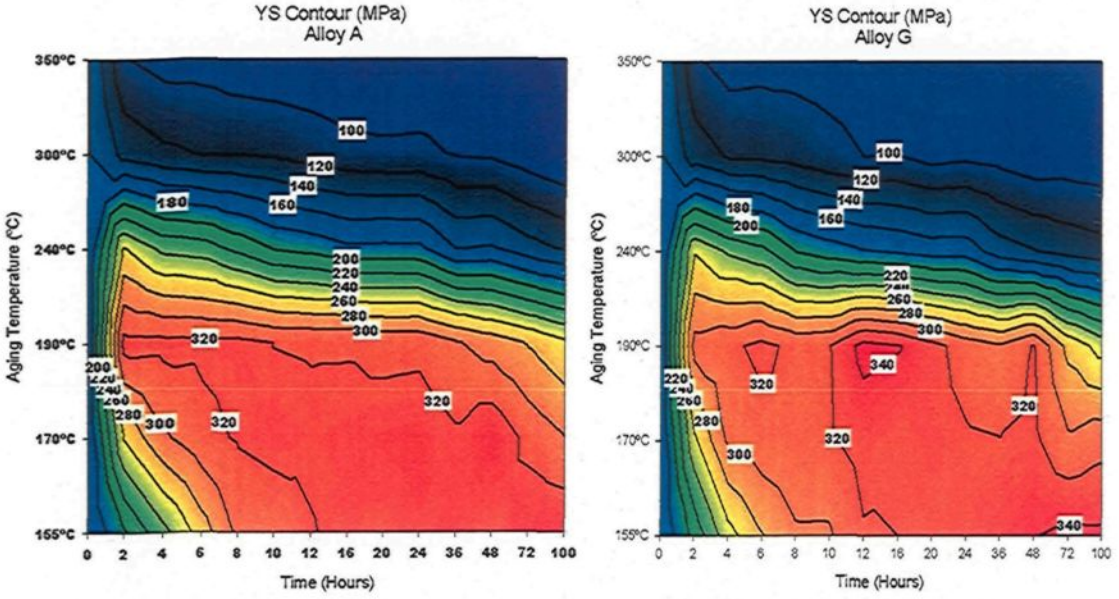

Figure 5.53 YS color-contour charts for alloys A and G.

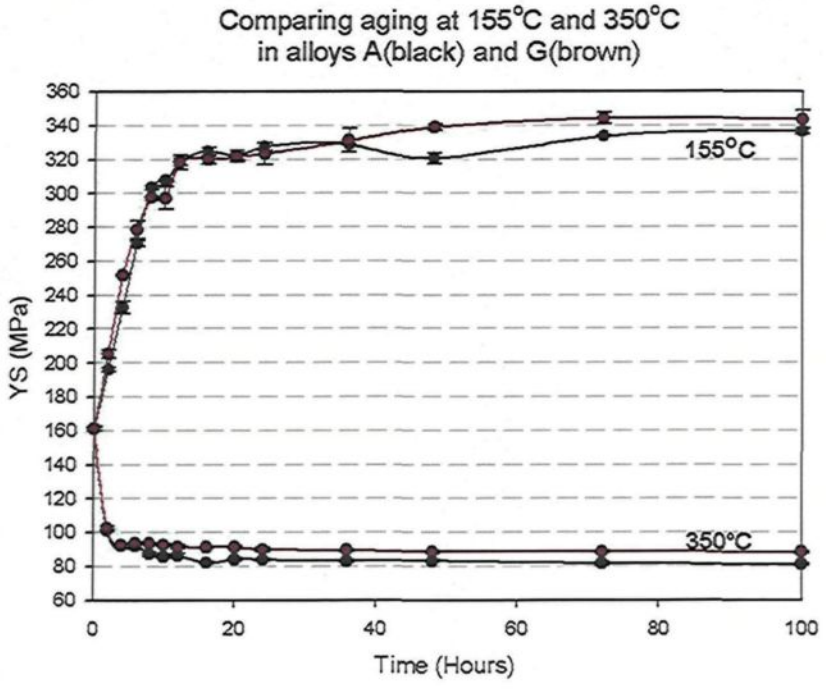

Figure 5.54 YS values plotted against aging time at aging temperatures of 155°C and 350°C for alloys A and G.

Alloy G, containing 0.2 wt. pct. Zr and 0.2 wt. pct. Ni, displays greater strength than alloy E, which contains 0.4 wt. pct. Zr, or greater even than alloy F, which contains 0.4 wt. pct. Zr plus 0.4 wt. pct Ni. The major difference which emerges upon examining the Zr-content of alloys E, F, and G, involves the fact that alloy G is a hypoperitectic alloy,[127] as mentioned previously in Chapter 4. According to the Al-Zr phase diagram,[125] at 0.2 wt. pct. Zr content, the *liquidus* temperature is approximately 720°C. Taking into consideration that, during casting procedures, the temperature of the melt was maintained at 760°C, it is fairly likely that the added Zr dissolved completely. Having a completely dissolved Zr-master alloy in the melt would be the first step in obtaining a strengthening of the alloys by means of Zr-rich precipitates. This argument is congruent with the percentage of insoluble phases observed, which displays smaller values upon comparison with the alloys containing additions of nickel and/or zirconium, namely alloys D, E, and F.

Figure 5.55 shows the quality index chart for the 20 selected heat treatment conditions for alloy G. In this figure, the general mechanical behavior of alloy G appears to be similar to that of the base alloy at aging temperatures above 190°C. Based on the comparison of the tensile properties between alloy G and the base alloy A, it will be observed that, below aging temperatures of 240°C, the quality index of alloy G decreases.

This behavior may be ascribed to the fact that the decrease in ductility, which is on the order of a 20 pct. reduction, is more substantial than the slight increase of YS and UTS values observed at *low* aging temperatures.

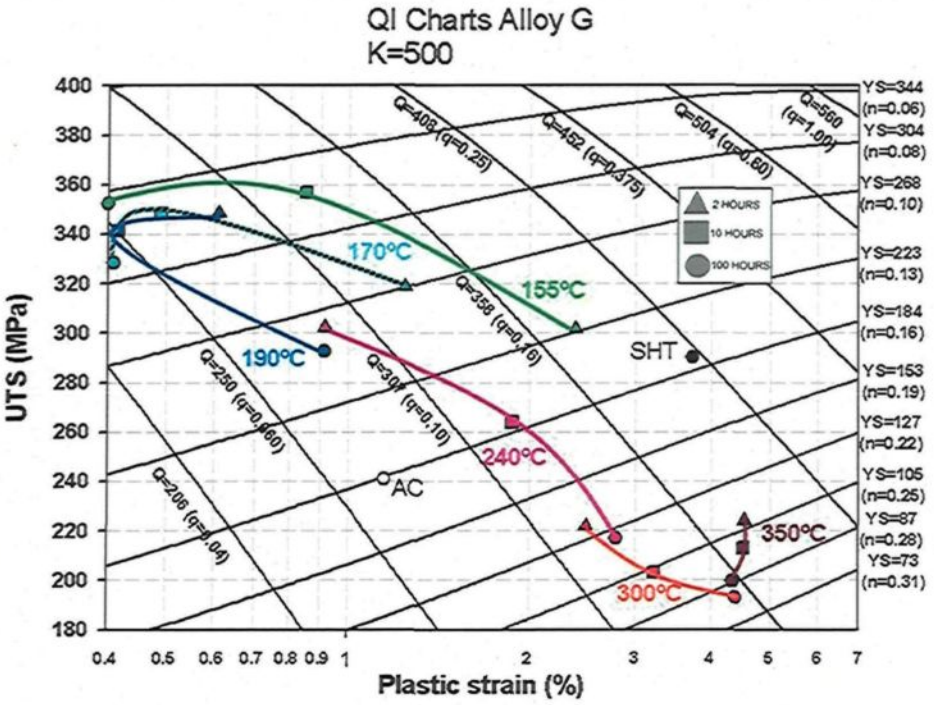

Figure 5.55 Quality index chart for alloy G.

Figure 5.56 shows the quality index chart for the prolonged exposure experiments at the aging temperature of 190°C. This chart compares the tensile values for UTS, YS, plastic strain, and quality index of the alloys G and A. It is observed in Figure 5.55 that, at higher strength values, the ductility decreases as the strength increases. Once the alloy softens through the application of an aging time of over 200 hours, the tensile properties of alloy G tend to display a greater similarity with the mechanical properties of the base alloy.

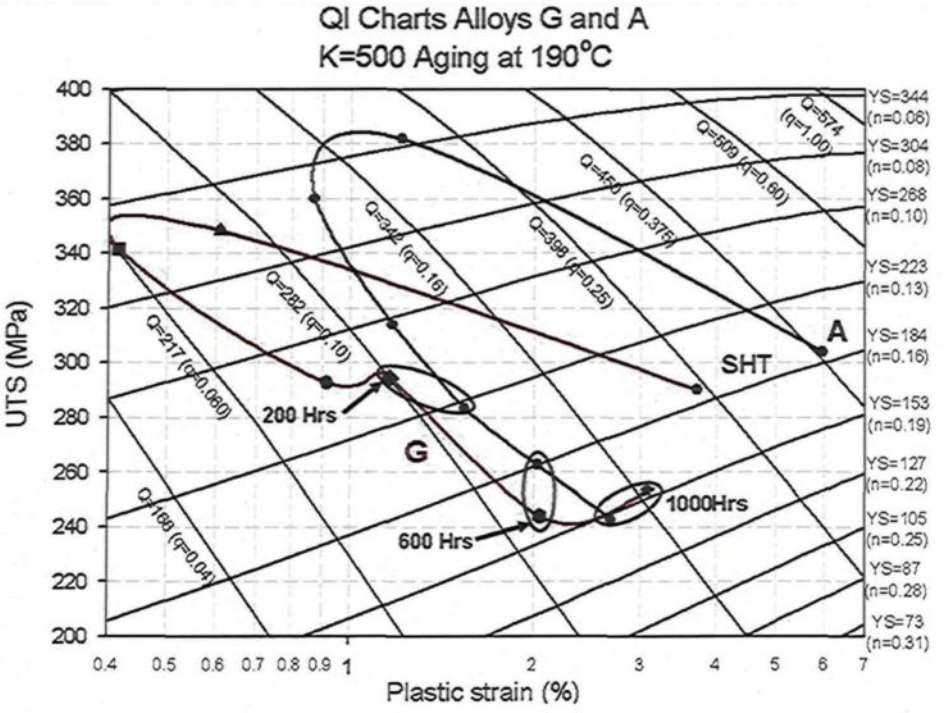

Figure 5.56 Quality index chart obtained for alloys G and A for long exposure times at 190°C aging temperature.

5.9 The Obtainable Quality Parameter ($Q_{Obtainable}$)

Upon examining the tensile properties of the alloys used in this research, the as-cast condition could be considered the point of reference of the heat treatments applied, since the quality index values for this condition indicate minimum values considering the entire series of heat treatments applied. With regard to alloys A through G, even if the minimum quality index values do not always correspond to the as-cast condition, they are, however, close to the as-cast quality index values, despite the considerable loss in strength due to overaging. On the other hand, as was mentioned in subsections 5.3 to 5.7, even if the strength was developed to a great extent, specifically at *low* aging temperature conditions, the quality index values reached their maximum in the solution heat-treated condition.

Based on these arguments, it is possible to suggest that, in alloys A through G for all the aging conditions investigated, the quality index values fluctuate between the as-cast (AC) and the solution heat-treated (SHT) conditions. The quality index chart for the seven alloys investigated is presented in Figure 5.57, for AC and SHT conditions.

By taking the above considerations into account, it is possible to assume that the maximum obtainable quality index values by means of heat treatment is the difference between the quality index values for the AC and SHT conditions. Table 5.11 shows these differences occurring between the quality index values obtained by applying Equation 2.9 to the seven alloys used in this project.

Figure 5.58 shows the $Q_{obtainable}$ parameter as obtained from Table 5.11 plotted against grain size. The figure summarizes the principal conclusions observed concerning the addition of elements/micro-particulates to alloy 354 in relation to the heat treatments applied: the obtainable quality is observed to decrease as the percentage of intermetallic or micro-particles is increased, so that the major effect of the addition of Zr lies in reducing the grain size rather than in increasing the quality index values.

Table 5.11 Obtainable Q parameters observed for the alloys used in this study

Alloy	$Q(Eq.2.9)_{AsCast}$	$Q(Eq2.9)_{SHT}$	$Q_{Obtainable}$
A	278	453	175
B	282	402	120
C	304	421	117
D	273	374	101
E	250	355	105
F	259	372	113
G	255	403	148

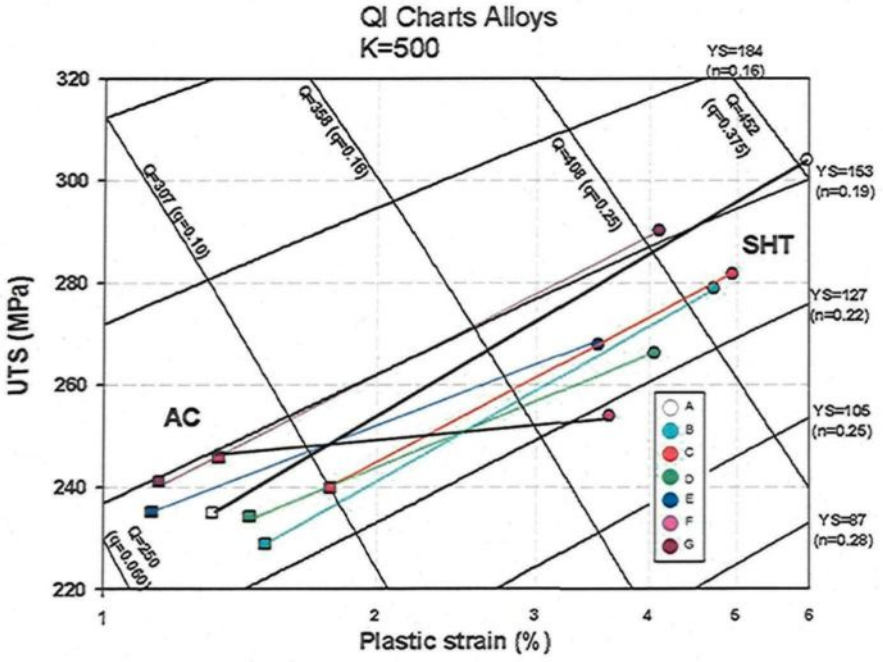

Figure 5.57 Quality index chart for the alloys A, B, C, D, E, F, and G corresponding to as-cast and solution heat treated conditions.

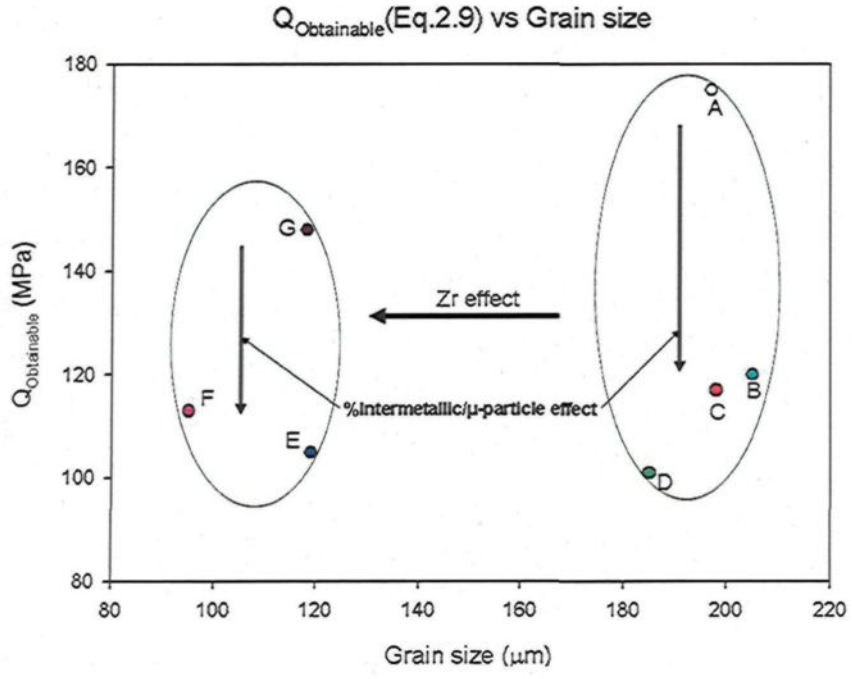

Figure 5.58 Obtainable Q parameter (MPa) plotted against grain size (μm).

5.10 High Temperature Tensile Tests

Tensile tests at different temperatures were performed to acquire knowledge of the effect of the additions of zirconium and nickel on the high temperature mechanical performance of the 354 cast aluminum alloy. Alloys B and C were not tested at high temperatures since such alloys did not seem to be promising alloys to be used at high temperature, as was evidenced by the high variability in their tensile properties at room temperature, reflected in the high standard deviations values observed for said properties.

Two conditions were selected for the experiments at elevated temperatures: the as-cast (AC) condition, and the T6 condition which corresponds to the maximum strength aging condition observed for the room temperature tensile results, *viz.*, 190°C/2hrs, for the alloys A, D, E, F and G alloys. For the T6 condition the temperatures selected for the tests were 25°C, 190°C, 250°C and 300°C while for the as-cast condition (AC) the temperatures were 25°C, 190°C and 300°C.

Table 5.12 shows the UTS values obtained at different test temperatures in a 354 alloy which has a chemical composition similar to that of the base alloy used in this research. These values, taken from Reference 88 are plotted together with those exhibited by alloy A for the purpose of comparison. Table 5.13 lists the tensile properties of all the experiments at ambient and at elevated temperatures.

Table 5.12 Tensile properties of Alloy 354-T6 (from Reference 88)

Identification	Test Temperature	UTS (MPa)
354-T6	24°C	380
354-T6	205°C	290
354-T6	260°C	195
354-T6	315°C	90

Figure 5.59 compares the UTS values displayed by the experiments in this study with those from Reference 88; even if there are slight differences in the temperature of the tests in both sets of experiments, a similar behavior is evidenced for alloys A-T6 and 354-T6 with respect to the strength displayed. Also, alloy A displays a more pronounced decrease in strength in the T6 condition than in the AC condition as the test temperature is increased from ambient to below 300°C; at 300°C the UTS values are quite similar for both AC and T6 conditions.

Table 5.13 Tensile properties values at different test temperatures

Identification Alloy/Condition	Test Temperature	UTS (MPa)		YS (MPa)		Elongation (%)	
		AV	SD	AV	SD	AV	SD
A/AC	25°C	233	5.8	153	4.8	1.60	0.24
A/AC	190°C	213	7.7	170	8.2	1.45	1.14
A/AC	300°C	101	7.4	96	6.2	3.33	1.06
D/AC	25°C	231	8.1	150	2.4	1.70	0.37
D/AC	190°C	208	19.4	164	16.1	2.08	1.01
D/AC	300°C	98	15.6	87	14.9	3.55	0.39
E/AC	25°C	233	2.7	160	1.7	1.40	0.09
E/AC	190°C	207	4.7	145	21.1	1.41	0.44
E/AC	300°C	94	10.1	87	9.7	3.52	0.59
F/AC	25°C	220	16.6	150	7.8	1.40	0.26
F/AC	190°C	230	21.2	199	10.9	1.36	0.38
F/AC	300°C	105	9.3	97	9.1	6.44	0.64
G/AC	25°C	250	6.6	160	5.6	1.60	0.29
G/AC	190°C	216	4.3	174	6.7	1.63	0.38
G/AC	300°C	172	8.2	115	10.3	5.21	0.29
A/T6	25°C	380	6.7	327	4.3	1.66	0.24
A/T6	190°C	275	7.4	249	8.9	1.84	1.3
A/T6	250°C	213	7.2	213	7.1	3.83	0.69
A/T6	300°C	115	9.8	112	8.5	4.5	0.04
D/T6	25°C	338	1.0	309	4.0	1.50	0.04
D/T6	190°C	276	2.0	264	3.6	1.99	0.7
D/T6	250°C	204	10.4	193	9.1	3.90	0.21
D/T6	300°C	104	1.2	100	2.2	4.06	0.57
E/T6	25°C	340	5.4	305	6.7	1.50	0.04
E/T6	190°C	273	3.4	262	11.3	1.40	0.17
E/T6	250°C	221	14.3	204	7.7	3.70	1.74
E/T6	300°C	104	10.4	101	9.3	5.61	0.43
F/T6	25°C	340	6.7	313	7.5	1.51	0.12
F/T6	190°C	270	6.1	260	7.9	1.41	0.98
F/T6	250°C	209	6.4	205	5.5	4.71	2.1
F/T6	300°C	133.97	10.3	112.7	5.7	5.78	0.57
G/T6	25°C	348.2	6.7	306.1	4.3	1.51	0.13
G/T6	190°C	286.3	6.2	263.3	12.1	2.02	0.49
G/T6	250°C	229.9	5.75	223.0	20.6	4.07	0.38
G/T6	300°C	128.2	10.6	121.3	10.5	5.30	0.59

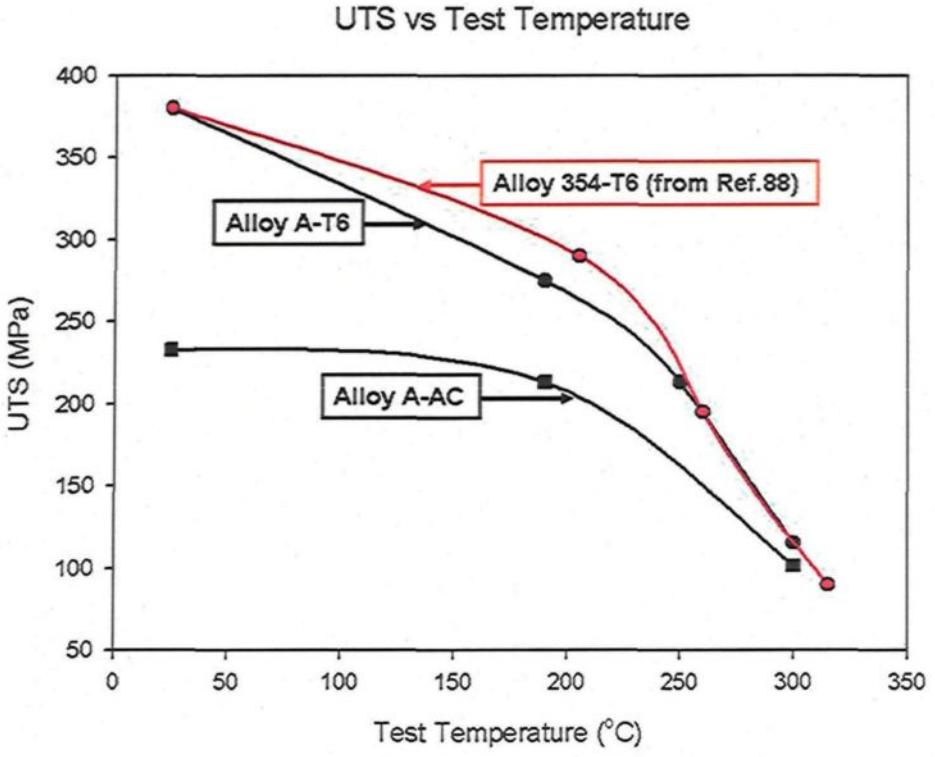

Figure 5.59 UTS values from experiments at ambient and at high temperature (Alloy A and Alloy 354 from Reference 88).

Figure 5.60 shows UTS values from ambient and high temperature tensile tests carried out for the AC and T6-treated A, D, E, F and G alloys. For the T6-treated samples, no significant difference in UTS values is observed in alloys D, E, F and G with respect to the base alloy. For the AC condition, alloys F and G display a slight increase in tensile properties among the alloys studied, particularly at 190°C and 300°C test temperatures.

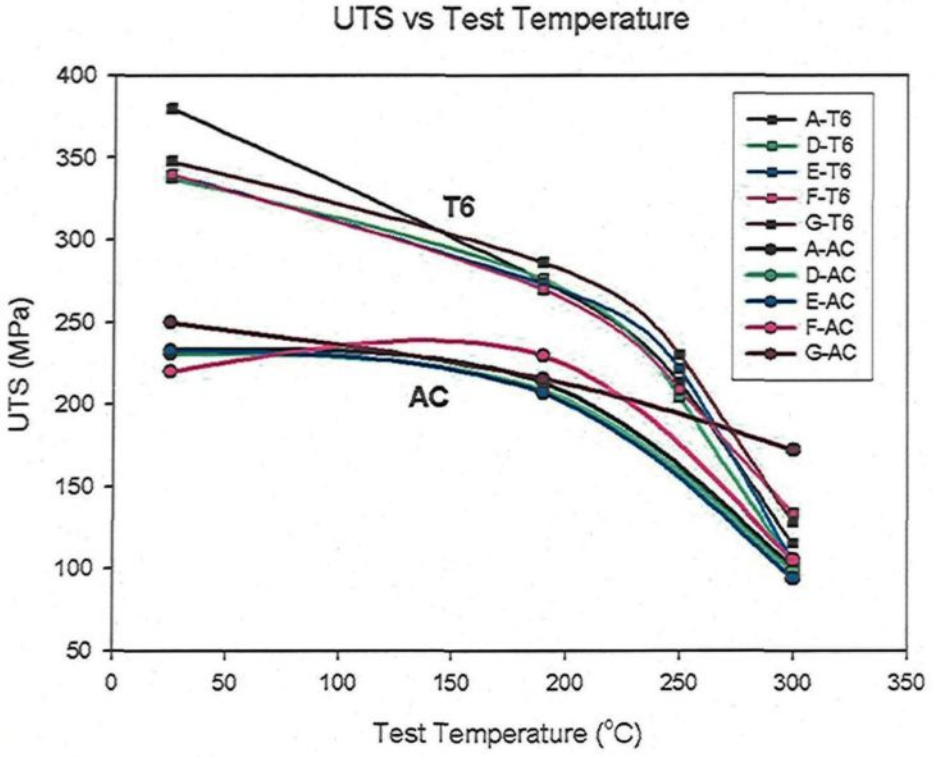

Figure 5.60 UTS values from experiments at ambient and at high temperatures for A through G alloys.

As may be observed from Table 5.13 and Figure 5.60, alloy G in the as-cast condition seems to be the most promising alloy with respect to mechanical properties at high temperatures, since at 300°C alloy G-AC displays the highest tensile properties taking into consideration the alloys tested in both AC and T6 conditions. As was discussed in Chapter 4, in alloy G with 0.2 wt pct Zr, the zirconium content is dissolved at a lower temperature than in the alloys E and F, with 0.4 wt pct Zr, according to the Al-Zr phase diagram of Figure 4.29, opening the possibility that the Zr content was able to completely dissolve within the liquid during the preparation of the alloy G samples. As was observed in the work of Knipling[83] with Al-Zr and Al-Zr-Ti alloys, Zr-rich nano-particles precipitate

during solidification forming coherent precipitates which are resistant to coarsening at temperatures in the order of 275°C-425°C; such Zr-rich particles would improve the mechanical properties at 300°C in the as-cast alloy G. As may be observed in Figure 5.60, alloy G in the T6 condition did not show a behavior similar to that observed for the as-cast condition; this contradictory behavior may be explained by the fact that alloys in the T6 condition were previously submitted to a solution heat treatment at 495°C, such temperature would change the coherency of the Zr-rich precipitates formed during the solidification of alloy G, as may be observed from Figure 5.61 which shows a proportional decrease as the time of permanence increases at 500°C, such linear decrease in strength is attributed to the coarsening of Zr-rich precipitates present in Al-Zr and Al-Zr-Ti alloys.[83]

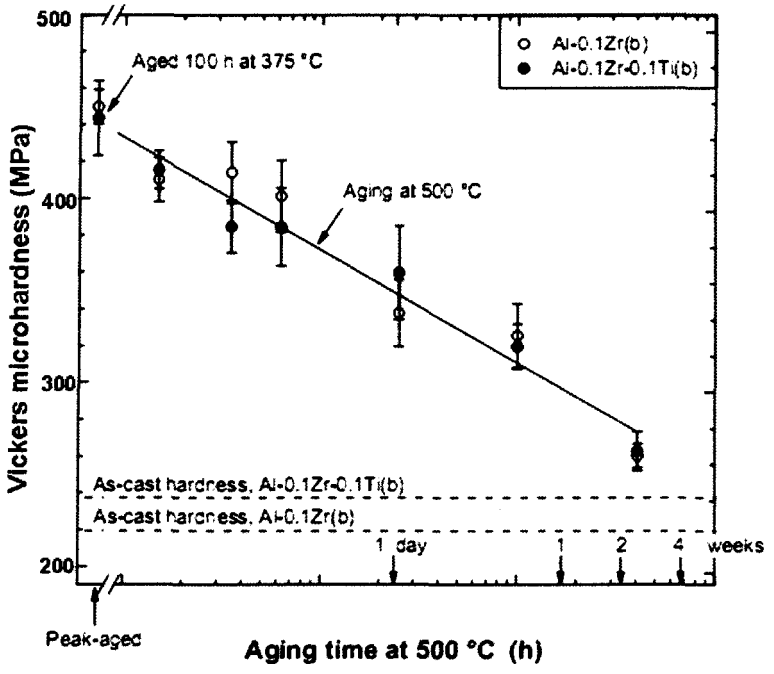

Figure 5.61 Vickers microhardness versus exposure time at 500°C in Al-Zr and Al-Zr-Ti alloys.[83]

CHAPTER 6

CONCLUSIONS AND RECOMMENDATIONS

CHAPTER 6

CONCLUSIONS AND RECOMMENDATIONS

The present study concentrates on the mechanical properties at ambient and at high temperatures of alloy 354 with additions of zirconium and nickel and micro-particles such as Al_2O_3 and SiC. Thermal analysis was effectuated with the objective of discerning the main phases observed in the microstructures of the alloys studied. Tensile tests were performed on alloy samples submitted to various aging treatments, with the aim of obtaining knowledge about the mechanical limits of the alloys studied as well as understanding the effects of the additions made on the tensile properties of these alloys.

6.1 Conclusions

From an analysis of the results obtained, the following conclusions may be formulated:

1. Similar to the 319 alloy, the 354 alloy presents well-defined reactions at temperatures below 500°C related to Cu-containing phases.
2. Zirconium reacts only with Ti, Si, and Al in the alloys examined to form the phases $(Al,Si)_2(Zr,Ti)$ and $(Al,Si)_3(Zr,Ti)$.
3. The Zr-rich intermetallic phases observed in this study appear in two different forms: the phase $(Al,Si)_2(Zr,Ti)$ containing high levels of silicon which is block-like

in form, and the phase $(Al,Si)_3(Zr,Ti)$ containing high levels of aluminum, which appears in needle-like form.

4. In the thermal analysis experiments carried out at the higher cooling rate, namely 4°C sec^{-1}, a reaction is observed within the temperature range of 667°-671°C which appears to be related to the precipitation of the Zr-rich phases; it was not possible to observe this reaction at the low cooling rate of 0.35°C sec^{-1}.
5. The use of quality index charts is a satisfactory method for presenting tensile test results, for assessing the effects of specific additions of elements/micro-particles (Al_2O_3, SiC, Ni and Zr) to the base alloy, and for evaluating heat treatment conditions.
6. The conditions/tensile properties which characterize the mechanical behaviour of the base alloy studied are located on the quality index charts constructed for alloy 354: Minimum and maximum quality index values, 259 MPa and 459 MPa, are observed for the as-cast and solution heat-treated conditions, respectively; the yield strength shows a maximum of 345 MPa and a minimum of 80 MPa within the whole series of aging treatments applied.
7. The addition of a low amount (0.5%) of micro-oxides/carbides to alloy 354 does not improve the tensile properties; rather, it promotes the occurrence of defects such as segregation of micro-particles and porosity, which may considerably decrease the tensile properties.
8. Addition of 0.4 wt% nickel to alloy 354, results in a decrease in tensile properties by about 10% compared to the base alloy, and is attributed to a nickel-copper

reaction which interferes with the formation of Al_2Cu precipitates, thereby affecting the age hardening process.

9. The needle-like phase $(Al,Si)_3(Zr,Ti)$ is the main feature observed in the microstructures of the tensile samples of alloys containing 0.2-0.4 wt% Zr additions.
10. The reduction in mechanical properties at aging temperatures between 155°C and 190°C, by addition of Zr and Ni, is attributed principally to the increase in the percentage of intermetallic phases formed during solidification; where such particles act as stress concentrators, and decrease the alloy ductility.
11. Tensile properties at ambient temperatures show a slight increase, of ~20 MPa, in the alloys with Zr and Zr+Ni additions, particularly at aging temperatures above 240°C.
12. At aging temperatures of 350°C, with aging times ranging from 2 to 100 hours, for the alloy containing 0.2 wt% Zr and 0.2 wt% Ni, room temperature tensile tests show an increase in the yield strength with respect to the other alloys studied, the increase in yield strength being about 13% higher than that of the base alloy.
13. The major effect of Zr addition lies in the drastic reduction of grain size, of about 40%, compared with the grain size of the base alloy, rather than in increasing the tensile properties at room temperature.
14. Additions of Zr and Zr+Ni increase the high temperature tensile properties, in particular, that of alloy G, containing 0.2 wt% Zr and 0.2 wt% Ni, in the as-cast

condition, which displays an increase of more than 30% (~70MPa) in the tensile properties at 300°C compared with the rest of the alloys.

6.2 Recommendations for future work

In spite of the work presented in this thesis, the results obtained may still be considered as representing the preliminary stage towards achieving a complete understanding of the effects of Zr-rich precipitates in improving the mechanical properties at high temperature in cast aluminum alloys. Further investigations are suggested along the following lines to complement this study:

- Analyze the Zr-rich nano-precipitates using transmission and scanning electron microscopy, in order to characterize their evolution during the aging treatments used in this research.

- Evaluate different melt and casting procedures for the alloys with Zr additions, such as increasing the melt temperature in order to obtain a better dissolution of the Zr in the melt prior to casting.

- Analyze the effects of different solution heat treatment times of 354 alloys using different contents of Zr on the resulting mechanical properties.

REFERENCES

REFERENCES

1. D. Gloria and J. Hernandez-Sandoval, "Nanotechnology to fit automotive industry increasing engine performance demands: Is it an alternative?," Taller internacional sobre el desarrollo, manufactura y uso responsable de nanomateriales, I.T.E.S.M., Campus Monterrey, México, Dec-11-2008.

2. K.J. Martchek, "Life cycle benefits, challenges, and the potential of recycled aluminum," *Proc. Air and Water Management 90th Ann. Meet.*, 1997, Paper 97-RP124B.01.

3. M.C. Campbell, "Non-ferrous metals recycling: A complement to primary metals production," *International Council on Metals and Environment (ICME)*, Canada, 1996, pp. 3-8.

4. M.F. Henstock, "The recycling of non-ferrous metals," *International Council on Metals and the Environment (ICME)*, Canada, 1996, pp. 9-17.

5. K. Logozar, G. Radonjic and M. Bastic, "Incorporation of reverse logistics model into in-plant recycling process: a case of aluminum industry," *Resources Conservation and Recycling,* Vol. 49, 2006, pp. 49-67.

6. B. Zhou, Y. Yang, M.A. Reuter and U.M.J. Boin, "Modeling of aluminum scrap melting in a rotary furnace," *Journal Miner. Eng.*, Vol. 19, 2006, pp. 299-308.

7. G. Hoyle, "Recycling opportunities in the UK for aluminum-bodies motor cars," *Resources Conservation and Recycling*, Vol. 15, 1995, pp. 181-191.

8. H. Amini, A. Moloodi, M. Golestanipour and E.Z.V. Karimi, "Recycling of aluminum alloy turning scrap via cold pressing and meeting with SALT flux," *Journal of Materials Processing Technology*, Vol. 209, 2009, pp. 3138-3142.

9. H.K. Buxmann "Ecological aspects of the use of aluminium in cars, with particular regard to recycling techniques," *Resources Conservation and Recycling*, Volume 10, Issues 1-2, 1994, pp. 17-23.

10. C.H. Cáceres, "Transient environmental effects of light alloy substitutions in transport vehicles," *Materials and Design*, Vol. 30, Issue 8, 2009, pp. 2813-2822.

11. M. Easton, W.Q. Song and T. Abbott, "A comparison of the deformation of magnesium alloys with aluminum and steel in tension, bending and buckling," *Materials Design*, Vol. 27, 2006, pp. 935–946.

12. M.E. Schlesinger, *Aluminum Recycling*, CRC Press, Taylor and Francis Group, Missouri, 2007.

13. D. Carle and G. Blount, "The sustainability of aluminum as an alternative material for car bodies," *Materials and Design*, Vol. 20, 1999, pp. 267-272.

14. C.H. Caceres, "Economical and environmental factors in light alloys automotive applications," *Metallurgical and Materials Transactions A*, Vol. 38A, 2007 pp. 1649-1662.

15. *ASM Handbook, Vol. 2: Properties and selection: Non ferrous alloys and special purpose materials*, 10th Edition, American Society for Metals, Materials Park, Ohio, 1990.

16. J. Gruzleski and B.M. Closset, *The Treatment of Liquid Aluminum –Silicon Alloys*, American Foundrymen's Society, Inc., Des Plaines, IL, 1990, pp 131-132.

17. C.H. Cáceres, M.B. Djurdjevic, T.J. Stockwell and J.H. Sokolowski, "The effect of Cu content on the level of microporosity in Al-Si-Cu-Mg casting alloys," *Scripta Materialia*, Vol. 40, 1999, pp. 631-637.

18. H. Ammar, "Effect of casting imperfections on the fatigue properties of aluminum-silicon casting alloys," Master's Thesis, Université du Quebec à Chicoutimi, Quebec, Canada, 2006.

19. Lu Shu-Zu and A. Hellawell. "The Mechanism of Silicon Modification in Aluminum-Silicon Alloys: Impurity induced Twinning," *Metallurgical Transactions A*, Vol. 18A, 1987, pp. 1721-1733.

20. B. Closset and J.E. Gruzleski, "A Study on the Use of Pure Metallic Strontium in the Modification of Al-Si Alloys," *AFS Transactions*, Vol. 89, 1981, pp. 801-808.

21. B. Closset, "Modification and Quality of Low Pressure Aluminum Castings," *AFS Transactions*, 1988, Vol. 96, pp. 249-260.

22. P. S. Mohanty, R.I.L. Guthrie and J.E. Gruzleski, "Studies on the Fading Behavior of Al-Ti-B Master Alloys and Grain Refinement Mechanism Using LiMCA," *Light Metals*, 1995, pp. 859-868.

23. M.M. Guzowski, G.K. Sigworth and D.A. Sentner, "The Role of Boron in the Grain Refinement of Aluminum with Titanium," *Metallurgical Transactions A*, Vol. 18A, 1987, pp. 603-619.

24. L.F. Mondolfo, *Aluminum Alloys - Structure and Properties*, Butterworths, London, 1976.

25. J.A. Marcantonio and L.F. Mondolfo, "Grain Refinement in Aluminum Alloyed with Titanium and Boron," *Metallurgical Transactions*, Vol. 2, 1971, pp. 456-471.

26. L.F. Mondolfo, S. Farooq and T.S.E. Chikai, "Grain Refinement of Aluminum Alloys by Titanium and Boron," in *Solidification Technology in the Foundry and Cast House*, The Metals Society, London, 1983, pp. 133-136.

27. *ASM Handbook, Vol. 4: Heat Treating of Aluminum Alloys*, 10th Edition, American Society for Metals, Materials Park, Ohio, 1991.

28. C. Krammer, *Aluminum Handbook, Vol. 2, Forming, Casting, Surface Treatment, Recycling and Ecology*, 1st Edition, Aluminum Verlag marketing and kommunikation, GmbH, Littmanddruck, Oldenburg, Germany, 2003, pp. 263; 388; 390; 403.

29. J.E. Hatch, *Aluminum: Properties and Physical Metallurgy*, ASM, Materials Park, Ohio, 1984.

30. I.J. Polmear, *Light alloys: Metallurgy of the light metals*, J. Wiley and Sons, New York, 1995, p. 362.

31. G. Wang, X. Bian, W. Wang and J. Zhang, "Influence of Cu and Minor Elements on Solution Treatment of Al-Si-Cu-Mg Cast Alloys," *Materials Letters*, Vol. 57, 2003, pp. 4083-4087.

32. R. Fuoco and E.R. Correa, "Incipient melting during solution heat treatment of Al-Si-Mg Alloys," *AFS Transactions*, Vol. 110, 2002, pp. 417-433.

33. J. Gauthier, P.R. Louchez and F.H. Samuel, "Heat Treatment of 319.2 Aluminum Automotive Alloy, Part 1: Solution Heat Treatment," *Cast Metals*, Vol. 8, 1995, pp. 91-106.

34. J. Gauthier and F.H. Samuel, "Tensile properties and fracture behavior of solution heat treated 319.2 Al automotive alloy," *AFS Transactions*, Vol. 103, 1995, pp. 849-857.

35. E. Sjölander and S. Seifeddine, "The heat treatment of Al-Si-Cu-Mg casting alloys," *Materials Processing Technology*, Vol. 210, 2010, pp. 1249-4259.

36. A.M. Samuel, J. Gauthier and F.H. Samuel, "Microstructural aspects of the dissolution and melting of Al_2Cu phase in Al-Si alloys during solution heat

treatment," *Metallurgical and Materials Transactions A*, Vol. 27A, 1996, pp. 1785-1798.

37. F.H. Samuel, "Incipient melting of $Al_5Mg_8Si_6Cu_2$ and Al_2Cu intermetallics in unmodified and strontium-modified Al-Si-Cu-Mg (319) alloys during solution heat treatment," *Journal of Materials Science*, Vol. 33, Number 9, 1988, pp. 2283-2297.

38. H.J. Li, S. Shivkumar, X.J. Luos and D. Apelian, "Influence of modification on the solution heat treatment response of cast Al-Si-Mg Alloys," *Cast Metals*, Vol. 1, 1989, pp. 227-234.

39. F. Paray and J.E. Gruzleski, "Microstructure-Mechanical Property Relationships in a 356 Alloy. Part 1: Microstructure," *Journal of Materials Science,* 1998, Vol. 33, pp. 2283-2297.

40. C.M. Estey, S.L. Cockcroft and D.M. Maijer, "Constitutive behavior of A356 during the quenching operation," *Materials Science and Engineering A*, Vol. 383, 2004, pp. 245-251.

41. D.R. Askeland, *The Science and Engineering of Materials*, 3rd Edition, Chapman and Hall, Boston, MA, 1996.

42. C. R. Hutchinson and S. P. Ringer, "Precipitation processes in Al-Cu-Mg alloys microalloyed with Si," *Metallurgical and Materials Transactions A*, Vol. 31A, 2000, pp. 2721-33.

43. S. Abis, M. Massazza, P. Mengucci and G. Tiontino, "Early Ageing Mechanisms in a High–Copper AlCuMg Alloy," *Scripta Materialia*, Vol. 45, 2001, pp. 685-691.

44. M. Taya and R.J. Arsenault, *Metal Matrix Composites - Thermomechanical Behavior*, Pergamon Press, New York, 1989.

45. A.J. Lee and P. Chen, High strength aluminum alloy for high temperature applications, US Patent No. 6918970, 2002.

46. J.D. Robson and P.B. Pragnell, "Modeling Al_3Zr dispersoid precipitation in multi-component aluminum alloys," *Materials Science and Engineering A*, Vol. 352, 2003, pp. 240-250.

47. A.M. Gokhale, M.D. Dighe and M. Horstemeyer, "Effect of Temperature on Silicon Particle Damage in A356 Alloy," *Metallurgical and Materials Transactions A*, Vol. 29A, 1998, pp. 905-907.

48. M. Brosnan and S. Shivkumar. "Elevated Temperature Tensile Properties and Fracture Behavior of A356 Castings," *AFS Transactions*, Vol. 103, 1996, pp. 727-737.

49. M.J. Couper, A.E. Neeson and J.R. Griffiths, "Casting Defects and the Fatigue Behaviour of an Aluminium Casting Alloy," *Fatigue & Fracture of Engineering Materials & Structures*, 1990, Vol. 13, pp. 213-227.

50. M.K. Surappa, E. Blank, and J.C. Jaquet, "Effect of Macro-Porosity on the Strength and Ductility of Cast Al-7Si-0.3Mg Alloy," *Scripta Metallurgica*, 1986, Vol. 20, pp. 1281-1286.

51. A.M. Samuel and F.H. Samuel, "A Metallographic Study of Porosity and Fracture Behavior in Relation to the Tensile Properties in 319.2 End Chill Castings," *Metallurgical and Materials Transactions A*, 1995, Vol. 26A, pp. 2359-2372.

52. M.D. Dighe and A.M. Gokhale, "Relationship between microstructural extremum and fracture path in a cast Al-Si-Mg alloy," *Scripta Materialia*, 1997, Vol. 37, pp. 1435-1440.

53. M. Hayashi, "High temperature strength of cast heat resisting alloy for combustion engine piston," *Proceedings of the Faculty of Engineering of Tokai University*, 1985, vol. 11, pp. 35-48.

54. E. Rincon, H.F. Lopez, M.M. Cisneros, H. Mancha, and M.A. Cisneros, "Effect of temperature on the tensile properties of an as-cast aluminum alloy A319," *Materials Science and Engineering A*, Vols 452-453, 2007, pp. 682-687.

55. A.J. Moffat, S. Barnes, B.G. Mellor and P. A.S. Reed, "The effect of silicon content on long crack fatigue behavior of aluminum-silicon piston alloys at elevated temperature," *International Journal of Fatigue*, Vol. 27, 2005, pp. 1564-1570.

56. M.F. Ashby, C. Gandhi and D.M.R. Taplin, "Fracture mechanism maps and their construction for f.c.c. metals and alloys,"*Acta Metallurgica*, Vol. 27, 1979, pp. 699-729.

57. S. Floreen and H.W. Hayden, "Some Observations of Void Growth during Tensile Deformation of a High Strength Steel," *Scripta Metallurgica*, Vol. 4, 1970, pp. 87-94.

58. V.M. Kevorkijan, "Aluminum Composites for Automotive Applications: A Global Perspective," *JOM*, November, 1999, pp. 54-58.

59. I.A. Ibrahim, F.A. Mohamed and E.J. Lavernia, "Particulate reinforced metal matrix composites – a review," *Journal of Materials Science*, Vol. 26, 1991, pp. 1137-1156.

60. M.K. Surappa and P.K. Rohatgi, "Preparation and properties of cast aluminum-ceramic particle composites," *Journal of Materials Science*, Vol. 16, 1981, pp. 983-993.

61. R.H. van Stone, T.B. Cox, J.R. Low and J.A. Psioda, *International Metals Reviews*, Vol. 30, 1985, pp. 157-176.

62. T.W. Clyne and P.J. Withers, *An Introduction to Metal Matrix Composites*, Cambridge University Press, Cambridge (UK), 1999.

63. A.M. Samuel, A. Gothmare and F.H. Samuel, "Effect of solidification rate and metal feedability on porosity and SiC/Al_2O_3 particle distribution in an Al-SiMg (359) Alloy," *Composites Science and Technology*, Vol. 53, 1995, pp. 301-315.

64. P.K. Rohatgi, F.M. Yarandi, Y. Liu and R. Asthana, "Segregation of silicon carbide by settling and particle pushing in cast aluminum-silicon-carbide particle composites," *Materials Science and Engineering*, Vol. 147-1, 1991, pp. L1-L6.

65. A. Labib, H. Liu and F.H. Samuel, "Effect of Remelting, Casting and Heat Treatment on Two Al-Si SiC-Particle Composites," *AFS Transactions*, Vol. 100, 1992, pp. 1033-1041.

66. A. Mortensen and I. Jin, "Solidification processing of metal matrix composites," *International Materials Reviews*, Vol. 37, 1992, pp. 101-128.

67. A.M. Samuel and F.H. Samuel, "Influence of casting and heat treatment parameters in controlling the properties of an Al-10 wt% Si-0.6 wt% Mg/SiC/20p composite," *Journal of Materials Science*, Vol. 29, 1994, pp. 3591-3600.

68. F.H. Samuel and A.M. Samuel, "Heat-treatment parameters for a $359/Al_2O_3/10p$ composite modified with 0.07% strontium," *Composites Science and Technology*, Vol. 53, 1995, pp. 85-98.

69. T.S. Srivatsan and J. Mattingly, "Influence of heat treatment on the tensile properties and fracture behaviour of an aluminum alloy-ceramic particle composite," *Journal of Materials Science*, Vol. 28, 1993, pp. 611-620.

70. R.J. Arsenault, "Strengthening mechanisms in particulate MMC: Remarks on a paper by Miller and Humpreys," *Scripta Metallurgica*, Vol. 25, 1991, page 2617.

71. A.M. Samuel, H. Liu and F.H. Samuel, "Effect of melt, solidification and heat treatment processing parameters on the properties of Al-SiMg/SiC(p) composites," *Journal of Materials Science*, Vol. 28, 1993, pp. 6785-6798.

72. C.H. Cáceres, I.L. Svensson and J.A. Taylor, "Strength-ductility behaviour of Al-SiCuMg casting alloys in T6 temper," *International Journal of Cast Metals Research*, Vol. 15 (5), 2003, pp. 531-543.

73. T.S. Srivatsan, "Microstructure, tensile properties and fracture behavior of Al_2O_3 particulate-reinforced aluminum alloy metal matrix composites," *Journal of Materials Science*, Vol. 31, 1996, pp. 1375-1388.

74. M. Taya and T. Mori, "Dislocations punched-out around a short fiber in metal matrix composite subjected to uniform temperature change," *Acta Metallurgica*, Vol. 35, Number 1, 1987, pp. 155-162.

75. C. Ramesh, A. Ahmed, B.H. Channabasappa and R. Keshavamurthy, "Development of Al6063-TiB2 in situ composites," *Materials and Design*, Vol. 31, 2010, pp. 2230-2236.

76. K. Cho and J. Gurland, "The Law of Mixtures Applied to the Plastic Deformation of Two-Phase Alloys of Coarse Microstructures," *Metallurgical Transactions A*, Vol. 19A, 1988, pp. 2027-2040.

77. M.V. Vogelsang, R.G. Arsenault and R.M. Fisher, "An In Situ HVEM Study of Dislocation Generation at Al/SiC Interfaces in Metal Matrix Composites," *Metallurgical Transactions A*, Vol. 17A, 1986, pp. 379-389.

78. D. Srinivasan and K. Chattopadahyay, "Metastable phase evolution and hardness of nanocrystalline Al-Si-Zr alloys," *Materials Science and Engineering A*, Vols 304-306, pp. 534-539.

79. P. Sepehrband, R. Mahmudi and F. Khomamizadeh, "Effect of Zr addition on the aging behavior of A319 aluminum cast alloy," *Scripta Materialia*, Vol. 52, 2005, pp. 253-257.

80. R. Mahmudi, P. Sepehrband and H.M. Ghasemi, "Improved properties of A319 aluminum casting alloy modified with Zr," *Materials Letters*, Vol. 60, 2006, pp. 2606-2610.

81. J.D. Robson and P.B. Pragnell, "Predicting recrystallised volume fraction in aluminium alloy 7050 hot rolled plate," *Materials Science and Technology*, Vol. 18, 2002, pp. 607-614.

82. B. Morere, C. Maurice, R. Shahani and J. Driver, "The influence of Al_3Zr dispersoids on the recrystallization of hot-deformed AA 7010 alloys," *Metallurgical and Materials Transactions A*, Vol. 32A, 2001, pp. 625-632.

83. K.E. Knipling, "Development of a nanoscale precipitation-strengthened creep-resistant aluminum alloy containing trialuminide precipitates," PhD Thesis, Northwestern University, Evanston, IL, 2006.

84. J.L. Murray: Alcoa, Alcoa Center, PA, Personal Communication, 2005.

85. K.I. Moon, K.Y. Chang, K.S. Lee, "The effect of ternary addition on the formation and the thermal stability of $L1_2$ Al_3Zr alloy with nanocrystalline structure by mechanical alloying," *Journal of Alloys and Compounds*, Vol. 312, 2000, pp. 273-283.

86. Z. Liu, "Thermodynamics of nanoscale precipitate strengthened Fe-Cu and Al-Transition-Metal systems from first principles calculations, PhD. Thesis, Northwestern University, Evanston, IL, 2006.

87. W.L. Manknis and S. Lamb, "Nickel and nickel alloys," *Metals Handbook, Vol. 2, Properties and Selection: Nonferrous Alloys and Special-Purpose Materials*, 10^{th} Edition, Materials Park, Ohio, 1990, pp. 1374-1380.

88. J.G. Kaufman, *Properties of aluminum alloys: Tensile, creep, and fatigue data at high and low temperatures*, ASM International, Materials Park, Ohio, 1999, pp. 714-724.

89. L. Sang-Yong, L. Jung-Hwan and L. Young-Seon, "Characterization of Al7075 alloys after cold working and heating in the semi-solid temperature range," *Journal of Materials Processing Technology,* Vol. 111, 2001, pp. 42-47.

90. P. Nash, M.F. Singleton and J.L. Murray, in *ASM Handbook, Vol.3: Alloy-Phase Diagrams*, 10^{th} Edition, ASM, Materials Park, Ohio,1992.

91. J.A. Catherall and R.F. Smart, "The effect of nickel in aluminum-silicon eutectic alloys", *Metallurgia*, Vol. 79, 1969, pp. 247-250.

92. T. Takahashi, A. Akihiko and Y. Kojima, "Effects of Ni and Fe addition on various properties in heat-resisting aluminum casting alloys," *Journal of the Japan Institute of Light Metals*, Vol. 23, 1973, pp. 26-32.

93. M. Drouzy, S. Jacob and M. Richard, "Interpretation of tensile results by means of quality index and probable yield strength," *AFS International Cast Metals Journal*, Vol. 5 (1980) pp. 43-50.

94. S. Shivkumar, C. Keller and D. Apelian, "Aging Behavior in Cast Al-Si-Mg. Alloy,"*AFS Transactions*, Vol. 98, 1990, pp. 905-911.

95. C.H. Caceres, T. Din, A.K.M.B. Rashid and J. Campbell, "Effect of ageing on quality index of an Al-Cu casting alloys," *Journal of Materials Science and Technology*, Vol. 15, 1999, pp.711-716.

96. L. Ceschini, I. Boromei, A. Morri, S. Seifeddine and I.L. Svensson, "Microstructure, tensile and fatigue properties of the Al–10%Si–2%Cu alloy with different Fe and Mn content cast under controlled conditions," *Journal of Materials Processing Technology*, Vol. 209, Issues 15-16, 2009, pp. 5669-5679.

97. C.H. Cáceres, "Microstructure design and heat treatment selection for casting alloys using the quality index", ASM-IMS 1999 Meeting, October 1-4, Cincinnati, 1999.

98. H.R. Ammar, C. Moreau, A.M. Samuel, F.H. Samuel and H.W. Doty, "Effects of aging parameters on the quality of 413-type commercial alloys," *Materials and Design,* Vol. 30, Issue 4, 2009, pp. 1014-1025.

99. H. Westengen, O. Holta, "Low pressure permanent mould casting of magnesium-Recent developments," *SAE International Congress and Exposition*, Detroit MI., Paper #880509, Publisher: SAE, Warrendale, PA, 1988.

100. N. Ryum, "Precipitation and recrystallization in an A1-0.5 WT.% Zr-alloy," *Acta Metallurgica,* Vol. 17, 1969, pp. 269-278.

101. C.H. Cáceres, "A Rationale for the Quality Index of Al-Si-Mg Casting Alloy," *International Journal of Cast Metals Research*, 1998, Vol. 10(5), pp. 293-299.

102. L. Bäckerud, G. Chai and J. Tamminen, *Solidification characteristics of aluminum alloys, Vol. 2: Foundry alloys*, AFS/SKANALUMINIUM, Des Plaines, IL, 1990.

103. J. Tamminen, "Thermal Analysis for Investigation of Solidification Mechanisms in Metals and Alloys," Doctoral dissertation, University of Stockholm, Sweden, 1988.

104. W. Chen, Y. Wang, J. Qiang and C. Dong, "Bulk metallic glasses in the Zr-Al-Ni-Cu system," *Acta Materialia*, Vol. 51, 2003, pp. 1899-1907.

105. Y. Zhan, J. Jiang, Z. Sun, J. Ma, Ch. Li and Z. Hu, "Phase equilibria of the Zr-Ti-Si ternary system at 773 K," *Journal of Alloys and Compounds*, Vol. 475, 2009, pp. 131-133.

106. W. Yuying, L. Xiangfa, J. Binggang and H. Cuanzhen, "Modification effect of Ni-38 wt% Si on Al-12 wt% Si alloy," *Journal of Alloys and Compounds*, Vol. 477, 2009, pp. 118-122.

107. M.A. Zamzam, A.S. El-Sabbagh and M.M. Milad, "Study of thermal effects of Al-Ni turbine blades on their lifetime," *Materials and Design*, Vol. 23, 2002, pp. 161-168.

108. B. R. Valdez, "Efecto del Sr en la solidificación de las aleaciones Al-Si A319 y su análisis térmico," Tesis de maestría, Instituto Tecnológico de Saltillo, Saltillo, Coahuila, Mexico, 2003.

109. S.G. Shabestari, and S. Ghodrat, "Assessment of modification and formation of intermetallic compounds in aluminum alloy using thermal analysis," *Materials Science and Engineering A,* Vol. 467, Issues 1-2, 15 October 2007, pp. 150-158

110. A.M.A. Mohamed, A.M. Samuel, F.H. Samuel and H.W. Doty, "Influence of additives on the microstructure and tensile properties of near-eutectic Al-10.8%Si cast alloy," *Materials and Design*, Vol. 30, Issue 10, 2009, pp. 3943-3957.

111. N.A. Belov, D.G. Eskin and A.A Aksenov, *Multicomponent phase diagrams: applications for commercial aluminum alloys*, Elsevier, Oxford, UK, 2005.

112. L.A. Dobrzanski, R. Maniara, J. Sokolowski and W. Kasprzak, "Effect of cooling rate on the solidification behaviour of AC $AlSi_7Cu_2$ alloy," *Journal of Materials Processing Technology,* Vol. 191, 2007, pp. 317-320.

113. R. Li, "Solution heat treatment of 354 and 355 cast alloys," *AFS Transactions*, Vol. 104, 1996, pp. 777-783.

114. G. Wang, X. Bian and Z. Junyan, "Gradual solution heat treatment of AlSiCuMg cast alloys," *Rare Metals*, Vol. 22, 2003, pp. 304-308.

115. M. Tash, F.H. Samuel, F. Mucciardi, H.W. Dotty and S. Valtierra, "Effect of metallurgical parameters on the machinability of heat-treated 356 and 319 aluminum alloys," *Materials Science and Engineering A*, Vol. 434, 2006, pp. 207-217.

116. N.A. Belov, D.G. Eskin and N.N. Avxentieva, "Constituent phase diagrams of the Al-Cu-Fe-Mg-Ni-Si system and their application on the analysis of aluminum piston alloys," *Acta Materialia*, Vol. 53, 2005, pp. 4709-4722.

117. M.I.Z. Cardoso, "Análisis de la solidificación de los precipitados de Cu en la aleación A319," Tesis de maestría, Instituto Tecnológico de Saltillo, Saltillo, Coahuila, Mexico, 2006.

118. F.H. Samuel, A.M. Samuel and H.W. Doty, "Factors controlling the type and morphology of Cu-containing phases in 319 Al alloys," *AFS Transactions*, Vol. 104, 1996, pp. 893-901.

119. W. Kurz and D.J. Fisher, *Fundamentals of Solidification*, 4th Revised Edition, TransTech. Publications Ltd., Uetikon-Zuerich, Switzerland, 1998.

120. J.E. Gruzleski, *Microstructure Development During Metalcasting*, American Foundrymen's Society, Inc., Des Plaines, IL, 2000, pp. 49-50.

121. T. Sato, A. Kamio and G.W. Lorimer, "Effects of Si and Ti additions on the nucleation and phase stability of the L12-type phase in Al-Zr alloys," *Materials Science Forum*, Vols 217-222, 1996, pp. 8895-8900.

122. E. Nes and H. Billdal, "Non-equilibrium solidification of hyper-peritectic Al-Zr alloys," *Acta Metallurgica*, Vol. 25, pp. 1031-1037.

123. E. Nes and H. Billdal, 'The mechanism of discontinuous precipitation of the metastable Al_3Zr phase from an Al-Zr solid solution," *Acta Metallurgica*, Vol. 25, 1977, pp. 1039-1046.

124. H.W. Kerr, J. Cisse and G.F. Bolling, "On equilibrium and non-equilibrium peritectic transformations," *Acta Metallurgica*, Vol. 22, 1974, pp. 677-686.

125. J.L. Murray, A. Peruzzi and J.P. Abriata, "The Al-Zr (aluminum-zirconium) system," *Journal of Phase Equilibrium*, Vol.13, 1992, pp. 277-291.

126. D.H. St. John and L.M. Hogan, "The peritectic transformation," *Acta Metallurgica,* Vol. 25, 1977, pp. 77-81.

127. D.H. St. John and L.M. Hogan, "Thermal analysis of peritectic alloys," *Journal of Materials Science*, Vol. 17, 1982, pp. 2413-2418.

128. D. Gloria, "Control of grain refinement of Al-Si alloys by thermal analysis,", PhD Thesis, McGill University, Montreal, Canada, 1999.

129. S. Nafisi, "Effects of grain refining and modification on the microstructural evolution of semi-solid 356 alloy," PhD Thesis, Université du Quebec à Chicoutimi, Chicoutimi, Canada, 2006.

130. ASTM, "E112-88: Standard test methods for determining average grain size", 1988.

131. D. Apelian, G.K. Sigworth and K.R. Whaler. "Assessment of grain refining and modification of Al-Si foundry alloys by thermal analysis," *AFS Transactions*, Vol. 92, 1984, pp. 297-307.

132. S.G. Shabestari and M. Malekan, "Assessment of the effect of grain refinement on the solidification characteristics of 319 aluminum alloy using thermal analysis," *Journal of Alloys and Compounds*, Vol. 492, Issues 1-2, March 2010, pp. 134-142.

133. AFS Thermal Analysis Committee (2-G), "Microstructure Control in Hypoeutectic Aluminum-Silicon Alloys", American Foundrymen's Society, Inc., Des Plaines, IL, 1986.

134. P.Y. Zhu and Q.Y. Liu, "Kinetics of granulation of discontinuous phase in eutectic structures," *Materials Science and Technology*, Vol. 2, May 1986, pp. 500-507.

135. S.K. Chaudhury and D. Apelian, "Fluidized bed heat treatment of cast Al-Si-Cu-Mg alloys," *Metallurgical and Materials Transactions A*, Vol. 37A, 2006, pp. 2295-2311.

136. H.R. Ammar, A.M. Samuel and F.H. Samuel, "Porosity and the fatigue behavior of hypoeutectic and hypereutectic aluminum–silicon casting alloys," *International Journal of Fatigue*, Vol. 30, Issue 6, June 2008, pp. 1024-1035.

137. C.H. Cáceres and J.A. Taylor, "Enhanced ductility in Al-Si-Cu-Mg casting alloys with high Si content," *Shape Casting: The John Campbell Symposium*, M. Tiryakiouglu and P. Crepeau (Eds), TMS, California, 2005, pp. 245-254.

138. W. Reif, J. Dutkiewiewicz and R. Ciach, "Effect of precipitates in Al-Si-Cu-Mg alloys," *Materials Science and Engineering A*, Vol. 234, 1997, pp. 165-168.

139. R.E. Stoltz and R.M. Pelloux, "The Bauschinger effect in precipitation strengthened aluminum alloys", *Metallurgical Transactions A*, Vol. 7A, 1976, pp. 1295-1306.

140. A. Daoud and W. Reif, "Influence of Al_2O_3 particulate on the aging response of A356 Al-based composites," *Journal of Materials Processing Technology*, Vol. 123, 2002, pp. 313-318.

141. A.M. Samuel and F.H. Samuel, "Aspects Involved in the Casting and Heat Treatment of SiC(p) Reinforced Al-Si-Mg Metal Matrix Composites," *Proc. Colloque: Les Composites à Matrice Metallique: Une Synthèse*, École de technologie supérieure, Montreal, June 14-16, 1993, J. Masounave et A. Thorel (eds), Presses de l'Université du Québec, Sainte-Foy (Québec), 1995, pp. 107-121.

142. E. Carrera, "Estudio de la influencia del Sr y los parámetros de envejecimiento sobre las propiedades mecánicas de una aleación Al-Si con 2.5% de Cu" Master's Thesis, Universidad Autónoma de Nuevo León, San Nicolás de los Garza, Mexico, 2006.

143. T. Savaskan and Y. Alemdag, "Effect of nickel additions on the mechanical and sliding wear properties of Al-40Zn-3Cu alloy," *Wear*, Vol. 268, 2010, pp. 564-570.

144. M. Huang and Z. Li, "Size effects on stress concentration induced by a prolate ellipsoidal particle and void nucleation mechanism," *International Journal of Plasticity*, Vol. 21, 2005, pp. 1568-1590.

145. B.J. Lee and M.E. Mear, "Stress concentration induced by an elastic spheroidal particle in a plastically deforming solid," *Journal of the Mechanics and Physics of Solids*, Vol. 47, 1999, pp. 1301-1336.

146. G.E. Dieter, *Mechanical Metallurgy*, 3rd Edition, McGraw-Hill, New York, 1986.

147. ASTM, "E646-98: Standard test method for tensile strain-hardening exponent (n-values) of metallic sheet materials," 1988.

APPENDIX I

Table I-1 Mean values of UTS and YS (MPa) and Plastic strain used to obtain Q (from equation 2.10) using a single K=500 MPa for Alloys B and C

$Q = UTS + 0.4K \cdot \log(S_f)$ Equation 2.10								
Identification	UTS (MPa)		YS (MPa)		Total Strain S_T (%)		Plastic Strain S_f (%)	Q (MPa) (Eq.2.10)
	AV	SD	AV	SD	AV	SD	AV	AV
B-AC	229	7.2	144	4.4	1.81	0.63	1.51	265
B-SHT	279	9.0	150	2.0	5.09	0.59	4.72	414
B1-155°C-2hrs	326	9.2	236	7.4	3.34	0.50	2.91	419
B5-155°C-10hrs	332	9.9	282	3.4	1.43	0.26	0.99	331
B13-155°C-100hrs	357	7.3	325	12.2	1.16	0.34	0.69	325
B14-170°C-2hrs	364	11.2	298	14.1	1.76	0.32	1.28	385
B18-170°C-10hrs	344	28.4	317	22.3	0.98	0.19	0.53	289
B26-170°C-100hrs	353	5.9	331	4.0	1.00	0.21	0.53	299
B27-190°C-2hrs	348	29.5	308	28.2	1.21	0.22	0.75	323
B31-190°C-10hrs	343	8.2	319	5.1	0.92	0.17	0.47	277
B39-190°C-100hrs	308	30.5	276	27.5	1.29	0.34	0.89	298
B40-240°C-2hrs	290	8.5	249	3.0	1.40	0.29	1.02	292
B44-240°C-10hrs	267	8.1	202	2.6	2.20	0.49	1.85	320
B52-240°C-100hrs	217	13.9	138	3.4	2.61	0.70	2.32	290
B53-300°C-2hrs	212	8.1	127	1.1	5.09	0.37	4.81	348
B57-300°C-10hrs	202	9.6	113	2.4	3.27	0.94	3.00	298
B65-300°C-100hrs	191	6.3	89	0.4	5.24	1.12	4.99	330
B66-350°C-2hrs	217	4.0	100	1.1	5.38	0.68	5.10	358
B70-350°C-10hrs	205	4.7	90	2.9	5.60	0.41	5.33	350
B78-350°C-100hrs	187	23.4	81	11.5	6.30	1.49	6.06	344
C-AC	240	8.8	143	6.6	2.01	0.82	1.78	290
C-SHT	282	4.3	146	2.3	5.32	0.64	4.94	421
C1-155°C-2hrs	305	20.8	212	20.0	3.19	0.28	2.78	394
C5-155°C-10hrs	344	3.4	295	7.4	1.29	0.13	0.84	328
C13-155°C-100hrs	359	8.0	326	5.1	1.09	0.15	0.62	317
C14-170°C-2hrs	341	26.9	280	23.9	1.75	0.16	1.30	364
C18-170°C-10hrs	348	13.4	324	6.2	0.87	0.11	0.41	271
C26-170°C-100hrs	356	6.7	318	6.5	1.57	0.35	1.10	364
C27-190°C-2hrs	370	5.2	320	13.3	1.57	0.27	1.08	377
C31-190°C-10hrs	338	7.7	314	7.2	0.98	0.07	0.53	283
C39-190°C-100hrs	284	5.2	237	6.9	1.60	0.02	1.23	302
C40-240°C-2hrs	308	0.9	250	2.0	2.00	0.13	1.59	348
G44-240°C-10hrs	265	10.9	201	5.5	2.04	0.80	1.69	311
C52-240°C-100hrs	236	9.0	147	2.5	3.43	0.72	3.12	335
C53-300°C-2hrs	238	2.7	138	1.9	3.63	0.11	3.32	342
C57-300°C-10hrs	216	8.0	115	1.6	4.33	1.25	4.05	338
C65-300°C-100hrs	195	4.5	88	3.3	5.41	0.26	5.16	337
C66-350°C-2hrs	221	2.9	102	1.4	4.77	0.54	4.48	351
C70-350°C-10hrs	204	3.3	94	0.7	4.43	0.25	4.17	328
C78-350°C-100hrs	199	15.1	83	8.7	6.88	1.71	6.62	363

Table I-2 Mean values of UTS and YS (MPa) and Plastic strain used to obtain Q (from equation 2.10) using a single K=500 MPa for Alloys D and E

$Q = UTS + 0.4K \cdot \log(S_f)$ Equation 2.10								
Identification	UTS (MPa)		YS (MPa)		Total Strain S_T (%)		Plastic Strain S_f (%)	Q (MPa) (Eq.2.10)
	AV	SD	AV	SD	AV	SD	AV	AV
D-AC	234	8.1	152	2.4	1.76	0.37	1.45	267
D-SHT	266	10.1	141	4.5	4.36	0.13	4.05	387
D1-155°C-2hrs	300	5.2	216	3.8	2.42	0.29	2.07	364
D5-155°C-10hrs	348	3.9	294	7.4	1.28	0.14	0.86	335
D13-155°C-100hrs	333	7.2	316	4.8	0.81	0.10	0.40	253
D14-170°C-2hrs	321	5.5	269	2.4	1.35	0.18	0.95	317
D18-170°C-10hrs	336	7.5	304	3.5	0.94	0.13	0.54	281
D26-170°C-100hrs	330	4.7	314	8.6	0.81	0.06	0.40	250
D27-190°C-2hrs	350	1.0	309	4.0	1.08	0.04	0.65	313
D31-190°C-10hrs	310	4.3	295	1.2	0.79	0.05	0.40	231
D39-190°C-100hrs	302	0.3	264	2.5	1.32	0.14	0.95	297
D40-240°C-2hrs	289	8.0	255	3.9	1.06	0.21	0.69	257
D44-240°C-10hrs	261	5.6	203	1.4	1.74	0.19	1.41	291
D52-240°C-100hrs	224	3.9	136	2.3	3.13	0.41	2.85	315
D53-300°C-2hrs	229	4.6	144	2.9	2.64	0.31	2.35	303
D57-300°C-10hrs	207	6.6	110	1.9	3.52	0.39	3.23	309
D65-300°C-100hrs	180	4.6	79	0.6	5.19	0.55	4.85	318
D66-350°C-2hrs	195	4.3	92	1.7	3.70	0.26	3.44	303
D70-350°C-10hrs	200	4.3	87	2.0	4.49	0.61	4.08	322
D78-350°C-100hrs	191	3.4	79	1.3	5.42	0.55	5.06	332
E-AC	235	2.7	162	1.7	1.44	0.09	1.13	246
E-SHT	268	6.7	156	0.9	3.86	0.26	3.51	377
E1-155°C-2hrs	282	6.1	202	5.1	2.22	0.25	1.87	336
E5-155°C-10hrs	347	4.9	300	3.1	1.16	0.07	0.73	320
E13-155°C-100hrs	359	3.4	333	3.2	0.85	0.06	0.41	277
E14-170°C-2hrs	324	7.7	268	3.8	1.46	0.18	1.07	330
E18-170°C-10hrs	367	8.3	322	6.2	1.18	0.04	0.75	342
E26-170°C-100hrs	347	9.0	328	3.9	0.87	0.13	0.45	277
E27-190°C-2hrs	340	5.4	304	6.7	0.98	0.04	0.56	289
E31-190°C-10hrs	336	4.7	313	3.9	0.85	0.08	0.43	263
E39-190°C-100hrs	286	8.0	254	2.5	1.13	0.18	0.76	263
E40-240°C-2hrs	313	5.2	266	3.0	1.46	0.23	1.08	320
E44-240°C-10hrs	264	2.7	198	3.2	2.10	0.25	1.77	313
E52-240°C-100hrs	214	6.2	127	3.1	2.97	0.48	2.66	299
E53-300°C-2hrs	225	12.2	139	4.3	2.59	0.56	2.27	297
E57-300°C-10hrs	202	2.9	103	2.8	3.70	0.58	3.37	307
E65-300°C-100hrs	185	6.0	83	1.6	4.54	1.15	4.20	309
E66-350°C-2hrs	204	3.3	95	2.1	3.95	0.40	3.61	315
E70-350°C-10hrs	202	3.2	85	1.3	4.70	0.49	4.03	322
E78-350°C-100hrs	190	3.8	82	1.3	4.57	0.51	4.23	315

Table I-3 Mean values of UTS and YS (MPa) and Plastic strain used to obtain Q (from equation 2.10) using a single K=500 MPa for Alloys F and G

Mean values of UTS and YS (MPa) and Plastic strain used to obtain Q (from equation 2.10) using a single K=500 MPa for Alloys F and G.

$$\mathbf{Q = UTS + 0.4K \cdot \log (S_f)} \qquad \text{Equation 2.10}$$

Identification	UTS (MPa)		YS (MPa)		Total Strain S_T (%)		Plastic Strain S_f (%)	Q (MPa) (Eq.2.10)
	AV	SD	AV	SD	AV	SD	AV	SD
F-AC	246	16.6	162	7.8	1.66	0.26	1.34	271
F-SHT	254	2.3	139	3.3	3.94	0.33	3.61	365
F1-155°C-2hrs	291	3.8	204	4.0	2.44	0.12	2.08	355
F5-155°C-10hrs	351	4.9	305	8.9	1.08	0.08	0.65	314
F13-155°C-100hrs	359	9.7	340	7.0	0.83	0.11	0.40	280
F14-170°C-2hrs	322	10.1	259	2.4	1.55	0.41	1.16	335
F18-170°C-10hrs	345	4.4	324	3.4	0.83	0.03	0.41	268
F26-170°C-100hrs	337	7.1	318	6.3	0.83	0.01	0.42	262
F27-190°C-2hrs	350	6.7	313	7.5	0.99	0.12	0.56	300
F31-190°C-10hrs	342	6.2	316	2.6	0.86	0.09	0.43	269
F39-190°C-100hrs	286	4.5	266	4.6	0.83	0.05	0.45	217
F40-240°C-2hrs	304	6.5	265	3.0	1.17	0.17	0.76	280
F44-240°C-10hrs	260	9.8	205	2.5	1.60	0.20	1.24	278
F52-240°C-100hrs	201	2.2	122	3.7	2.50	0.27	2.19	269
F53-300°C-2hrs	227	6.6	138	1.5	2.67	0.42	2.32	300
F57-300°C-10hrs	202	5.4	105	2.7	3.53	0.32	3.23	304
F65-300°C-100hrs	182	3.7	79	2.1	4.89	0.46	4.51	313
F66-350°C-2hrs	205	4.7	101	0.5	3.66	0.62	3.34	310
F70-350°C-10hrs	198	3.2	84	1.1	4.73	0.09	4.37	326
F78-350°C-100hrs	186	10.0	85	1.5	3.92	1.04	3.55	296
G-AC	241	6.6	162	5.6	1.47	0.29	1.15	253
G-SHT	290	6.6	161	1.9	4.1	0.47	3.72	404
G1-155°C-2hrs	302	1.4	205	5.3	2.78	0.13	2.39	377
G5-155°C-10hrs	357	5.7	297	13.1	1.30	0.20	0.85	343
G13-155°C-100hrs	352	1.7	344	10.4	0.84	0.09	0.40	273
G14-170°C-2hrs	319	4.2	256	4.7	1.66	0.18	1.24	338
G18-170°C-10hrs	348	3.3	318	4.0	0.94	0.06	0.49	286
G26-170°C-100hrs	328	8.2	313	6.8	0.83	0.14	0.41	253
G27-190°C-2hrs	348	6.7	308	4.3	1.06	0.13	0.61	305
G31-190°C-10hrs	341	7.6	319	3.7	0.85	0.17	0.42	265
G39-190°C-100hrs	293	6.0	252	7.1	1.30	0.07	0.92	285
G40-240°C-2hrs	302	4.9	258	3.3	1.29	0.21	0.92	295
G44-240°C-10hrs	264	2.9	189	3.7	2.24	0.25	1.88	319
G52-240°C-100hrs	217	5.0	128	3.0	3.11	0.43	2.79	306
G53-300°C-2hrs	222	7.0	131	2.9	2.81	0.29	2.48	301
G57-300°C-10hrs	203	5.6	105	1.7	3.57	0.51	3.23	305
G65-300°C-100hrs	193	5.1	87	1.7	4.78	0.61	4.38	322
G66-350°C-2hrs	224	4.2	103	2.2	4.91	0.10	4.53	356
G70-350°C-10hrs	213	4.4	93	1.2	4.96	0.51	4.53	344
G78-350°C-100hrs	200	4.8	88	1.7	4.73	0.76	4.33	327

Table I-4 Mean values of UTS and YS (MPa) and Plastic strain used to obtain Q (from equation 2.10) using a single K=500 MPa for Alloys B, C, D, E, F, and G at aging temperature of 190°C

$Q = UTS + 0.4K \cdot \log(S_f)$ Equation 2.10								
Identification	UTS (MPa)		YS (MPa)		Total Strain S_T (%)		Plastic Strain S_f (%)	Q (MPa) (Eq.2.10)
	AV	SD	AV	SD	AV	SD	AV	AV
B-200HRS	274	16.2	229	10.3	1.52	0.61	1.15	286
C-200HRS	301	13.2	241	9.2	2.15	0.45	1.74	350
D-200HRS	285	3.2	242	3.0	1.33	0.21	0.94	280
E-200HRS	275	2.1	227	2.0	1.60	0.01	1.19	290
F-200HRS	298	3.3	256	3.1	1.40	0.1	1.00	298
G-200HRS	294	2.2	240	2.1	1.56	0.1	1.16	308
B-600HRS	248	14.5	176	11.3	2.38	0.56	2.03	310
C-600HRS	251	13.2	180	10.2	2.47	0.65	2.12	316
D-600HRS	259	2.3	209	2.2	1.69	0.12	1.33	284
E-600HRS	246	3.1	180	2.9	2.19	0.13	1.84	299
F-600HRS	250	4.5	178	4.3	2.26	0.12	1.98	310
G-600HRS	244	2.3	158	2.2	2.40	0.14	2.05	306
B-1000HRS	229	15.3	152	12.3	2.97	0.62	2.63	313
C-1000HRS	243	12.3	162	11.2	3.28	0.58	2.91	336
D-1000HRS	228	4.6	148	4.1	2.82	0.2	2.48	307
E-1000HRS	215	6.5	130	3.6	3.29	0.13	2.97	310
F-1000HRS	235	4.6	159	4.1	2.47	0.16	2.11	300
G-1000HRS	253	2.1	156	2.0	3.46	0.19	3.08	351

Table I-5 Q values using Equation 2.9, K and n values obtained from single sample plots σ-ε for Alloys B, C, D, E, F and G for aging at 190°C

$Q = K\,[(qn)^n e^{-qn} + 0.4 \log (100\,qn)]$ Equation 2.9 $\%Error = ([Q_{Eq.2.10} - Q_{Eq.2.9}]/Q_{Eq.2.9}) \cdot 100$ Equation 5.1					
Identification	K	n	q	Q (MPa) (Eq. 2.9)	% Error (Eq. 6.x)
B-200HRS	497	0.1234	0.093	295	2.94
C-200HRS	467	0.1064	0.164	343	1.84
D-200HRS	504	0.1164	0.081	285	1.88
E-200HRS	481	0.1241	0.096	289	0.64
F-200HRS	474	0.0979	0.102	299	0.22
G-200HRS	494	0.1147	0.101	306	0.55
B-600HRS	437	0.1402	0.145	302	2.70
C-600HRS	418	0.1378	0.154	295	7.15
D-600HRS	499	0.1411	0.094	292	2.90
E-600HRS	439	0.1355	0.136	297	0.70
F-600HRS	460	0.1484	0.133	307	0.97
G-600HRS	474	0.1686	0.122	300	1.99
B-1000HRS	441	0.1744	0.151	302	3.56
C-1000HRS	438	0.1645	0.177	319	5.36
D-1000HRS	443	0.1638	0.151	306	0.44
E-1000HRS	434	0.2003	0.148	290	6.69
F-1000HRS	444	0.1635	0.129	289	3.84
G-1000HRS	502	0.1907	0.162	349	0.62

Table I-6 Q values using Equation 2.9, K and n values obtained from single sample plots σ-ε for Alloys B and C

$Q = K\,[(qn)^n e^{-qn} + 0.4 \log(100\,qn)]$ Equation 2.9 $\%Error = ([Q_{Eq.2.10} - Q_{Eq.2.9}]/Q_{Eq.2.9}) \cdot 100$ Equation 5.1					
Identification	K	n	q	Q (MPa) (Eq. 2.9)	% Error (Eq. 6.x)
B-AC	590	0.211	0.072	282	6.17
B-SHT	515	0.204	0.232	402	2.81
B1-155°C-2hrs	520	0.1482	0.196	395	5.97
B5-155°C-10hrs	516	0.0765	0.130	359	7.67
B13-155°C-100hrs	481	0.0479	0.145	346	5.89
B14-170°C-2hrs	499	0.0823	0.156	366	5.40
B18-170°C-10hrs	540	0.082	0.065	290	0.30
B26-170°C-100hrs	467	0.0596	0.089	289	3.44
B27-190°C-2hrs	554	0.081	0.093	343	5.63
B31-190°C-10hrs	476	0.0559	0.084	289	3.89
B39-190°C-100hrs	531	0.1062	0.084	308	3.26
B40-240°C-2hrs	585	0.1392	0.073	308	5.33
B44-240°C-10hrs	559	0.1789	0.103	329	2.56
B52-240°C-100hrs	487	0.1897	0.122	304	4.66
B53-300°C-2hrs	504	0.21	0.229	391	11.10
B57-300°C-10hrs	507	0.2411	0.125	308	3.44
B65-300°C-100hrs	439	0.2811	0.178	302	9.23
B66-350°C-2hrs	536	0.2821	0.181	372	3.59
B70-350°C-10hrs	497	0.2766	0.193	354	1.09
B78-350°C-100hrs	539	0.3264	0.186	372	7.60
C-AC	588	0.213	0.084	304	4.59
C-SHT	516	0.19	0.260	421	0.04
C1-155°C-2hrs	518	0.1461	0.191	391	0.82
C5-155°C-10hrs	517	0.0743	0.113	343	4.44
C13-155°C-100hrs	467	0.051	0.122	320	0.74
C14-170°C-2hrs	500	0.0912	0.143	355	2.42
C18-170°C-10hrs	560	0.0797	0.052	274	1.15
C26-170°C-100hrs	467	0.0659	0.167	351	3.70
C27-190°C-2hrs	550	0.079	0.137	388	2.86
C31-190°C-10hrs	489	0.0559	0.095	309	8.35
C39-190°C-100hrs	535	0.108	0.114	348	13.23
C40-240°C-2hrs	578	0.128	0.124	381	8.65
G44-240°C-10hrs	589	0.1761	0.096	336	7.44
C52-240°C-100hrs	486	0.1979	0.158	333	0.53
C53-300°C-2hrs	500	0.23	0.144	325	5.09
C57-300°C-10hrs	499	0.2412	0.168	342	1.34
C65-300°C-100hrs	450	0.2911	0.177	309	9.28
C66-350°C-2hrs	545	0.2698	0.166	367	4.49
C70-350°C-10hrs	502	0.28	0.149	322	1.80
C78-350°C-100hrs	534	0.3213	0.206	384	5.42

Table I-7 Q values using Equation 2.9, K and n values obtained from single sample plots σ-ε for Alloys D and E

$Q = K\,[(qn)^n e^{-qn} + 0.4 \log(100\,qn)]$ Equation 2.9 $\%Error = ([Q_{Eq.2.10} - Q_{Eq.2.9}]/Q_{Eq.2.9}) \cdot 100$ Equation 5.1					
Identification	K	n	q	Q (MPa) (Eq. 2.9)	% Error (Eq. 6.x)
D-AC	580	0.21	0.069	273	2.21
D-SHT	518.6	0.2177	0.186	374	3.86
D1-155°C-2hrs	465	0.1116	0.186	354	2.58
D5-155°C-10hrs	452	0.0595	0.144	326	2.76
D13-155°C-100hrs	453	0.0561	0.060	243	1.68
D14-170°C-2hrs	440	0.0709	0.135	310	2.30
D18-170°C-10hrs	453	0.0596	0.090	281	0.24
D26-170°C-100hrs	426	0.0496	0.080	254	1.84
D27-190°C-2hrs	530	0.0883	0.074	298	4.88
D31-190°C-10hrs	439	0.075	0.042	196	7.22
D39-190°C-100hrs	449	0.0871	0.109	292	1.66
D40-240°C-2hrs	618	0.1457	0.047	258	0.18
D44-240°C-10hrs	488	0.1406	0.101	294	1.03
D52-240°C-100hrs	445	0.191	0.149	300	4.94
D53-300°C-2hrs	518	0.203	0.116	313	3.20
D57-300°C-10hrs	506	0.2461	0.131	314	1.56
D65-300°C-100hrs	472	0.2928	0.166	315	0.84
D66-350°C-2hrs	424	0.234	0.147	277	9.23
D70-350°C-10hrs	507	0.2829	0.144	321	0.32
D78-350°C-100hrs	457	0.2823	0.179	316	5.09
E-AC	589	0.2005	0.056	250	1.52
E-SHT	519	0.2177	0.161	355	6.31
E1-155°C-2hrs	427	0.1147	0.163	312	7.72
E5-155°C-10hrs	475	0.0675	0.109	313	2.24
E13-155°C-100hrs	577	0.0822	0.047	268	2.92
E14-170°C-2hrs	492	0.0906	0.118	329	0.30
E18-170°C-10hrs	472	0.0584	0.128	328	4.04
E26-170°C-100hrs	511	0.0682	0.066	281	1.31
E27-190°C-2hrs	590	0.1041	0.054	283	2.36
E31-190°C-10hrs	532	0.0847	0.051	256	2.69
E39-190°C-100hrs	430	0.082	0.093	266	1.19
E40-240°C-2hrs	534	0.1093	0.099	329	2.85
E44-240°C-10hrs	477	0.1414	0.125	312	0.35
E52-240°C-100hrs	510	0.2257	0.118	306	2.34
E53-300°C-2hrs	448	0.1854	0.123	281	5.51
E57-300°C-10hrs	504	0.2585	0.130	309	0.67
E65-300°C-100hrs	405	0.2445	0.172	280	10.46
E66-350°C-2hrs	600	0.3042	0.119	344	8.45
E70-350°C-10hrs	495	0.275	0.146	316	1.88
E78-350°C-100hrs	551	0.3204	0.132	330	4.50

Table I-8 Q values using Equation 2.9, K and n values obtained from single sample plots σ-ε for Alloys F and G

$Q = K\,[(qn)^n e^{-qn} + 0.4 \log (100\,qn)]$ $\%Error = ([Q_{Eq.2.10} - Q_{Eq.2.9}]/Q_{Eq.2.9}) \cdot 100$				Equation 2.9 Equation 5.1	
Identification	K	n	q	Q (MPa) (Eq. 2.9)	% Error (Eq. 6.x)
F-AC	583	0.2124	0.063	259	4.48
F-SHT	528	0.2081	0.173	372	1.90
F1-155°C-2hrs	435	0.1043	0.199	340	4.44
F5-155°C-10hrs	431	0.0465	0.140	307	2.45
F13-155°C-100hrs	434	0.0349	0.097	273	3.05
F14-170°C-2hrs	430	0.0724	0.160	319	5.03
F18-170°C-10hrs	520	0.0728	0.056	266	0.52
F26-170°C-100hrs	438	0.0492	0.081	263	1.91
F27-190°C-2hrs	424	0.0432	0.130	295	1.94
F31-190°C-10hrs	485	0.0663	0.065	266	1.18
F39-190°C-100hrs	501	0.1037	0.043	216	0.60
F40-240°C-2hrs	463	0.0867	0.088	279	0.40
F44-240°C-10hrs	504	0.1411	0.088	286	2.78
F52-240°C-100hrs	432	0.2025	0.108	254	6.13
F53-300°C-2hrs	550	0.2263	0.103	310	3.09
F57-300°C-10hrs	509	0.2525	0.128	311	2.32
F65-300°C-100hrs	573	0.3361	0.134	343	8.75
F66-350°C-2hrs	553	0.2781	0.120	324	4.28
F70-350°C-10hrs	660	0.3544	0.123	377	13.54
F78-350°C-100hrs	715	0.3787	0.094	352	15.98
G-AC	629	0.214	0.054	255	0.47
G-SHT	536	0.1855	0.200	403	0.39
G1-155°C-2hrs	410	0.0925	0.258	345	9.21
G5-155°C-10hrs	490	0.0686	0.124	337	1.80
G13-155°C-100hrs	430	0.0366	0.072	245	3.58
G14-170°C-2hrs	365	0.0466	0.267	308	9.72
G18-170°C-10hrs	460	0.0556	0.088	284	0.98
G26-170°C-100hrs	500	0.0745	0.052	248	0.38
G27-190°C-2hrs	490	0.0682	0.090	302	1.17
G31-190°C-10hrs	440	0.0532	0.078	260	1.87
G39-190°C-100hrs	420	0.076	0.121	285	0.03
G40-240°C-2hrs	550	0.118	0.078	305	3.37
G44-240°C-10hrs	430	0.1237	0.152	305	4.46
G52-240°C-100hrs	380	0.1466	0.190	286	6.82
G53-300°C-2hrs	600	0.2505	0.099	327	7.92
G57-300°C-10hrs	526	0.2599	0.124	316	3.38
G65-300°C-100hrs	460	0.2634	0.166	311	3.32
G66-350°C-2hrs	640	0.3107	0.146	402	11.56
G70-350°C-10hrs	572	0.3017	0.150	365	5.65
G78-350°C-100hrs	740	0.3851	0.113	400	18.25